THE SYNTHESIS OF *N*-ACETYLLACTOSAMINE FUNCTIONALIZED DENDRIMERS, AND THE FUNCTIONALIZATION OF SILICA SURFACES USING TUNABLE DENDRONS AND *β*–CYCLODEXTRINS

by

Jessica Helen Ennist

A dissertation submitted in partial fulfillment
of the requirements for the degree

of

Doctor of Philosophy

in

Chemistry

MONTANA STATE UNIVERSITY
Bozeman, Montana

July 2017

DEDICATION

This dissertation is dedicated to my family, for their unconditional love and encouragement.

ACKNOWLEDGEMENTS

I would like to thank my advisor, Dr. Mary Cloninger, for her constant encouragement and support. I am grateful for her continual guidance and sacrifice of her time. I would like to thank the members of the Cloninger group: Dr. Anna Michel, Dr. Candace Goodman, Dr. Amanda Mattson, Harrison VanKoten, Dr. Jon Cousin, Sam Bernhard, Mackenzie Fricke, Jessi Langlais, and undergraduates who have been supportive throughout my PhD career. Thank you to Dr. Kristian Schlick and Garrett Moraski for guidance in the laboratory. I would like to thank Dr. Recep Avci and ICAL staff for their guidance and training in XPS and Auger spectroscopy. I would also like to thank Dr. Eric A. Gobrogge for the work he performed with me on the surface chemistry project and for his friendship. Thank you to Dr. Thomas Nicholas Jones and his group members for providing the catalyst functionalized dendrimers used for experiments described in chapter 5. Thank you to Kyle Tweedy for his assistance with cellular assay data analysis. I would like to thank the members of my committee: Dr. Robert Walker, Dr. Tom Livinghouse, and Dr. Brian Bothner for their continuous support and guidance in my pursuit of a PhD. I would like to thank my mentors, especially my undergraduate mentor Dr. Duncan Quarless and my aunt Renee Danboise, for cultivating my love for research. Finally, I would like to thank my family and friends, who have been like family, for their constant love and support.

TABLE OF CONTENTS

TABLE OF CONTENTS — CONTINUED

TABLE OF CONTENTS — CONTINUED

TABLE OF CONTENTS — CONTINUED

LIST OF TABLES

Table Page

LIST OF FIGURES — CONTINUED

LIST OF FIGURES — CONTINUED

Figure Page

LIST OF FIGURES — CONTINUED

Figure Page

LIST OF FIGURES — CONTINUED

Figure Page

LIST OF FIGURES — CONTINUED

Figure Page

LIST OF FIGURES — CONTINUED

Figure Page

LIST OF FIGURES — CONTINUED

Figure Page

LIST OF FIGURES — CONTINUED

Figure Page

LIST OF FIGURES — CONTINUED

Figure Page

LIST OF FIGURES — CONTINUED

Figure Page

LIST OF FIGURES — CONTINUED

Figure Page

LIST OF FIGURES — CONTINUED

Figure Page

LIST OF FIGURES — CONTINUED

Figure Page

LIST OF EQUATIONS

Equation Page

LIST OF SCHEMES

Scheme Page

ABSTRACT

Galectin-3 is *β*-galactoside binding protein which is found in many healthy cells. In cancer, the galectin-3/tumor-associated Thomsen-Friedenreich antigen (TF antigen) interaction has been implicated in heterotypic and homotypic cellular adhesion and apoptotic signaling pathways. However, a stronger mechanistic understanding of the role of galectin-3 in these processes is needed. *N*-acetyllactosamine (Lac*N*Ac) is a non-native ligand for galectin-3 which binds with comparable affinity to the TF antigen and therefore an important ligand to study galectin-3 mediated processes.

To study galectin-3 mediated homotypic cellular aggregation, four generations of polyamidoamine (PAMAM) dendrimers were functionalized with *N*-acetyllactosamine using a four-step chemoenzymatic route. The enzymatic step controlled the regiochemistry of the galactose addition to *N*-acetylglucosamine functionalized dendrimers using a recombinant *β*-1,4-Galactosyltransferase-/UDP-4‘-Gal Epimerase Fusion Protein (lgtB-galE). Homotypic cellular aggregation, which is promoted by the presence of galectin-3 as it binds to glycosides at the cell surface, was studied using HT-1080 fibrosarcoma, A549 lung, and DU-145 prostate cancer cell lines. In the presence of small Lac*N*Ac functionalized PAMAM dendrimers, galectin-3 induced cancer cellular aggregation was inhibited. However, the larger glycodendrimers induced homotypic cellular aggregation.

Additionally, novel poly(aryl ether) dendronized silica surfaces designed for reversible adsorbtion of targeted analytes were synthesized, and characterization using X-ray Photoelectron Spectroscopy (XPS) was performed. Using a Cu(I) mediated cycloaddition “click” reaction, *β*-cyclodextrin was appended to dendronized surfaces via triazole formation and also to a non-dendronized surface for comparison purposes. First generation G(1) dendrons have more than 6 times greater capacity to adsorb targeted analytes than slides functionalized with monomeric *β*-cyclodextrin and are 2 times greater than slides functionalized with larger generation dendrons. This study reported *β*-cyclodextrin functionalized surfaces can undergo a triggered release of the adsorbent, but otherwise retained the targeted analyte through multiple aqueous washes. Therefore, a new generation of G(1) dendronized surfaces capable of reversible adsorption were developed by heterogeneously appending sulfonic acid/pyridine end-groups. Auger Electron Spectroscopy (AES) was used to quantify the ratio of groups installed. Furthermore, G(1) dendronized surfaces were functionalized homogenously with sulfonic acid and pyridine for comparison and with chiral amino acids for chiral recognition studies.

CHAPTER ONE

INTRODUCTION TO MOLECULAR RECOGNITION AND CATALYSIS IN SUPRAMOLECULAR SYSTEMS

Molecular Recognition in Supramolecular Systems

The field of supramolecular chemistry broadly includes the interdisciplinary study, design, and synthesis of molecular assemblies that endow novel functionalities that can direct selective recognition, catalytic and chemical reactivity, and the transfer of energy or molecular information through means of various noncovalent intermolecular forces.[1, 2] Although these individual interactions are inherently weak, for example 2 to 4 kJ mol^{-1} for van der Waals interactions, compared to ionic or covalent bond strengths (418 kJ mol^{-1} for a covalent bond between hydrogen and carbon and 786 kJ mol^{-1} for the measured lattice energy for NaCl), complex molecular structures in nature have evolved to utilize multivalent forces in many biological processes.[3, 4] Non-covalent interactions facilitate substrate binding in signaling pathways or on cell membranes, for protein folding, and in biological architectures such as the double stranded helical structure of DNA.[5-10] Early developments of synthetic systems include crown ethers, spherands, and cryptands[11-13] which contained molecular assemblies that used both non-specific and specific interactions for selective recognition (Figure 1). These systems set the precedence for the development of complex synthetic supramolecular systems, self-assemblies, biomaterials and nanomaterials.[14]

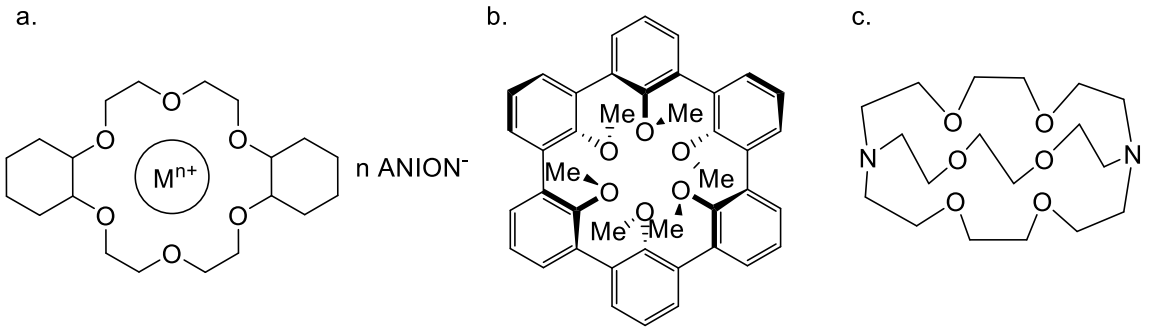

Figure 1. Schematic of molecular recognition complexes (a) Crown ether complex. Adapted with permission from Pedersen *et al* [9]. Copyright (1967) American Chemical Society. (b) Cram's guest host complex. Adapted with permission from Cram *et al*[10]. Copyright (1985) American Chemical Society. (c) Lehn's cryptand. Adapted with permission from Dietrich *et al* [11]. Copyright (1969) Tetrahedron Letters.

Molecular recognition is the interaction between two or more molecules that bind non-covalently through interactions such as van der Waal forces, π-stacking, hydrogen bonding, electrostatic, hydrophobic, hydrophilic, and steric interaction. These non-covalent interactions determine the selectivity of the receptor for the substrate and the length of time the complexation occurs. Traditionally, the approach for selectivity in supramolecular systems was driven by the design of the receptor. However, this has since been broadened to include ligand design and the microenvironment of the interaction. These approaches have been extensively discussed in notable reviews.[2, 15-17] Using either approach, the specificity of the complex can be tuned to be stereospecific, selectively bind targeted biological substrates, ions, or classes of compounds.

The length of time the association between ligand and receptor occurs is greatly influenced by the non-covalent interactions involved in the guest-host complex. These forces can range in strength from approximately 2 kJ mol^{-1} for dipole-induced dipole

interactions to 42 kJ mol^{-1} for very short, strong hydrogen bonds. Although these non-covalent intermolecular forces are relatively weak when compared to ionic (335-1050 kJ mol^{-1}) or covalent (63-920 kJ mol^{-1}) bonds, this enables the reversibility of many ligand-substrate complexes, although multiple interactions can be involved. [18, 19] Reversibility can be an attractive quality for applications of synthetic frameworks and materials. In many systems there is a direct correlation between increasing association constants and additional positive interactions. However, even with multiple forces enhancing the interaction, these monomeric binding events can still be relatively weak with measured disassociation constants (K_D) in the micromolar range. Because of the relative weakness of these associations, they are not physiologically relevant in biological pathways. Therefore nature has evolved to use multiple recognition events to increase the affinity and specificity over the monomeric recognition event.

Multivalent Interactions

Multivalency is defined by multiple molecular recognition events that occur between multiple ligands displayed on one framework, whether biological or synthetic, and an array of receptors on a secondary framework.[20-22] This term is used to describe a wide variety of interactions, some of which are depicted in Figure 2.

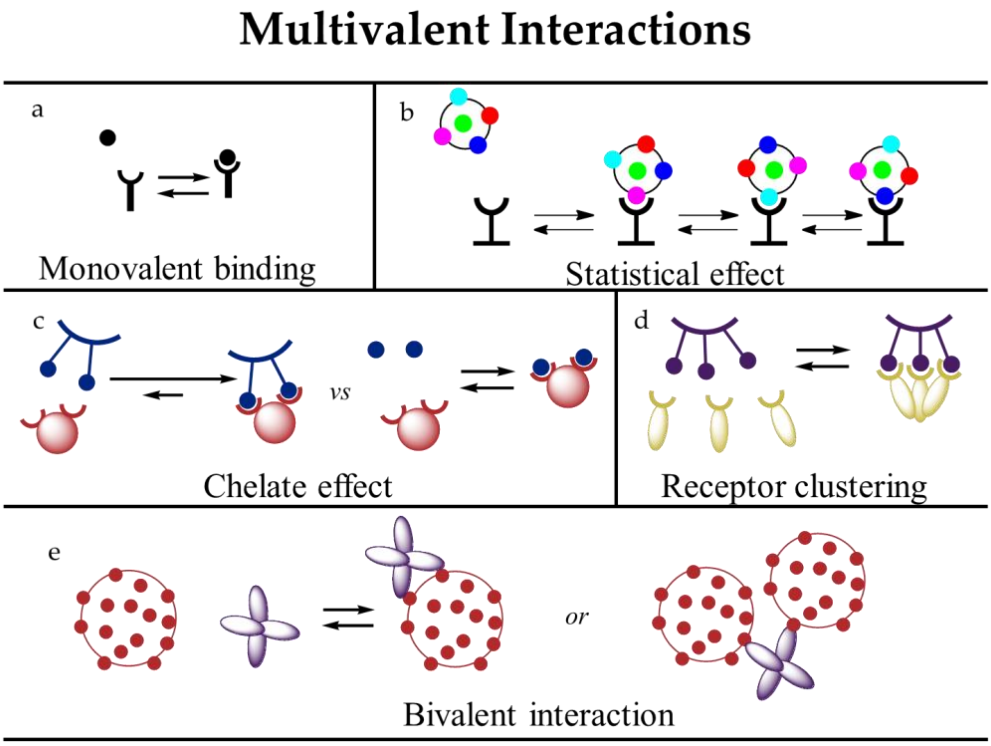

Figure 2: Schematic of different types of multivalent interactions.

The statistical effect, which is depicted in Figure 2b, can be envisioned as a framework which displays multiple copies of the same ligand that bind to a receptor binding site. The first ligand complexes with the receptor for a period of time and then disassociates from the receptor. Unlike a monovalent binding event (Figure 2a), once this binding event occurs and the ligand diffuses away there is a second ligand in close proximity to the first which is available to bind. This can continue to repeat with the ligands that are displayed on the framework, effectively increasing the time the framework is associated with the receptor.

The chelate effect (Figure 2c) describes the cooperative entropic stability of the complexation of two tethered ligands over the binding of the two monovalent ligands. In molecular recognition events where two substrates are required to bind to one receptor, the entropic energy associated with bringing three entities together in a sterically congested environment can be significant to the overall thermodynamics of the binding event. Assuming positive cooperativity and an overall negative change in enthalpy between the bound and unbound states, an appropriate linker between two or more ligands can reduce the entropic energy of the second binding event.[23]

Receptor clustering, which is represented in Figure 2d, is the result of multiple ligands bound to an array of receptors. As the ligands bind to the receptors, the receptors are reorganized. This re-patterning of receptors is involved in a variety of cellular mechanisms such as homotypic cellular aggregation, chemotaxis, and signaling pathways.[24-28]

In a bivalent interaction (Figure 2e) two frameworks which display multiple ligands can bind intramolecularly to a single oligovalent receptor, or a single framework can bind bivalently to the same receptor. One can envision the preference for either interaction is impacted by the thermodynamic stability of the complex which is influenced by the distance between the bound and unbound ligands, the distance between the receptors, and the rigidity of the scaffolds.

This is by no means meant to be a comprehensive list of all multivalent interactions. Within this small representation of multivalent methods of interacting one could envision various iterations of a single example such as varying the nature of the

ligand/receptor event, displaying the ligands and receptors heterogeneously, and diversifying the scaffolds. It is this accessible variability in multivalent recognition events which is used to enhance selectivity and avidity in many biological signaling pathways such as cell-cell recognition, innate immune responses, virus and bacterium mediated cascade events, and cancer cell recognition.[29-32]

Dendrimers

Dendrimers are highly branched, symmetrical molecules formed by a reiterative synthesis that increases the size of the polymer and the number of terminal groups with every reaction cycle. Dendrimers have been synthesized with two general approaches, and are shown schematically in Figure 3.[33] The divergent synthesis of a dendrimer, first reported by Fritz Vögtle in 1978, described the synthesis of large cavities that had the ability to form guest-host interactions with targeted ions or molecules as the "cascade like" or "nonskid-chain-like" pathway. [34] The reiterative synthesis started with a reaction of a diamine and acrylonitrile which efficiently added two cyano end groups to every amine available. The cyano groups were reduced by cobalt(II) ion-catalyzed reduction regenerating new terminal amines that could further undergo the repetitive transformation.

Using the reiterative synthetic approach for the synthesis of dendrimer subunits followed by their attachment to a central core, the convergent synthesis was described by Fréchet and Hawker in 1990.[35] Dendrons (Figure 3b) were synthesized from a core

monomer which could be enlarged in the same way by repetitive sequential synthetic steps. As with the divergent synthesis, this exponentially increased the number of terminal end-groups as well. In a final step, the dendrons were "converged" by ligation to yield a symmetrical dendrimer.

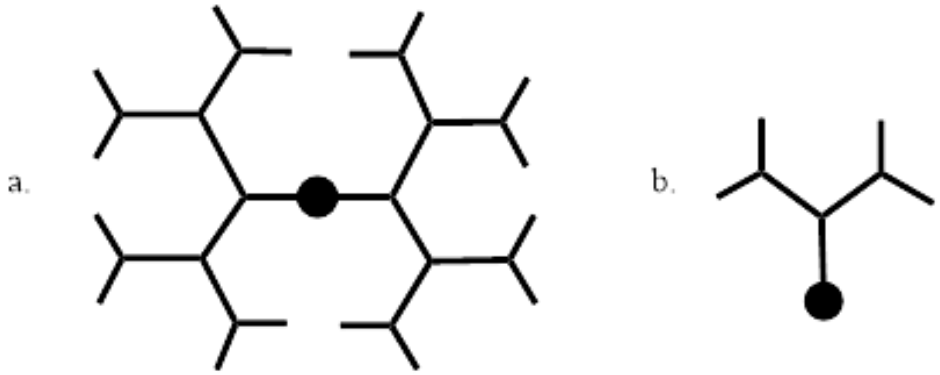

Figure 3: Schematic representation of a (a) dendrimer and (b) dendron.

Poly(amido amine) (PAMAM) dendrimers (Figure 4) are dynamic polymers first synthesized by Tomalia *et al* by a divergent synthesis using a sequence of reiterative steps. [36] The first generation of PAMAM (G0 PAMAM) dendrimer is synthesized by Michael additions of a methyl ester acrylate to an amine core followed by an amidation reaction with ethylene diamine (Figure 4 black core). Each time these steps are repeated, a new generation of PAMAM dendrimer is produced and the number of terminal amino groups accessible for functionalization is doubled (Figure 4 generation 1 and generation 2). Each new generation is produced uniformly and is systematically increased by 1 nm in diameter with a measured polydispersity (M_w/M_n) of approximately 1.0 where M_w is the weighted average molecular weight of the PAMAM and M_n is the number average molecular weight.[37]

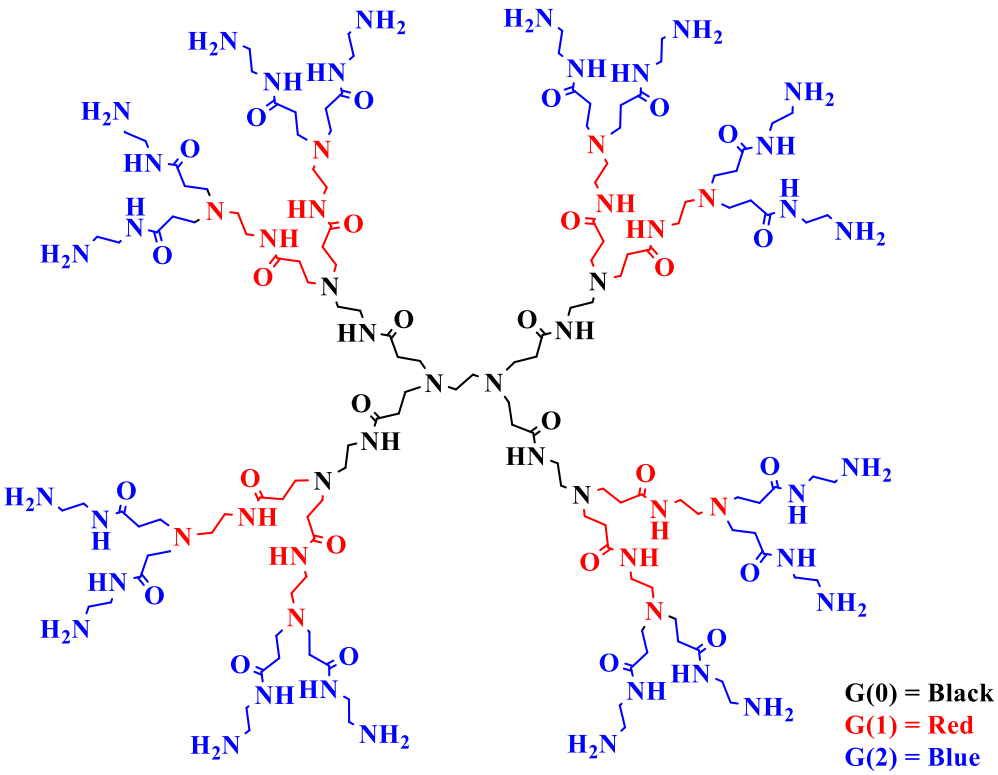

Figure 4: Schematic of a G(2) polyamidoamine dendrimer.

The repeating units of the PAMAM architecture mimic a protein backbone which provides a flexible and dynamic scaffold. This scaffold shows conformational changes but structural stability in a range of pH, ionic strengths, and solvent polarity.[33] Through functionalization or masking of the cationic end groups, these scaffolds are non-cytotoxic, biocompatible, and non-immunogenic.[38-40] Their availability in a diverse range of sizes and surface functionality, flexibility, and biopermeability has allowed them to be dependable platforms for biomimicry, nanomedicine, as encapsulation vessels and chelates for diagnostic imaging agents, as well as for therapeutic delivery.[41-46]

Molecular Recognition with PAMAM Dendrimers

Galectin-3.

Lectins are a family of proteins that contain recognition domains that specifically bind carbohydrates. Within this family of carbohydrate binding proteins, a major group called galectins consists of fourteen known proteins that recognize carbohydrates with a terminal β-galactoside.[47] All galectins contain a highly conserved carbohydrate recognition domain (CRD). For all known galectins, either they contain a mono-CRD as with galectin-1, 2, 3, 5, 7, 10, 13, 14, and 15 or two CRD as with galectin-4, 6, 8, 9, and 12. Galectin-3 is the only member of the galectins in invertebrates defined as a chimera type. Galectin-3 has a second N-terminal, collagen like domain which distinguishes this protein in this class (Figure 5). This terminal collagen like tail is currently considered unstructured. Galectin-3 is known to dimerize through non-covalent interactions between the tails of the monomeric proteins. Higher oligomerization states have also been reported when the concentration has been increased. [47-49]

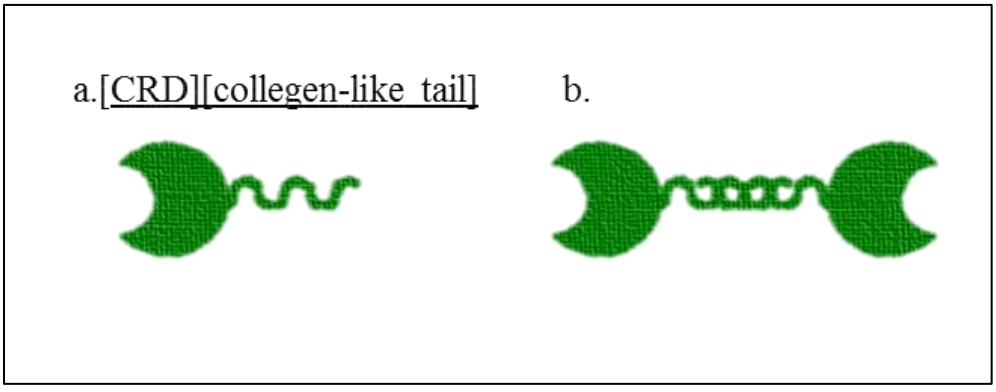

Figure 5: Schematic representation of galectin-3. a. CRD and N-terminal domain. b. Dimeric form of galectin-3.

Galectin-3 is an intra- and extracellular protein which has been implicated in the regulation of inflammation, mRNA splicing, adhesion, and apoptotic signaling pathways.[48, 50, 51] During pathological expression, this protein has been shown to be up-regulated in many types of cancer. It has been demonstrated to play a role both in apoptotic signaling pathways and homotypic and heterotypic cell adhesion in metastatic cancer.[52-56] Zhao *et al.* reported galectin-3 mediated cancer cellular aggregation is promoted as it binds to a heavily glycosylated transmembrane protein, Mucin-1(MUC-1), at the cell surface.[24, 57] MUC-1 which is typically found on the apical face of healthy epithelial cells, is found to be over expressed and covering the entire cellular surface of carcinoma cells. In addition to this, MUC-1 on carcinoma cells has been shown to have aberrant glycosylation which causes the protein to have an atypical truncated glycan layer exposing the tumor-associated Thomsen-Friedenreich antigen (TF antigen) [52, 54, 58] Galectin-3 binds to this β-galactoside, clustering the surface proteins, which in turn exposes adhesion molecules on the cell's surface. Galactosides multivalently bind to galectin-3 aggregates to elicit this biological response. This allows for cellular aggregation to occur (Figure 6). [24, 59, 60] Given the implications of galectin-3 in more aggressive cancer phenotypes, this protein is an attractive target in cancer research.[52, 61, 62]

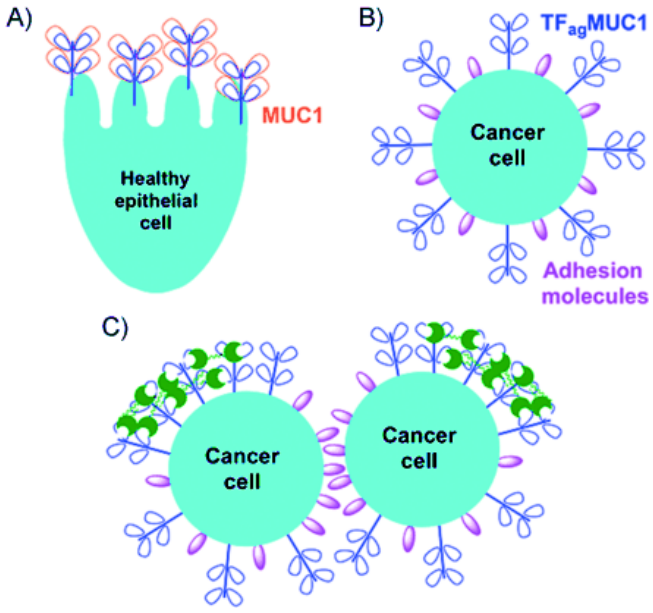

Figure 6: Galectin-3 mediated cancer cellular aggregation. (A) a healthy epithelial cell expressing normally glycosylated MUC1 on the apical surface, (B) Loss of apical polarization and aberrantly glycosylated MUC1 is expressed over the entire surface of the cancer cell, (C) MUC1 is clustered on the cell surface, adhesion molecules shown in purple are exposed inducing cellular aggregation. Reprinted with permission from Michel *et al*.[60] adapted from Yu *et al*.[63]

Galectin-3 and *β*-Galactosides.

The CRD of galectin-3 has a concave binding domain which specifically hosts *β*-galactosides (Figure 7).[56, 61, 64, 65] It can accommodate four saccharides in its four specified domains A, B, C, and D. A fifth binding domain, E, has also been identified yet has not been structurally defined (Figure 8). The C binding unit, which is specific for *β*-galactose binding, is highly conserved across the galectin family of proteins. It is adjacent to D which binds the second sugar of the disaccharide.[48]

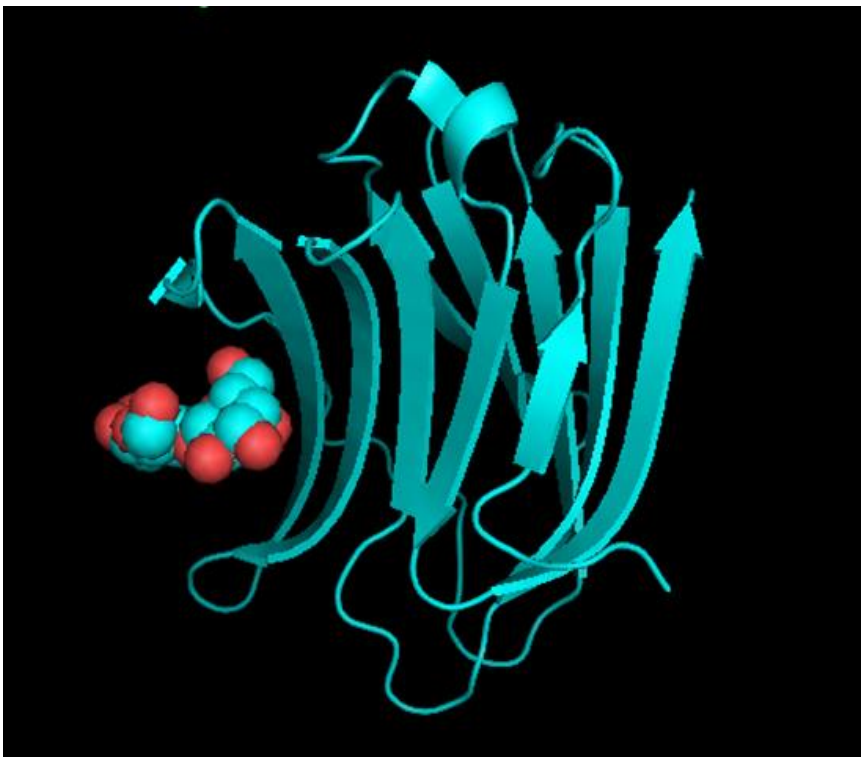

Figure 7: Ribbon diagram of *N*-acetyllactosamine in the binding pocket of the CRD of galectin-3 was created in PMOL.[49]

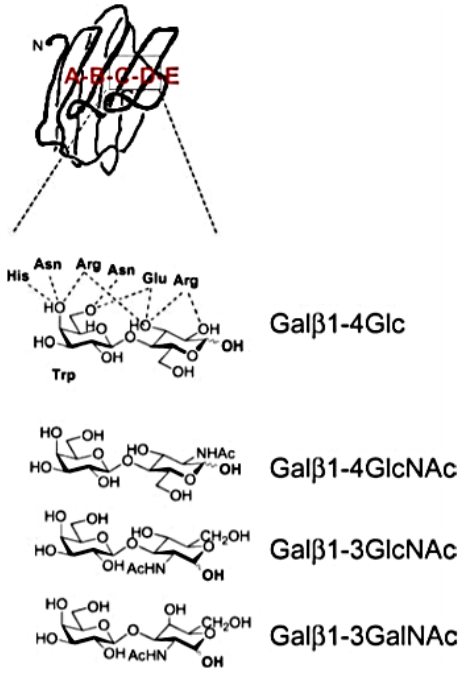

Figure 8: The galectin carbohydrate-binding site. At top is an artist's view of the CRD as in Figure 2 with the four established subsites indicated as A, B, C and D and a more loosely defined proposed site as E. Reprinted with permission from Leffler *et al.*[48]

These two subunits have a K_D of 220 μM for binding to lactose, 67 μM for *N*-acetyllactosamine and 43 μM for TF antigen.[66-68] Although TF antigen is the native ligand for galectin-3, *N*-acetyllactosamine and lactose have close enough binding affinities that they are important ligands for the study of galectin-3 mediated cancer cellular aggregation.

Carbohydrate/Protein Study with *N*-Acetyllactosamine Functionalized Dendrimers

Because PAMAM dendrimers are available in different generations which are uniform in size and reactive surface groups, they have been an attractive scaffold for studies of multivalent interactions. Additionally, because PAMAM dendrimers have the ability to display a functional end-group multivalently, they have also been an attractive framework to elicit enhancement in specificity and avidity in a plethora of biomedical and nanomaterial applications.[43, 69-72] This scaffold's robustness has been established. There is precedence for synthetic manipulation of PAMAM dendrimers with carbohydrates and the characterization of heterogenous[73,74, 75] and homogenous[76, 77] glycodendrimers. The development of frameworks to mimic the polyvalent carbohydrate-protein interaction present in the metastatic cascade broadens the understanding of galectin-3 mediated protein-carbohydrate interactions in cancer pathways. Woller *et al*. synthesized a series of PAMAM dendrimers functionalized with mannose, a known ligand for legume lectin Concanavalin A (Con A).[76] This study revealed that the smaller mannose functionalized dendrimers bind Con A monovalently. This is a result of the size of the dendrimers and therefore the accessibility of mannose on the dendrimer for the carbohydrate binding domains. The larger dendrimers had an increased activity of two orders of magnitude over the monomeric saccharide. This enhanced activity suggested Con A was binding the larger dendrimers multivalently. [76] Further demonstrating the tunability of these systems, heterogeneously glucose/mannose functionalized dendrimers were synthesized and characterized by NMR and MALDI. A series of the larger

generations dendrimers, which increased mannose surface presentation, further demonstrated polyvalent avidity as a result of the multivalent displays.[74] Further studies of carbohydrate functionalized PAMAM dendrimers demonstrated their ability to enhance binding through multivalency and established them as a useful tool to study carbohydrate/protein interactions.[65, 73, 74, 76-87] In a study of galectin-3 mediated homotypic cellular aggregation using four generations of lactose functionalized PAMAM dendrimers, Michel *et al*. found galectin- 3 induced aggregation could be inhibited by the smallest glycodendrimers (generation 2). It was also found that the largest functionalized dendrimer, generation 6, induced cancer cellular aggregation.[88] In a previous study Wolfenden *et al.* showed the avidity of the multivalent associations in carbohydrate functionalized PAMAM dendrimers/lectin binding can be predicted by the association constant of the monomeric interaction which was described by Whitesides' model shown in Equation 1.[74, 89]

$$K_N^{POLY} = K^{(MONO)\alpha N} \qquad \text{(eq. 1)}$$

In Equation 1, the polyvalent binding of a ligand (K_N^{POLY}) should be equivalent to the monovalent interaction (K^{MONO}) raised to the number of ligand-receptor interactions (N) multiplied by a cooperativity factor (α).[89]Although the monomer binding strength of methyl D-mannoside and methyl D-glucoside only differed by a factor of 4, mannose functionalized PAMAM dendrimers had a measured activity of almost 16 fold greater than glucose functionalized PAMAM dendrimers in hemagglutination assays of Con A.[74]

The hypothesis which guided this work is that although *N*-acetyllactosamine (Lac*N*Ac) is a non-native ligand for galectin-3, it binds with three fold higher affinity than lactose and with comparable affinity to TF antigen. Therefore, Lac*N*Ac is an important ligand for the study of galectin-3 mediated processes.

Molecular Recognition with Dendronized Surfaces

Poly(benzylether) dendrons.

Dendrons (Figure 3b) are dendritic macromolecules which were first reported by Hawker and Fréchet *et al*. in the "convergent-growth approach" for dendrimer synthesis.[90] As previously discussed, the synthesis is reiterative, much like the divergent synthesis of dendrimers. The size of the dendron is uniformly increased and the number of terminal groups doubles with each synthesis of a new generation. Poly(benzyl ether) dendrons contain core aryl ethers decorated with peripheral propargyl groups which were incorporated for further functionalization (Figure 9).[91,92]

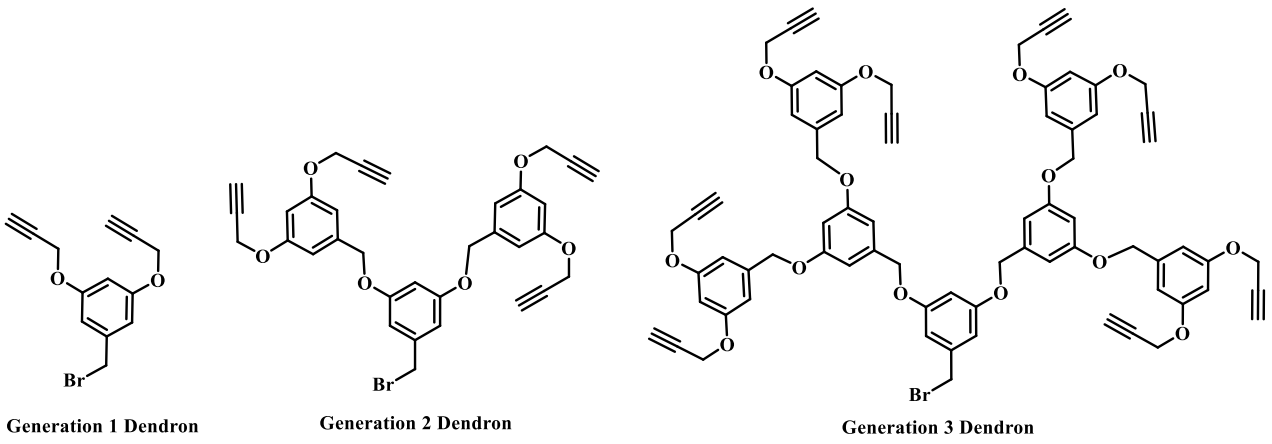

Figure 9: Schematic representation of three generations of poly(benzyl ether) dendrons.

Copper-catalyzed azide-alkyne cycloaddition (CuAAC).

In 1964 Huisgen described the synthesis of five membered heterocycles by a concerted 1,3-dipolar reaction of a 1, 3 dipolar molecule and a dipolarophile.[93, 94] Further, he demonstrated the synthesis of triazoles formed from the 1, 3-cycloaddition of an alkyne and azide. Commonly these reactions were performed at elevated temperature with both regioisomers being formed. Rostovtsev later reported that these reactions, when catalyzed by copper (I) were not only regioselective for 1,4-triazole formation, but also tolerated a wide scope of substitution on both the terminal alkynes and azides.[95] Products were also found to be easily accessible at room temperature. Copper (I) could readily be used as a salt or could be generated with a reductant, such as ascorbic acid, from copper (II) salts such as copper sulfate. Copper (I)-catalyzed azide-alkyne transformations to form triazoles have been reported to be high yielding and with a broad scope of reactants. Therefore, this Huisgen 1, 3-cycloaddition variant provides an efficient method to install a desired modification to the terminal alkynyl groups of the poly(benzyl ether) dendrons.[96-98]

Synthesis of Functionalized Poly(arylether) Dendronized Surfaces Capable of Adsorption of Organic Analytes

Non-covalent interactions in molecular recognition events determine the selectivity and the length of time the complexation occurs. Therefore, the development of

surfaces which are capable of specific and reversible absorption of organic analytes from aqueous solutions can be accomplished by exploiting these non-covalent interactions. Chlorobenzenes and chlorophenols are a class of compounds that are common agricultural and industrial pollutants in which some isomers have been designated as carcinogenic or as suspected carcinogens (Figure 10).[99, 100] Chronic exposure to these compounds has been linked to cell toxicity in the endocrine, hepatic, neurological, dermal, immunological, and renal systems.[99-102] Therefore, the synthesis and characterization of surfaces capable of targeting this class of compounds and undergoing triggered deadsorption would be a useful tool for the understanding and development of new separation systems.

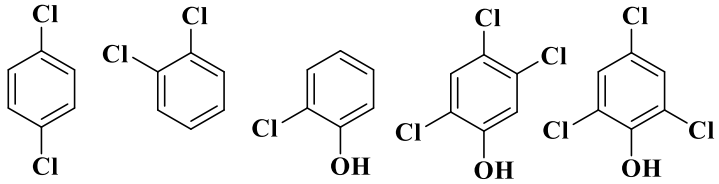

Figure 10: Schematic representation of analytes capable of guest-host interactions with the dendronized surfaces; chlorobenzenes and chlorophenols.

<u>*β*-Cyclodextrin functionalized poly(arylether) dendronized surfaces</u>.

β-Cyclodextrins are composed of seven covalently linked glucopyranoside units. This barrel shaped molecule contains a hydrophobic interior with a 0.78 nm cavity.[103] Because of this hydrophobic cavity, *β*-cyclodextrin has been shown to have favorable guest host interactions with a variety of organic compounds.[104-106] Schofield *et al.* reported the immobilization of *β*-cyclodextrins onto a hydrophobic pulsed plasma-deposited poly(4-vinylbenzy chloride) surface. These surfaces were then shown to

capture a series of chlorophenols and chlorobenzenes. Furthermore, Schofield *et al.*were able to trigger deadsorption and quantify the guest molecules (Figure 11). Secondary hydroxyl groups of the oligosaccharide, which line the interior of the molecular assembly, have a pKa of approximately 11.7. Submersion of the surface into a basic buffer destabalized the hydrophobic cavity by creating coulomb repulsions when the hydroxyl groups were converted to their corresponding alkoxides. This repulsion therefore triggered the release of the encapsulated targeted guests.[103]

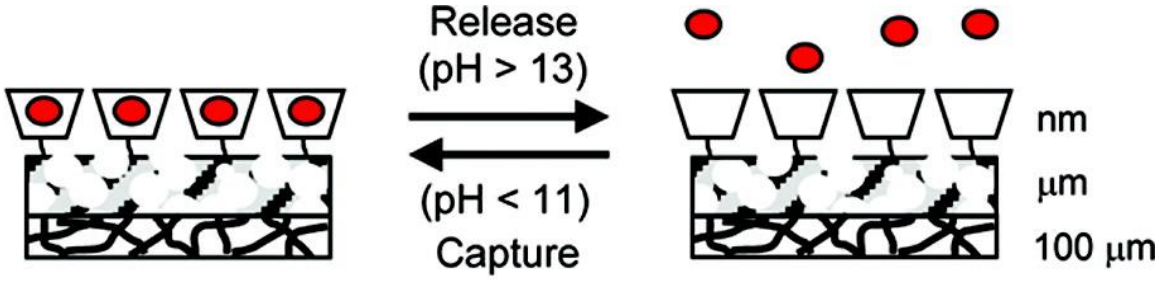

Figure 11. Schematic representation of the triggered release of an organic analyte from beta-cyclodextrins. Reprinted with permission from Schofield *et al*. Copyright 2013 American Chemical Society

Poly(benzyl ether) dendrons are an attractive scaffold for this study because they are available in different generations which are uniform in size and are decorated with peripheral alkynyl groups that can be further functionalized. The core of the dendron has a leaving group that allows for the dendron to be anchored to a surface. In addition to this, the terminal alkynes can readily undergo a Huisgen 1, 3-cycloaddition variant reaction to modify the alkynyl end-groups. Synthesizing a series of poly(benzyl ether) dendronized surfaces and further modifying the terminal end-groups with *β*-cyclodextrin

will be an important tool for the study of the effects of dendritic frameworks on the capture of targeted analytes.

Heterogeneous surfaces designed for reversible adsorption.

After developing the synthesis and methodology for the characterization of the *β*-cyclodextrin functionalized poly(arylether) dendronized surfaces, this same methodology was applied to the development of surfaces capable of binding the same targeted analytes in the absence of the *β*-cyclodextin.

The poly (arylether) dendrons are proposed to accommodate chlorophenols and chlorobenzenes as guest molecules. The total π-π interaction binding energy, in the face-to-face confirmation, of benzene is approximately -0.717 kcal/mol. With the addition of substituents, the calculated interaction energetics are additive and in most cases as high as ~ -3.58 kcal/mol.[107] In addition to the non-covalent interactions between two substituted aryl compounds, the array of substituted aryl groups provide flexibility within the recognition site in the absence of molecular structural specificity. Further modification of the terminal alkyne will add stabilize the complex. For example, at neutral pH amino acids will form salt bridges between carboxylate and substituted ammonium groups. With a change in pH, this interaction can be destabilized, offsetting the total interaction energetics of the pi-stacking, and therefore trigger the release of the analyte (Figure 12). Furthermore, the efficiency of these dendronized surfaces to bind targeted analytes can be quantified, and further modifications can be adapted in the synthesis of the dendronized architecture.

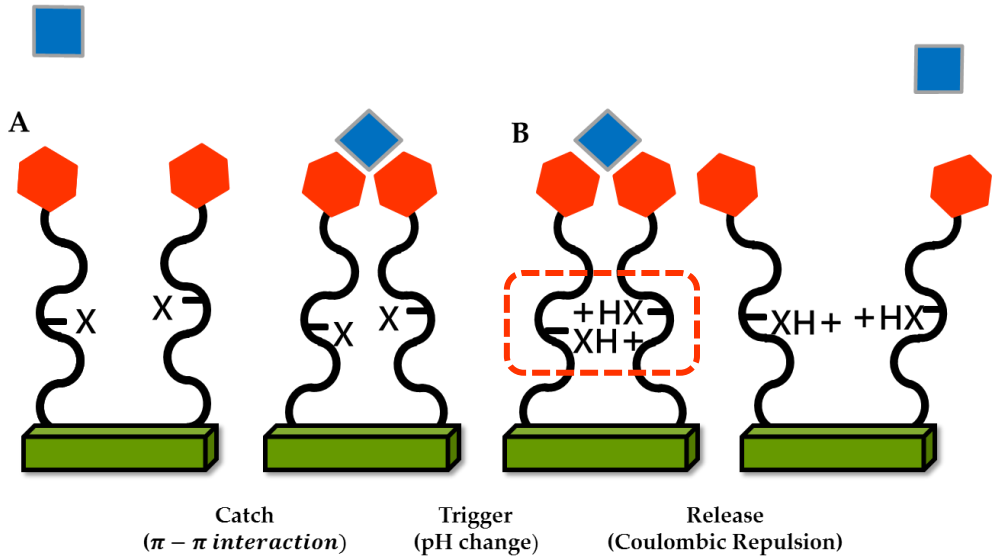

Figure 12: Schematic representation of reversible deadsorption of a targeted analyte (a) molecular recognition and (b) disruption of non-covalent reactions through pH change.
.

The hypothesis which guided this work is that non-covalent interactions in molecular recognition allow for the development of surfaces capable of selective and reversible absorption of organic analytes from aqueous solutions. The efficiency of a synthetic surface to bind targeted molecules is dependent on the design of the complex and therefore the total interaction energetics associated with the system. Therefore dendronized architectures that can specifically host target analytes were proposed.

Chiral Poly(arylether) Dendronized Surfaces.

Because there are a wide variety of applications using chiral recognition by surfaces in industrial processes, pharmaceuticals, and analysis, the design of new, synthetic, chiral surfaces is an area of significant interest.[108-110] Chiral discrimination is

the strong selectivity of one enantiomer over the other in recognition events. Although the difference in interaction energy between a pair of chiral species can be as small as 2 KJ/ mol, nature can recognize biological substrates with specificity. An example of this is metabolic chiral discrimination for D-sugars and L-amino acids. One major challenge with chiral recognition by surfaces is the inability to perform with such selectivity. [111, 112] The synthesis of a chiral organic monolayer would provide a surface displaying terminal chiral end-groups with a high degree of homogeneity and therefore control over the enantioselectivity of the surface.[109, 113, 114]

The synthesis and characterization of dendronized chiral organic surfaces provides dendritic scaffolds that display chiral end-groups which can be analyzed by XPS. Further, dendronized surfaces will be functionalized with chiral amino acid S-proline. Corey *et al.* demonstrated that the intramolecular aldol condensation of two ketones could be catalyzed by S-proline in the total synthesis of Desogestrel.[115] List *et al.* reported a broad scope of this amine based mimic of Class I adolases.[116] This class of enzymes catalyzes the C-C bond formation of an aldol reaction through an enamine mechanism. The asymmetric aldol condensation between acetone and substituted aldehydes catalyzed by proline in high yields and enantiospecific preference was described (Figure 13).[116]

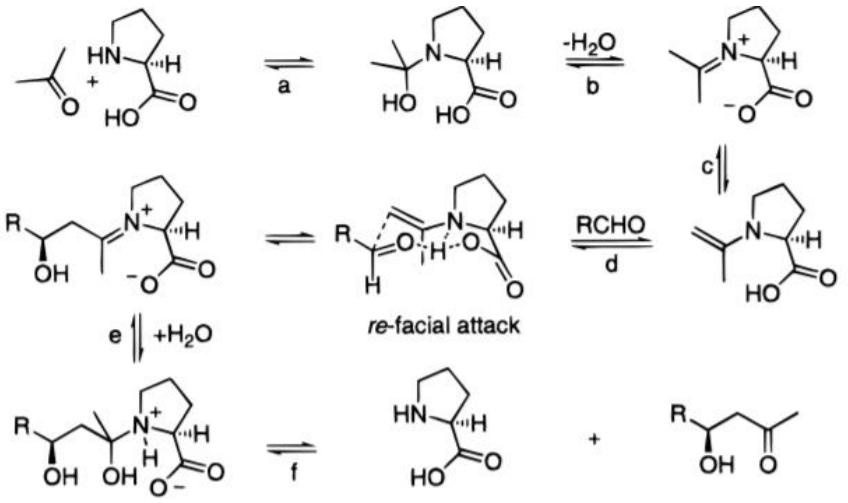

Figure 13: Proposed Enamine Mechanism of the Proline Catalyzed Asymmetric Aldol Reaction by List *et al.*[116] Reprinted with permission from List *et al.* Copyright 2000 American Chemical Society.

Elmekawy *et al.* described the synthesis of S-proline functionalized silica gel.[117] He reported the efficiency of the tethered proline to catalyze the asymmetric aldol reactions. He demonstrated their scope with a variety of previously described reactions.[116] It was reported the supported proline had greater activity than proline alone. In addition to this, the catalytic activity of the surface persisted through multiple reaction submissions.

The hypothesis which guided this work is that chiral dendronized surfaces would efficiently mediate chiral recognition events. Therefore chiral amino acids were installed on generation 1 dendronized surface. Furthermore, a generation 2 dendronized surface was also modified with S-proline. These two generations of chiral proline functionalized dendronized surfaces can further be studied for their efficiency to recruit and adsorp prochiral species and catalyze their asymmetric aldol condensation.

Summary of the Research Described Herein

To further explore the carbohydrate-protein interaction in cell-cell recognition, this dissertation reports the full syntheses of *N*-acetyllactosamine functionalized generation 2, abbreviated as G(2), generation 3 (G(3)), generation four (G(4)), and generation 6 (G(6)) PAMAM dendrimers. Further, *N*-acetyllactosamine functionalized dendrimers were used in galectin-3 mediated cancer cellular aggregation assays. The synthesis and the results of these studies are further discussed in Chapter 2.

This dissertation will additionally focus on the functionalization and characterization of silica surfaces. The synthesis of β-cyclodextrin functionalized surfaces and the methodology for characterization by X-ray Photoelectron Spectroscopy (XPS) are discussed in Chapter 3. Surfaces designed and synthesized for reversible adsorption are discussed further in Chapter 4, and the synthesis of chiral organic surfaces is described in Chapter 5. The conclusion of the galectin-3 mediated cancer cellular aggregation assays and their comparison to previously described studies using lactose functionalized PAMAM dendrimer, and the conclusion of the synthesis and characterization results of the functionalized dendronized surfaces are summarized in chapter 6 of this thesis.

CHAPTER TWO

THE SYNTHESIS OF *N*-ACETYLLACTOSAMINE FUNCTIONALIZED DENDRIMERS AND THEIR ROLE IN GALECTIN-3 MEDIATED CANCER CELLULAR AGGREGATION STUDIES

Contribution of Authors and Co-Authors

Manuscript in Chapter 2

Author: Jessica. H Ennist

Contributions: Performed experiments and obtained results for all syntheses. Performed expression and purification of Galectin-3. Performed cancer cell homotypic aggregation studies and analysis.

Co-Author: Co-Author: Mary J. Cloninger

Contributions: Primary Investigator. Conceived of the project and provided funding. Provided guidance throughout the project. Provided feedback and edited drafts of the manuscript.

Manuscript Information Page

Jessica H. Ennist, Mary J. Cloninger

Status of Manuscript:
__X_ Prepared for submission to a peer-reviewed journal
____ Officially submitted to a peer-review journal
____ Accepted by a peer-reviewed journal
____ Published in a peer-reviewed journal

The synthesis of *N*-acetyllactosamine functionalized dendrimers and their role in galectin-3 mediated cancer cellular aggregation studies.

Jessica H. Ennist, Mary J. Cloninger*

Department of Chemistry and Biochemistry, Montana State University, Bozeman, MT 59717

* Corresponding author. Tel: +1 406 994 3051; Fax: +1 406 994 5407; e-mail: mcloninger@chemistry.montana.edu

KEYWORDS. Galectin-3, dendrimers, glycodendrimer, chemoenzymatic, *N*-acetyllactosamine, aggregation, cancer.

Abstract

Galectin-3, a member of the family of lectins, which contain a carbohydrate recognition domain that recognizes *β*-galactosides, is overexpressed in many types of cancer. The galectin-3/tumor-associated Thomsen-Friedenreich antigen (TF antigen) interaction has been proposed to play an important role during heterotypic and homotypic cell adhesion and apoptotic signaling. However, a stronger mechanistic understanding of the multivalent role of galectin-3 in these processes is needed. *N*-acetyllactosamine, or 2-acetamido-2-deoxy-4-*O*-*β*-D-galactopyranosyl-D-glucopyranose (Lac*N*Ac) is a non-native ligand for galectin-3 that binds with comparable affinity to the native ligand TF antigen. Therefore as an important ligand for the study of galectin-3 mediated processes, and since multivalent binding of galactosides to galectin-3 aggregates is necessary in order to elicit a biological response, Lac*N*Ac poly(amido amine) (Lac*N*Ac PAMAM) functionalized dendrimers have been synthesized, and cell-based assays with these compounds have been performed. The efficient synthesis of Lac*N*Ac functionalized dendrimers incorporates an enzymatic addition of galactose onto *N*-acetylglucosamine functionalized dendrimers. The homotypic cancer cellular assay, which serves as an important *in vitro* model for tumor formation, indicated that the small glycodendrimers inhibit galectin-3 meditated cancer cellular aggregation and that the large glycodendrimers increase cellular aggregation.

Introduction

Multivalency plays an important role in many cellular recognition and binding events.[52-56] Synthetic multivalent frameworks for the study and mediation of these events are being increasingly recognized for their importance.[118] Monovalent protein/carbohydrate binding, for example, is usually weak and not physiologically relevant, and therefore nature invokes multivalent binding events to increase the avidity and specificity of otherwise promiscuous ligands that commonly have monovalent dissociation constants in the μM range. [20, 22, 89] The use of multivalent bioinspired nano materials to study cell-cell recognition, pathogen mediated cascade events, and cancer cell recognition pathways has demonstrated how exploiting the affinity enhancement of multivalent binding systems can be used. The advancement of new multivalent materials will help us to better understand both natural and disease states for the development of potential therapeutics.[29-32]

In efforts to understand the mechanistic role of multivalency in protein/carbohydrate interactions, the design and development of these multivalent frameworks to elucidate their role in signaling pathways has become of paramount importance.[47] We and others have demonstrated that tunable scaffolds, such as poly(amidoamine)(PAMAM) dendrimers,[36, 119] can be synthetically modified to present terminal carbohydrates, homogenously or heterogeneously, and they have been an important tool to elucidate protein/carbohydrate mediated processes.[76, 77, 80, 83-87, 120, 121]

Galectin-3, a lectin that contains a carbohydrate recognition domain that recognizes β-galactosides, is a versatile intra- and extracellular protein implicated in the regulation of inflammation, mRNA splicing, adhesion, and apoptotic signaling pathways.[48, 50, 51] During pathological expression, galectin-3 has been shown to be up or down regulated in regulatory pathways depending on the localization, expression, and cancer cell phenotypic expression.[61, 62] In cancer, the tumor-associated Thomsen-Friedenreich antigen (TF antigen)/galectin-3 interaction has been proposed to play an important role in the sequential steps of heterotypic cell adhesion to endothelium cells, promotion of homotypic cell adhesion during tumor formation, apoptotic signaling pathways, and the expression of more aggressive phenotypes.[52, 54, 58] The TF antigen is buried within the heavily glycosylated layer on the transmembrane protein Mucin-1 (MUC-1) of healthy epithelial cells.[57, 59] Contrarily, on cancer cells TF antigen is more accessible due to an atypical truncated glycan layer on MUC-1 and antigen over expression.[24, 57] MUC-1, which is localized on the apical face of healthy epithelia, can also be over expressed and delocalized over the whole surface of cancer cells, attenuating adhesion. However, as galectin-3 binds to the galactosides exposed on MUC-1, the protein clusters the MUC-1 and effectively polarizes the cell surface display, which exposes cell adhesion molecules.[24, 59] To elicit a biological response, galactosides multivalently bind to galectin-3 aggregates, however a stronger mechanistic understanding of the role of galectin-3 in these processes is needed.

In previous studies, we have demonstrated that the activity of the multivalent associations in carbohydrate functionalized PAMAM dendrimers/lectin binding can be

predicted by the association constant of the monomeric interaction. Mannose functionalized PAMAM dendrimers had a measured activity of almost 16 fold greater than glucose functionalized PAMAM dendrimers in hemagglutination assays using Concanavalin A, a plant lectin, although the monomer binding strength of methyl D-mannoside and methyl D-glucoside only differed by a factor of 4.[74] We have reported the synthesis and study of galectin-3 recruitment by galactose/lactose functionalized PAMAM dendrimers.[75] In this study, the dendrimers which presented lactose recruited more galectin-3 than dendrimers presenting galactose. The linear dependence of the ratio of low to high affinity ligands multivalently displayed to the measurable protein/carbohydrate interaction was observed. Lactose has a measured disassociation constant(K_D) of 220 μM for binding to galectin-3, while *N*-acetyllactosamine has a K_D of 67μM. [66,67] The increased monovalent binding strength of *N*-acetyllactosamine relative to lactose for galectin-3 should reasonably predict a greater amplification in the multivalent associations of glycodendrimers functionalized with *N*-acetyllactosamine when compared to those of lactose functionalized dendrimers.

This paper describes the chemoenzymatic synthesis and characterization of 2-Acetamido-2-deoxy-4-O-*β*-D-galactopyranosyl-D-glucopyranose functionalized poly(amido amine) (Lac*N*Ac PAMAM) functionalized dendrimers in four steps. The enzymatic addition of galactose to *N*-acetylglucosamine functionalized dendrimers reduces the requisite number of synthetic steps for the full chemical synthesis of *N*-acetyllactosamine to four steps. The use of this efficient synthetic design, gave us access to four generations of *N*-acetyllactosamine dendrimers. Although a non-native ligand for

galectin-3, *N*-acetyllactosamine binds with three fold higher monovalent affinity than lactose and with comparable affinity to the putative native ligand, TF antigen.[68] Therefore *N*-acetyllactosamine is an important ligand for the study of galectin-3 mediated processes. These Lac*N*Ac functionalized PAMAM dendrimers were used in cancer cellular aggregation assays to study galectin-3 mediated processes.

Experimental Procedures

Materials and Methods.

PAMAM dendrimers were purchased from Dendritech. Uridine diphosphate-α-D-glucose (UDP-α-D-glucose) was purchased from Calbiochem, and all other reagents used were purchased from Sigma-Aldrich. High purity organic solvents were purchased from Fisher Scientific. Dialysis tubing was purchased from Millipore. Column chromatography was performed using 60 Å silica gel. ^{13}C and ^{1}H NMR were recorded for purified compounds on a Bruker DRX 500 MHz Spectrometer.

1-*O*-(5-isothiocyanato-3-oxopentyl)-3,4,6-tri-*O*-acetyl-*β*-D-*N*-acetylglucosaminopyranoside (3). Alcohol **2** was synthesized as previously described.[76] 0.368 g of 1,3,4,6-tetra-*O*-acetyl-*β*-D-*N*-acetylglucosaminopyranoside (0.945 mmol, 1.00 equiv.) and alcohol **2** (0.510 g, 3.461 mmol, 3.66 equiv.) were dissolved in dry CH_2Cl_2 (10 mL). Activated 4-8 mesh molecular sieves were added, and the reaction mixture was stirred for 5 min at 21 ºC. $FeCl_3$ (0.402 g, 2.481 mmol, 2.47 equiv.) was added over 1 min to the reaction, and the resulting red suspension was stirred for 22 h. 0.4 g of $NaHCO_3$

was added to the mixture, and the mixture was filtered over celite. The solvent was removed *in vacuo* to afford a red viscous oil. The residue was dissolved in 100 mL of EtOAc and washed with three 25 mL portions of water. The aqueous layers were extracted with 25 mL of EtOAc and the combined organic layers were dried over $MgSO_4$ and concentrated. The residue was purified by flash column chromatography with ethyl acetate eluent (R_f 0.23) to provide the *N*-acetylglucosaminopyranoside derivative **3** (0.214 g, 47%) as a light yellow oil. ^{1}H NMR (500 MHz, d_6-DMSO) δ 7.95 (d, *J* = 9.1 Hz, 1H), 5.08 (t, *J* = 9.8 Hz, 1H), 4.83 (t, *J* = 9.8 Hz, 1H), 4.66 (d, *J* = 8.5 Hz, 1H), 4.18 (dd, *J* = 12.1, 4.7 Hz, 1H), 4.03 (d, *J* = 12.1 Hz, 1H), 3.88 – 3.76 (m, 5H), 3.72 (dd, *J* = 18.9, 9.1 Hz, 1H), 3.65 – 3.52 (m, 4H), 2.02 (s, 3H), 1.97 (s, 3H), 1.91 (s, 3H), 1.76 (s, 3H) ppm.^{13}C NMR (126 MHz, $CDCl_3$) δ 170.68, 170.68, 170.46, 169.42, 132.08, 100.85, 72.47, 71.67, 70.40, 69.17, 68.75, 68.67, 62.12, 54.33, 45.37, 23.21, 20.73, 20.65, 20.60 ppm. HRMS (Micro-TOF0) m/z 477.1551 (calculated m/z M+H = 477.1537 for C19H28N2O10S).

General procedure for the synthesis of PAMAM-based thiourea-linked 1-*O*-(5-isothiocyanato-3-oxopentyl)-3,4,6-tri-*O*-acetyl-*β*-D-*N*-acetylglucosaminopyranoside dendrimers 4a-d. Lyophilized PAMAM amine terminated dendrimer (1 equiv.) was dissolved in a solution of excess **3** in dimethylsulfoxide (DMSO). The reaction was allowed to stir at 21 ºC for 72 h. The products were purified by dialysis (3,500 MWCO tubing) against 1 L of DMSO for 3 h. This was repeated twice. Lyophilization afforded a yellow viscous oil. ^{1}H NMR and

MALDI-TOF MS were used to determine the degree of carbohydrate functionalization of the dendrimers. **4a:** ^{1}H NMR (500 MHz, d_6-DMSO) δ 8.04 (bs, 1H), 7.99 (d, *J* = 9.0, 1H), 7.87 (bs, 0.4H), 7.69 – 7.38 (m, 1H), 5.05 (t, *J* = 9.8 Hz, 1H), 4.79 (t, *J* = 9.8 Hz, 1H), 4.62 (d, *J* = 8.7 Hz, 1H), 4.15 (dd, *J* = 11.2, 3.2 Hz, 1H), 3.98 (d, *J* = 11.2 Hz, 1H), 3.85 – 3.72 (m, 3H), 3.68 (ddd, *J* = 9.0, 9.0, 9.0 Hz, 1H), 3.63 – 3.36 (m, 10H), 3.14 (bs, 2H), 3.05 (bs, 2H), 2.62 (bs, 5H), 2.18 (bs, 4H), 1.98 (s, 3H), 1.93 (s, 3H), 1.87 (s, 3H), 1.73 (s, 3H) ppm. ^{13}C NMR (126 MHz, d_6-DMSO) δ 171.62, 171.15, 169.97, 169.57, 169.31, 169.21, 100.24, 72.48, 70.57, 69.10, 68.81, 68.56, 68.26, 61.77, 53.10, 52.16, 49.61, 43.38, 43.14, 40.41, 38.15, 36.81, 33.07, 22.59, 20.44, 20.33, 20.26 ppm. MALDI-TOF (pos) m/z 8,300.

4b: ^{1}H NMR (500 MHz, d_6-DMSO) δ 7.99 (bs, 1H), 7.93 (d, *J* = 8.9 Hz, 1H), 7.79 (bs, *J* = 8.9 Hz, 1H), 7.60 – 7.40 (m , 2H), 5.05 (t, *J* = 9.7 Hz, 1H), 4.79 (t, *J* = 9.7 Hz, 1H), 4.61 (d, *J* = 8.0 Hz, 1H), 4.15 (dd, *J* = 11.6, 3.3 Hz, 1H), 3.97 (d, *J* = 11.6 Hz, 1H), 3.85 – 3.72 (m, 2H), 3.68 (dd, *J* = 17.3, 8.0 Hz, 1H), 3.62 – 3.39 (m, 8H), 3.12 (bs, 2H), 3.05 (bs, 2H), 2.61 (bs, 4H), 2.38 (bs, *J* = 12.1 Hz, 2H), 2.16 (bs, 3H), 1.98 (s, 3H), 1.93 (s, 3H), 1.87 (s, 3H), 1.73 (s, 3H) ppm. ^{13}C NMR (126 MHz, d_6-DMSO) δ 171.48, 171.02, 169.84, 169.43, 169.20, 169.07, 100.10, 72.46, 70.54, 68.96, 68.67, 68.42, 68.13, 61.63, 52.97, 52.01, 49.32, 43.26, 42.98, 40.24, 38.02, 36.58, 32.89, 22.44, 20.29, 20.18, 20.10 ppm. MALDI-TOF (pos) m/z 16,800.

4c: ^{1}H NMR (500 MHz, d_6-DMSO) δ 8.01 – 7.93 (m, 1H), 7.91 (d, *J* = 9.2 Hz, 1H), 7.75 (bs, 1H), 7.54 – 7.37 (m, 1H) 5.05 (t, *J* = 8.9 Hz, 1H), 4.79 (t, *J* = 8.9 Hz, 1H), 4.62 (d, *J*

= 8.2 Hz, 1H), 4.15 (dd, *J* = 11.9, 2.7 Hz, 1H), 3.98 (d, *J* = 11.9 Hz, 1H), 3.83 – 3.73 (m, 3H), 3.68 (ddd, *J* = 9.2, 9.2, 9.2 Hz, 2H), 3.62 – 3.35 (m, 12H), 3.14 (bs, 2H), 3.06 (bs, 2H), 2.62 (bs, 5H), 2.17 (bs, 4H), 1.99 (s, 3H), 1.93 (s, 3H), 1.88 (s, 3H), 1.73 (s, 3H) ppm. ^{13}C NMR (126 MHz, d_6-DMSO) δ 171.52, 171.21, 170.01, 169.61, 169.39, 169.25, 100.27, 72.63, 70.71, 69.13, 68.84, 68.59, 68.31, 61.80, 53.14, 52.14, 49.47, 43.42, 43.11, 40.41, 38.21, 36.66, 33.14, 22.62, 20.46, 20.35, 20.28 ppm. MALDI-TOF (pos) m/z 35,000.

4d: ^{1}H NMR (500 MHz, d_6-DMSO) δ 7.99 (bs, 1H), 7.93 (d, *J* = 8.6 Hz, 1H), 7.81 (bs, 1H), 7.66 – 7.39 (m, 1H), 5.05 (t, *J* = 9.3 Hz, 1H), 4.79 (t, *J* = 9.3 Hz, 1H), 4.62 (d, *J* = 7.8 Hz, 1H), 4.15 (d, *J* = 9.9 Hz, 1H), 3.98 (d, *J* = 9.9 Hz, 1H), 3.82 – 3.73 (m, 3H), 3.68 (ddd, *J* = 8.6, 8.6, 8.6 Hz, 1H), 3.63 – 3.35 (m, 15H), 3.13 (bs, 3H), 3.06 (bs, 3H), 2.60 (bs, 3H), 2.16 (bs, 5H), 1.98 (s, 3H), 1.93 (s, 3H), 1.87 (s, 3H), 1.73 (s, 3H) ppm. ^{13}C NMR (126 MHz, d_6-DMSO) δ 171.71, 171.21, 170.01, 169.61, 169.42, 169.25, 100.27, 72.62, 70.71, 69.13, 68.84, 68.59, 68.34, 68.32, 61.80, 53.13, 49.41, 43.42, 43.12, 42.10, 40.41, 38.19, 36.70, 33.00, 22.61, 20.45, 20.35, 20.29 ppm. MALDI-TOF (pos) m/z 120,000.

General procedure for the synthesis of PAMAM-based thiourea-linked 1-*O*-(5-isothiocyanato-3-oxopentyl)-*β*-D-*N*-acetylglucosaminopyranoside dendrimers 5a-d. In 2 mL scintillation vials, lyophilized dendrimers **4a-d** were separately dissolved in a 1:1 mixture of methanol and water (2 mM). Using a 0.8 M NaOMe in MeOH solution, 0.2 equiv. of NaOMe were added per each peripheral sugar on the dendrimer. The

reaction was stirred at 21 ºC for 2 h. 0.2 equiv. of NaOMe was added per each peripheral sugar, and the reaction was allowed to stir for an additional 1 h. 0.2 equiv. of NaOMe were periodically added until the solution maintained a persistent pH of 10 (litmus) and became a yellow transparent solution. The reactions were brought to pH 7 (litmus) with 0.1 M aqueous HCl. The products were purified by dialysis (3,500 MWCO tubing) against 1 L of Milli-Q water (18.2 MΩ·cm) for 2 h. This was repeated twice. The solvent was frozen and lyophilized to yield a white fluffy solid. ^{1}H NMR and MALDI-TOF MS were used to determine deacetylation of the carbohydrate functionalized dendrimers. **5a:** ^{1}H NMR (500 MHz, d_6-DMSO) δ 7.96 (bs, 0.6H), 7.75 (bs, 0.6H), 7.67 (d, *J* = 8.7 Hz, 1.1H), 7.54 (bs, 0.7H), 7.39 (bs, 0.7H), 5.01-4.96 (m, Hz, 0.7H), 4.50 (s, 0.8H), 4.28 (d, *J* = 8.2 Hz, 0.9H), 3.83 – 3.72 (m, 1.4H), 3.65 (d, *J* = 11.6 Hz, 1.9H), 3.58 – 3.33 (m, 14.8H), 3.14 (s, 2.6H), 3.04 (s, 4.1H), 2.63 (s, 4.4H), 2.17 (s, 3.3H), 1.81 (s, 3H) ppm.^{13}C NMR (151 MHz, d_6-DMSO) δ 172.22, 171.75, 169.82, 101.52, 77.47, 74.68, 71.05, 69.82, 69.32, 68.21, 61.50, 55.89, 52.69, 49.96, 44.04, 43.46, 40.53, 38.67, 37.34, 33.66, 23.60, 23.57 ppm. MALDI-TOF (pos) m/z 7,000.

5b: ^{1}H NMR (500 MHz, d_6-DMSO) δ 8.02 (s, 1.2H), 7.81 (s, 1.1H), 7.74 (d, *J* = 8.2 Hz, 1.3H), 7.60 (s, .8H), 7.46 (s, .8H), 5.01-4.95 (m, 2H), 4.57 (s, 1.1H), 4.32 (d, *J* = 8.1 Hz, 1.1H), 3.84 – 3.77 (m, 1.2H), 3.68 (d, *J* = 12.4 Hz, 1.6H), 3.64 – 3.38 (m, 12.1H), 3.29 (bs, 1.3H), 3.17 (bs, 2.6H), 3.08 (bs, 4H), 2.66 (bs, 4.1H), 2.42 (bs, 1.8H), 2.20 (bs, 4.2H), 1.81 (s, 3H) ppm. ^{13}C NMR (126 MHz, d_6-DMSO) δ 171.46, 171.06, 169.41,

101.01, 76.91, 74.16, 70.57, 69.31, 68.80, 67.70, 61.00, 55.38, 52.03, 49.39, 43.44, 43.06, 39.93, 38.26, 36.39, 32.56, 23.02 ppm. MALDI-TOF (pos) m/z 14,100.

5c: ^{1}H NMR (500 MHz, d_6-DMSO) δ 8.17 – 7.83 (m, 1.5H), 7.72 (bs, 0.7H), 7.61 (bs, 0.6H), 7.46 (bs, 0.6H), 4.98 (s, 2.3H), 4.56 (s, 0.9H), 4.28 (d, *J* = 7.4 Hz, 0.9H), 3.89 – 3.39 (m, 22H), 3.15 (bs, 4.3H), 3.05 (bs, 2.1H), 2.76 (bs, 1.3H), 2.26 (bs, 2.6H), 1.78 (s, 3H) ppm. ^{13}C NMR (126 MHz, d_6-DMSO) δ 171.49, 171.21, 169.62, 101.18, 77.05, 74.33, 70.73, 69.48, 68.97, 67.89, 61.16, 55.55, 52.16, 49.51, 43.65, 43.16, 40.58, 38.44, 36.48, 32.42, 23.19 ppm. MALDI-TOF (pos) m/z 30,000.

5d: ^{1}H NMR (500 MHz, DMSO) δ 8.18 – 7.78 (m, 2.4H), 7.72 (bs, 0.8H), 7.58 (bs, 0.4H), 7.43 (bs, .3H), 4.98 (bs, 2H), 4.55 (bs, 0.7H), 4.28 (d, *J* = 6.7 Hz, 0.8H), 3.91 – 3.36 (m, 16.5H), 3.14 (bs, 1.9H), 3.05 (bs, 2.7H), 2.66 (bs, 1H), 2.20 (bs, 1.6H), 1.78 (s, 3H) ppm. ^{13}C NMR (126 MHz, d_6-DMSO) δ 171.47, 170.86, 169.56, 101.01, 76.86, 74.16, 70.56, 69.31, 68.80, 67.73, 61.00, 55.39, 51.93, 49.38, 43.49, 43.08, 40.41, 38.26, 36.34, 32.36, 23.02 ppm. MALDI-TOF (pos) m/z 104,600.

General procedure for the synthesis of heterogeneously functionalized PAMAM-based thiourea-linked 1-*O*-(5-isothiocyanato-3-oxopentyl)-*β*-D-*N*-acetyllactosaminopyranoside, 1-*O*-(5-isothiocyanato-3-oxopentyl)-*β*-D-*N*-acetylglucosaminopyranoside dendrimers 6a-d. This procedure was adapted for PAMAM functionalization from a previously published method.[122] PAMAM-based thiourea-linked 1-*O*-(5-isothiocyanato-3-oxopentyl)-*β*-D-N-acetylglucosaminopyranoside

dendrimer **5** was added to a solution of excess UDP-α-D-glucose in sodium cacodylate buffer (pH 7.5, 36 mM). 1.5 mL of cell lysis solution containing the fusion protein IgtB-galE (*E. coli* cells overexpressing the fusion protein were provided by Dr. Wakerchuck) was added to the reaction and allowed to stir for at least 6 d at 21 ºC. 150 µL of 2.5% 10x Trypsin was added to the reaction flask, and the reaction was allowed to stir for 7 d. The products were purified by dialysis (3,500 MWCO tubing) against 1 L of Milli-Q water (18.2 MΩ·cm). This was repeated at least three times a day for 4 d to yield a homogenous solution. The solvent was removed by lyophilization to yield a white fluffy solid. ^{1}H NMR was used to determine the amount of galactose that was added. MALDI-TOF (pos) was used to validate the degree of galactose addition. **6a:** ^{1}H NMR (600 MHz, d_6-DMSO) δ 8.22 – 7.95 (m, 1.1H), 7.92 – 7.68 (m, 1.7H), 7.60 (bs, 0.7H), 7.48 (bs, 0.5H), 5.10 (s, 0.7H), 5.00 (d, *J* = 22.0 Hz, 0.4H), 4.82 (s, 0.8H), 4.73 – 4.58 (m, 2.3H), 4.54 (s, 0.9H), 4.36 (dd, *J* = 27.4, 7.4 Hz, 1H), 4.22 (s, 0.8H), 3.80 (dd, *J* = 14.6, 9.3 Hz, 2.3H), 3.73 – 3.35 (m, 24.9H), 3.19 (bs, 2.7H), 3.10 (bs, 1.2H), 2.67 (bs, 1.3H), 2.23 (bs, 1.3H), 1.82 (s, 3H) ppm. ^{13}C NMR (151 MHz, d_6-DMSO) δ 169.05, 168.76, 168.72, 104.00, 101.02, 100.88, 81.36, 75.56, 74.99, 74.18, 73.19, 72.18, 70.58, 70.54, 69.29, 69.21, 68.84, 68.18, 67.91, 61.00, 60.49, 60.43, 55.39, 54.71, 49.43, 43.52, 42.95, 40.04, 38.25, 37.56, 29.03, 23.02 ppm. MALDI-TOF (pos) m/z 8,700.

6b: ^{1}H NMR (600 MHz, d_6-DMSO) δ 8.02 (bs, 2.5H), 7.91 – 7.69 (m, 3.2H), 7.59 (bs, 1.7H), 7.46 (bs, 1.8H), 5.11 (s, 1.1H), 5.05 – 4.91 (m, 1.7H), 4.82 (s, 1.5H), 4.76 – 4.47 (m, 4.2H), 4.35 (dd, *J* = 26.7, 5.2 Hz, 2H), 4.22 (s, 1.4H), 3.86 – 3.45 (m, 14.8H), 3.19

(bs, 2.7H), 3.10 (bs, 3.1H), 2.68 (bs, 3.3H), 2.22 (bs, 3.6H), 1.82 (s, 3H) ppm. ^{13}C NMR (151 MHz, d_6-DMSO) δ 176.44, 176.31, 175.93, 104.56, 103.87, 102.78, 102.70, 80.16, 77.56, 77.01, 76.43, 75.50, 74.17, 74.09, 72.61, 71.58, 71.34, 70.62, 70.59, 70.19, 62.67, 62.43, 61.75, 57.20, 56.68, 53.06, 50.80, 40.34, 38.38, 34.22, 23.97 ppm. MALDI-TOF (pos) m/z 16,400.

6c: ^{1}H NMR (600 MHz, d_6-DMSO) δ 8.02 (bs, 1.6H), 7.91 – 7.67 (m, 0.5H), 7.59 (bs, 0.7H), 7.46 (bs, 0.9H), 5.10 (bs, 0.9H), 5.01 (bs, 0.7H), 4.83 (bs, 0.6H), 4.75 – 4.43 (m, 2.1H), 4.35 (ap.d, *J* = 22.8 Hz, 0.7H), 4.22 (s, 0.6H), 3.98 – 3.41 (m, 11.4H), 3.19 (bs, 1.5H), 3.10 (bs, 2H), 2.68 (bs, 2.6H), 2.22 (bs, 3.3H), 1.82 (s, 3H) ppm. ^{13}C NMR (151 MHz, d_6-DMSO) δ 176.43, 175.97, 175.91, 104.58, 104.57, 102.80, 102.72, 102.71, 80.19, 77.58, 77.02, 76.44, 75.52, 74.19, 74.10, 72.63, 71.60, 71.34, 70.59, 70.20, 62.68, 62.45, 61.77, 57.22, 56.69, 53.09, 50.80, 40.36, 38.41, 34.21, 24.01 ppm. MALDI-TOF (pos) m/z 37,000.

6d: ^{1}H NMR (600 MHz, d_6-DMSO) δ 8.04 (bs, 1.6H), 7.91 – 7.67 (m, 2.8H), 7.61 (bs, 1.1H), 7.47 (bs, 1.1H), 5.09 (s, 0.9H), 5.01 (s, 1.2H), 4.81 (s, 1H), 4.72 – 4.42 (m, 3.4H), 4.36 (ap.d, *J* = 15.0 Hz, 1.3H), 4.22 (s, 0.9H), 4.10 – 3.39 (m, 17.8H), 3.18 (bs, 2.1H), 3.11 (bs, 3.3H), 2.70 (bs, 3H), 2.24 (bs, 3.5H), 1.83 (s, 3H) ppm. ^{13}C NMR (151 MHz, d_6-DMSO) δ 175.49, 175.04, 175.00, 103.73, 101.95, 101.87, 79.32, 76.74, 76.17, 75.58, 74.68, 74.39, 73.35, 71.77, 70.77, 70.51, 69.74, 69.34, 61.84, 61.62, 60.92, 56.37, 55.83, 52.25, 49.99, 43.97, 39.75, 37.50, 33.33, 23.20 ppm. MALDI-TOF (pos) m/z 119,400.

MALDI. Matrix assisted laser desorption ionization (MALDI) mass spectra were acquired using a Bruker Autoflex III Smartbeam Time of Flight (TOF) mass spectrometer. Samples of all dendrimers were prepared using a trans-3-indoleacrylic acid matrix, and spectra were acquired with an approximate matrix-analyte ratio of 500:1 to 20000:1 using estimated weighted molecular weights. Myoglobin (MW 16,951 g/mol), Trypsinogen (MW 23,982 g/mol), and Bovine serum albumin (MW 66,431 g/mol) were used as external standards. Dendrimer (1-4 nmol)/matrix sample was deposited on the laser target and positive ion mass spectra were acquired in linear mode. Ions were generated by using a Nd:YAG laser pulsed at 100 Hz with a pulse width of 5-7 ns. Ions were accelerated at 20 kV and amplified using a Multi-Channel Plate multiplier. Spectra were summed using an Agilent U1069A Acqiris DP240 PCI digitizer. All data processing was performed using a Compass for flex series 1.3 flexanalysis Version 3.3.

General method to determine GlcNAc/LacNAc functionalization of PAMAM dendrimers 6a-d. MALDI-TOF MS spectra were obtained for acetylated glucosamine functionalized dendrimers **4a-d**, and the change in the weighted average molecular weight, M_w, was divided by the M_w of the protected *N*-acetylglucosaminopyranoside derivative **3** denoted here as A (Equation (1)) to calculate the total number of monosaccharides that were appended to the PAMAM. This value was also determined by dividing the change in M_w for deacetylated functionalized dendrimers **5a-d** by the M_w of the deprotected *N*-acetylglucosaminopyranoside denoted here as B (Equation (2)), and also by dividing the change in M_w for acetylated *N*-acetylglucosamine functionalized

dendrimers upon deprotection by 126 (the loss of 3 acetyl groups) denoted here as C (Equation (3)). The values obtained from these three methods for determining the total amount of *N*-acetylglucosaminopyranoside addition were averaged, denoted by D (Equation (4)). The change in M_w upon galactose addition to the deacetylated *N*-acetylglucosamine dendrimers was divided by 162 (the addition of galactose) denoted here as E (Equation (5)) to calculate the total number of galactose units added to the glc*N*Ac functionalized dendrimers. ^{1}H Nuclear Magnetic Spectroscopy (NMR) was used as a second method to determine the degree of functionalization with *N*-acetyllactosamine. Through integration analysis of heterogeneously functionalized PAMAM-based dendrimers **6a-d**, the degree of Lac*N*Ac functionalization was determined by the integration of the H-2 *N*-acetylglucosamine resonance (4.36 ppm), which was set to one proton, and the galactose resonances (for example, the broad singlet at 4.22 ppm). The integration of resonance of HX′ was multiplied by D which is denoted by F (Equation (6)) to give the total addition of galactose. These two methods to determine the total number of galactose added to the dendrimer were then averaged, denoted as G (Equation (7)). Sample numbers using data from compound **6c** (G(4) PAMAM based) are provided in the equations below. The calculated M_w and functionalization of dendrimers **6a-d** are shown in Table

$$A = \frac{M_w \text{ (Protected Glc}N\text{Ac)} - M_w \text{ (PAMAM)}}{} = \frac{35000 - 13600}{} = 45 \quad \text{(eq 1)}$$

$$B = \frac{M_w \text{ (Deprotected Glc}N\text{Ac)} - M_w \text{ (PAMAM)}}{\frac{476}{350}} = \frac{30000 - 13600}{\frac{476}{350}} = 47 \quad \text{(eq 2)}$$

$$C = \frac{M_w \text{ (Protected Glc}N\text{Ac)} - M_w \text{ (Deprotected Glc}N\text{Ac)}}{126} = \frac{35000\text{-}30000}{126} = 40 \quad \text{(eq 3)}$$

$$D = \frac{A + B + C}{3} = \frac{45 + 47 + 40}{3} = 44 \quad \text{(eq 4)}$$

$$E = \frac{M_w \text{ (Lac}N\text{Ac)} - M_w \text{ (Deprotected Glc}N\text{Ac)}}{162} = \frac{37000 - 30000}{162} = 43 \quad \text{(eq 5)}$$

$$F = \int (4.15\text{ppm to } 4.25\text{ppm}) \times D = 0.89 \times 44 = 39 \quad \text{(eq 6)}$$

$$G = \frac{E + F}{2} = \frac{43 + 39}{2} = 41 \quad \text{(eq 7)}$$

Compound	Glc*N*Ac Functionalization	Lac*N*Ac Functionalization (G)	M_W (g/mol)
6a	1	10	8600
6b	9	16	18000
6c	2	41	36000
6d	38	95	120000

Table 1. Functionalization and M_W values for Lac*N*Ac functionalized dendrimers.

Galectin-3. Galectin-3 was expressed, purified, and diluted to a final protein concentration of 0.5 mg/mL in 1x PBS as previously reported.[55, 65]

Cell Lines and Cultures. All human fibrosarcoma HT-1080, lung carcinoma A549, and prostate DU-145 cell lines were purchased from ATCC (HT1080 (ATCC® CCL121™), A549 (ATCC® CCL185™), DU 145 (ATCC® HTB81™)). Cells were cultured as recommended by ATCC and have been passaged less than 10 times.

Homotypic Aggregation Assay. This procedure was adapted for Lac*N*Ac PAMAM dendrimers from a previously published method.[60] A solution of 16 million cells/mL in serum-free media (SFM) was prepared from 1-2 growth plates of the same cancer cell line. 2 mg/mL solutions of Lac*N*Ac PAMAM dendrimers **6a-c** and a 2.5 mg/mL solution of **6d** were prepared in Milli-Q water (18.2 MΩ·cm). For the homotypic aggregation assays in the presence of galectin-3, 15 μL of protein (16.7 μM, 250 ρmol), Lac*N*Ac PAMAM dendrimer solution (0 μL, 10 μL, 20 μL, 30 μL, or 40 μL), and enough SFM to total 53 μL per sample were added to a 1.5 mL Eppendorf tube and mixed. This was repeated in the absence of galectin-3. Cell suspension (15 μL, 240,000 cells) was then added to each reaction, gently vortexed for 1 sec., and incubated at 37 °C for 1 h with gentle rotation. On a Jenco BC-364 inverted microscope, three 10 μL aliquots from each tube were viewed and four images from each sample were randomly captured. These images were converted to monochrome in GNU Image Manipulation Program 2.8.14, and the image was analyzed using the software Pixcavator IA Standard Edition 5.0 for free and aggregated cells (pixels equivalent to 3 or less cells were considered free cell images).

Results and Discussion

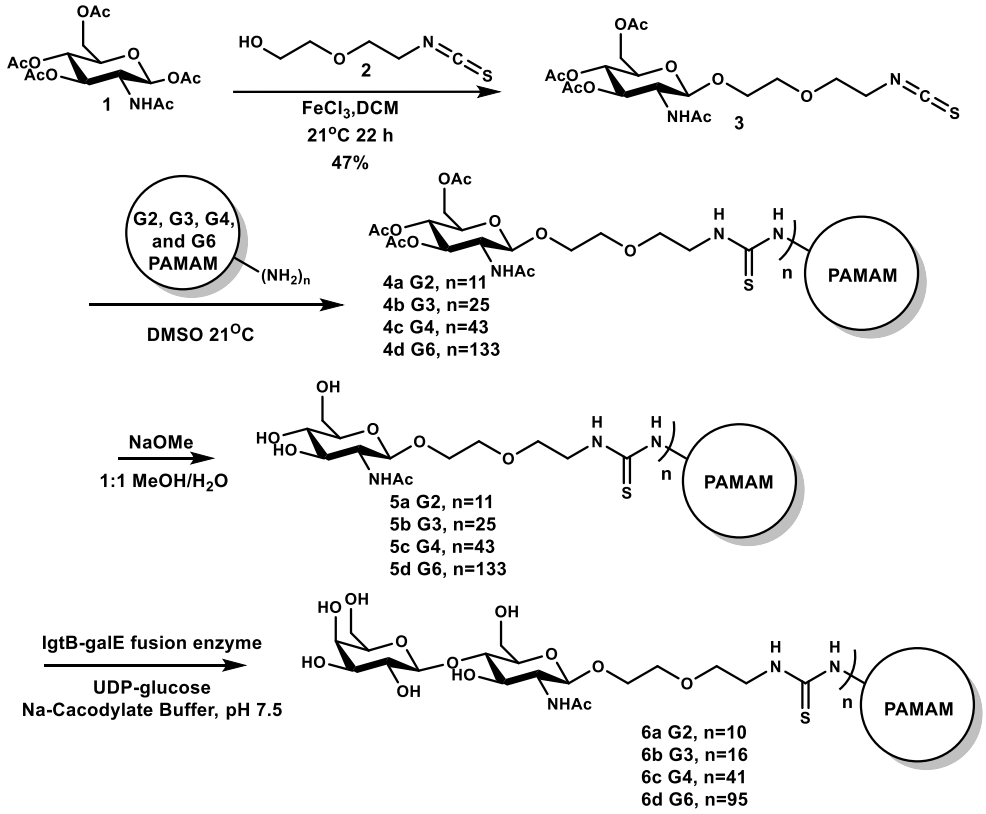

Scheme 1. Synthesis of *N*-acetyllactosamine-functionalized dendrimers.

The glycosylation reaction of 2-(2-isothiocyanatoethoxy)ethanol (**2**) with 2-acetamido-2-deoxy-1, 3, 4, 6-tetra-*O*-acetyl-beta-D-glucopyranose (protected Glc*N*Ac, **1**) was catalyzed by $FeCl_3$ to provide the glucosaminopyranoside product **3.** Through neighboring group participation, only the beta product **3** was observed. Functionalization of the PAMAM dendrimers (G2, G3, G4, and G6) with protected Glc*N*Ac **3** was accomplished at room temperature in slight excess of **3,** yielding the acetylated *N*-acetylglucosamine functionalized dendrimers **4a-d**. Deacetylation of the protected

Glc*N*Ac endgroups was achieved using Zemplén conditions to access Glc*N*Ac functionalized dendrimers **5a-d**. The final step in the synthesis of Lac*N*Ac functionalized dendrimers is a glycosylation reaction for the *β*-1-4 addition of **5** to the anomeric *β*-position of galactose. Blixt *et al*. developed the recombinant *β*-1,4-Galactosyltransferase-/UDP-4'-Gal Epimerase Fusion Protein (lgtB-galE) with which they demonstrated the selectivity and specificity of the enzyme to synthesize Lac*N*Ac derivatives from Glc*N*Ac derivatives which had various acceptors in the anomeric *β*-position.[122] The fusion enzyme is composed of two catalytic sites. The first subunit, galE, catalyzes the epimerization of uridine-5'-diphosphoglucose (UDP-Glc) to uridine 5'-diphosphogalactose (UDP-α-D-Gal). UDP- α-D-Gal then sequentially binds to the catalytic site of lgtB and is enzymatically transferred to the C_4-*β*-position of the dendrimer tethered Glc*N*Ac yielding the *β*-1,4-disaccharide functionalized dendrimers **6a-d**. In the absence of any additional functionalities that could be vulnerable on the PAMAM scaffold, crude lysate was used without further purification. After completion of the reaction and enzymatic degradation of the fusion protein and any additional proteins present in the lysate, Lac*N*Ac functionalized dendrimers were purified by dialysis. ^{1}H NMR spectroscopy and MALDI-TOF mass spectrometry (pos) were used to determine the degree of functionalization as described above. This synthesis afforded access to four generations of Lac*N*Ac functionalized dendrimers. In previous work, the preference of galectin-3 for *β*-galactoside clusters[77, 86, 123] was exploited using lactose functionalized dendrimers in homotypic cancer cell aggregation using *β*-lactoside dendrimers.[60] It was established that cancer cell homotypic aggregation can be mediated by the multivalent lactoside display

on PAMAM dendrimers. Therefore, cancer cell assays were performed for each Lac*N*Ac dendrimer with A-549 lung carcinoma cells in the presence and absence of excess galectin-3. In the absence of galectin-3, the smallest dendrimer, Lac*N*Ac functionalized G(2) dendrimer **6a**, seemed to have no effect on the free cancer cells after incubation (Figure 1a). When the same cell line was exposed to excess galectin-3 and incubated, galectin-3 was observed to have induced cellular aggregation (Figure 1a, red, 0 μM dendrimer concentration). In the presence of increasing amounts of **6a (**Figure 1a) inhibition of the galectin-3 induced aggregation was observed. Lac*N*Ac functionalized G(3) dendrimer **6b** induced similar effects as the smallest glycodendrimer **6a**, although the effects with **6b** were less pronounced. In contrast to this observation, the larger dendrimers, Lac*N*Ac functionalized G(4) dendrimer **6c** and Lac*N*Ac functionalized G(6) dendrimer **6d,** showed no apparent inhibition of galectin-3 induced cell aggregation. In the absence of added galectin-3, both dendrimers **6c** and **6d** induced aggregation.

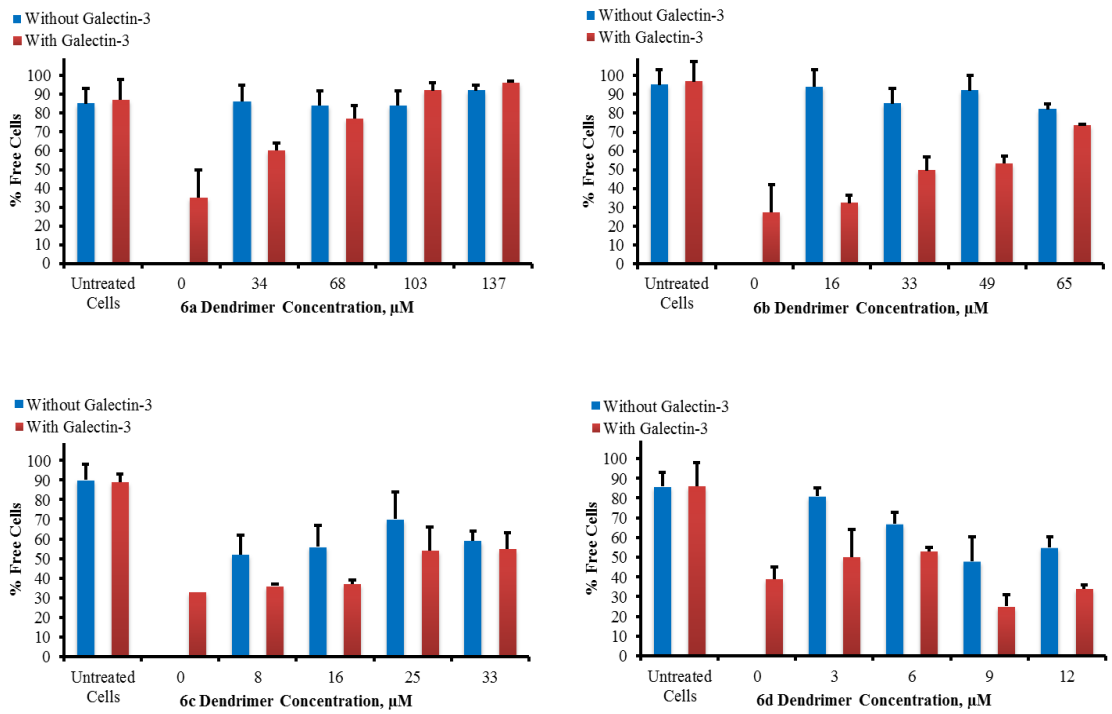

Figure 1. Results of *N*-acetyllactosamine functionalized dendrimers on galectin-3 induced homotypic aggregation of A-549 cells. A. Effects of *N*-acetyllactosamine functionalized G(2) dendrimer **6a** on A-549 cancer cell aggregation studies. B. Effects of *N*-acetyllactosamine functionalized G(3) dendrimer **6b** on A-549 cancer cell aggregation studies. C. Effects of *N*-acetyllactosamine functionalized G(4) dendrimer **6c** on A-549 cancer cell aggregation studies. D. Effects of *N*-acetyllactosamine functionalized G(6) dendrimer **6d** on A-549 cancer cell aggregation studies.

The effects of Lac*N*Ac functionalized dendrimers on cancer cellular aggregation were also investigated with DU-145 prostate cancer cells and HT-1080 fibrosarcoma cancer cells. These cell lines were selected because DU-145 contained more native galectin-3 then A-549 lung cancer cells, and HT-1080 contained less. [54, 57, 60, 124] Homotypic cancer cell aggregation studies were repeated in the presence and absence of exogenous galectin-3 with these lines, and the results of these assays are shown in figures two and three. As with A-549's cells, the smallest glycodendrimers **6a** and **6b** again had

no effect on the cells in the absence of exogenous galectin-3 (Figure 2a-d without galectin-3). When galectin-3 was added and incubated with the dendrimers **6a** and **6b**, again the galectin-3 induced cancer cellular aggregation was inhibited. The complete inhibition of the galectin-3 induced aggregation of DU-145 cells by dendrimer **6a** was observed even at the lowest initial concentration that was used. Assays were repeated again with Lac*N*Ac functionalized G(2) dendrimer **6a** at concentrations of 10 µM and 20 µM (Figure 2a and 2b). DU-145 cancer cell induced aggregation was shown to be inhibited more completely at thr lower concentrations of **6a,** which can be inferred to be the result of the increased amount of available native galectin-3 available in this cell line compared to the HT-1080 cells. This possible explanation also supports the lack of induced galectin-3 aggregation by dendrimer **6c** in the HT-1080 cancer cell assays. While induced aggregation by the Lac*N*Ac functionalized glycodendrimer G(4) dendrimer **6c** in DU-145 (Figure 3b) was less pronounced than with the largest glycodendrimer **6d** (Figure 3d), this effect was absent in assays using the HT-1080 cell line(Figure 3a). This same effect was observed in the HT-1080 cell assays with **6d** (Figure 3c). Although the induced aggregation was not entirely absent, there was a significant reduction of induced aggregation observed when compared to Lac*N*Ac functionalized G(6) dendrimer **6d** / DU-145 aggregation study.

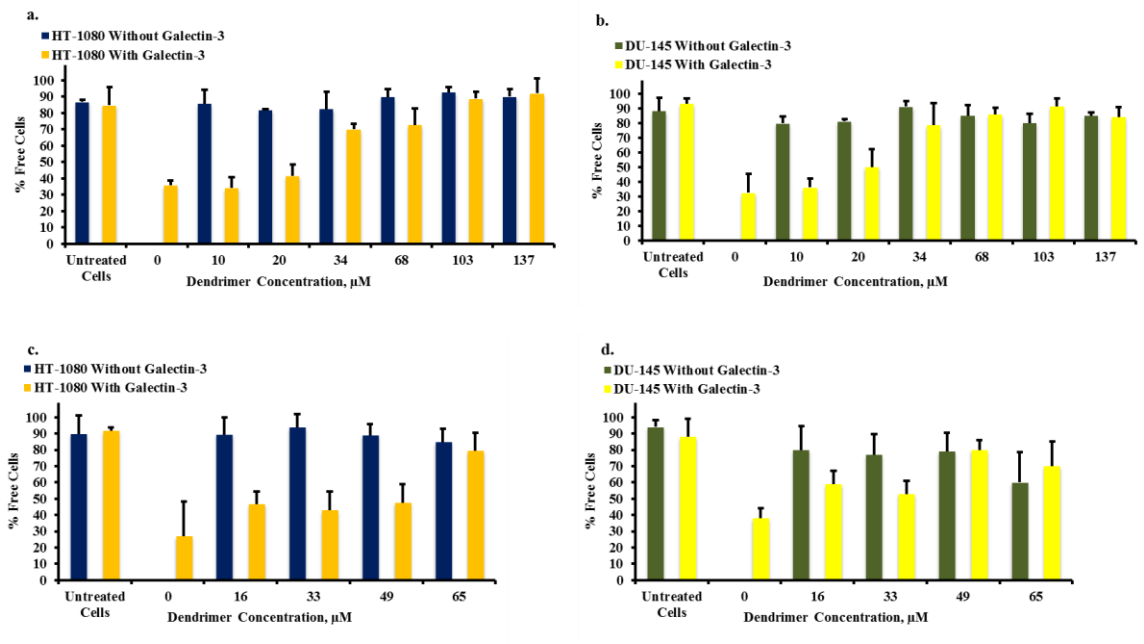

Figure 2. Results of *N*-acetyllactosamine functionalized G(2) and G(3) dendrimers on galectin-3 induced homotypic aggregation of HT-1080 and DU-145 cells. A. Effects of *N*-acetyllactosamine functionalized G(2) dendrimer **6a** on HT-1080 cell aggregation studies. B. Effects of *N*-acetyllactosamine functionalized G(2) dendrimer **6a** on DU-145cancer cell aggregation studies. C. Effects of *N*-acetyllactosamine functionalized G(3) dendrimer **6b** on HT-1080 cancer cell aggregation studies. D. Effects of *N*-acetyllactosamine functionalized G(3) dendrimer **6b** on DU-145 cancer cell aggregation studies.

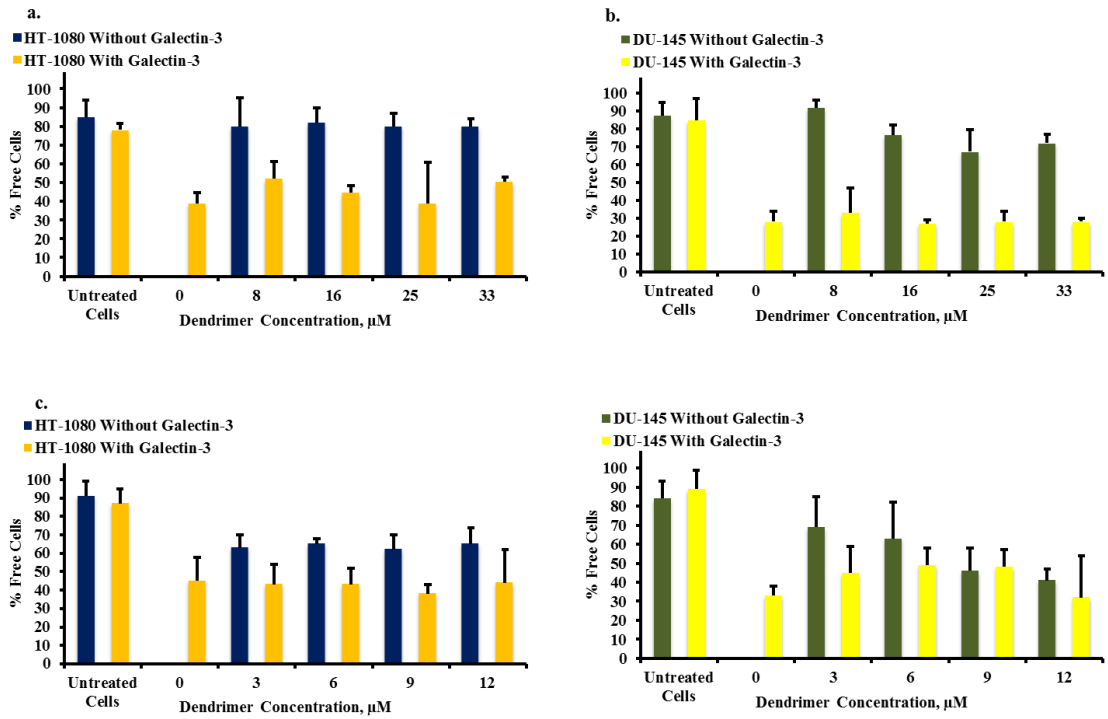

Figure 3. Results of *N*-acetyllactosamine functionalized G(4) and G(6) dendrimers on galectin-3 induced homotypic aggregation of HT-1080 and DU-145 cells. A. Effects of *N*-acetyllactosamine functionalized G(4) dendrimer **6c** on HT-1080 cell aggregation studies. B. Effects of *N*-acetyllactosamine functionalized G(4) dendrimer **6c** on DU-145 cancer cell aggregation studies. C. Effects of *N*-acetyllactosamine functionalized G(6) dendrimer **6d** on HT-1080 cancer cell aggregation studies. D. Effects of *N*-acetyllactosamine functionalized G(6) dendrimer **6d** on DU-145 cancer cell aggregation studies.

Previously we have demonstrated that lactose functionalized dendrimers mediated homotypic cellular aggregation by modifying the galectin-3/MUC1 pathway through multivalent crosslinking (large dendrimers) or by diverting galectin-3 from binding to its traditional glycoclusters on the cell surface.[60] Here we have shown that by decorating PAMAM scaffolds with *N*-acetyllactosaminosides, which have a monomeric association constant three-fold greater than lactososide for galectin-3, we were able to mediate homotypic cellular aggregation with a series of four Lac*N*Ac dendrimers. The

concentration of *N*-acetyllactosamine was kept constant relative to the through each series so that we could study the impacts of the four different generations of the multivalent glycodendrimers. The concentrations of these dendrimers were also kept relative to the lactose concentrations of previous lactoside functionalized PAMAM dendrimers studies[60] so the impact of differences in monomeric binding associations on the ability of glycodendrimers to mediate homotypic cancer cellular aggregation could be assessed. The smallest glycodendrimers, Lac*N*Ac functionalized G(2) dendrimer **6a** and Lac*N*Ac functionalized G(3) dendrimer **6b** both inhibited cancer cellular aggregation in all three cell lines. Both dendrimers **6a** and **6b** had similar glycoside functionalization as the smallest lactosides functionalized dendrimers previously studied.[60] Although they all displayed similar effects, **6b** was able to completely inhibit induced aggregation of HT-1080 cancer cell where inhibition was negligible with the Lac*N*Ac functionalized G(3) dendrimer **6a**.

In studies using larger generations G(4) and G(6) glycodendrimers **6c** and **6d** no observable differences were measured using HT-1080 cells; both **6c** and **6d** were unable to induce significant aggregation of HT-1080 cells but were able to induce aggregation of A-549 cells. Interestingly Lac*N*Ac functionalized G(4) dendrimer **6c** were able to induce aggregation of DU-145 cells. Although not as a prominent as the cellular aggregates formed with lactose or Lac*N*Ac functionalized G(6) dendrimers, this represents an important derivation from previous results using lactose functionalized dendrimers of the same generation. Both lactose and Lac*N*Ac functionalized dendrimers induced aggregation of A-549 and DU-145 cancer cells.

In previous studies we have shown the avidity of multivalent associations can be predicted in a reliable way for PAMAM dendrimers based on the monovalent affinity of the ligand.[74] These results were consistent with Whitesides' model, which suggested the association constant of the polyvalent interactions should equal the association constant of the monovalent interaction raised to the αN, where α is the cooperativity factor and N is equal to the number of interactions that occur between the receptor and ligand.[89] A possible explanation for the results described here considers the difference of the monovalent associations for galectin-3 binding to *N*-acetyllactosaminoside and lactoside. The difference of the individual monovalent association, although small may be significantly augmented when the ligands are displayed multivalently. The monovalent binding differences may account for the higher activity of Lac*N*Ac functionalized G(3) and Lac*N*Ac functionalized G(4) dendrimers **6b** and **6c** in comparison to lactose functionalized dendrimers of the same generations.

Conclusion

Lac*N*Ac functionalized PAMAM dendrimers were synthesized using a four-step chemoenzymatic route. The enzymatic step controlled the regiochemistry of the addition of galactose to *N*-acetylglucosaminoside functionalized dendrimers using a recombinant β-1,4-Galactosyltransferase-/UDP-4'-Gal Epimerase Fusion Protein (lgtB-galE). Homotypic cellular aggregation, which is promoted by the presence of galectin-3 as it binds to glycosides at the cell surface, was studied using HT-1080 fibrosarcoma, A-549

lung, and DU-145 prostate cancer cell lines. This study revealed that in the presence of small Lac*N*Ac functionalized PAMAM dendrimers (**6a** and **6b**) displaying monomeric affinity comparable to TF-antigen, its putative binding ligand on cancer cells, galectin-3 was diverted from its normal MUC1/galectin-3 pathway. Inhibition of homotypic cancer cellular aggregation was observed with **6a** and **6b.** The larger glycodendrimers (**6c** and **6d**) were able to induce cellular aggregation. The results of these studies demonstrated that using a tunable, multivalent scaffold functionalized with *N*-acetyllactosamine, which has only a threefold increase in monomeric affinity over lactose for galectin-3 homotypic cellular aggregation was effectively mediated. In addition to this, induced aggregation was observed over broader ranges of concentrations and with smaller deviations from the measured averages for Lac*N*Ac functionalized PAMAM dendrimers.

CHAPTER THREE

CYCLODEXTRIN-FUNCTIONALIZED CHROMATOGRAPHIC MATERIALS TAILORED FOR REVERSIBLE ADSORBTION

Contributions of Authors

Manuscript in Chapter 3

Author: Jessica H. Ennist

Contributions: Performed synthesis of mono-6-deoxy-6-azido-*β*-cyclodextrin, *N*-(3-(trimethoxysilyl)propyl)propiolamide, and all functionalized slides. Performed x-ray photoelectron spectroscopy experiments and analysis. Co-wrote initial draft of the manuscript.

Co-Author: Eric A. Gobrogge

Contributions: Performed experiments and obtained results for all fluorescence spectroscopy and vibrational sum frequency generation experiments. Co-wrote initial draft of the manuscript.

Co-Author: Kristian H. Schlick

Contributions: Performed the synthesis of G1 and G2 dendrons and performed prelimanay xps experiments on amine, G1, and G2.

Co-Author: Robert A. Walker

Contributions: Primary Investigator. Conceived of the project and provided funding. Provided guidance throughout the project. Provided feedback and edited drafts of the manuscript

Co-Author: Mary J. Cloninger

Contributions: Primary Investigator. Conceived of the project and provided funding. Provided guidance throughout the project. Provided feedback and edited drafts of the manuscript.

Manuscript Information Page

Jessica H. Ennist, Eric A. Gobrogge, Kristian H. Schlick, Robert A. Walker, Mary J. Cloninger

ACS Applied Materials and Interfaces

Status of Manuscript:
____ Prepared for submission to a peer-reviewed journal
____ Officially submitted to a peer-review journal
____ Accepted by a peer-reviewed journal
_x__ Published in a peer-reviewed journal

Published by American Chemical Society
ACS Appl. Mater. Interfaces, 2014, 6 (20), pp 18087–18097

Cyclodextrin-functionalized Chromatographic Materials Tailored for Reversible Adsorption.

Jessica H. Ennist[†]*, Eric A. Gobrogge*[†]*, Kristian H. Schlick, Robert A. Walker*, Mary J. Cloninger**

Department of Chemistry and Biochemistry, Montana State University, Bozeman, MT 59717

KEYWORDS. Reversible adsorption, dendrimers, dendrons, β-cyclodextrin, silica, XPS, fluorescence, coumarin, SFG

ABSTRACT

Novel dendronized silica substrates were synthesized. First and second generation polyaryl ether dendrons were appended to silica surfaces. Using Cu(I) mediated cycloaddition "click" chemistry, β-cyclodextrin was tethered to the dendronized surfaces and also to a non-dendronized surface for comparison purposes. This synthesis strategy affords a modular, versatile method for surface functionalization in which the density of functional groups can be readily varied by changing the generation of dendron that is used. The surfaces, which are capable of adsorbing target analytes, have been characterized and studied using x-ray photoelectron spectroscopy (XPS) and vibrational sum frequency spectroscopy (VSFS). Fluorescence spectroscopy was used to study the surfaces' ability to retain coumarin 152 (C152). These studies indicated that the β-cyclodextrin functionalized surfaces not only adsorbed, but also retained C152 through multiple aqueous washes. Furthermore, these observations were quantified showing that substrates functionalized with first generation dendrons have more than 6 times greater capacity to adsorb C152 than slides functionalized with monomeric β-cyclodextrin. The first generation dendrons also have 2 times greater the capacity than the larger generation dendrons. This result is explained by describing a dendron that has an increased number of β-cyclodextrin monomers, but when covalently bound to silica, has a footprint too large to optimize the number of accessible monomers. Overall, both dendronized surfaces

demonstrated an increased capacity to adsorb targeted analytes over the slides functionalized with monomeric β-cyclodextrin. The studies reported provide a methodology for characterizing and evaluating the properties of novel, highly functional surfaces.

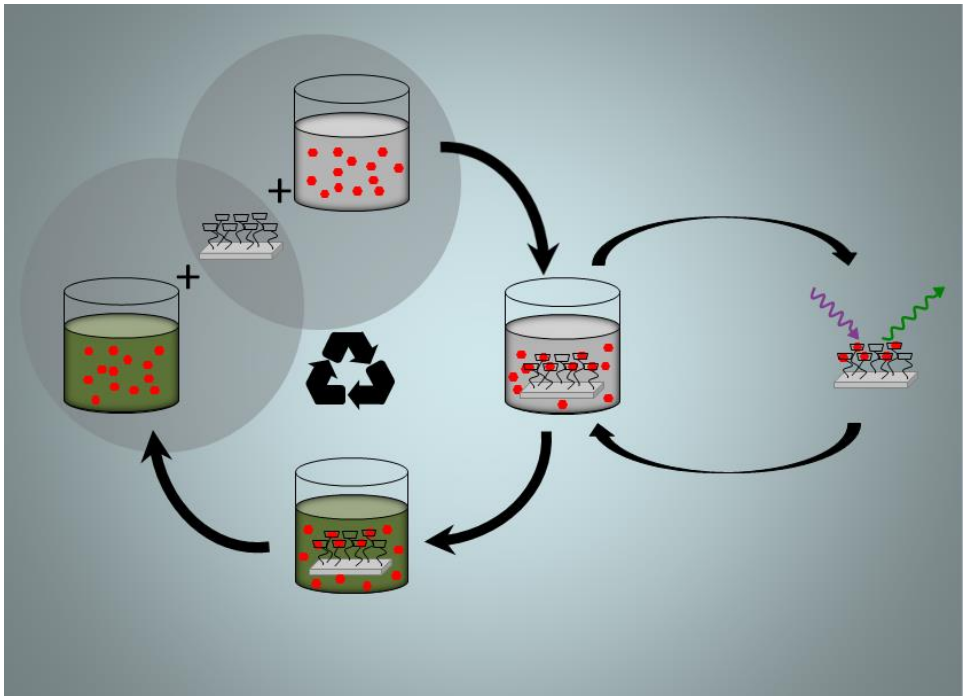

INTRODUCTION

Removing organic analytes from an aqueous solution plays a critical role in a host of environmental and technology related challenges. For example, the Environmental Protection Agency's Safe Drinking Water Act ensures the quality of drinking water by limiting the amounts of over 90 different contaminants, with new contaminants being added to the list every five years.[125] Nearly 60% of these contaminants are organic and have been determined to cause side effects ranging from organ damage to increased risk of cancer when exposure to the maximum allowed levels are exceeded.[125] Examples include aromatic species used to manufacture insecticides such as benzene (0.005 mg/L) and chlorobenzene (0.1 mg/L), two chemicals that are also used in textile processing. One current and popular method for removing such contaminants from water includes using a high surface area substrate such as activated charcoal or soda ash.[126,127] While this method can remove a wide variety of pollutants, the resulting contaminated material cannot be reused and must be disposed of after the sorption process. In applications where large volumes of solution must be processed in order to remove relatively small amounts of a targeted solute, one ideally wants to employ a system that concentrates the solute and can be recycled for further use.

A recyclable substrate that can remove solutes from solution requires that adsorption be reversible. For reversible adsorption to be a viable mechanism for

removing solutes from solution, binding energies must be large enough so that adsorption is thermodynamically favorable under application-specific conditions, but weak enough so that solutes will desorb with modest changes in solution phase temperature, pH, or composition. Such requirements preclude standard covalent bond formation between the substrate and solute and, instead, must rely on reversible interactions to remove organic solutes from aqueous solution.[128] Spontaneous self-assembly and molecular recognition are two common phenomena that rely on non-covalent forces to drive association and aggregation in solution and at surfaces, and from the perspective of reversibly binding solutes to surfaces,[129-131] exploiting the ability of *β*-cyclodextrin as a host for hydrophobic organic guests is an attractive option.

Surfaces functionalized with *β*-cyclodextrin have been used to form guest-host inclusion complexes.[132-134] *β*-cyclodextrin forms a hydrophobic cavity through a series of α-1,4 linkages between seven glucoside monomers.[135] This structure forms a complex of intramolecular hydrogen bonds rendering the interior cavity hydrophobic and the exterior surface hydrophilic.[136] Representative binding energies for *β*-cyclodextrin complexes with organic analytes generally range from -25 to -5 kJ/mol.[132] To put these binding energies into the context of reversible adsorption, equilibrium conditions necessitate that removal of 50% of the solute molecules from a 10 μM aqueous solution at room temperature requires an adsorption (or binding) energy of approximately -19 kJ/mol, and removal of 90% requires an adsorption energy of -24 kJ/mol. In order for the functionalized surface saturated with the bound analyte to be recycled and reused, the

analyte desorption must overcome this host-guest association in a way that leaves the surface intact and ready for re-use.

Previous studies have used surface tethered β-cyclodextrin to form guest-host complexes for numerous purposes such as reversible chlorophenol and chlorobenzene removal,[133] and controlled fragrance release.[134] Such surfaces, however, have a capacity limited by the surface coverage of β-cyclodextrin sites. In principle, more sites would improve the substrate's capacity. Work described below overcomes the saturation limitation commonly associated with using functionalized surfaces to promote chemical processes. Surfaces have a limited number of sites that are available to accommodate the adsorption of solutes from solution. By functionalizing silica substrates with dendrimers containing multiple β-cyclodextrin units, we show how the useful ability of β-cyclodextrin to form host-guest self-assemblies can be amplified by the multivalent properties of dendrimer chemistry. Substrates functionalized with first and second generation dendrons as well as surfaces functionalized with only single β-cyclodextrin monomers (as shown in Figure 1) are tested for reversible adsorption behavior using Coumarin 152 (C152) – a fluorescent organic dye having a trifluoromethyl group in the 4 position and a dimethyl amino group in the 7 position. C152 was chosen for the fluorescence studies because of this solute's well-characterized photophysical behavior in a wide variety of solvents.[137-140] From previous studies, C152's emission wavelength has been shown to shift with solvent polarity due to differences between the ground-state and excited-state dipole moments as well as the solute's sensitivity to hydrogen bonding

opportunities presented by the solvent.[138, 140, 141,142, 143,144,145] Affinity of the coumarin solutes for the surfaces can be estimated from bulk solution binding constants. The studies reported here demonstrate that C152 has an affinity for the β-cyclodextrin functionalized surfaces and is retained even after multiple washings with a pure aqueous solvent. A small volume rinse of the saturated surface with methanol results in complete release of the solute. Quantifying these results show that substrates functionalized with first generation dendrons (containing multiple β-cyclodextrin sites) have a greater capacity than slides functionalized either with monomeric β-cyclodextrin or with higher order dendrons. This result can be understood in terms of the tradeoff between maximizing the number of accessible β-cyclodextrin monomers per dendron vs. the number of dendrons that can be covalently bound to a silica substrate.

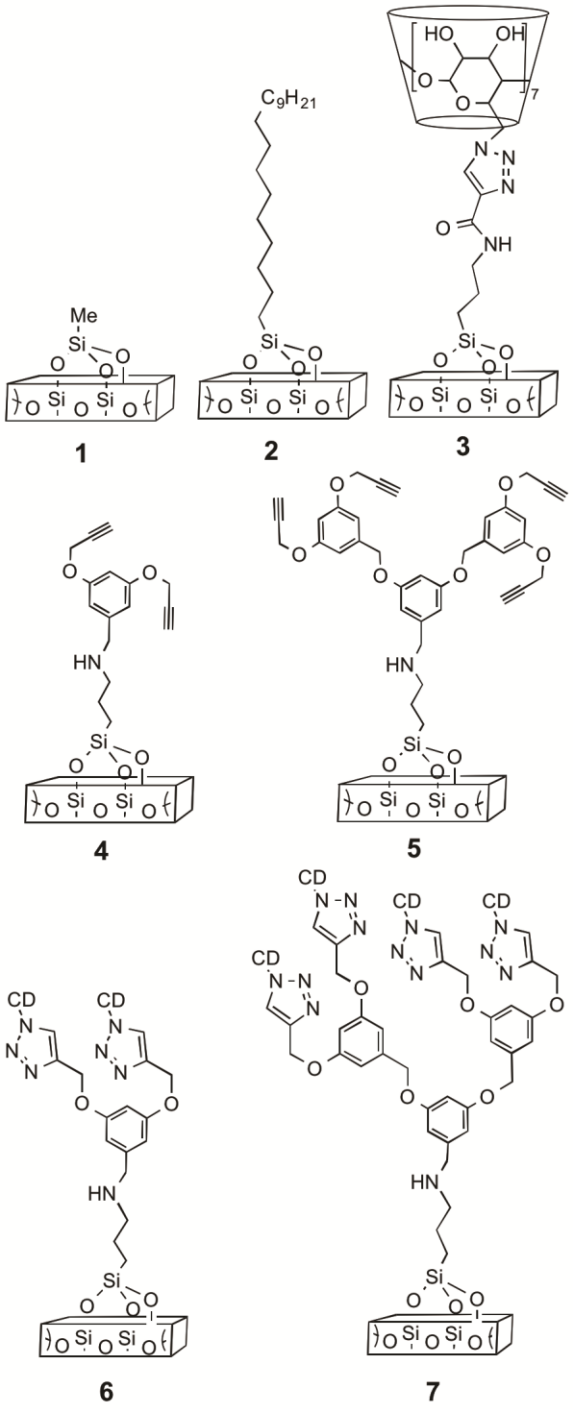

Figure 1. Schematic representations of functionalized surfaces. CD = β-cyclodextrin.

Experimental Methods

Materials and Methods. The quartz slides (25 x 25 x 0.5 mm) used in these studies were purchased from SPI Supplies. Prior to experimental use, the quartz slides were cleaned in a 1 : 1 mixture (by volume) of nitric acid and sulfuric acid (Macron Chemicals) for one hour and rinsed with deionized water (Millipore, 18.2 MΩ). *N*, *N*'-Dicyclohexylcarbodiimide and all high purity organic solvents were purchased from Fisher Scientific. All other chemicals used were purchased from Sigma-Aldrich.

Alkyl Monolayer Functionalized Surfaces 1 and 2. Strategies for creating silica surfaces having different functional group composition were adapted from Jones' SAM formation using THF/Cyclohexane.[146] A 10 mL Teflon beaker equipped with a stir bar was placed inside a 50 mL Teflon beaker. Both beakers were placed inside a sealable glass container with an inert atmosphere. The silica slides were placed along the inside wall of the outer Teflon beaker, and toluene (40 mL) was added. A stock solution of alkyltrichlorosilane (0.03 mmol in 2 mL of Tetrahydrofuran (THF) and 75 µL of 6M HCl) was stirred for 4 h at room temperature and added to the 50 mL Teflon beaker. The reaction was allowed to stir for 3 h under argon. To remove excess solvents, slides were sonicated for 3 min in 50 mL of toluene, for 3 min in 50 mL of Milli-Q water (18.2 MΩ·cm), and for 3 min in 50 mL of methanol. The sequential sonications with water and

methanol were repeated two more times. Slides were dried under a stream of argon and stored under vacuum.

1-*β*-cyclodextrin-*N*-(3-(silyl)propyl)-1H-1,2,3-triazole-4-carboxamide Functionalized Surface 3. Mono-6-deoxy-6-azido-*β*-cyclodextrin was synthesized using previously described methods.[147,148] *N*-(3-(trimethoxysilyl)propyl)propiolamide was synthesized by the method that was reported for the analogous tri-ethoxy compound.[149] The synthesis of functionalized surface **3** was adapted from silica beads to slides.[150] A 10 mL Teflon beaker equipped with a stir bar was placed inside a 50 mL Teflon beaker. Toluene (40 mL) was added to the 50 mL Teflon beaker, and two slides were placed along the inside wall of the 50 mL Teflon beaker. *N*-(3-(trimethoxysilyl)propyl)propiolamide (90 mg, 390 μmol) was dissolved in the toluene, and the solution was stirred at reflux for 2 h. The slides were washed in 40 mL of toluene. The slides and 40 mL of *N*,*N*-dimethylformamide (DMF) were added to a new 50 mL Teflon beaker equipped with a 10 mL Teflon beaker holding a stir bar and heated to 80 ºC. Mono-6-deoxy-6-azido-*β*-cyclodextrin (330 mg, 280 μmol, 1 equiv.) and $CuI(PPh_3)_3$ catalyst (13 mg, 28 μmol, 0.1 equiv.) was added, and the reaction was stirred for 4 d. Slides were washed with 40 mL of DMF, and were sonicated for 3 min in 50 mL of toluene. Slides were sonicated for 3 min in 50 mL of Milli-Q water (18.2 MΩ·cm) and for 3 min in 50 mL of methanol. The sequential sonications with water and methanol were repeated two more times. Slides were dried under a stream of argon and stored under vacuum.

Polyaryl Ether Dendron Functionalized Surfaces 4 and 5. Two generations of polybenzyl ether dendrons were synthesized by previously described methods.[151,91,35] Silica surfaces were functionalized by general silanization methods.[152,153] The slides were placed along the inside wall of a 50 mL Teflon beaker containing a 10 mL Teflon beaker equipped with a stir bar. 3-aminopropyltrimethoxysilane was added to 40 mL of toluene in the 50 mL Teflon beaker and refluxed for 2 h. Slides were washed with 40 mL of toluene and were added to a new 50 mL Teflon beaker equipped with a 10 mL Teflon beaker containing a stir bar and 40 mL of toluene. The toluene was brought to reflux, and the dendron (50 μmol) and 2 mL of Hunig's base were added. The reaction was stirred for 2 d. Slides were sonicated for 3 min in 50 mL of toluene. Slides were sonicated for 3 min in 50 mL of Milli-Q water (18.2 MΩ·cm) and for 3 min in 50 mL of methanol. The sequential sonications with water and methanol were repeated two more times. Slides were dried under a stream of argon and stored under vacuum.

***β*-Cyclodextrin Functionalized Polyaryl Ether Dendronized Surfaces 6 and 7.** Polyaryl ether dendron functionalized slide **4** or **5** was placed along the inside wall of a 50 mL Teflon beaker equipped with a 10 mL Teflon beaker holding a stir bar. DMF (40 mL) was added, and the system was heated to 80 ºC. Mono-6-deoxy-6-azido-*β*-cyclodextrin (110 mg, 100 μmol, 1 equiv.) and $CuI(PPh_3)_3$ catalyst (10 μmol, 0.10 equiv.) were added and allowed to stir for 2 d. Slides were washed with 40 mL of DMF, and ultrasonically cleaned for 3 min in 50 mL of toluene. Slides were sonicated for 3 min in 50 mL of toluene. Slides were sonicated for 3 min in 50 mL of Milli-Q water (18.2

MΩ·cm) and for 3 min in 50 mL of methanol. The sequential sonications with water and methanol were repeated two more times. Slides were dried under a stream of argon and stored under vacuum.

X-ray Photoelectron Spectroscopy (XPS). The functionalized slides were characterized using XPS. The analysis was conducted on a Physical Electronics 5600ci XPS system equipped with monochromatized Al Kα X-rays. The analysis area of the sample was 0.8 mm in diameter. Electron emissions were collected at 45° to the normal of the surface, and the spherical-sector-analyzer pass energy was selected as 23.5 eV for high-resolution scanning and as 46.95 eV for a survey to achieve optimum energy resolution and count rate. Initial representative survey scans were acquired from 0 to 600 eV for 10 sweeps (sw) at 0.4 eV/step, and 20 mS/step (figure 2). For further elemental analysis, high resolution (HR) scans were acquired for the C 1s (~280 to 291 eV, 2 sw), N 1s (~394 to 405 eV, 5 sw), O 1s (~528 to 537 eV, 2 sw), and Si 2p (~98 to 106 eV, 3 sw) regions. The acquisition parameters were run for 10 cycles at 0.50 eV/step and 20mS/step. For all spectra, the background of all regions were subtracted using the Shirley background.[13] Peak positions were normalized to the C 1s peak at 285.0 eV and were fitted to functions having a 100% Gaussian line shape. Binding energies were normalized to the C 1s.The data acquisition and data analysis were performed using RBD AugerScan software. Quantitative analysis to determine the site composition was performed using methodologies previously described by Geiger and coworkers.[130] Specific expressions relevant to our analysis are shown in the Supporting Information.

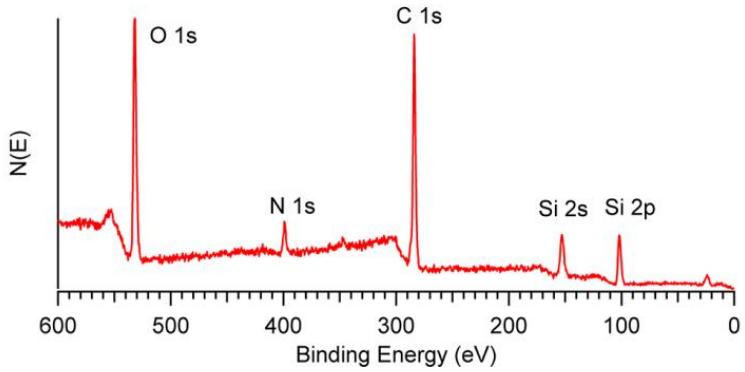

Figure 2. Survey scan of functionalized surface **3**.

Fluorescence Spectroscopy. The functionalized slides were characterized using fluorescence spectroscopy and the fluorescent dye C152. This system (functionalized surface/fluorescent dye) was used to test the ability of different slides to retain adsorbed analytes. Steady state fluorescence spectra were recorded using a Jobin Yvon Horiba Fluorolog 3 FL3-11. Bulk measurements were acquired with 1 nm instrumental resolution accumulating signal for 0.5 seconds at each step. Bulk solution measurements were made with no polarizers in either the excitation or emission paths. Surface fluorescence measurements were acquired in 0.5 nm increments integrating for 1.5 seconds at each point with the excitation and emission polarizers set 90° apart.[139] This procedure reduced the amount of background scatter in the surface excitation and emission spectra so that adsorbed species could be observed clearly.

In order to evaluate the ability of β-cyclodextrin-functionalized surfaces to adsorb organic solutes from solution, the bulk solution behavior of C152 was characterized in hexane and aqueous solvents (in the absence and presence of co-dissolved β-

cyclodextrin). All bulk solution experiments were performed with C152 concentrations of 10 μM (2.6 mg/L). To measure the guest-host complex's fluorescence properties, excess (2.3 : 1 mole ratio) *β*-cyclodextrin was added to the aqueous solution. For the surface measurements, 10 μM aqueous solutions of C152 were prepared and functionalized slides were then allowed to equilibrate in the solution for one hour. Additional equilibration time did not lead to any observed changes in the data. The slides were removed slowly from the solution, and excess solvent was allowed to evaporate from the bottom of the slide. Fluorescence measurements were acquired from the top of the slide, the incident light striking the sample at a 30° angle with respect to normal. Previous studies have shown that this procedure probes adsorbed films that are not influenced by excess solute accumulation following evaporation.[139, 154, 155] After the initial scan, the slide was immersed in pure Milli-Q water for 60 seconds and then removed. Excess water was allowed to evaporate and a second surface fluorescence spectrum was measured. This rinse-and-measure procedure was repeated to test the retention abilities of the functionalized surfaces. Control experiments were performed using the same procedure with unfunctionalized slides and slides that had been functionalized with terminal alkyl monolayers. The hydrophilic control slides were cleaned prior to use by soaking in a 50:50 mixture of concentrated sulfuric and nitric acid. The hydrophobic control slides were rinsed with excess methanol and dried at ambient temperature before use.

To quantify the amount of analyte bound to the functionalized surfaces, a similar fluorescence procedure was used. The slide of interest was initially allowed to again

soak in a 10 μM aqueous solution of C152. After one hour had elapsed, the slide was removed from the solution and the excess solvent allowed to evaporate. Upon evaporation, the slide was soaked in water for 60 seconds, removed, and again the slide was allowed to dry. The slide was then washed and sonicated in 50 mL of methanol and the fluorescence excitation of the wash at C152's emission wavelength (513 nm) was measured. Comparing the excitation intensity of the wash to standard solutions having known concentrations allowed the number of molecules adsorbed to the surface to be determined quantitatively. Assuming a uniform distribution of adsorbates on the surface, these results were converted into surface coverages.

Vibrational Sum Frequency Generation (VSFG). VSFG is a 2^{nd} order nonlinear optical process that measures vibrational spectra of molecules in environments lacking inversion symmetry. In a VSFG experiment, two high intensity fields (one visible and one infrared) induce a coherent, nonlinear polarization in molecules at a surface or interface. This polarization oscillates at a frequency equal to the sum of the incident visible and IR fields, and is responsible for the detected signal. When the IR frequency is resonant with a vibrational mode of a surface molecule, the sum frequency (SF) response experiences resonance enhancement. By altering the polarization of the light incident on the sample and the polarization at which the SF beam is collected, orientation data from detected surface species can also be obtained by solving for the four independent non-zero elements of the 27 element second order susceptibility tensor. The individual polarizations in such a VSFG experiment are identified by a three-letter symbol (e.g. *ssp*

or *sps*) where *s* indicates the electric field vector of the light is parallel to the surface, and *p* indicates the electric field vector is perpendicular to the surface. These three letters represent the polarization of the three frequencies in order of decreasing energy (i.e. SF, visible, IR).[156] A more in-depth description of the SFG process and SFG theory has appeared elsewhere.[156-158]

VSFG characterization employs an assembly described previously.[159] Briefly, the system uses a Libra-HE Ti:sapphire laser (Coherent, 3.3W 85 fs pulse duration, 1kHz repetition rate) coupled to a visible optical parametric amplifier (Coherent OPerA Solo) to generate IR light. VSFG experiments were performed with co-propagating IR and visible fields with both fields passing through the 0.5 mm silica slide and the signal being detected in the reflected direction. The IR wavelength was tuned from 3.2 to 3.7 μm in 0.5 μm increments and the IR field was focused onto the sample at an angle of 73° with respect to normal. The visible beam was spectrally stretched and sliced using an 1800 g/mm grating and variable width slits resulting in a spectrally narrowed visible beam (20 cm^{-1}). After passing through two different delay stages, this beam was focused onto the surface at an angle of 67° with respect to normal. When the IR and visible fields were spatially and temporally overlapped, sum frequency signal was generated and directed into a monochromator (SpectraPro-300i, Acton Research Corporation) where it was dispersed onto a 1340x100 pixel CCD (PIXIS100B, Princeton Instruments). SFG spectra were combined and normalized to a nonresonant gold system response using homemade routines written in Igor Pro (v.6). VSFG spectra were corrected first for IR power using

the nonresonant SFG response across the frequency region of interest from a gold-coated silicon wafer. Spectra were then normalized by the SFG signal from a clean, hydrophilic silica/vapor interface acquired under the appropriate polarization condition. All spectra were then calibrated using the 2910 cm^{1} methyl symmetric stretch of DMSO at the liquid/vapor interface.[160]

A sample VSFG spectrum can be seen below in Figure 3. This representative figure, taken in the *ssp* polarization combination, shows the C-H stretching region of the solid/vapor interface of a methyl terminated silica surface.

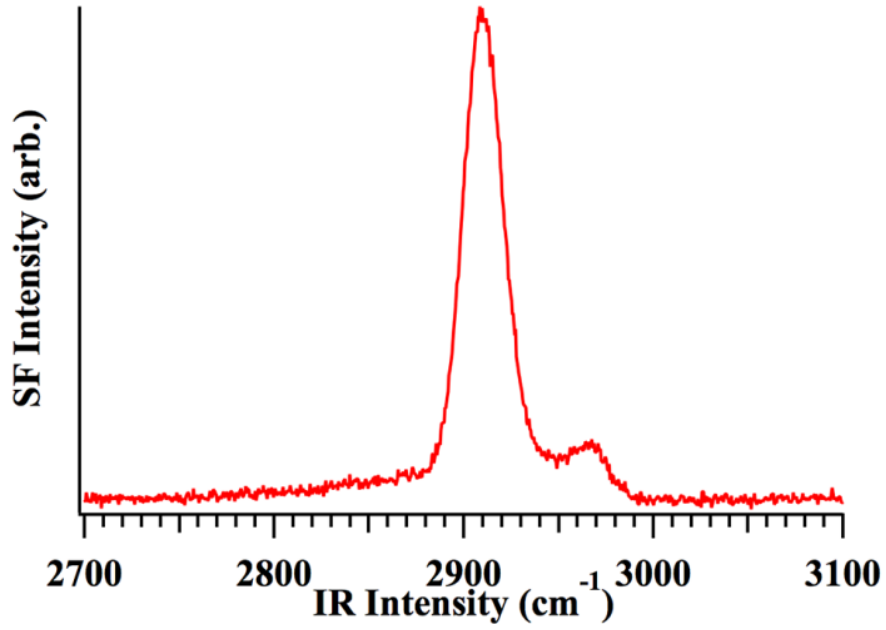

Figure 3. VSFG spectrum of the solid/vapor interface of a methyl-terminated silica substrate in the *ssp* polarization combination.

In this sample spectrum, two peaks are evident at 2910 cm^{-1} and 2967 cm^{-1}. These two peaks result from the methyl group symmetric and antisymmetric stretch, respectively, and are consistent with previously reported data.[161] The intensity difference between the peaks also suggests that the methyl groups are arranged predominantly with their methyl C_3 axes normal to the surface.

RESULTS AND DISCUSSION

Scheme 1. Synthesis of functionalized silica surfaces. (a) *β*-Cyclodextrin attachment to the silica surface; (b) dendronization of the silica surface followed by attachment of *β*-cyclodextrin to the dendrons.

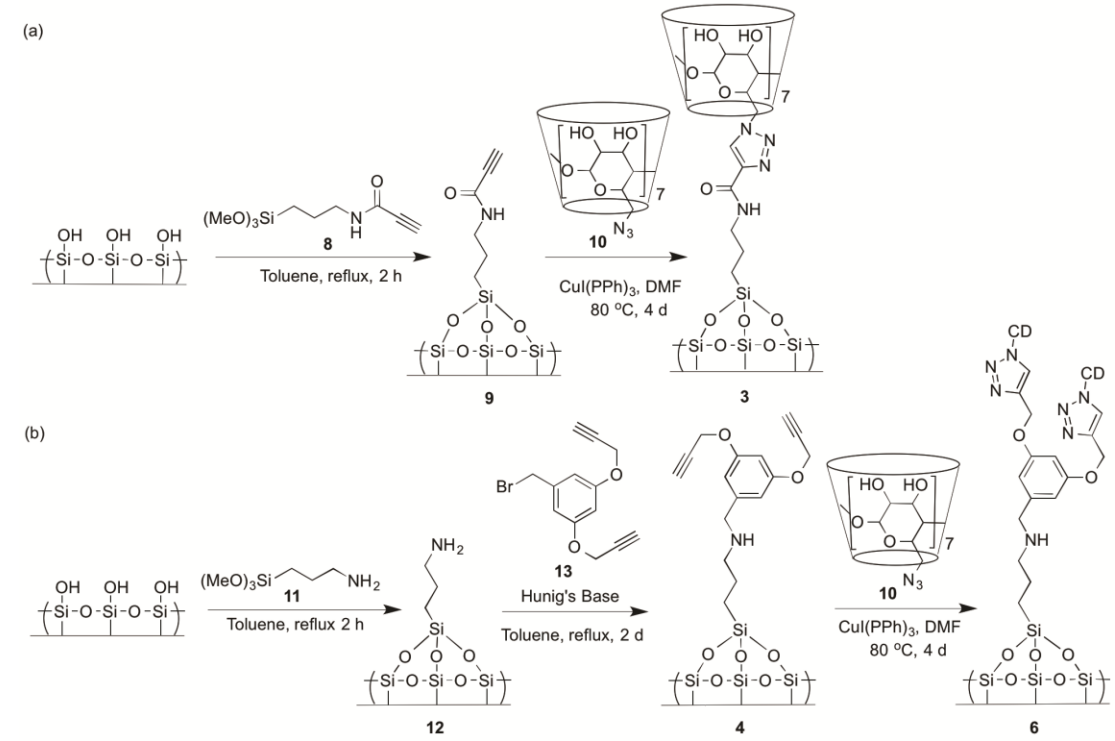

Silica surfaces were modified to display terminal alkynes by silanization using *N*-(3-(trimethoxysilyl)propyl)propiolamide (**8**). The terminal alkynes **9** were reacted with *β*-cyclodextrin azide **10** by a Cu(I) mediated cycloaddition[162,95] to afford surface **3** (Scheme 1a). Silica surfaces were modified to display terminal amines by silanization using 3-aminopropyltrimethoxysilane (**11**) to form surface **12**. Addition of the dendron **13** was accomplished by S_N2 displacement of the core bromide by the terminal amines presented on the silica surface to afford surface **4**. The alkyne endgroups on the G1 dendron were further modified by a Cu(I) mediated cycloaddition using *β*-cyclodextrin azide **10** to yield surface **6**.

Prior to characterization, slides were sonicated once in toluene and then three times sequentially in Milli-Q water and methanol. This purification method minimized the environmental carbon and nitrogen that was present on the product slides, as evidenced by XPS. High resolution narrow scans of the C 1s and N 1s regions of the control after being washed by this purification method are shown in Figures 4a and 4b respectively. The carbon 1s signal contains contributions from multiple carbon sources. First, the signal was fit with a central peak at 285 eV that was attributed to the binding energy of sp^2 and sp^3 hybridized carbons that are bound to carbon or hydrogens as shown in Figure 4a (C-H/C-C peak). Second, a higher energy peak was fit that was attributed to the oxygen and nitrogen bound sp^3 C 1s emission (C-O/C-N peak in Figure 4a). A third peak was fit that is in agreement with silicon bound C 1s emission (Si-C peak in Figure 4a).[163,164] The signal from the scan of the N 1s region shown in Figure 4b was minimal (as expected) and is consistent with emission from a small amount of residual nitrogen at the surface.

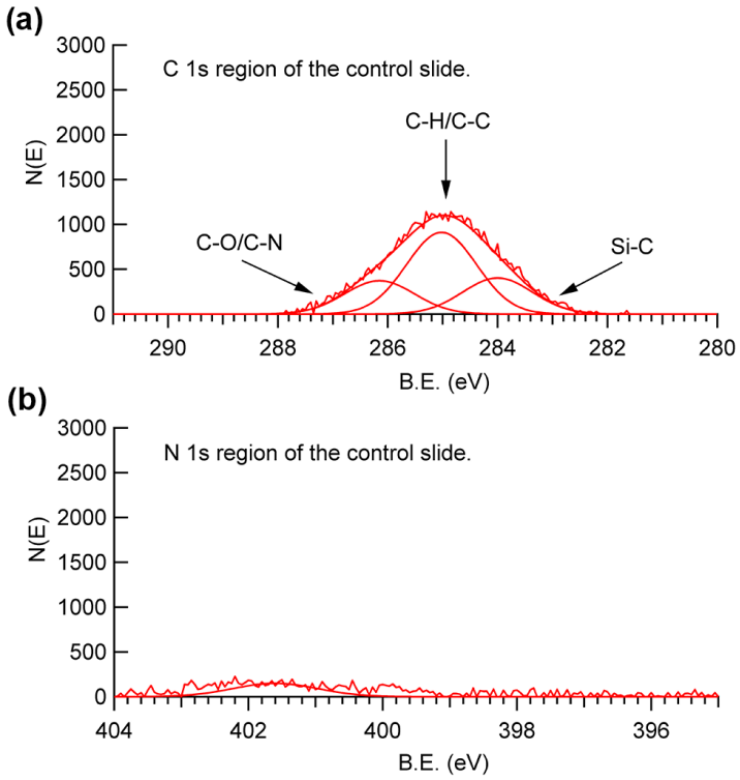

Figure 4. XPS spectra of unfunctionalized surfaces. (a) High resolution scan of the carbon 1s region. (b) High resolution scan of the nitrogen 1s region.

Surfaces **1** and **2** were fully characterized to assist in the identification of more complicated features of the other surfaces discussed in this work. Figures 5a and 5b show the narrow C 1s spectra of the methyl and octadecyl terminated surfaces respectively. Both of these C 1s signals were fitted with two peaks, the C-H/C-C peak at 285 eV assigned to sp^3 hybridized carbon emission, and the C-Si peak at 283.9 eV assigned to the silicon bound carbon 1s emission.[163] The increased atomic concentration on the surface of **2** was observed in an increased C-H/C-C peak because **2** is functionalized with an 18 carbon alkyl chain while **1** is functionalized with a single methyl group.

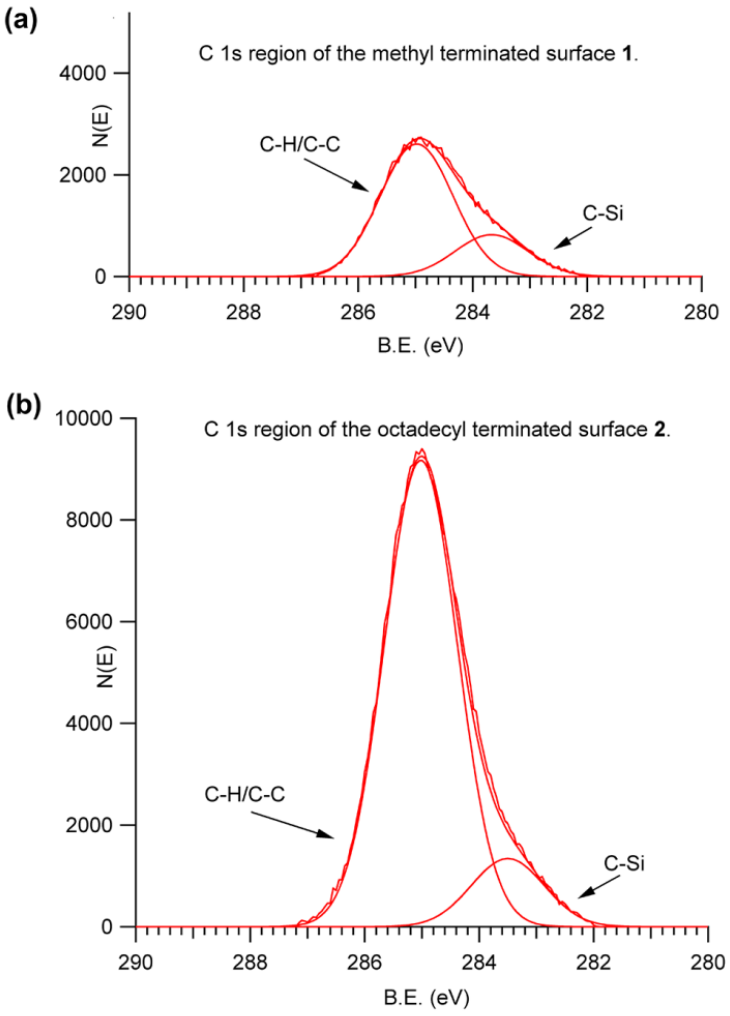

Figure 5. (a) High resolution XPS scan of the carbon 1s region of surface **1**. (b) High resolution XPS scan of the carbon 1s region of surface **2**.

Figures 6a and 6b show the C 1s and N 1s spectra of the 1-*β*-cyclodextrin-*N*-(3-(silyl)propyl)-1H-1,2,3-triazole-4-carboxamide functionalized surface **3**. In Figure 6a, the C 1s signal was broad with a shoulder centered at 288 eV. The spectrum was deconvoluted into five overlapping peaks in agreement with the expected atomic structure of the organic monolayer. Two peaks, labeled C-H/C-C and C-Si are consistent

with the C 1s emission attributed to sp^3 and sp^2 hybridized carbons and to C-Si bonds as previously described. The higher energy broadening of the signal was resolved into two peaks. The C=O peak in Figure 6a was fitted under the shoulder and centered at 288 eV. This peak fitting is consistent with both the C 1s emission of the amide carbonyl carbon of the tether and with the anomeric carbons in the β-cyclodextrin. The second peak, which is centered at 286.2 eV, was assigned to the C 1s emission from nitrogen bound carbons and hydroxyl bound carbons in the β-cyclodextrin and is labeled C-O/C-N in Figure 6a.[163, 165] The lower energy broadening of the signal was fitted with a peak centered at 283.1 eV, in agreement with the emission from the sp hybridized carbons. The sp C peak indicates that some alkynes remain unfunctionalized in the conversion of **9** to **3** (Scheme 1).[166]

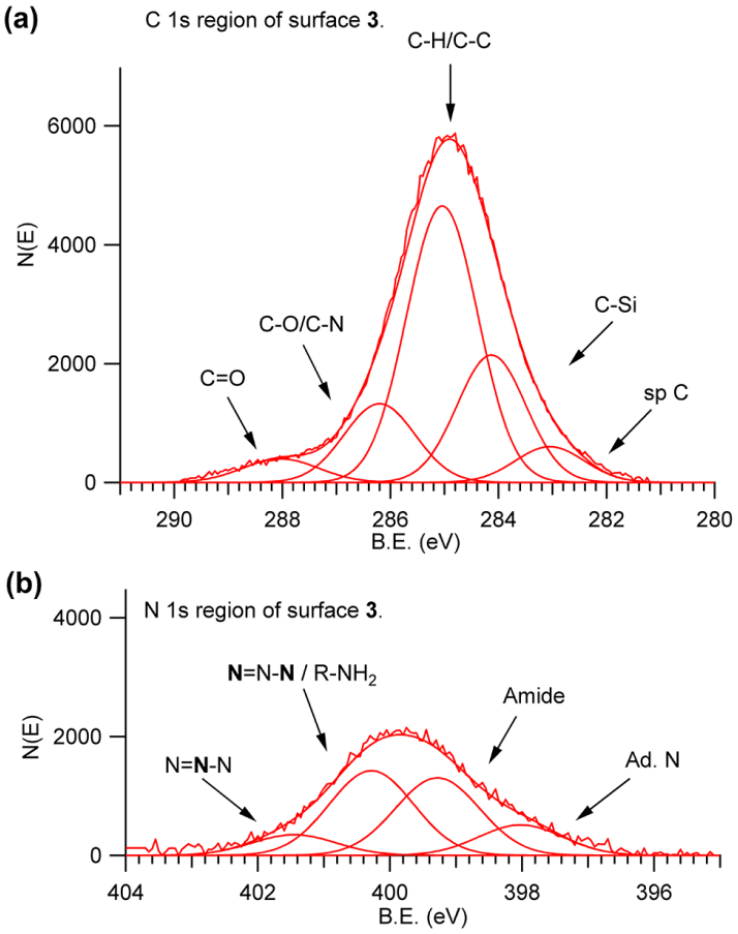

Figure 6. (a) High resolution XPS scan of the carbon 1s region of surface **3**. (b) High resolution XPS scan of the nitrogen 1s region of surface **3**.

Additional evidence of the triazole formation is supported by the higher energy broadening in the N 1s spectrum from surface **3** (Figure 6b), an effect that is absent in data acquired with surface **9** (Figure S1 in the Supporting Information) This high energy region is fitted with an additional peak centered at 401.5 eV in agreement with the binding energy of the 1s emission of the central nitrogen (N=**N**-N) of the triazole.[167,168] Additionally, the **N**=N-**N**/R-NH_2 peak centered at 400.3 eV (Figure 6b) has increased in

magnitude relative to the C-NH_2 peak centered at 400.3 eV (Figure S1 in the supporting Information) because of the additional nitrogen contribution from the 1s emission of the N1 (**N**-N=N) and N3 (N-N=**N**) of the triazole ring.[167,168] Both spectra were fit with peaks centered at 398.1 eV (Figure 6b, Ad. N peak) in agreement with the N 1s emission that is attributed to adventitious nitrogen and at 399.4 eV (Figure 6b, Amide peak) that is assigned to the amide nitrogen. The observed lower energy shift relative to 399.8 eV[163] is attributed to the amide nitrogen being in proximity to an electron donating group.

Further analysis of the N 1s region of surfaces **9** and **3** was used to quantitatively determine successful triazole formation; the calculations for this analysis are fully described in the Supporting Information. The results indicated that 31% of the propiolamides of **9** were successfully converted to the triazoles of **3** (Table 1). Overall, the XPS spectra in Figures 4, 5, and 6 indicate that XPS is a very useful method for the characterization of surfaces bearing alkyl, alkynyl, triazole-containing, and β-cyclodextrin functionalities. Based on comparison to these spectra and on additional in-depth analysis, XPS was used successfully to characterize and quantify the dendronized surfaces.

The XPS spectra of the C 1s and N 1s regions of dendronized surfaces **4** and **6** are shown in Figure 7. When the narrow C 1s spectra of **4** and **6**, which are shown in Figures 7a and 7c, respectively, are compared to the C 1s spectrum of **3** (Figure 6a), important differences are notable. The C-O/C-N peak for both **4** and **6** is larger than the same peak for **3** (288.1 eV), indicating the difference between the alkyl tether and the dendron. This peak arises from emissions of oxygen bound carbons in the polyaryl ether dendrons and

the nitrogen bound carbons.[163,164] The C-O/C-N peak in Figure 7c for **6** is significantly larger than the same peak for **4** in Figure 7a, indicating that addition of *β*-cyclodextrin was successfully achieved. The O-C-O/C=O peak in Figure 7c for **6** is also larger than the C=O peak in 7a for **4**, and this peak has a binding energy that is in agreement with the anomeric C 1s emission of the acetals present in 1,4-oligoglucosides. The size increase for this peak was attributed to the presence of the *β*-cyclodextrin present on the surface.[163,169,170] XPS C 1s spectra for **3**, **4**, and **6** (Figures 6a, 7a, and 7c, respectively), all display a peak at 283.1 eV, indicating alkyne functionality is present. This is fully expected in Figure 7a for compound **4** and indicates incomplete triazole formation (most likely because of steric hindrance) for **3** and **6**. Comparison of the spectra of the narrow scan N 1s regions for **3** (Figure 6b), **4** (Figure 7b), and **6** (Figure 7d) also indicates that the XPS spectra are as expected for the reported surfaces.[171,172]

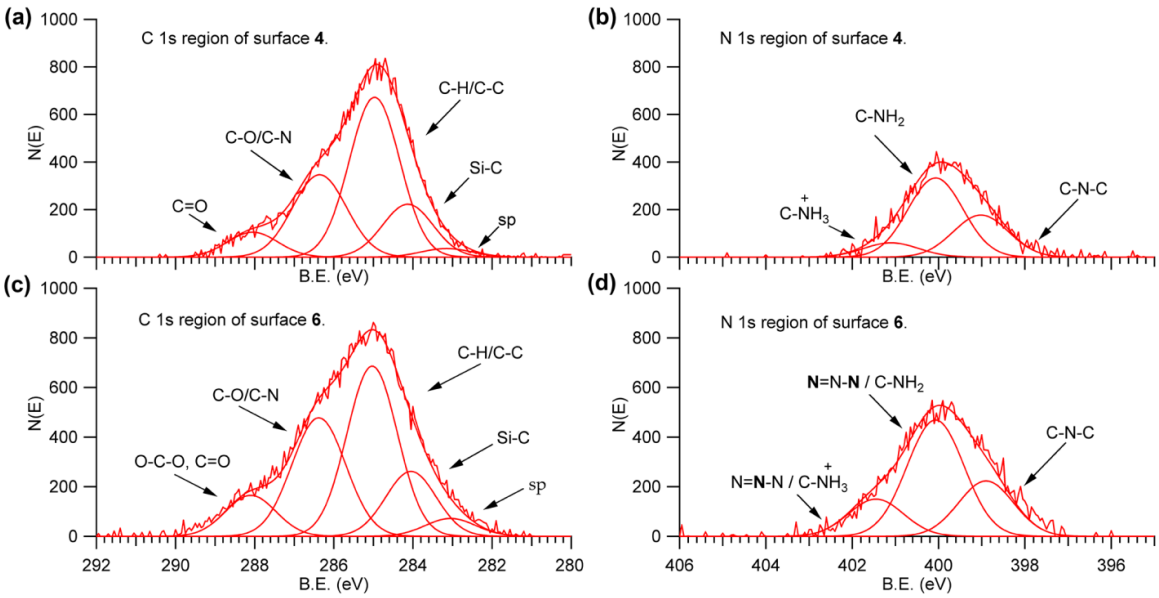

Figure 7. XPS spectra of G1 dendron functionalized surface **4** and *β*-cyclodextrin functionalized dendronized surface **6**. (a) High resolution scan of the carbon 1s region of surface **4**. (b) High resolution scan of the nitrogen 1s region of surface **4**. (c) High resolution scan of the carbon 1s region of surface **6**. (d) High Resolution Scan of the nitrogen 1s region of surface **6**.

Quantitative analysis of the N 1s region of surfaces **4** and **6** was used to quantify the percent dendronization of the terminal amines of surface **12** and the percent triazole formation to yield surface **6**. Equations are provided in the Supporting Information. Amine functionalized surface **12** was converted to dendronized surface **4** with a 35% conversion rate. The same analysis was performed for the formation of G2 dendronized surface **5,** which was formed from **12** with 27% conversion. Addition of the bulkier G2 polyaryl system was less efficient. The percent triazole formation was calculated per dendron to be 31% and 48% for surfaces **6** (G1) and **7** (G2), respectively. Thus, the overall amounts of *β*-cyclodextrins on surfaces **6** and **7** was determined based on the combined yields for dendronization and triazole formation and was found to be very nearly equivalent. Because the overall amount of *β*-cyclodextrin on the dendronized surfaces was constant, the efficiency of binding of C152 to the dendronized surfaces is directly comparable (see below). The results garnered from the quantitative analysis of the XPS spectra of dendronized surfaces are summarized in Table 1.

Table 1. Surface reaction yields determined using quantitative analysis of XPS.

Slide	Dendronization	Triazole Formation

	(surface)	(surface)
Single Layer		31% (**3**)
Generation 1	36% (**4**)	31% (**6**)
Generation 2	27% (**5**)	48% (**7**)

Further characterization of the functionalized surfaces was performed using surface-specific VSFG spectroscopy. Figure 8 shows the *ssp* spectra of the *β*-cyclodextrin functionalized surface **3** (Figure 8b), of the first two generations of *β*-cyclodextrin functionalized dendrons **6** and **7** (Figures 8c and 8d, respectively), and of the methylated surface **1** for comparison purposes (Figure 8a).

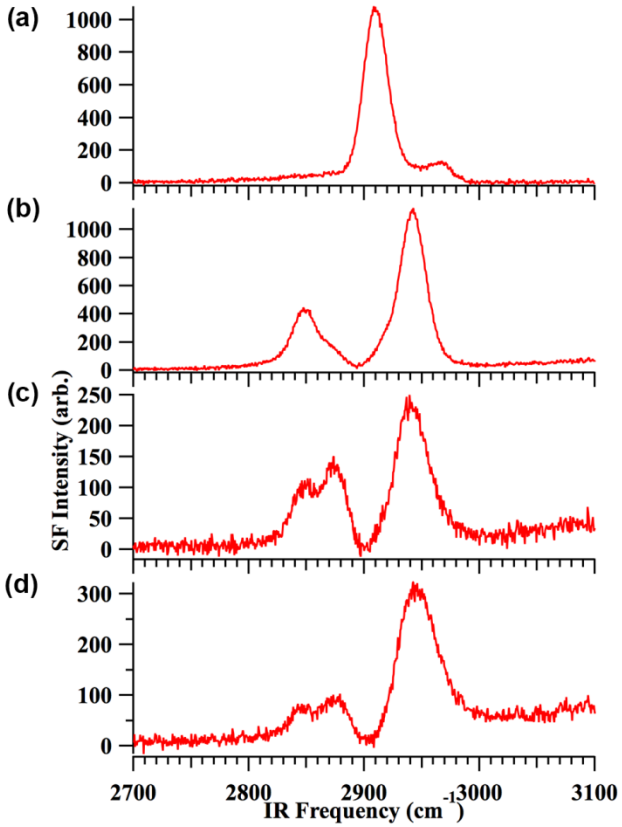

Figure 8. VSFG spectra of (a) methylated silica surface **1**, (b) a silica surface with tethered *β*-cyclodextrin **3**, (c) *β*-cyclodextrin functionalized generation 1 dendron surface **6**, (d) *β*-cyclodextrin functionalized generation 2 dendron surface **7**. All traces were taken in the *ssp* polarization combination.

Peak assignments for the methyl-terminated surface were described in the Experimental Methods section. Assignments for the various *β*-cyclodextrin terminated surfaces have been made based on both previous experimental and computational Raman/IR data,[173] and previous SFG data.[161] All three *β*-cyclodextrin terminated surfaces share three main features at 2848 cm^{-1}, 2873 cm^{-1}, and 2943 cm^{-1}. The 2848 cm^{-1} and 2943 cm^{-1} peaks have been assigned to the methylene symmetric and antisymmetric stretches, respectively. As these are well-documented frequencies for alkane methylene stretches, they are assigned to the alkane chain connecting the dendron – or simply the *β*-cyclodextrin – to the silica substrate. The assignment of the peak at 2873 cm^{-1} is less straightforward. This feature lies where one would expect a methyl symmetric stretch to occur, but no methyl groups are present on surfaces **6** or **7**. The most likely explanation for the peak at 2873 cm^{-1} is that it is due to the symmetric stretch of the methylene group directly adjacent to the silicon atom. As seen in Figure 8a, C-H stretches for the surface methyl groups that are directly adjacent to silicon atoms have been shown to shift to higher frequencies. One can also learn of general trends in orientational order by examining the signal/noise ratio. The peaks in the un-dendronized surface spectrum of **3** (Figure 8b) are distinctly more pronounced from the noise than the peaks in the spectra of

either of the dendronized surfaces **6** or **7** (Figures 8c and 8d, respectively). The observed loss in signal/noise suggests that either fewer C-H containing functional groups are present on the surface *or* more orientational disorder occurs with the more bulky dendronized surfaces **6** and **7** than with **3**. The increased ability of the dendronized surfaces to bind C152 molecules (described below) provides evidence suggesting that the decrease in signal/noise is caused by a more disordered surface and not a less functionalized one.

To evaluate the ability of each surface to remove and retain solutes from aqueous solution, experiments were performed with a coumarin solute, C152, dissolved in aqueous solution. (Also, see Figure S3 in the Supporting Information.) In aqueous solution, C152's emission maximum is 527 nm, and the emission maximum is 424 nm in hexane. Upon addition of *β*-cyclodextrin to the bulk aqueous solution, the maximum emission wavelength shifts 7 nm to a shorter wavelength, indicating that the *β*-cyclodextrin is binding to the C152 and changing the solute's local solvation environment.

The ability of *β*-cyclodextrin surfaces to retain C152 was tested using the procedure described in the methods section above. The same general trends observed in the bulk solution measurements hold true for the surfaces. Figure 9 shows a blue shift for C152 molecules both bound by *β*-cyclodextrin (503 nm) and adsorbed to the hydrophobic surface (499 nm) when compared to the unfunctionalized silica (511 nm). This observation matches the blue shift seen upon addition of *β*-cyclodextrin to the bulk C152

solution, and again suggests that adsorbed coumarins are experiencing a nonpolar environment. Functionalized surfaces showed repeatedly reproducible behavior with minimal signs of degradation after repeated cycling.

1.

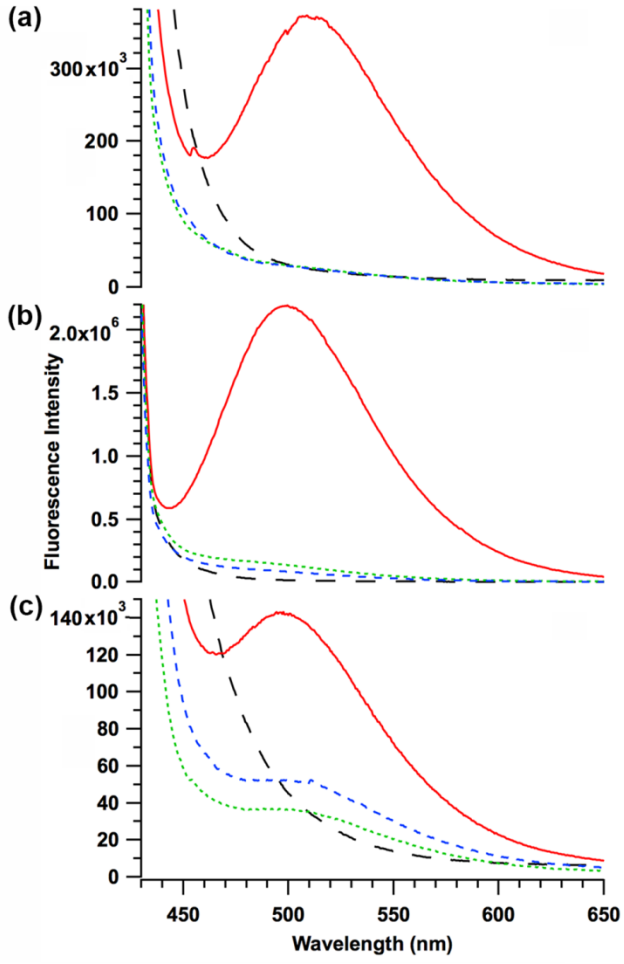

Figure 9. Coumarin 152 adsorbed to (a) a clean slide, (b) a methyl functionalized slide **1**, and (c) a *β*-cyclodextrin functionalized slide **3**. Black dashed traces are prior to addition of the solution, solid red traces are after an hour of equilibration in the solution, dotted

green traces are after the first soak in water, and short dashed blue traces are after the second soak in water.

The sharp rise on the shorter wavelength end of the spectra is due to scatter off the silica from the excitation light. This rise is present in both the functionalized and unfunctionalized slides and is extremely sensitive to slide position and angle. This scatter cannot be eliminated in a consistent manner from the individual spectra but contributes only minor inconsistencies in baselines and absolute emission intensities. Data in Figure 9 (red trace) shows that C152 adsorbs spontaneously to all three types of silica substrates – hydrophilic (Figure 9a), hydrophobic (Figure 9b) and *β*-cyclodextrin terminated (Figure 9c) – but adsorbed C152 is retained *only* by the *β*-cyclodextrin functionalized slide after rinsing with water (dotted green and short dashed blue traces are comparable to black dashed traces in Figure 9a and Figure 9b but not in Figure 9c). This observation reinforces the hypothesis that retention of the dye by cyclodextrin functionalized surfaces is due to specific binding interactions between *β*-cyclodextrin and C152, and that regardless the number of C152 molecules non-specifically bound to hydrophobic interfaces, they are all removed upon rinsing with water. As noted in the experimental section above, the fluorescence results are sensitive to slide positioning; the blue and green traces in Figure **9** are equivalent within experimental limits.

Figure 10 shows that similar data is acquired from the slides functionalized with *β*-cyclodextrin bound to 1st and 2nd generation dendrons **6** and **7**. Both samples appear to retain C152 following several 60 second rinses with pure water. Furthermore, the

emission wavelength of the C152 bound by both generations of *β*-cyclodextrin dendrons (503 nm) is consistent with the wavelength of the C152 bound by surface **3** with *β*-cyclodextrin functionalization but lacking the dendron subcomponent. To summarize these results, only a short (60 second) washing time was required to remove non-specifically bound C152 from **6** (G1); repeated washings of surface **6** do not reduce the amount of C152 that is bound. For surface **7** (G2), a second washing did remove additional C152, indicating that more C152 is bound non-specifically to **7** and also that **7** less effectively retains the solute from the solution via a specific binding mechanism.

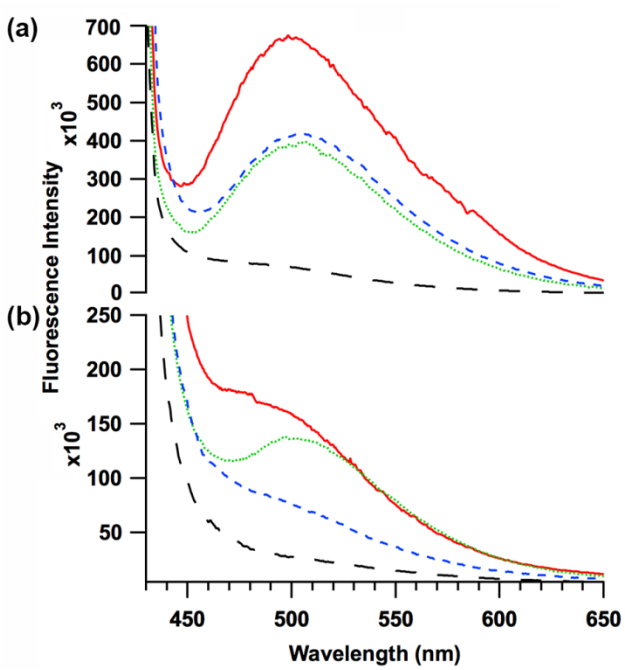

Figure 10. Coumarin 152 adsorbed to (a) *β*-cyclodextrin functionalized generation 1 dendron surface **6** and (b) *β*-cyclodextrin functionalized generation 2 dendron surface **7**. Black traces are prior to introduction to the solution, red are after an hour of equilibration

in the solution, green are after the first soak in water, and blue are after the second soak in water.

While Figures 9 and 10 show that all of the slides functionalized with *β*-cyclodextrin retained C152, the fluorescence data from the silica surfaces cannot resolve the absolute amount of C152 retained. To quantify the relative capacities of the three different surfaces, each sample was rinsed with 50 mL of methanol to remove all detectable C152 from the surface. Figure 11a and 11b, respectively show retention of C152 after a 60 second wash in water and complete desorption triggered by sonication in methanol. The fluorescence excitation intensity of the wash was measured and compared to the excitation from prepared C152/methanol standards. The amount of C152 rinsed from each sample was assumed to represent the accessible number of *β*-cyclodextrin sites on the surface, and this number was converted into a surface coverage of *β*-cyclodextrins capable of forming complexes with organic solutes in aqueous solution. The spectra from the methanol washes of **6** and **7** are shown in Figures 12a and 12b, respectively. With regards to Coumarin concentrations used in these experiments (2.6 mg/L), these concentrations are higher than are typical for regulated pesticides in ground water but only by a factor of ~3-4 in some cases. The signal to noise of our reported data exceeded 10 in many instances, inspiring confidence that these functionalized surface can, in fact, be relevant for waste water remediation. The results, which are summarized in Table 2, were informative: silica surfaces functionalized with 1st generation dendrons **6** showed the highest C152 binding capacity with a surface coverage of 2 x 10^{14} sites/cm^2, followed

by 2nd generation dendrons **7** with 1 x 10^{14} sites/cm^2 and finally β-cyclodextrin functionalized slides **3** with 3 x 10^{13} sites/cm^2. All values are the average of at least three trials.

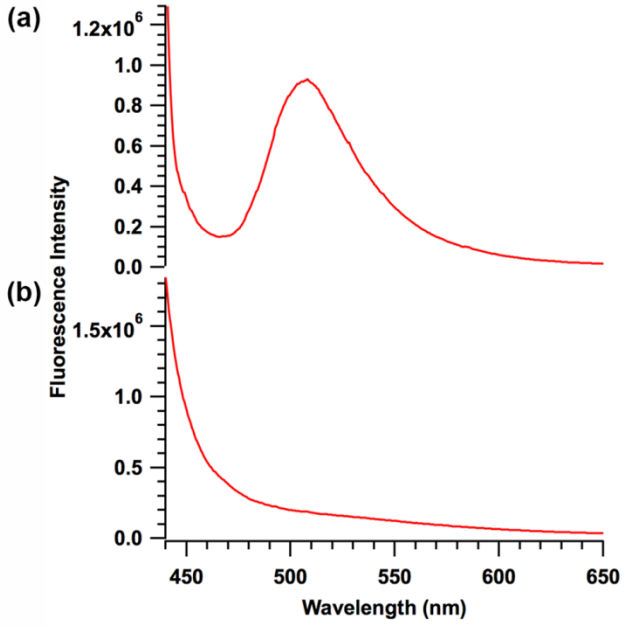

Figure 11. Representative spectra showing (a) retention of C152 after a 60 second wash in water, and (b) complete desorption triggered by sonication in methanol.

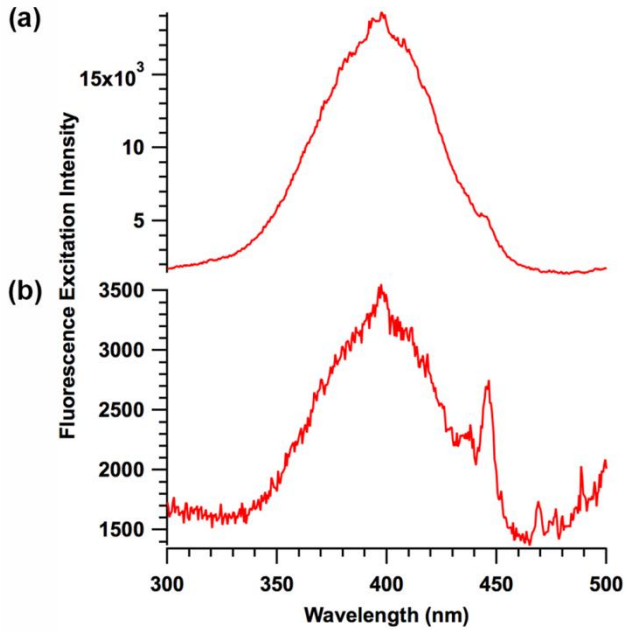

Figure 12. Representative spectra of the methanol wash from (a) surface **6** and (b) surface **7**.

Table 2. Summary of results for the quantification of desorbed C152.

Slide (compound)	**[C152] (nM)**	**C152 molecules/cm^2 (x 10^{13})**
Single Layer (**3**)	11	3
Generation 1 (**6**)	78	20
Generation 2 (**7**)	44	10

As expected, both *β*-cyclodextrin dendronized surfaces **6** and **7** adsorb more analyte molecules than surface **3**, which presented singly tethered *β*-cyclodextrin molecules at the surface. The observation that the first generation dendronized surface **6** adsorbs more C152 than the second generation surface **7** is counterintuitive, however, since both surfaces bear the same overall amount of *β*-cyclodextrin. One likely possible explanation for the fact that surface **6** shows twice the binding capability of surface **7** is that many of the terminal *β*-cyclodextrin hosts on the second generation dendron of **7** are inaccessible for binding by C152. The larger dendron appears to angle more of its terminal cyclodextrins toward the surface so that they are unable to encapsulate C152 because of steric crowding of large *β*-cyclodextrins on the dendron. Although dendronization of **12** did not occur quantitatively *en route* to formation of either **6** or **7**, the increased density of coumarin binding sites available for adsorption of C152 using dendronized surfaces still enabled the adsorption of more C152 than could be adsorbed on the non-dendronized surface **3.**

CONCLUSIONS

Novel *β*-cyclodextrin functionalized silica surfaces that absorb targeted analytes from bulk aqueous solutions were synthesized and characterized. First and second generation polyaryl ether dendrons were tethered to silica surfaces. Cu(I) catalyzed

cycloaddition “click” chemistry was used to append *β*-cyclodextrin onto the dendronized surfaces, and a *β*-cyclodextrin functionalized surface without the dendron was also reported for comparison purposes. These complex surfaces were characterized using XPS and VSFS analysis. Both techniques indicated that the proposed architecture was successfully synthesized. Although the synthesis procedure reported here was used for the appendage of *β*-cyclodextrin units onto dendronized surfaces, the route is highly flexible, and a wide variety of endgroups can be added onto the alkynes on the dendrons via triazole formation. Different generations of dendrons afford different surface densities for the endgroup functionality.

These surfaces possess the adsorption and retention capabilities they were designed for: the functionalized surfaces can be used repeatedly with highly reproducible results. The adsorption ability was observed from fluorescence spectra of the functionalized slides. These results showed that C152 had an affinity for the *β*-cyclodextrin functionalized surfaces that persisted through multiple aqueous washings. Additionally, the adsorptive capabilities of the slides were quantified by analyzing the wash from the slides after desorption was triggered. These results indicate that substrates functionalized with first generation dendrons had a greater binding capacity than slides functionalized either with monomeric *β*-cyclodextrin or with larger generation dendrons. This result can be understood in terms of the tradeoff between maximizing the density of *β*-cyclodextrin on the surface *vs.* maximizing the number of *β*-cyclodextrins that can be accessed by a binding partner such as C152. The studies reported here have provided a

methodology for characterizing and evaluating the properties of novel, highly functional surfaces.

ASSOCIATED CONTENT

Supporting Information. XPS of nitrogen 1S region of **9**; fluorescence spectra for an aqueous solution of C152 with and without CD, for C152 adsorbed to a CD functionalized surface, and for C152 in hexane; calibration plot for quantifying wash from functionalized slides; and the equations used for the quantitative XPS analysis of surface functionalization. This material is available free of charge via the Internet at http://pubs.acs.org.

AUTHOR INFORMATION

Corresponding Authors

*M. J. Cloninger. E-mail: mcloninger@chemistry.montana.edu

*R. A. Walker. Email: rawalker@chemistry.montana.edu

Author Contributions

The manuscript was written through contributions of all authors. All authors have given approval to the final version of the manuscript. ‡These authors contributed equally.

ACKNOWLEDGMENT

This work was supported by NSF ICC 1026870.

ABBREVIATIONS

C152, Coumarin 152; CD, *β*-cyclodextrin; VSFS, vibrational sum frequency spectroscopy; XPS, x-ray photoelectron spectroscopy.

CHAPTER FOUR

SURFACES DESIGNED FOR CATCH AND RELEASE OF TARGETED ANALYTES

Background

The synthesis and characterization of functionalized glass surfaces, which were designed for reversible adsorption, was the focus of this synthesis. These surfaces are capable of binding the targeted class of compounds, chlorobenzenes and chlorophenols, non-covalently in aqueous solutions. They are also capable of "release" through an external trigger. The design of these surfaces was driven by the hypothesis that by creating a complementary host environment through attractive intramolecular forces for the targeted analytes, these surfaces would be capable of pulling the targeted molecules out of aqueous solutions. After the target molecules are encapsulated, the surface could be triggered by a non-destructive stimulus which would disrupt the non-covalent interactions. This disruption would trigger the release of the target molecule and regenerate the surface. This design is shown in Figure 14.

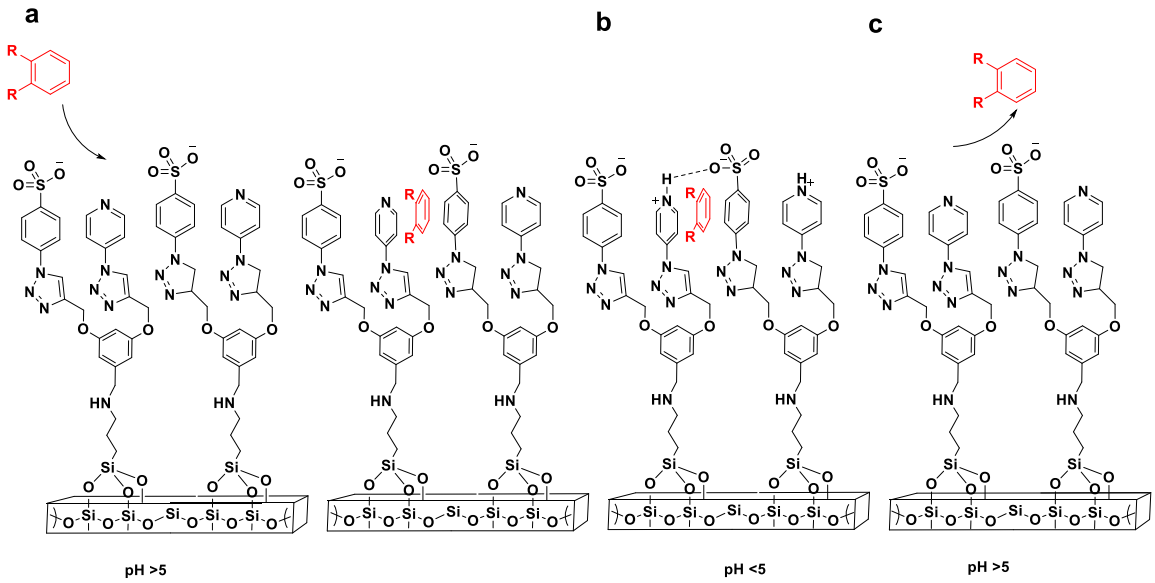

Figure 14: Idealized schematic of "catch and release" of a targeted molecule. a) Targeted molecule is able to form a guest-host complex with the heterogeneously functionalized G1 dendron silica surfaces, b) is “trapped” by intramolecular forces at a pH less than 6, and then de-adsorbed c) by triggered release.

The polyaryl ether dendronized surfaces, which were previously described, provided an array of substituted aryl groups capable of π-π stacking and provide a flexible framework. Further functionalization of the dendritic terminal propargyl groups would enable the installation of additional aryl groups for π-π stacking. However, these endgroups capable of forming salt bridges which respond to changes in pH. Terminal alkyne modifications could be completed again by triazole formation using a Huisgen Cu(I) mediated cycloaddition. Pyridine and benzene sulfonic acid were chosen as primary candidates for this synthesis. Benzene sulfonic acid will be in an unprotonated form in all pH ranges. Pyridine, which has a pKa of ~5.2, is in a deprotonated form at higher pH.

Although pyridine's pKa indicates the salt bridge between the sulfonic acid could be disrupted at a pH as low as 6, the triazole could significantly influence the pKa of this analogue, and therefore experiments to determine the pH for the disruption will be pertinent. A substituted amine in the para position of the pyridine will increase the pKa, however this substitution should still allow pyridine to be in its deprotonated form in higher pH environments. In addition to this, the sulfonic acid provides an emission in the 2p region for XPS analysis that is absent in the pyridine. This feature would allow the quantification of the percent of 4-azido benzene sulfonic acid which was installed relative to the total triazole formation on the heterogeneous surface.

Results and Discussion

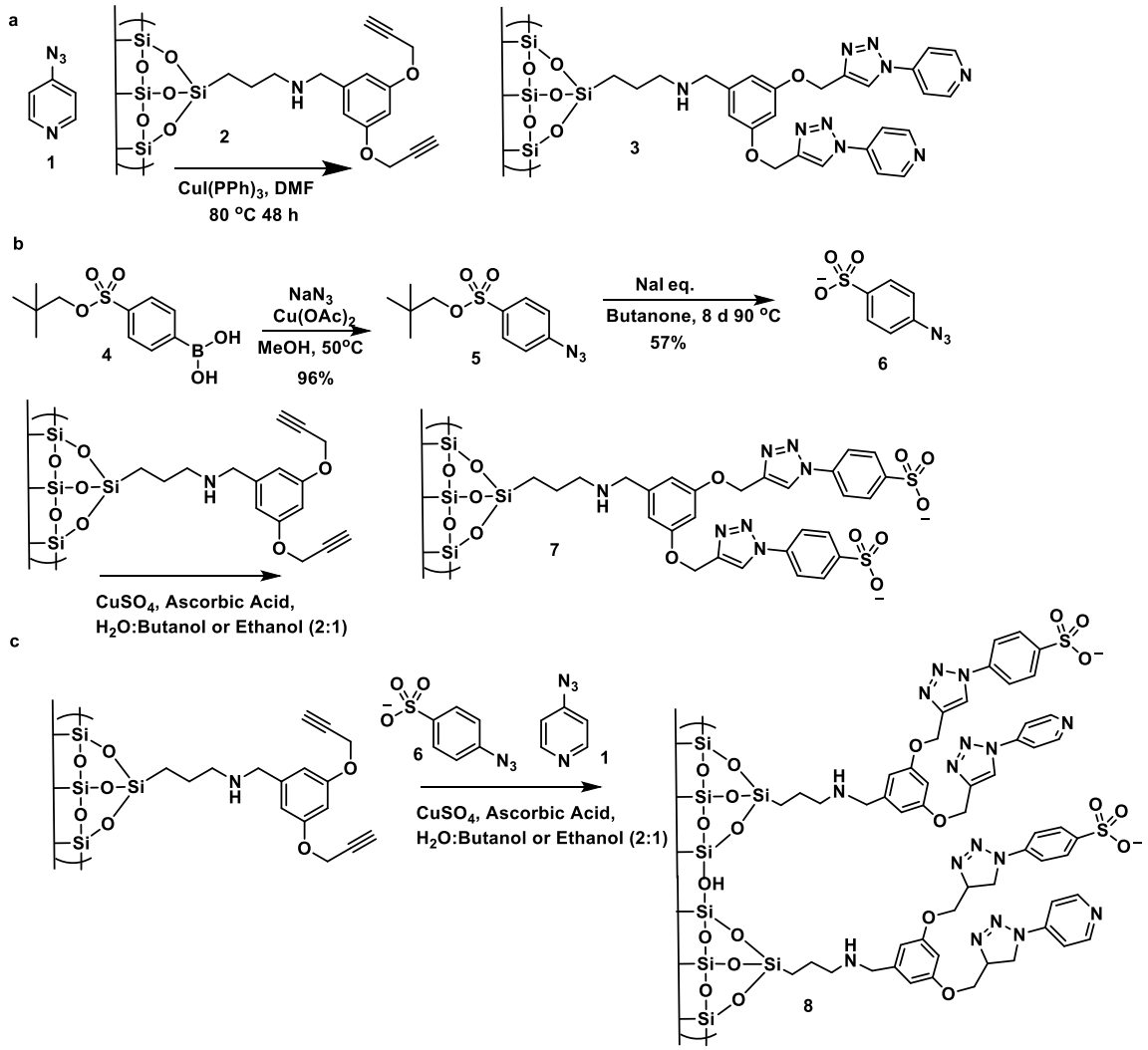

Scheme 1: Synthesis of functionalized silica surfaces. (a) Synthesis of pyridine dendronized surfaces; (b) sulfonyl dendronized surfaces; (c) heterogeneously functionalized surfaces.

4-azidopyridine 1 was synthesized from 4-chloropyridine by aromatic nucleophilic substitution as previously reported.[174] G1 polyaryl ether dendron functionalized surface 2, which was previously reported,[175] was functionalized using

Cu(I) mediated 1,3-cycloaddition of the terminal alkynes with azido pyridine 1. To synthesize the 4-azidobenzene sulfonic acid 6, a neopentyl protected sulfonyl benzene boronic acid 3 was converted to an azide by an Cu(II)-catalyzed conversion of aryl boronic acids.[176] The neopentyl group was removed by a Finklestein reaction to give the deprotected azido benzene sulfonic acid **6**. G1 polyaryl ether dendronized surface **2** was functionalized with the terminal benzene sulfonic acids by Cu(I) mediated 1,3-cycloaddition to give benzene sulfonic acid functionalized surface **7**. The synthesis of the heterogeneously functionalized surface **8** was accomplished by the addition of **6** and **1** after optimizing a solvent system for both azido compounds.

The surfaces bearing terminal pyridine, sulfonic acid, and a mix of both were characterized using X-ray Photoelectron Spectroscopy (XPS). The carbon 1s signal from surface **2** contains contributions from multiple carbon sources. This signal was fit in agreement with the expected organic monolayer. The conversion of the terminal alkynes were supported by the analysis of carbon emissions of surfaces **2**, **3**, **7**, and **8** as previously described (Figure 204, Figure 204, Figure 203, Figure 206), but further analysis of the N 1s was needed. [175]

The XPS spectra of the N 1s regions of G1 dendronized surface **2**, terminal pyridine surface **3**, terminal sulfonic acid surface **7**, and heterogeneous functionalized surface **8** were analyzed to confirm successful triazole formation. Each figure contains a spectrum (Figure 15-17a) of the N 1s region of the G1 dendronized surface prior to functionalization with azide **1**, **6**, and a mix of **1** and **6**. These spectra were fit with three peaks attributed to N 1s emissions of the secondary, primary and protonated amines

present in the organic monolayer. Following Cu(I)-catalyzed triazole formation with azide **1** or **6**, and a mix of **1** and **6** a higher energy broadening is present(Figure 15-17b). A peak centered at 401.5 eV in agreement with the electron rich N2 (N=**N**-N) triazole nitrogen was fitted to this region. In addition to this new feature, the peak centered at 400.3 eV which was in agreement to the presence of unfunctionalized primary amines, increased in magnitude which was attributed to the additional contribution from the N1 and N3 (**N**-N=**N**) 1s emissions. Further quantitative analysis of each spectra in Figure 15, Figure 16, and Figure 17 validated that consistent dendronization was observed in each synthesis and supported successful triazole formation using azide **1** or **6**, and a mix of **1** and **6**. Quantitative analysis of surface **3,** and **7** was used to determine the site composition by dividing 1 equivalent of the signal from the triazoles divided by one equivalent of signal from all of the species present (dendron, amine, and secondary amine). This was repeated for each species, as described in the quantitative analysis of the XPS experimental.[130, 175] Results for azide **1** and **6** are reported below (Table 1).

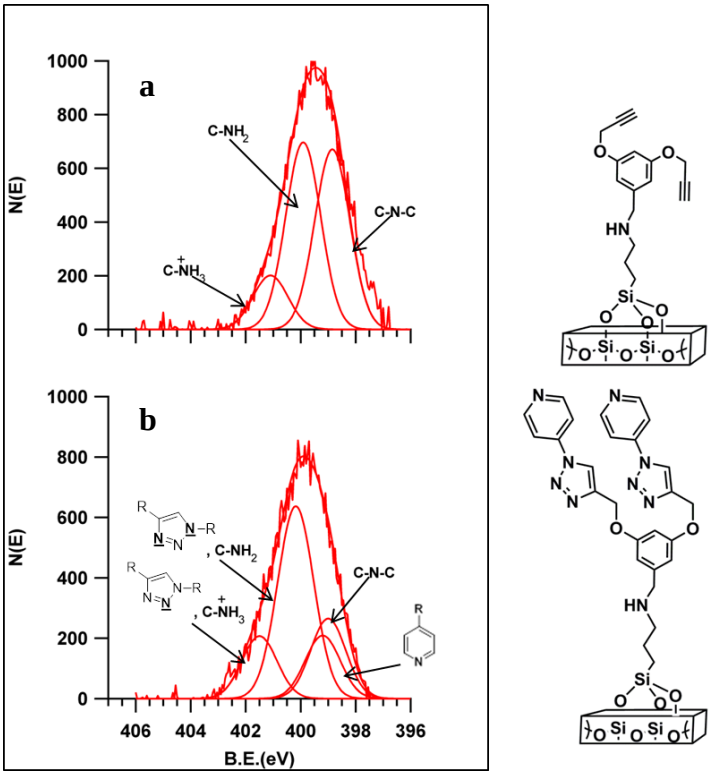

Figure 15: (a) High resolution XPS scan of the nitrogen 1s region of surface **2**. (b) High resolution XPS scan of the nitrogen 1s region of surface **3**.

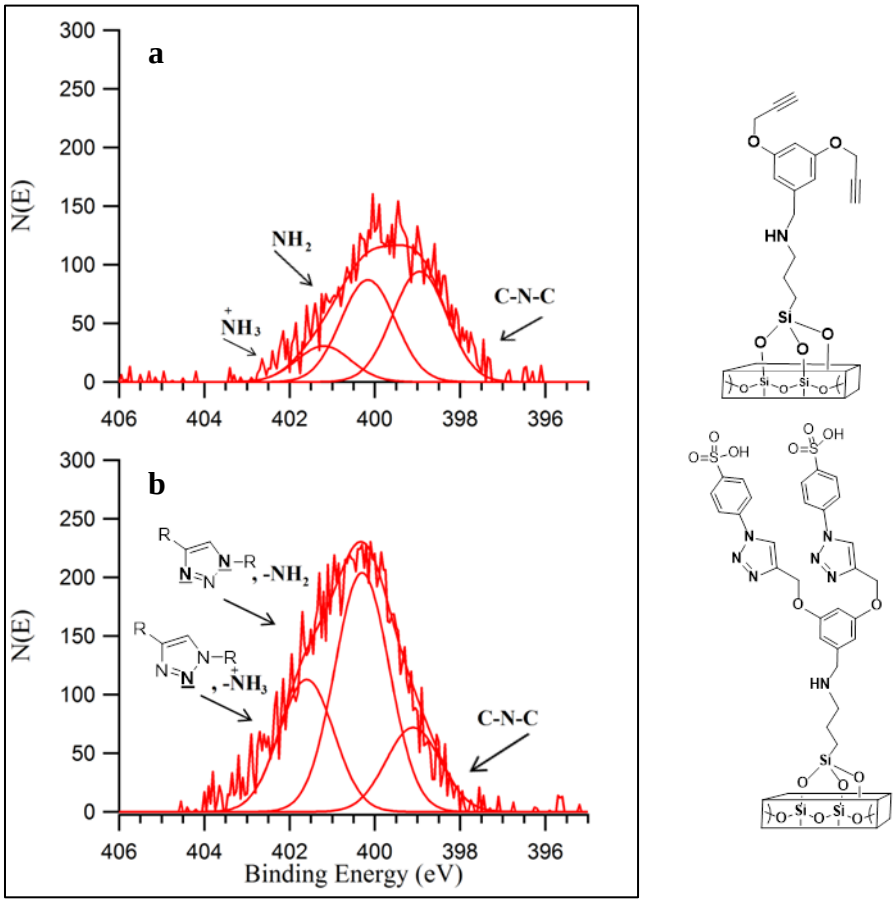

Figure 16: (a) High resolution XPS scan of the nitrogen 1s region of surface **2**. (b) High resolution XPS scan of the nitrogen 1s region of surface **7**.

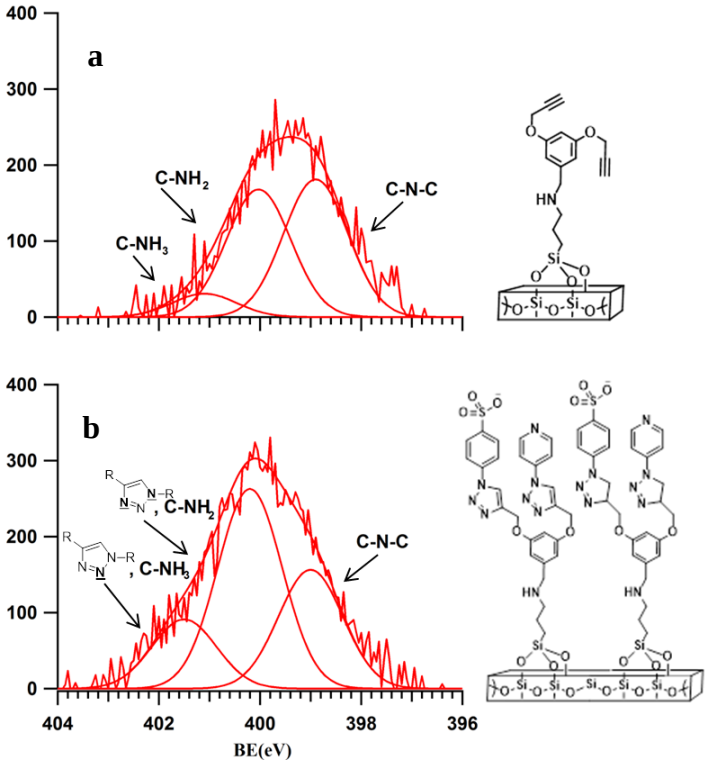

Figure 17: (a) High resolution XPS scan of the nitrogen 1s region of surface **2**. (b) High resolution XPS scan of the nitrogen 1s region of surface **8**.

Slide	**Site Compositions**		
	Amine	Dendron	Triazole
3	32%	44%	23%
7	34%	39%	26%

Table 1: Site compositions determined using quantitative analysis of XPS. Surface composition of surface **8** could not be determined by this. Adventitious N is not reported but was sometimes detected, which is why the site composition numbers do not always equal 100%

The resonance attributed to the sulfonic acid on surface **7** was observed on the high resolution scan of the S 2p region, again confirming the sulfonic acid terminal groups were successfully installed. In comparison to the S 1s region of the G1

dendronized surface **2** control (Figure 18 black trace), the intensity of this signal was small (Figure 18 red trace), which gave a calculated one to two atomic percent for the surface **7** (Figure 18). Given the expected atomic structure of the organic monolayer, the S 2p signal would be minimal. To confirm this peak was indeed a result of the sulfonic acid presented at the surface and not residual copper sulfate ($CuSO_4$), a survey scan was performed to confirm a signal attributed to $CuSO_4$ was absent (Figure 19). In addition to this, a high resolution scan was acquired of the S 2p of **6** which was deposited on a silicon wafer. This confirmed the signal centered at ~168 eV was attributed to the benzenesulfonic acid and not from a different sulfur containing species (Figure 201 in Appendix B).

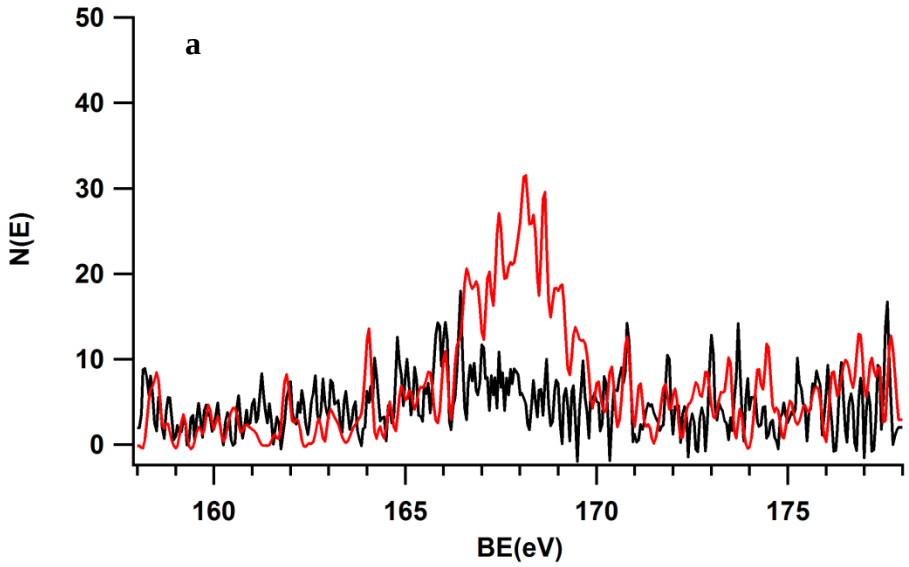

Figure 18: (a) Smoothed high resolution XPS narrow scan of the sulfur 2p region of surface **7.** The sulfur 2p signal of G1 dendronized surface **2** is absent as shown in the black trace of figure 18. The presence of the sulfur 2p signal of sulfonic acid functionalized surface **7** is shown as red trace.

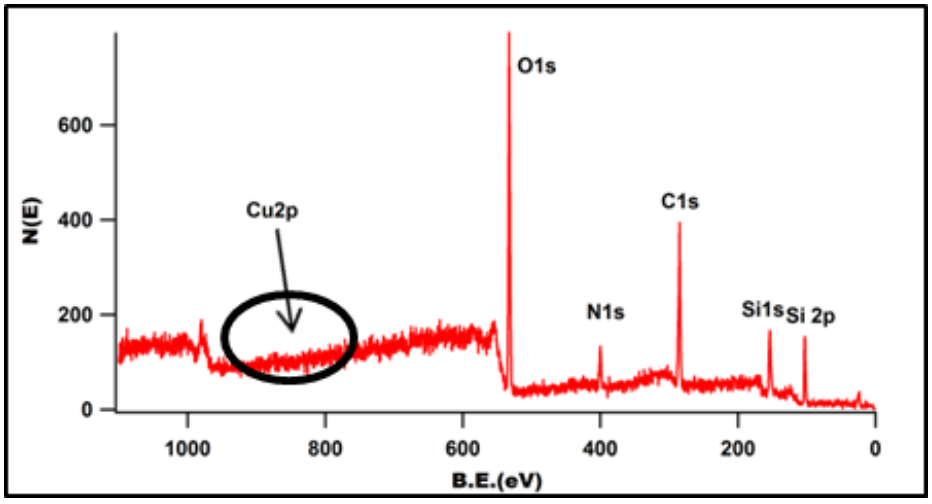

Figure 19: (a) Survey scan of heterogeneously functionalized surface **8.**

XPS spectral analysis and quantitative analysis of spectra in Figure 17 validated successful triazole formation using a mix of **1** and **6**. However, quantifying the amount of the triazole formation by **1** and **6** could not be performed by XPS. In prior analysis of the pyridine functionalized surface **3**, the N 1s emission from the pyridine heterocycle (C-**N**=C) was centered at 399.1 eV.[163, 177] The magnitude of this peak was fit in relation to the peak centered at 401.5 eV which arose from the emission of the N2 (N-**N**=N) in the triazole ring and protonated amines. Therefore, the magnitude of the peak centered at 399.1 eV should correlate to the magnitude of the emission of N2 minus the signal from the protonated amine. In the analysis of heterogeneously functionalized surface **8**, the triazole formation as a result of pyridine addition could not be distinguished from the triazole of the sulfonic acid end group. Therefore, the imine nitrogen of the heterocyclic ring (C-**N**=C) did not correspond to the magnitude of to the N2 of the triazole and could not be fit as a result of this. Quantifying the amount of triazole formation attributed to the

functionalization of surface **3** with sulfonic acid by XPS was also unsuccessful. Given the signal intensity from the S 2p region from surface **8** it was not surprising that there was an absence of this signal in the same region (Figure 207). The signal would be expected to decrease at least 50% for the heterogeneous slide **9** and therefore would fail to reach the instrument's detection threshold.

Auger spectroscopy (AES) was performed using a Scanning Auger NanoProbe. Auger electrons have low kinetic energy values, and therefore their escape depth is limited to a few atomic layers from the bulk organic surface. Since Auger is a surface-sensitive technique, evaluating ~1 to 5 nm in depth, compared to XPS (100 nm), would allow the surface analysis of the terminal sulfur present. In addition to this sensitivity, high resolution secondary electron imaging of the analysis area could be performed.

High resolution scans of the sulfur region were first performed on the homogenous surface **7**. (Figure 208) XPS analysis and quantification supported the successful installation of the terminal sulfonic acids. G1 dendronized surface **2** was used as a control (Figure). High resolution secondary electron imaging of the analysis area of G1dendronized surface **2** and sulfonic acid homogenously functionalized surface **7** are shown in Figure 20 (a and b respectively). The detection of sulfur was absent for G1 dendronized surface **2** and present sulfonic acid homogeneously functionalized G1 surface **7** (Figure 20, blue). The results from these initial optimization experiments confirmed the success of this technique. This experiment was repeated for heterogeneous surface **9** (Figure 20c). The signal for the sulfur Auger electrons were detected as shown in Figure 21. From the theoretical calculation of nitrogen to sulfur ratio for

heterogeneously functionalized surface **8**, the experimental ratio was quantified. These results support that approximately 68 % of the alkynyl groups were converted to triazoles containing pyridine endgroups and 32 % triazoles containing sulfonic acid (Table 2). The high resolution secondary electron imaging of analysis area (Figure 20c) further supported the presence of sulfur, a feature which was absent on the G1 dendronized surface **3**. This image area is shown again in Figure 20d after removing the secondary electron imaging of carbon.

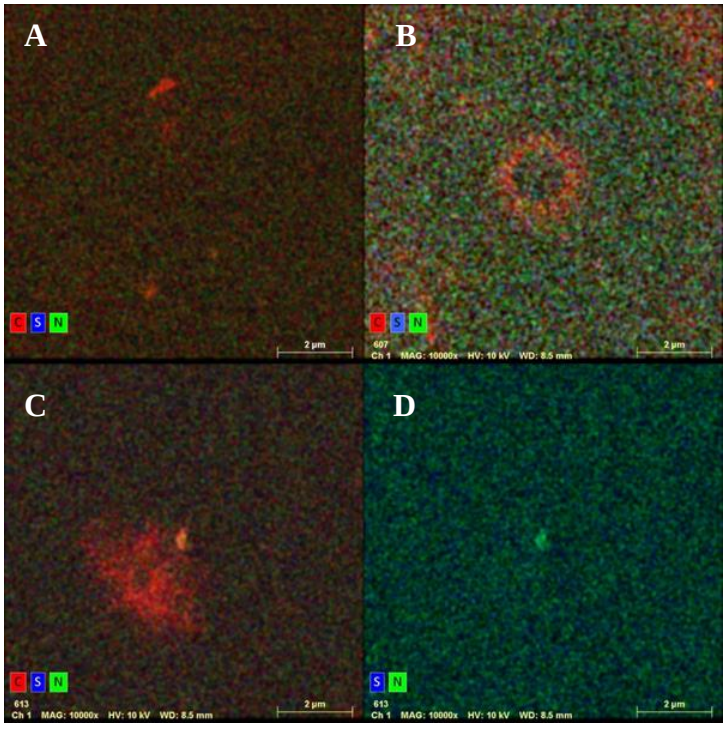

Figure 20: High resolution secondary electron imaging of analysis area of (a) G1 dendronized surface **2** has an absence of sulfur detected(in blue) (b) Sulfonic acid homogeneously functionalized G1 surface **7**. Sulfur electron mapping is shown in blue. (c) Heterogeneously functionalized G1 surface **8**. Sulfur electron mapping is shown in blue. (d) To aid the visualization of the sulfur electron mapping sulfur of heterogeneously functionalized G1 surface **8**, high resolution secondary electron imaging of carbon atomic mapping was removed. Observed red bleaching in the images is an artifact of the AES as atomic layers were removed, exposing carbon saturated areas.

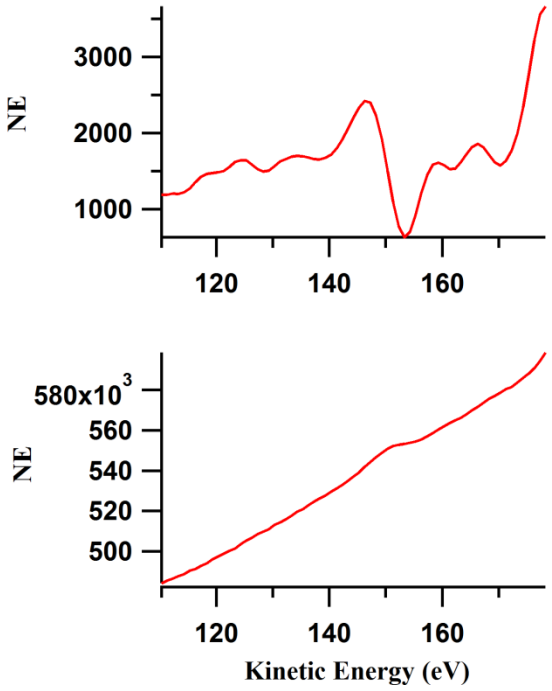

Figure 21: AES spectra from the high resolution scan of the sulfur LVV region for heterogeneously functionalized G1 surface **8**. (a) The derivative of the sulfur signal (b) acquired from heterogeneously functionalized surface **8**.

Slide	**Reaction Yields**		
	Dendronization	Theoretical N/S ratio for 1:1 mix	Experimental
4	45%	11 : 1	*7.8 : 1 = ~68 % Pyridine

Table 2: Dendronization and triazole formation of **8** determined using quantitative analysis of XPS. * Results from the experimental analysis to determine percent sulfonic acid functionalization of surface **9** by AES.

An unexpected result was the presence of copper, which was resolved in the high resolution secondary electron imaging of analysis area of heterogeneously functionalized

surface **8** (Figure 22). The scanning electron microscope (SEM) image of a copper particle is shown in Figure 22a. High resolution secondary electron imaging of the analysis area of supported the copper signal detected was from copper oxide, not from $CuSO_4$. To further support this, high resolution electron imaging of sulfur electrons was performed on the analysis area. The atomic mapping spectra supported the copper containing species was not composed of sulfur (Figure 22c).

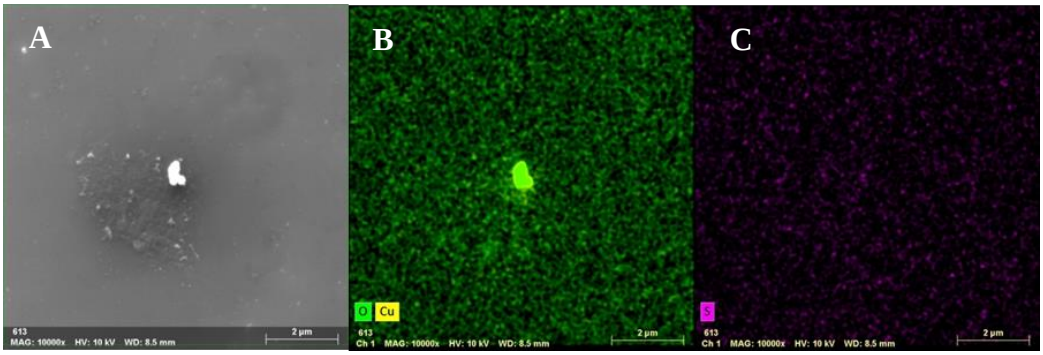

Figure 22: (a) SEM of imaging area of copper detection. High resolution secondary electron imaging of the analysis area of heterogeneously functionalized G1 surface **8**. (b) Imaging of copper oxide and (c) sulfur atomic mapping of the same area on heterogeneously functionalized G1 surface **8**.

Conclusion

Dendronized surfaces bearing **1** or **6**, and a mix of **1** and **6** were synthesized and characterized. The homogenous slides **3** and **7** were characterized using XPS, and the degree of surface functionalization was adapted from methods previously described.[175] Heterogeneous functionalized surface **8** was also characterized for successful triazole formation by XPS. However, the quantification of how much of the triazole formation on **8** could be attributed to the successful addition of the 4-azidobenzene sulfonic acid was

limited due to the sensitivity limits of the XPS methodology. Therefore, AES using a Scanning Auger NanoProbe and high resolution secondary electron imaging of the analysis area were performed. The functionalized surfaces reported here will be used by collaborators in spectroscopic studies to determine their ability to absorb targeted analytes and respond to triggered de-absorption.

Experimental Method

Materials and Methods

Quartz slides (25 x 25 x 0.5 mm) were purchased from SPI Supplies. Prior to use slides were cleaned in a 1 : 1 mixture (by volume) of sulfuric acid and nitric acid (Macron Chemicals) for one hour and rinsed with deionized water (Millipore, 18.2 MΩ). 4-Cloropyridine hydrochloride was purchased from AK Scientific Inc, and 4-(neopentloxysulfonyl)phenylboronic acid was purchased from Combi-blocks. High purity organic solvents were purchased from Fisher Scientific. All other chemicals used were purchased from Sigma-Aldrich.

Pyridine Functionalized Polyaryl Ether Dendronized Surfaces 3. Polyaryl ether dendron functionalized slide **3** (0.2 slide) was placed along the inside wall of a 1 dram vial holding a stir bar. Azide **2** was synthesized as previously reported.[178] Azide **2** (88 mg, 730 μmol, 243 mM), $CuSO_4$ catalyst (73 mg, 294 μmol, 98 mM), and ascorbic acid (99 mg, 501 mmol, 167 mM) were dissolved in a 2:1 mixture of water and ethanol (2 mL) and allowed to stir for 18 h. Slides were washed with 40 mL of Milli-Q water.

Slides were sonicated for 1 min in 30 mL of Milli-Q water and for 1 min in 30 mL of methanol. Sequential sonications with water and methanol were repeated two additional times. Slides were dried under a stream of argon and stored under vacuum.

2,2-dimethylpropyl 4-azidobenzenesulfonate (5). 4-(Neopentylsulfonyl)phenylboronic acid 5. (292 mg, 1.1 mmol, 22 mM) was converted to an azide by a Cu(II)-catalyzed conversion of aryl boronic acids.[176] After 6 h, the reaction was concentrated on celite. The celite was packed on silica and was purified by flash column chromatography with 1:9 mixture of ethyl acetate and hexanes (R_f = 0.6) to provide the neopentyl protected 4-azidobenzene sulfonic ester product **6** (0.278 g, 96%) as a white solid. ^{1}H NMR (500 MHz, MeOD) δ 7.90 (d, *J* = 8.6 Hz, 2H), 7.29 (d, *J* = 8.6 Hz, 2H), 3.68 (s, 2H), 0.87 (s, 9H) ppm. ^{13}C NMR (126 MHz, MeOD) δ 146.12, 131.81, 129.62, 129.62, 119.35, 119.35, 79.49, 31.06, 24.87, 24.87, 24.87 ppm. HRMS (Micro-TOF) m/z 292.0721 (calculated m/z M+Na = 292.0721 for $C_{11}H_{15}N_3O_3S$).

4-azidobenzenesulfonate (6). In a 10 mL round bottom equipped with a stir bar, 2,2-dimethylpropyl 4-azidobenzenesulfonate **6** (119 mg, 443 μmol, 89 mM) was dissolved in butanone (5 mL), and the reaction was brought to reflux. 10 equiv. of NaI was added to the reaction and allowed to stir for 2 d. This was repeated twice. The reaction was monitored by NMR over 8 d until complete conversion was indicated, which yielded the product as a yellow precipitate. The product was removed by filtration and washed with 3 times with 2 mL of butanone to give sodium 4-azidobenzenesulfonate **7** (0.050g, 57%) as a light yellow solid. ^{1}H NMR (500 MHz, DMSO-d_6) δ 7.57 (d, *J* = 8.3

Hz, 2H), 7.02 (d, *J* = 8.3 Hz, 2H) ppm. ^{1}H NMR (500 MHz, MeOD) δ 7.76 (d, *J* = 8.1 Hz, 2H), 7.04 (d, *J* = 8.1 Hz, 2H).^{13}C NMR (126 MHz, $CDCl_3$) δ 139.70, 131.72, 127.78, 127.78 118.73, 118.73 ppm HRMS (Micro-TOF m/z 197.9965 (calculated m/z M = 197.9968 for $C_6H_4N_3O_3S$).

Benzene Sulfonic Acid Functionalized Polyaryl Ether Dendronized Surfaces

8. Polyaryl ether dendron functionalized slide **3** was broken into 1/5 of the standard slide size and one piece was placed along the inside wall of a 2 dram vial holding a stir bar. Azide **7** (12.3 mg, 63 μmol, 32 mM), $CuSO_4$ catalyst (104 mg, 419 μmol, 210 mM), and ascorbic acid (185 mg, 933 mmol, 467 mM) were dissolved in a 2:1 mixture of water and ethanol (2 mL) and allowed to stir for 18 h. Slides were washed with 40 mL of Milli-Q water. Slides were sonicated for 1 min in 30 mL of Milli-Q water and for 1 min in 30 mL of methanol. Sequential sonications with water and methanol were repeated two more times. Slides were dried under a stream of argon and stored under vacuum.

Heterogenous Functionalized Polyaryl Ether Dendronized Surfaces 9.

Polyaryl ether dendron functionalized slide **3** (silica or silicon oxide) was placed along the inside wall of a 20 mL scintillation vial holding a weighted down 2 dram vial and a stir bar. Azide **2** (117 mg, 971 μmol, 97 mM), azide **7** (54 mg, 274 μmol, 27 mM), $CuSO_4$ catalyst (73 mg, 293 μmol, 27 mM), and ascorbic acid (99 mg, 501 μmol, 0 mM) were dissolved in a 2:1 mixture of water and ethanol (2 mL) and allowed to stir for 22 h. Slides were washed with 40 mL of Milli-Q water. Slides were sonicated for 1 min in 30 mL of Milli-Q water and for 1 min in 30 mL of methanol. Sequential sonications with water and

methanol were repeated two more times. Slides were dried under a stream of argon and stored under vacuum.

Auger spectroscopy (AES) Physical Electronics model 710 Scanning Auger NanoProbe. Elemental analysis was performed using <8nm with a 20kV, 1nA electron beam as an enhanced lateral spatial resolution. The instrument is equipped with a cylindrical mirror electron analyzer, and Schokty field emission electron source.

Quantitative XPS Analysis of Surface Functionalization. Quantitative analysis of the XPS was performed using the methodology published by Geiger and co-workers and previously reported for dendronized surfaces. [130, 175] Dendronization: The data from the XPS N 1s spectra of heterogeneously functionalized surface **8** was used to calculate the dendronization as expressed in the Equation 2.

$$\%\, Dendonization = \frac{A_{399}}{A_{399} + A_{400} + A_{401}}(100)$$

Equation 2: Calculation for percent dendronization of dendronized surfaces.

The integrated areas from the peaks centered at 399.0 eV, 400.1 eV and 401.2 eV are expressed as A_{399}, A_{400}, and A_{401}, respectively; these areas are attributed to the secondary amine formed from successful dendronization, the primary amine, and the protonated amine signal, respectively. The percent dendronization is calculated using the A_{399} term, which is assigned to one equivalent of the assigned functional group. This term is divided by the denominator, which is composed of one total equivalent of amine, in its unprotonated and protonated form, and the secondary amine.

Site Composition: 1 equivalent of the signal that is assigned to each triazole formed is determined using equation 2. One equivalent of signal from triazole species A_{Tri} is equal to the change in the integrated area centered at 401.5 eV, $A_{401.5}$, minus the signal from the protonated amine species, as shown in equation 3. Equation 4 was derived to calculate this with an asterisk used to designate the integrated areas after the 1,3-cycloaddition occurred.

$$\frac{A_{399}}{A_{401.5}} = \frac{A*_{399}}{A*_{401.5} - A_{Tri}} \quad \text{(eq. 2)}$$

$$A_{Tri} = A*_{401.5} - \left(\frac{A_{401.5} \cdot A*_{399}}{A_{399}}\right) \quad \text{(eq. 3)}$$

The site composition of the triazole species was calculated by dividing 1 equivalent of the signal from the triazoles divided by one equivalent of signal from all of the species present (dendron, amine, and secondary amine). This was repeated for each species, as shown in equations 5, 6, and 7.

$$Total\ triazole\ \% = \frac{A_{Tri}}{A*_{399} + A*_{400} + A*_{401.5} - 2A_{Tri}} \quad \text{(eq. 4)}$$

$$Total\ dendron\ \% = \frac{A*_{399}}{A*_{399} + A*_{400} + A*_{401.5} - 2A_{Tri}} \quad \text{(eq. 5)}$$

$$Total\ amine\ \% = \frac{A*_{400} + A*_{401.5} - 3A_{Tri}}{A*_{399} + A*_{400} + A*_{401.5} - 2A_{Tri}} \quad \text{(eq. 6)}$$

Although pyridine contributed an additional N 1s signal, this did not affect the calculations. This resonance was present in the final step, centered ~ 399.1 and equivalent to the A_{Tri}. Therefore this peak was set to an equivalent intensity to N=**N**=N to accurately assign the intensity of the C-**N**-C peak attributed to successful dendronization.

CHAPTER FIVE

CHIRAL SURFACES AND CATALYTIC SUPRAMOLECULAR SYSTEMS

Background

The development of chiral organic surfaces capable of chiral discrimination or catalytic activity was the focus of this synthesis. Because of the limitations of predictive tools for chiral crystalline materials, there is a great need for rational design of new, synthetic, chiral surfaces. [108-110] The synthesis of these surfaces was driven by the hypothesis that by using the previously described dendronized surfaces, chiral modifications could be accomplished by copper mediated 1,3-cycloadditions. A challenge for chiral or prochiral recognition by chiral surfaces is overcoming the steric forces to allow for adsorption. The poly(aryl ether) dendron frameworks provide flexibility, which allow the relief of steric strains as well as providing terminal alkynyl groups that facilitate modular incorporation of endgroups.

The difference in interaction energy (~ 2 KJ/ mol) between a pair of chiral species can be small. [111, 112] Because of this, another challenge in the development of chiral surfaces is developing synthetic methods which preserve the homogeneity of the surface. The synthetic design of a chiral organic surface would enable control over the chirality of the surface and therefore provide preservation of enantioselectivity in reactions catalyzed by the surface. [109, 113, 114] Mild conditions of the 1,3-cycloaddition would preserve the integrity of both the monolayer and the chiral centers, providing homogeneous coverage.

Results and Discussion

A small sample of chiral amino acids was chosen to demonstrate the compatibility of the dendronized framework. An azido alanine analogue **5**, an amphiphilic azido ornithine **6**, and a bulky azido proline **7** were chosen as a diverse representation for this surface functionalization (Scheme 1). Further, because of the precedence in the literature for the (2S)-proline catalyzed asymmetric aldol reaction, two generations of proline functionalized dendronized surfaces capable of this enzymatic transformation were synthesized.[116, 117]

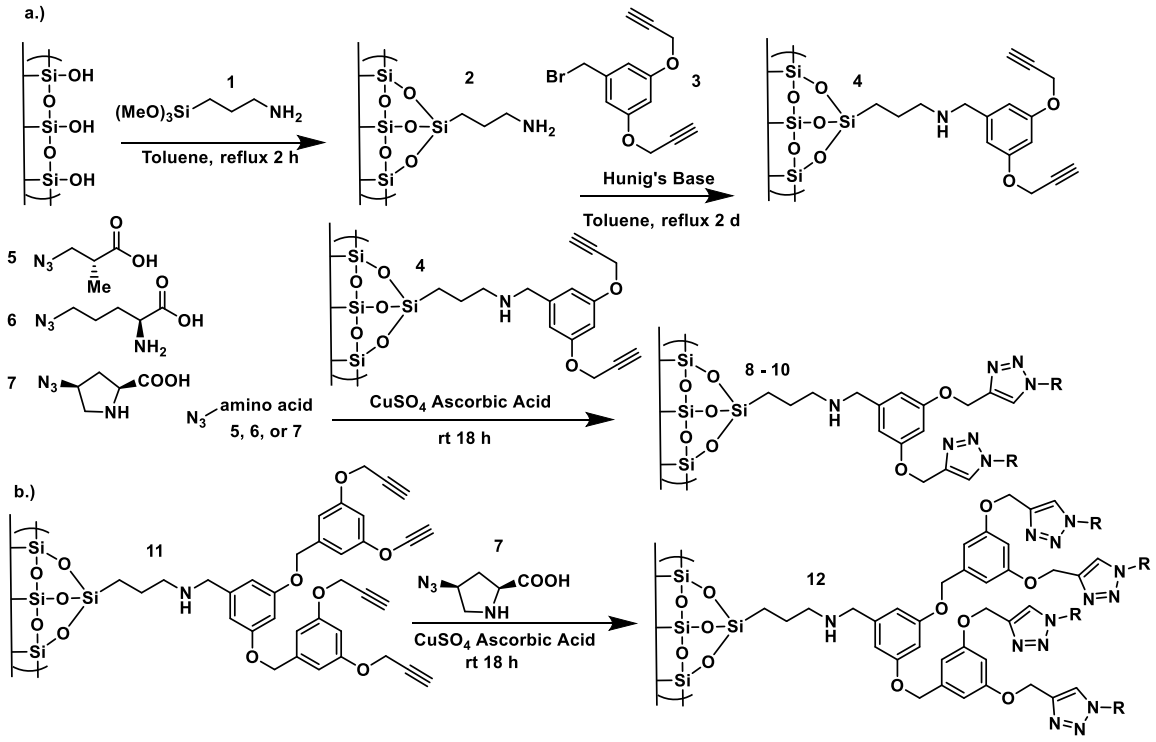

Scheme 1: Schematic of the synthesis of functionalized silica surfaces. (a) Synthesis of chiral dendronized surfaces; (b) (2S, 4S)-4-azidoproline attachment to G2 dendronized surfaces.

Dendronization of silica slides was accomplished by first forming a monolayer of terminal amines using aminoproyltrimethoxysilane (APTS) **2**. Further modification by S_N2 displacement of the core bromide on the dendron **3** decorated the surface with terminal alkynes as previously described to form **4**.[175] The terminal alkynes of the G1 dendronized surface were further elaborated by Cu(I)-catalyzed triazole formation using optimized Huisgen 1,3-cycloaddition reactions for azide **5**, **6**, and **7** to give surfaces **8**, **9**, and **10**. G2 dendronized surface **11** was functionalized with azide **7** to give proline functionalized G2 dendronized surface **12**.

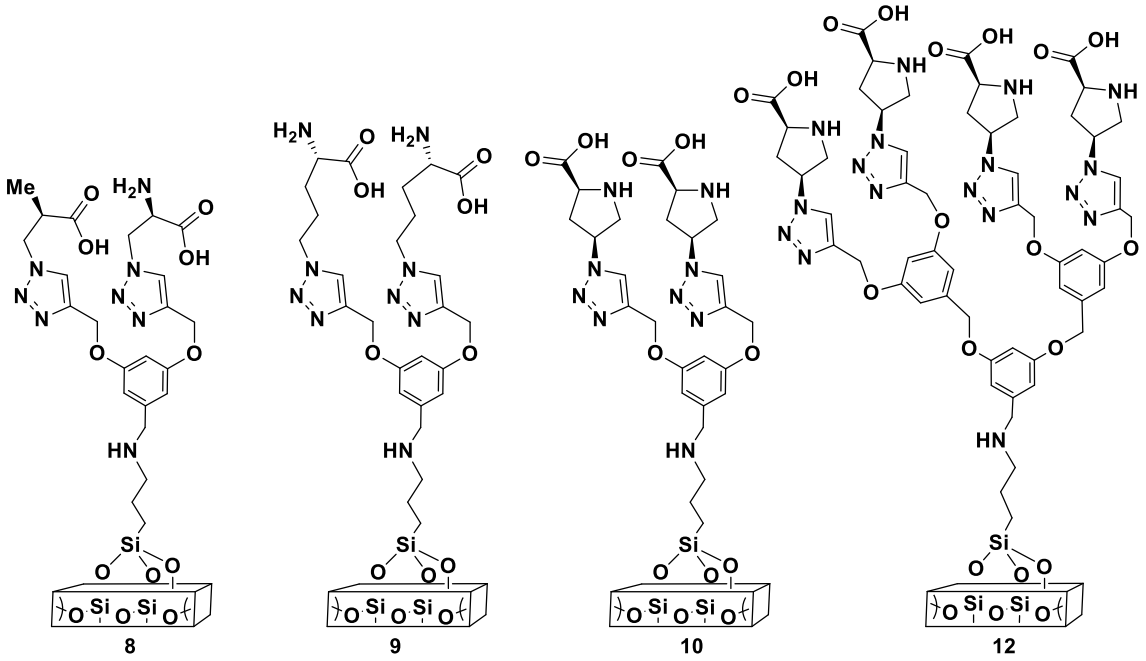

Figure 23: Schematic representations of chiral dendronized surfaces.

Full characterization of surfaces **8**, **9**, **10,** and **12** were performed using XPS. The analysis of the C 1s region of the activated amine surface **2** and dendronized surface **4** or

11 has been previously described.[175] Chiral surfaces **8**, **9**, **10,** and **12** did not have any new distinct carbon features and therefore were assigned C-H/C-C, C-O/C-N, and a Si-C peaks.[163,164,175] The increased intensity of the C 1s emission was attributed to the addition of the chiral amino acids. However, further analysis of the N 1s region was needed.

A stack plot of the N 1s region of the terminal amine functionalized surface **2**, dendronized surface **4**, and alanine functionalized surface **8** is shown in Figure 24. Successful dendronization of surface **2** was evident by the appearance of a low energy broadening in the spectrum of surface **4**. A peak centered at 399 eV (Figure 24, purple trace) was fit under this broadening and is consistent with the presence of secondary amines as a result of the dendronization of the surface. Following the copper catalyzed 1,3-cycloaddition, the formation of the triazole provided a distinct high energy broadening in the N 1s region that was absent in the dendronized surface. In addition to this new feature, the intensity of the peak centered at 400.3 eV increased. This is attributed to the emission of the N1 (**N**-N=N) and N3 (N-N=**N**) of the triazole ring.[167] This analysis was again repeated for the ornithine functionalized surface **9**, proline functionalized surfaces **10** (Figure 25), and proline functionalized G2 surface **12** (Figure 26).

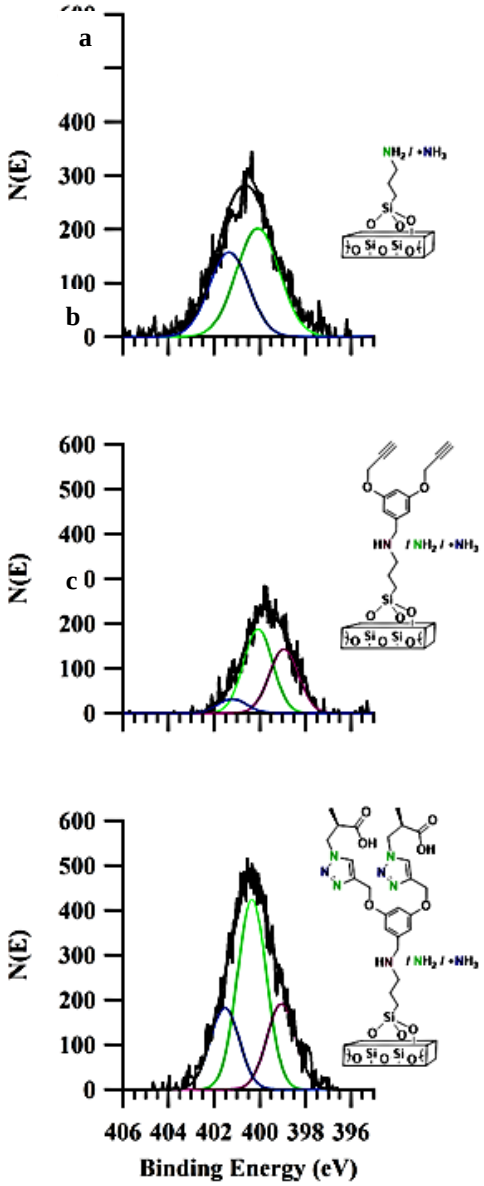

Figure 24: XPS spectra of the synthesis of alanine functionalized surface. High resolution scan of the nitrogen 1s region of (a) amine functionalized surface **2**, (b) G1 dendronized surface **4**, and (c) alanine functionalized aryl ether dendron surface **8**.

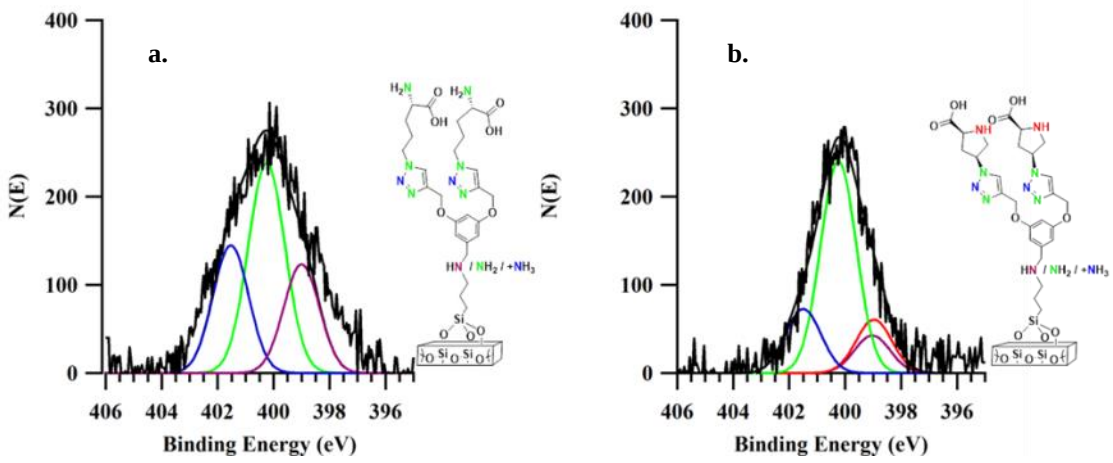

Figure 25: XPS spectra of chiral amino acid functionalized surfaces. High resolution scan of the nitrogen 1s region of (a) ornithine functionalized dendronized surface **9**, and (b) ornithine functionalized surface **10**.

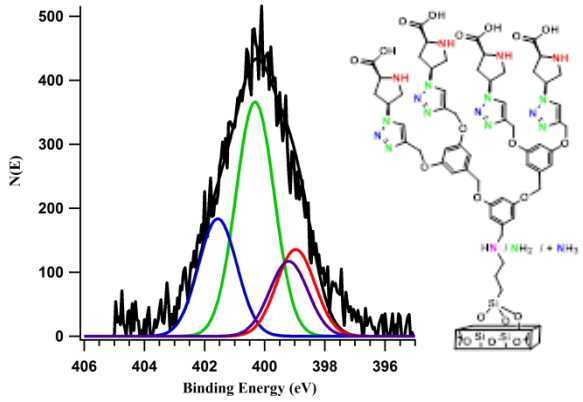

Figure 26: XPS spectra of proline functionalized G2 dendronized surface **12**.

Quantitative analysis of surface **8**, **9**, **10,** and **12** was used to determine the site composition by dividing 1 equivalent of the signal from the triazoles divided by one equivalent of signal from all of the species present (dendron, amine, and secondary amine). This was repeated for each species, as described in the quantitative analysis of the XPS experimental. [130, 175] The results of this analysis is summarized in Table 3.

Surface	Site Compositions		
	Amine	Dendron	Triazole
8	48%	32%	20%
9	33%	45%	21%
10	47%	27%	26%
12	43%	30%	36%

Table 3: Site composition results from the quantitative analysis of surface **8**, **9**, **10,** and **12**. Adventitious N is not reported but was sometimes detected, which is why the site composition numbers do not always equal 100%

The smallest chiral azido group **5** yielded a 38% conversion of terminal alkynes to triazoles on surface **8**. The bulkier azido ornithine groups were less efficiently appended, with a 32 % calculated triazole formation. However, the chiral proline conversion rate from surface **4** to G1 dendronized proline surface **10** was 49 % and surface **11 to** G2 dendronized proline surface **12** was 55 %.

In addition to silica surface functionalization with chiral amino acids, PAMAM dendrimers functionalized with catalyst were prepared by collaborators. Phenylalanine and imidazolidinone functionalized G(2) PAMAM dendrimer **13** and **14** were by XPS. Their synthesis and use as catalyst for enantioselective reactions is being evaluated and will be reported by the collaborators.

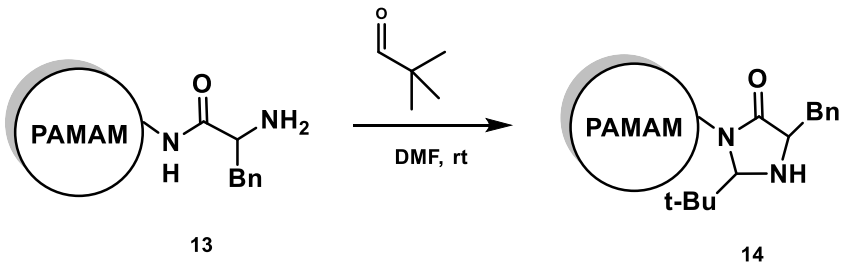

Scheme 2: Schematic representation of the condensation reaction to yield imidazolidone functionalized PAMAM G(2) dendrimer.

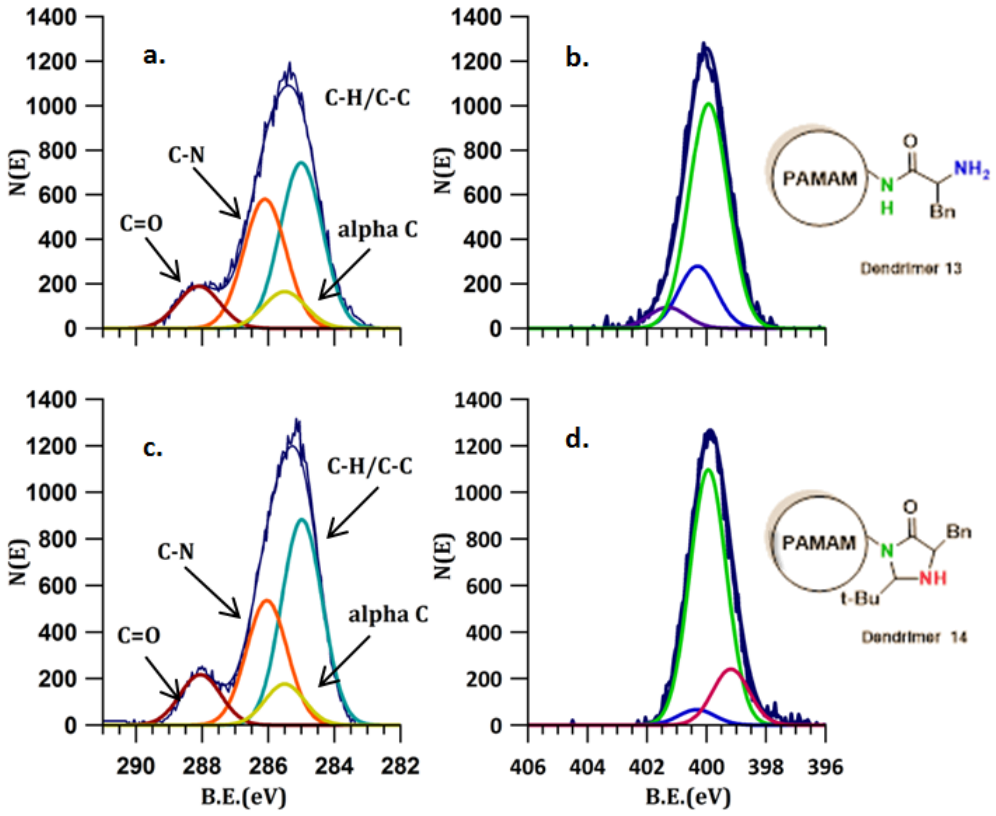

Figure 27: XPS spectra of phenylalanine functionalized PAMAM G(2) dendrimer **13** and imidazolidinone functionalized PAMAM G(2) dendrimer **14**. (a) High resolution scan of the carbon 1s region of dendrimer **13**. (b) High resolution scan of the nitrogen 1s region of dendrimer **13**. (c) High resolution scan of the carbon 1s region of dendrimer **14**. (b) High resolution scan of the nitrogen 1s region of dendrimer **14**.

XPS was used to confirm the successful condensation of phenylalanine functionalized dendrimers and pivaldehyde (Scheme 2). The high-resolution narrow scans of the C 1s and N1s regions of **13** and **14** are shown in Figure 27 a, c and b, d respectively. The carbon 1s signal of phenylalanine functionalized dendrimer **13** was broad and contained a high energy shoulder, as shown in Figure 27 a. This signal was deconvoluted into four peaks which were consistent with the distinct features of phenylalanine functionalized dendrimers**.** First, the signal was fit with a peak at 285 eV which is in agreement to the emission of the sp^2 and sp^3 hybridized carbons of the benzylic end groups (C-H/C-C peak in Figure 27a).[163] Next, the higher energy broadening of the signal was resolved into two peaks centered at 286.1 eV and 285.5 eV which were labeled C-N and alpha C respectively.[163, 165] These peaks were fit in agreement with the C 1s emission of nitrogen bound carbons and the alpha carbons to the carbonyls of the amides present in the multivalent scaffold. A peak, which was centered under the high energy shoulder as shown in Figure 4a, was fit at 288.1 eV and was attributed to the carbonyl carbons present in the PAMAM dendrimer and terminal phenylalanine groups (C=O peak in Figure 27 a). The signal of the N 1s region of dendrimer **13** was centered 399.9 eV with a high energy tailing. A peak, in agreement with the N 1s emission of amide nitrogen and tertiary amines, was centered at this energy as shown by the green trace in Figure 27 b.[175, 179-181] The peak centered at 400.2 eV (blue trace in Figure 27 b) was assigned to the presence of the terminal amines on dendrimer **13**.[163, 182] A small overlapping peak at 401.3 eV indicated the presence of protonated terminal amines (purple trace in Figure 27 b).[183]

Further analysis of the C 1s and N 1s narrow scans supports the successful formation of the imidazolidinone functionalized PAMAM G(2) dendrimer **14**. The C 1s atomic concentration increase is evident of the successful addition of the tert-butyl group. This is supported by the ratio of the C-H/C-C peak to C-N peak which increased in magnitude compared to the uncyclized dendrimer **13** (Figure 27 a). In addition to this, the N 1s spectrum centered at 399.9 eV has low energy broadening which is absent in dendrimer **13.** This region was fit with a peak at 399.2 eV in agreement to the presence of secondary amines which implies the successful cyclization to form the imidazolidinone ring.[163, 175] The higher energy broadening of the N 1s narrow scan of dendrimer **13** is nearly diminished in the same region of dendrimer **14.** A single small peak was centered 400.2 eV which arises from the presence of terminal amines and therefore indicated there was not a quantitative conversion of phenylalanine to the imidazolidinone. This was further supported by ^{1}H NMR analysis demonstrating the usefulness of this characterization method with catalytic dendrimers physio-adsorbed to silica wafers.

Conclusion

Chiral surfaces were synthesized and characterized using XPS. Three azido amino acids, **5**, **6**, and **7** were successfully appended to G1 dendronized surfaces. G2 dendronized surface **11** was also functionalized with (2S, 4S)-4-azidoproline **7.** This yielded a second generation of catalyst functionalized dendronized surfaces. Both surfaces are currently under study as catalyst for enantioselective reaction. A small, but

diverse sample of chiral amino acids was chosen to demonstrate the scope of the modification reaction. The functionalization of dendronized surfaces could easily be tuned to display various chiral endgroups capable of chiral recognition. This method of characterization was applied to the XPS spectra of phenylalanine and imidazolidinone functionalized PAMAM G(2) dendrimers. These dendrimers were deposited on silica wafers and XPS was performed. The experimental analysis confirmed successful cyclization of dendrimer **13** and pivaldehyde to afford **14**. This data was in agreement with the conversion rate of 88%, which was determined by ^{1}H NMR.

Experimental Methods

Materials and Methods

Quartz slides (25 x 25 x 0.5 mm) were purchased from SPI Supplies. Cyclohexylamine (R)-2-azidopropanoate (D-azidoalanine CHA salt) and (S)-2-(((9H-fluoren-9-yl)methoxy)carbonylamino)-5-azidopentanoic acid ((Fmoc-L-azidoornithine) was purchased from Chiralix. (2S, 4S)-Boc-4-azidoproline was purchased from Combi-Blocks. Prior to use slides were cleaned in a 1 : 1 mixture (by volume) of sulfuric acid and nitric acid (Macron Chemicals) for one hour and rinsed with deionized water (Millipore, 18.2 MΩ). High purity organic solvents were purchased from Fisher Scientific. All other chemicals used were purchased from Sigma-Aldrich.

G1 Polyaryl Ether Dendron Functionalized Surfaces 4. G1 polybenzyl ether dendrons were synthesized by previously described methods.[92,91,90] Silanization of silica

surfaces was accomplished as reported.[184,185] Synthesis of **4** was adapted from previous work.[175] A 10 mL Teflon beaker equipped with a stir bar was placed in a 50 mL Teflon beaker filled with 40 mL of toluene and brought to reflux. Two slides were placed between the walls of the coated beakers and 3-aminopropyltrimethoxysilane was added and stirred for 2 h. Slides were sonicated for 30 s in 40 mL of toluene. In a new 50 mL Teflon beaker equipped with a 10 mL Teflon beaker containing a stir bar, 40 mL of toluene was brought to reflux. Slides were placed along the inside of the 50 mL beaker. G1 dendron (50 μmol) and 2 mL of Hunig's base were added and was stirred for 2 d. Slides were ultrasonically cleaned for 1 min in 30 mL of toluene. Slides were sonicated for 1 min in 30 mL of Milli-Q water (18.2 MΩ·cm) and for 1 min in 30 mL of methanol. Sequential sonications with water and methanol were repeated two more times. Slides were dried under a stream of argon and stored under vacuum.

Alanine Functionalized Polyaryl Ether Dendronized Surfaces 8. (R)-2-azido-D-proponoate cyclohexanaminium salt (265 mg, 1230 μmol, 130mM) was dissolved in water (10 mL) and 1 M NaOH (aq) was added dropwise to bring the solution to pH 11. The aqueous layer was washed with 5 mL portions of DCM three times and the combined organic layers were extracted with 5 mL of water. The water layers were combined and lyophilized. The resulting solid was dissolved in DMSO, filtered, and the solvent was removed by lyophilization to give the sodium salt of **5** (169 mg, 98 %) as a white solid. ^{1}H NMR was consistent with previously reported data.[186] Polyaryl ether dendron functionalized slide **4** (0.33 slide) was placed along the inside wall of a 2 dram vial

holding a stir bar. 3-Azido-D-alanine (28 mg, 218 μmol, 44mM) , $CuSO_4$ catalyst (82 mg , 329 μmol, 66mM), and ascorbic acid (95mg, 481 μmol l, 96mM) were dissolved in a 2:1 mixture of water and butanol (5 mL) and allowed to stir for 18 h. Slides were washed with 40 mL of Milli-Q water. Slides were sonicated for 1 min in 30 mL of Milli-Q water and for 1 min in 30 mL of methanol. Sequential sonications with water and methanol were repeated two more times. Slides were dried under a stream of argon and stored under vacuum.

5: ^{1}H NMR (300 MHz, $CDCl_3$) δ 3.84 (q, *J* = 7.1 Hz, 1H), 1.43 (d, *J* = 7.1 Hz, 3H) ppm.

Ornithine Functionalized Polyaryl Ether Dendronized Surfaces 9. Fmoc-L-azidoornithine was deprotected using standard conditions to give (S)-5-azidoornithine.[187-189] Polyaryl ether dendron functionalized slide **4** (0.2 slide) was placed along the inside wall of a 2 dram vial holding a stir bar. 5-Azido-L-ornithine (41.1 mg, 260 μmol, 21mM) and $CuSO_4$ catalyst (87.7 mg, 352 μmol, 176mM), and ascorbic acid (359 mg, 1.81 mmol, 907mM) were dissolved in a were dissolved in a 2:1 mixture of water and ethanol (2 mL) and allowed to stir for 18 h. Slides were washed with 40 mL of Milli-Q water. Slides were sonicated for 1 min in 30 mL of Milli-Q water and for 1 min in 30 mL of methanol. Sequential sonications with water and methanol were repeated two more times. Slides were dried under a stream of argon and stored under vacuum.

Proline Functionalized Polyaryl Ether Dendronized Surfaces 10. (2S, 4S)-Boc-4-azidoproline was deprotected using standard conditions[190, 191] to give (2S, 4S)-4-azidoproline. Polyaryl ether dendron functionalized slide **4** placed in a 50 mL Teflon

beaker containing a 10 mL Teflon beaker equipped with a stir bar and 8ml. (2S, 4S)-4-azidoproline (37.3 mg, 139 μmol, 12.0 mM) and $CuSO_4$ catalyst (109 mg, 436 μmol, 35 mM) and ascorbic acid (217 mg, 1.09 mmol, 87 mM) dissolved in a 2:1 mixture of water and ethanol (12.5 mL) and allowed to stir for 18 h placed in between the inside wall of the 50 mL beaker and outer wall of the 10 mL beaker, and allowed to stir for 18 h. Slides were washed with 40 mL of Milli-Q water. Slides were sonicated for 1 min in 30 mL of Milli-Q water and for 1 min in 30 mL of methanol. Sonications with water and methanol were repeated two more times. Slides were dried under a stream of argon and stored under vacuum.

Phenylalanine and Imidazolidinone Samples. Silica wafers were washed with acetone, dried under nitrogen, and then treated by ozonolysis for 1 h. 200 μL of MeOH was washed over phenylalanine functionalized PAMAM G(2) dendrimer **13** (20 mg) and then 20 μL was deposited on silicon wafer and dried under a stream of nitrogen. This was repeated with imidazolidinone functionalized PAMAM G2 dendrimer **14** on a new silicon wafer.

X-ray Photoelectron Spectroscopy (XPS). The functionalized slides were characterized using XPS. The analysis was conducted on a Physical Electronics 5600ci XPS system equipped with monochromatized Al Kα X-rays. The analysis area of the sample was 0.8 mm in diameter. Electron emissions were collected at 45° to the normal of the surface, and the spherical-sector-analyzer pass energy was selected as 23.5 eV for high-resolution scanning and as 46.95 eV for a survey to achieve optimum energy

resolution and count rate. Initial representative survey scans were acquired from 0 to 600 eV for 5 sweeps (sw) at 0.4 eV/step, and 20 mS/step. For further elemental analysis, high resolution (HR) scans were acquired for the C 1s (~280 to 291 eV, 2 sw), N 1s (~394 to 405 eV, 5 sw), O 1s (~528 to 537 eV, 2 sw), and Si 2p (~98 to 106 eV, 3 sw) regions. The acquisition parameters were run for 6 cycles at 0.50 eV/step and 20mS/step. For all spectra, the background of all regions were subtracted using the Shirley background.[192] Peak positions were normalized to the C 1s peak at 285.0 eV and were fitted to functions having a 100% Gaussian line shape. Binding energies were normalized to the C 1s.The data acquisition and data analysis was performed using RBD AugerScan software.

Quantitative XPS Analysis of Surface Functionalization. Quantitative analysis of the XPS was performed using the methodology published by Geiger and co-workers.[130] Calculations for azides **5** and **6** were performed by previously reported adapted methods for dendronized surfaces.[175] This method is demonstrated below for azide **6**.

Site composition: To determine the site composition, 1 equivalent of the signal that is assigned to each triazole formed is determined using equation 1. One equivalent of signal from triazole species A_{Tri} is equal to the change in the integrated area centered at 401.5 eV, $A_{401.5}$, minus the signal from the protonated amine species, as shown in equation 2. Equation 4 was derived to calculate this change, with an asterisk used to designate the integrated areas after 1,3 cycloaddition has occurred.

$$\frac{A_{399}}{A_{401.5}} = \frac{A*_{399}}{A*_{401.5} - A_{Tri}} \qquad \text{(eq. 1)}$$

$$A_{Tri} = A*_{401.5} - \left(\frac{A_{401.5} \cdot A*_{399}}{A_{399}}\right) \qquad \text{(eq. 2)}$$

The site composition of the triazole species for surface **9** was calculated by dividing 1 equivalent of the signal from the triazoles divided by one equivalent of signal from all of the species present (dendron, amine, and secondary amine). This was repeated for each species, as shown in equations 3, 4, and 5.

$$Total\ triazole\ \% = \frac{A_{Tri}}{A*_{399}+A*_{400}+A*_{401.5}-3A_{Tri}}(100) \qquad \text{(eq. 3)}$$

$$Total\ dendron\ \% = \frac{A*_{399}}{A*_{399}+A*_{400}+A*_{401.5}-3A_{Tri}}(100) \qquad \text{(eq. 4)}$$

$$Total\ amine\ \% = \frac{A*_{400}+A*_{401.5}-4A_{Tri}}{A*_{399}+A*_{400}+A*_{401.5}-3A_{Tri}}(100) \qquad \text{(eq. 5)}$$

These calculations were adapted for the addition contribution from the amine signal as a result of ornithine addition. The signal for each terminal ornithine addition was set to 1 equivalent of A_{Tri}.

CHAPTER SIX

SUMMARY AND CONCLUSIONS

Galectin-3 has been shown to be up-regulated in many types of cancer and has been implicated to play a role in more aggressive phenotypes. Therefore, it is important to develop frameworks to mimic the polyvalent carbohydrate-galectin-3 interactions present in these metastatic pathways. To study the effect of multivalency on galectin-3 mediated homotypic cellular aggregation, four polyamidoamine (PAMAM) dendrimers (G2, G3, G4, and G6) were functionalized with *N*-acetyllactosamine. An efficient four-step chemoenzymatic route was developed for which the regiochemistry of the galactose addition to *N*-acetylglucosamine functionalized dendrimers was controlled using a recombinant β-1,4-Galactosyltransferase-/UDP-4'-Gal Epimerase Fusion Protein (lgtB-galE). HT-1080 fibrosarcoma, A549 lung, and DU-145 prostate cancer cell lines were used in cellular aggregation studies. In the presence of G(2) and G(3) Lac*N*Ac PAMAM dendrimers, galectin-3 was diverted from its normal galectin-3/MUC1 pathway which inhibited aggregation. However, in the presence of the larger glycodendrimers, homotypic cellular aggregation was induced. Although the *N*-acetyllactosaminosides have similar observable effects on cellular aggregation to the effects that were previously reported with lactosides functionalized dendrimers, the results obtained here indicate that broader effective ranges of concentrations and smaller deviations from the measured averages can be obtained for glycodendrimers that are functionalized with higher affinity monomers (i.e. the Lac*N*Ac functionalized PAMAM dendrimers)..

Novel poly(aryl ether) dendronized silica surfaces designed for reversible adsorbtion of targeted analytes were synthesized, and a methodology for characterization using X-ray Photoelectron Spectroscopy (XPS) was developed. Using a Cu(I) mediated cycloaddition "click" reaction, *β*-cyclodextrin was appended to dendronized surfaces and also to a non-dendronized surface for comparison purposes. *β*-cyclodextrin functionalized G(1) dendronized surfaces adsorbed targeted analytes with greater efficiency than surfaces functionalized with monomeric *β*-cyclodextrin and larger generation dendrons. *β*-Cyclodextrin functionalized surfaces retained C152 through multiple aqueous washes, but its reversibility was demonstrated by analyte deadsorption when exposed to a "triggered" release. In addition to this, the integrity of the organic monolayer was preserved and provided reproducible results through multiple trials.

Therefore, G(1) dendronized surfaces were further modified to develop a new class of surfaces capable of reversible adsorption. A heterogeneous mixture of sulfonic acid and pyridine was appended to the dendronized surface. Due to the limited sensitivity of the XPS, AES was used to quantify a ~ 7 : 1 ratio of pyridines to sulfonic acids installed. Homogenous sulfonic acid and pyridine G(1) dendronized surfaces were functionalized and characterized for comparison.

Additionally, G(1) dendronized surfaces were functionalized with chiral amino acids. R-alanine, S-ornithine, and S-proline surfaces were synthesized and characterized for chiral recognition studies. These chiral amino acids are capable of forming salt bridges, and it would be of interest to study their efficiency for reversible adsorbtion. G(2) dendronized surfaces were additionally functionalized with S-proline, and both G(1) and

G(2) proline functionalized slides will be compared to a monomeric proline functionalized surface for their efficiency to catalyze asymmetric aldol reactions.

REFERENCES CITED

1. Lehn, J. M., SUPRAMOLECULAR CHEMISTRY. *Science* **1993,** *260* (5115), 1762-1763.

2. Lehn, J. M., CRYPTATES - CHEMISTRY OF MACROPOLYCYCLIC INCLUSION COMPLEXES. *Accounts of Chemical Research* **1978,** *11* (2), 49-57.

3. Berg, J., Tymoczko, JL, Stryer, L., Biochemistry. 5th edition. ed.; W H Freeman: New York, 2002.

4. Dasent, W. E., *Inorganic Energetics: An Introduction*. 2nd Edition ed.; Cambridge University Press: Cambridge, 1982.

5. Cheng, A. C.; Chen, W. W.; Fuhrmann, C. N.; Frankel, A. D., Recognition of Nucleic Acid Bases and Base-pairs by Hydrogen Bonding to Amino Acid Side-chains. *Journal of Molecular Biology* **2003,** *327* (4), 781-796.

6. Hermann, T.; Patel, D. J., Stitching together RNA tertiary architectures1. *Journal of Molecular Biology* **1999,** *294* (4), 829-849.

7. Luscombe, N. M.; Laskowski, R. A.; Thornton, J. M., Amino acid–base interactions: a three-dimensional analysis of protein–DNA interactions at an atomic level. *Nucleic Acids Research* **2001,** *29* (13), 2860-2874.

8. Lodish H, B. A., Zipursky SL, et al., Molecular Cell Biology. 4th Edition ed.; W. H. Freeman: New York, 2000.

9. Yeagle, P. L., Non-covalent binding of membrane lipids to membrane proteins. *Biochimica et Biophysica Acta (BBA) - Biomembranes* **2014,** *1838* (6), 1548-1559.

10. Stasyuk, O. A.; Jakubec, D.; Vondrášek, J.; Hobza, P., Noncovalent Interactions in Specific Recognition Motifs of Protein–DNA Complexes. *Journal of Chemical Theory and Computation* **2017,** *13* (2), 877-885.

11. Pedersen, C. J., Cyclic polyethers and their complexes with metal salts. *Journal of the American Chemical Society* **1967,** *89* (26), 7017-7036.

12. Cram, D. J.; Lein, G. M., Host-guest complexation. 36. Spherand and lithium and sodium ion complexation rates and equilibria. *Journal of the American Chemical Society* **1985,** *107* (12), 3657-3668.

13. Dietrich, B.; Lehn, J. M.; Sauvage, J. P., Diaza-polyoxa-macrocycles et macrobicycles. *Tetrahedron Letters* **1969,** *10* (34), 2885-2888.

14. Beuerle, F., Supramolecular chemistry: Unexplored territory for self-assembly. *Nature* **2016,** *540* (7634), 529-531.

15. Persch, E.; Dumele, O.; Diederich, F., Molecular Recognition in Chemical and Biological Systems. *Angewandte Chemie International Edition* **2015,** *54* (11), 3290-3327.

16. Ariga, K.; Ito, H.; Hill, J. P.; Tsukube, H., Molecular recognition: from solution science to nano/materials technology. *Chemical Society Reviews* **2012,** *41* (17), 5800-5835.

17. Baron, R.; McCammon, J. A., Molecular Recognition and Ligand Association. *Annual Review of Physical Chemistry* **2013,** *64* (1), 151-175.

18. Gutowski, W., Thermodynamics of Adhesion. In *Fundamentals of Adhesion*, Lee, L.-H., Ed. Springer US: Boston, MA, 1991; pp 87-135.

19. Perrin, C. L.; Nielson, J. B., "Strong" hydrogen bonds in chemistry and biology. *Annu Rev Phys Chem* **1997,** *48*, 511-44.

20. Cloninger, M. J.; Bilgiçer, B.; Li, L.; Mangold, S. L.; Phillips, S. T.; Wolfenden, M. L., Multivalency. In *Supramolecular Chemistry*, John Wiley & Sons, Ltd: 2012.

21. Krishnamurthy, V. M.; Estroff, L. A.; Whitesides, G. M., Multivalency in Ligand Design. In *Fragment-based Approaches in Drug Discovery*, Wiley-VCH Verlag GmbH & Co. KGaA: 2006; pp 11-53.

22. Kiessling, L. L.; Lamanna, A. C., Multivalency in Biological Systems. In *Chemical Probes in Biology: Science at the Interface of Chemistry, Biology and Medicine*, Springer Netherlands: Dordrecht, 2003; pp 345-357.

23. Christensen, T.; Gooden, D. M.; Kung, J. E.; Toone, E. J., Additivity and the Physical Basis of Multivalency Effects: A Thermodynamic Investigation of the Calcium EDTA Interaction. *Journal of the American Chemical Society* **2003,** *125* (24), 7357-7366.

24. Zhao, Q. C.; Barclay, M.; Hilkens, J.; Guo, X. L.; Barrow, H.; Rhodes, J. M.; Yu, L. G., Interaction between circulating galectin-3 and cancer-associated MUC1 enhances tumour cell homotypic aggregation and prevents anoikis. *Molecular Cancer* **2010,** *9*, 12.

25. Bray, D.; Levin, M. D.; Morton-Firth, C. J., Receptor clustering as a cellular mechanism to control sensitivity. *Nature* **1998,** *393* (6680), 85-88.

26. Cochran, J. R.; Aivazian, D.; Cameron, T. O.; Stern, L. J., Receptor clustering and transmembrane signaling in T cells. *Trends in Biochemical Sciences* **2001,** *26* (5), 304-310.

27. Germain, R. N., T-cell signaling: The importance of receptor clustering. *Current Biology* **1997,** *7* (10), R640-R644.

28. Thomason, P. A.; Wolanin, P. M.; Stock, J. B., Signal Transduction: Receptor Clusters as Information Processing Arrays. *Current Biology* **2002,** *12* (11), R399-R401.

29. Reichardt, N.-C.; Martin-Lomas, M.; Penades, S., Opportunities for glyconanomaterials in personalized medicine. *Chemical Communications* **2016,** *52* (92), 13430-13439.

30. Bennett, N. R.; Zwick, D. B.; Courtney, A. H.; Kiessling, L. L., Multivalent Antigens for Promoting B and T Cell Activation. *Acs Chemical Biology* **2015,** *10* (8), 1817-1824.

31. Hudak, J. E.; Belardi, B.; Appel, M. J.; Solania, A.; Robinson, P. V.; Bertozzi, C. R., Piperidine-based glycodendrons as protein N-glycan prosthetics. *Bioorganic & Medicinal Chemistry* **2016,** *24* (20), 4791-4800.

32. Chen, W. C.; Sigal, D. S.; Saven, A.; Paulson, J. C., Targeting B lymphoma with nanoparticles bearing glycan ligands of CD22. *Leukemia & Lymphoma* **2012,** *53* (2), 208-210.

33. Boas, U., Christensen, J. B., Heegaard, P. M. H., Dendrimers: Design, Synthesis and Chemical Properties. In *Dendrimers in Medicine and Biotechnology: New Molecular Tools*, The Royal Society of Chemistry: 2006; pp 1-27.

34. Buhleier, E.; Wehner, W.; Vogtle, F., CASCADE-CHAIN-LIKE AND NONSKID-CHAIN-LIKE SYNTHESES OF MOLECULAR CAVITY TOPOLOGIES. *Synthesis-Stuttgart* **1978,** (2), 155-158.

35. Hawker, C. J.; Frechet, J. M. J., Preparation of polymers with controlled molecular architecture - a new convergent approach to dendritic macromolecules. *J. Amer. Chem. Soc.* **1990,** *112* (21), 7638-7647.

36. Tomalia, D. A.; Baker, H.; Dewald, J.; Hall, M.; Kallos, G.; Martin, S.; Roeck, J.; Ryder, J.; Smith, P., A NEW CLASS OF POLYMERS - STARBURST-DENDRITIC MACROMOLECULES. *Polymer Journal* **1985,** *17* (1), 117-132.

37. Esfand, R.; Tomalia, D. A., Poly(amidoamine) (PAMAM) dendrimers: from biomimicry to drug delivery and biomedical applications. *Drug Discovery Today* **2001,** *6* (8), 427-436.

38. Jevprasesphant, R.; Penny, J.; Jalal, R.; Attwood, D.; McKeown, N. B.; D'Emanuele, A., The influence of surface modification on the cytotoxicity of PAMAM dendrimers. *International Journal of Pharmaceutics* **2003,** *252* (1–2), 263-266.

39. Kesharwani, P.; Banerjee, S.; Gupta, U.; Mohd Amin, M. C. I.; Padhye, S.; Sarkar, F. H.; Iyer, A. K., PAMAM dendrimers as promising nanocarriers for RNAi therapeutics. *Materials Today* **2015,** *18* (10), 565-572.

40. Roberts, J. C.; Bhalgat, M. K.; Zera, R. T., Preliminary biological evaluation of polyamidoamine (PAMAM) StarburstTM dendrimers. *Journal of Biomedical Materials Research* **1996,** *30* (1), 53-65.

41. Naylor, A. M.; Goddard, W. A.; Kiefer, G. E.; Tomalia, D. A., Starburst dendrimers. 5. Molecular shape control. *Journal of the American Chemical Society* **1989,** *111* (6), 2339-2341.

42. Wiener, E. C.; Brechbiel, M. W.; Brothers, H.; Magin, R. L.; Gansow, O. A.; Tomalia, D. A.; Lauterbur, P. C., DENDRIMER-BASED METAL-CHELATES - A NEW CLASS OF MAGNETIC-RESONANCE-IMAGING CONTRAST AGENTS. *Magnetic Resonance in Medicine* **1994,** *31* (1), 1-8.

43. Roberts, J. C.; Adams, Y. E.; Tomalia, D.; Mercer-Smith, J. A.; Lavallee, D. K., Using starburst dendrimers as linker molecules to radiolabel antibodies. *Bioconjugate Chemistry* **1990,** *1* (5), 305-308.

44. Tomalia, D. A.; Reyna, L. A.; Svenson, S., Dendrimers as multi-purpose nanodevices for oncology drug delivery and diagnostic imaging. *Biochemical Society Transactions* **2007,** *35*, 61-67.

45. Scott, R. W. J.; Ye, H.; Henriquez, R. R.; Crooks, R. M., Synthesis, Characterization, and Stability of Dendrimer-Encapsulated Palladium Nanoparticles. *Chemistry of Materials* **2003,** *15* (20), 3873-3878.

46. Shadrack, D. M.; Mubofu, E. B.; Nyandoro, S. S., Synthesis of Polyamidoamine Dendrimer for Encapsulating Tetramethylscutellarein for Potential Bioactivity Enhancement. *International Journal of Molecular Sciences* **2015,** *16* (11), 26363-26377.

47. Lee, R. T.; Lee, Y. C., Affinity enhancement by multivalent lectin-carbohydrate interaction. *Glycoconjugate Journal* **2000,** *17* (7-9), 543-551.

48. Leffler, H.; Carlsson, S.; Hedlund, M.; Qian, Y.; Poirier, F., Introduction to galectins. *Glycoconjugate Journal* **2002,** *19* (7), 433-440.

49. Sorme, P.; Arnoux, P.; Kahl-Knutsson, B.; Leffler, H.; Rini, J. M.; Nilsson, U. J., Structural and thermodynamic studies on cation-Pi interactions in lectin-ligand complexes: high-affinity galectin-3 inhibitors through fine-tuning of an arginine-arene interaction. *J Am Chem Soc* **2005,** *127* (6), 1737-43.

50. Henderson, N. C.; Sethi, T., The regulation of inflammation by galectin-3. *Immunological Reviews* **2009,** *230* (1), 160-171.

51. Dagher, S. F.; Wang, J. L.; Patterson, R. J., Identification of galectin-3 as a factor in pre-mRNA splicing. *Proceedings of the National Academy of Sciences of the United States of America* **1995,** *92* (4), 1213-1217.

52. Glinsky, G. V.; Glinskii, O. V.; Huxley, V. H.; Turk, J. R., Intravascular metastatic cancer cell homotypic aggregation at the sites of primary attachment to the endothelium. *Cancer research (Baltimore)* **2003,** *63* (13), 3805-3811.

53. Inohara, H.; Raz, A., FUNCTIONAL EVIDENCE THAT CELL-SURFACE GALECTIN-3 MEDIATES HOMOTYPIC CELL-ADHESION. *Cancer Research* **1995,** *55* (15), 3267-3271.

54. Nangia-Makker, P.; Balan, V.; Raz, A., Regulation of Tumor Progression by Extracellular Galectin-3. *Cancer Microenvironment* **2008,** *1* (1), 43-51.

55. Nangia-Makker, P.; Balan, V.; Raz, A., Galectin-3 Binding and Metastasis. In *Metastasis Research Protocols*, Dwek, M.; Brooks, S. A.; Schumacher, U., Eds. Humana Press: Totowa, NJ, 2012; pp 251-266.

56. Raz, A.; Lotan, R., Endogenous galactoside-binding lectins: a new class of functional tumor cell surface molecules related to metastasis. *Cancer and Metastasis Reviews* **1987,** *6* (3), 433-452.

57. Zhao, Q.; Guo, X.; Nash, G. B.; Stone, P. C.; Hilkens, J.; Rhodes, J. M.; Yu, L.-G., Circulating galectin-3 promotes metastasis by modifying MUC1 localization on cancer cell surface. *Cancer research* **2009,** *69* (17), 6799-6806.

58. Khaldoyanidi, S. K.; Glinsky, V. V.; Sikora, L.; Glinskii, A. B.; Mossine, V. V.; Quinn, T. P.; Glinsky, G. V.; Sriramarao, P., MDA-MB-435 human breast carcinoma cell homo- and heterotypic adhesion under flow conditions is mediated in part by Thomsen-Friedenreich antigen-galectin-3 interactions. *J Biol Chem* **2003,** *278* (6), 4127-34.

59. Yu, L.-G.; Andrews, N.; Zhao, Q.; McKean, D.; Williams, J. F.; Connor, L. J.; Gerasimenko, O. V.; Hilkens, J.; Hirabayashi, J.; Kasai, K.; Rhodes, J. M., Galectin-3 interaction with Thomsen-Friedenreich disaccharide on cancer-associated MUC1 causes increased cancer cell endothelial adhesion. *Journal of Biological Chemistry* **2007,** *282* (1), 773-781.

60. Michel, A. K.; Nangia-Makker, P.; Raz, A.; Cloninger, M. J., Lactose-Functionalized Dendrimers Arbitrate the Interaction of Galectin-3/MUC1 Mediated

Cancer Cellular Aggregation. *Chembiochem : a European journal of chemical biology* **2014,** *15* (14), 2106-2112.

61. Raz, A.; Lotan, R., Lectin-like Activities Associated with Human and Murine Neoplastic Cells. *Cancer Research* **1981,** *41* (9 Part 1), 3642.

62. Perillo, N. L.; Marcus, M. E.; Baum, L. G., Galectins: versatile modulators of cell adhesion, cell proliferation, and cell death. *Journal of Molecular Medicine* **1998,** *76* (6), 402-412.

63. Yu, L. G.; Andrews, N.; Zhao, Q.; McKean, D.; Williams, J. F.; Connor, L. J.; Gerasimenko, O. V.; Hilkens, J.; Hirabayashi, J.; Kasai, K.; Rhodes, J. M., Galectin-3 interaction with Thomsen-Friedenreich disaccharide on cancer-associated MUC1 causes increased cancer cell endothelial adhesion. *Journal of Biological Chemistry* **2007,** *282* (1), 773-781.

64. Seetharaman, J.; Kanigsberg, A.; Slaaby, R.; Leffler, H.; Barondes, S. H.; Rini, J. M., X-ray crystal structure of the human galectin-3 carbohydrate recognition domain at 2.1-angstrom resolution. *Journal of Biological Chemistry* **1998,** *273* (21), 13047-13052.

65. Goodman, C. K.; Wolfenden, M. L.; Nangia-Makker, P.; Michel, A. K.; Raz, A.; Cloninger, M. J., Multivalent scaffolds induce galectin-3 aggregation into nanoparticles. *Beilstein Journal of Organic Chemistry* **2014,** *10*, 1570-1577.

66. Sörme, P.; Arnoux, P.; Kahl-Knutsson, B.; Leffler, H.; Rini, J. M.; Nilsson, U. J., Structural and Thermodynamic Studies on Cation−Π Interactions in Lectin−Ligand Complexes: High-Affinity Galectin-3 Inhibitors through Fine-Tuning of an Arginine−Arene Interaction. *Journal of the American Chemical Society* **2005,** *127* (6), 1737-1743.

67. Tejler, J.; Leffler, H.; Nilsson, U. J., Synthesis of O-galactosyl aldoximes as potent LacNAc-mimetic galectin-3 inhibitors. *Bioorganic & Medicinal Chemistry Letters* **2005,** *15* (9), 2343-2345.

68. Bian, C. F.; Zhang, Y.; Sun, H.; Li, D. F.; Wang, D. C., Structural basis for distinct binding properties of the human galectins to Thomsen-Friedenreich antigen. *PLoS One* **2011,** *6* (9), e25007.

69. Wiener, E.; Brechbiel, M. W.; Brothers, H.; Magin, R. L.; Gansow, O. A.; Tomalia, D. A.; Lauterbur, P. C., Dendrimer-based metal chelates: A new class of magnetic resonance imaging contrast agents. *Magnetic Resonance in Medicine* **1994,** *31* (1), 1-8.

70. Singh, P.; Moll, F.; Lin, S. H.; Ferzli, C.; Yu, K. S.; Koski, R. K.; Saul, R. G.; Cronin, P., Starburst dendrimers: enhanced performance and flexibility for immunoassays. *Clinical Chemistry* **1994,** *40* (9), 1845.

71. Majoros, I. J.; Myc, A.; Thomas, T.; Mehta, C. B.; Baker, J. R., PAMAM Dendrimer-Based Multifunctional Conjugate for Cancer Therapy: Synthesis, Characterization, and Functionality. *Biomacromolecules* **2006,** *7* (2), 572-579.

72. Shukla, R.; Thomas, T. P.; Peters, J. L.; Desai, A. M.; Kukowska-Latallo, J.; Patri, A. K.; Kotlyar, A.; Baker, J. R., HER2 Specific Tumor Targeting with Dendrimer Conjugated Anti-HER2 mAb. *Bioconjugate Chemistry* **2006,** *17* (5), 1109-1115.

73. Walter, E. D.; Morgan, J. R.; Singel, D. J.; Cloninger, M. J., Altering the strength of lectin binding interactions and controlling the amount of lectin clustering using mannose/hydroxyl-functionalized dendrimers. *Journal of the American Chemical Society* **2003,** *125* (29), 8820-8826.

74. Wolfenden, M. L.; Cloninger, M. J., Mannose/glucose-functionalized dendrimers to investigate the predictable tunability of multivalent interactions. *Journal of the American Chemical Society* **2005,** *127* (35), 12168-12169.

75. Wolfenden, M.; Cousin, J.; Nangia-Makker, P.; Raz, A.; Cloninger, M., Glycodendrimers and Modified ELISAs: Tools to Elucidate Multivalent Interactions of Galectins 1 and 3. *Molecules (Basel, Switzerland)* **2015,** *20* (4), 7059-7096.

76. Woller, E. K.; Cloninger, M. J., The lectin-binding properties of six generations of mannose-functionalized dendrimers. *Organic Letters* **2002,** *4* (1), 7-10.

77. Andre, S.; Ortega, P. J.; Perez, M. A.; Roy, R.; Gabius, H. J., Lactose-containing starburst dendrimers: influence of dendrimer generation and binding-site orientation of receptors (plant/animal lectins and immunoglobulins) on binding properties. *Glycobiology* **1999,** *9* (11), 1253-61.

78. Using PAMAM dendrimer frameworks to investigate multivalent binding in protein-carbohydrate interactions. Montana State University, Montana State University, 2009-12-15.

79. Cloninger, M. J. In *Mannose/glucose functionalized dendrimers as tools for probing tunable multivalency*, 2006; pp 702-702.

80. Cloninger, M. J., Using glycodendrimers to study protein-carbohydrate interactions. *Glycobiology* **2006,** *16* (11), 1109-1109.

81. Kaltgrad, E.; Wolfenden, M. L.; Cloninger, M. J.; Finn, M. G., Measurement of monovalent and polyvalent carbohydrate-lectin binding by back-scattering interferometry. *Analytical chemistry (Washington)* **2009,** *81* (12), 4889-4897.

82. Schlick, K. H.; Udelhoven, R. A.; Strohmeyer, G. C.; Cloninger, M. J., Binding of Mannose-Functionalized Dendrimers with Pea (Pisum sativum) Lectin. *Molecular Pharmaceutics* **2005,** *2* (4), 295-301.

83. Schlick, K. H.; Cloninger, M. J., Inhibition binding studies of glycodendrimer/lectin interactions using surface plasmon resonance. *Tetrahedron* **2010,** *66* (29), 5305-5310.

84. Wolfenden, M. L. Using PAMAM dendrimer frameworks to investigate multivalent binding in protein-carbohydrate interactions. Montana State University, Montana State University, 2009-12-15.

85. Woller, E. K.; Walter, E. D.; Morgan, J. R.; Singel, D. J.; Cloninger, M. J., Altering the Strength of Lectin Binding Interactions and Controlling the Amount of Lectin Clustering Using Mannose/Hydroxyl-Functionalized Dendrimers. *Journal of the American Chemical Society* **2003,** *125* (29), 8820-8826.

86. Chabre, Y. M.; Roy, R., Design and creativity in synthesis of multivalent neoglycoconjugates. *Adv Carbohydr Chem Biochem* **2010,** *63*, 165-393.

87. Roy, R.; Shiao, T. C.; Rittenhouse-Olson, K., Glycodendrimers: versatile tools for nanotechnology. *Brazilian Journal of Pharmaceutical Sciences (Impresso); Vol 49 (2013): special issueDO - 10.1590/S1984-82502013000700008* **2013**.

88. Michel, A. K.; Nangia-Makker, P.; Raz, A.; Cloninger, M. J., Lactose-Functionalized Dendrimers Arbitrate the Interaction of Galectin-3/MUC1 Mediated Cancer Cellular Aggregation. *ChemBioChem* **2014,** *15* (14), 2106-2112.

89. Mammen, M.; Choi, S.-K.; Whitesides, G. M., Polyvalent Interactions in Biological Systems: Implications for Design and Use of Multivalent Ligands and Inhibitors. *Angewandte Chemie International Edition* **1998,** *37* (20), 2754-2794.

90. Frechet, J. M. J., Preparation of polymers with controlled molecular architecture. A new convergent approach to dendritic macromolecules. *Journal of the American Chemical Society* **1990,** *112* (21), 7638-7647.

91. Malkoch, M.; Schleicher, K.; Drockenmuller, E.; Hawker, C. J.; Russell, T. P.; Wu, P.; Fokin, V. V., Structurally diverse dendritic libraries: A highly efficient functionalization approach using Click chemistry. *Macromolecules* **2005,** *38* (9), 3663-3678.

92. Antoni, P.; Nystrom, D.; Hawker, C. J.; Hult, A.; Malkoch, M., A chemoselective approach for the accelerated synthesis of well-defined dendritic architectures. *Chemical Communications* **2007,** (22), 2249-2251.

93. Huisgen, R.; Bayer, H. O.; Schaefer, F. C.; Gotthardt, H., A New Type of Mesoionic Aromatic Compound and Its 1,3-Dipolar Cycloaddition Reactions with Acetylene Derivatives. *Angewandte Chemie international edition* **1964,** *3* (2), 136-&.

94. Huisgen, R.; Gotthardt, H.; Bayer, H. O., Azlactones as 1,3-Dipoles; A New Pyrrole Synthesis. *Angewandte Chemie International Edition in English* **1964,** *3* (2), 135-136.

95. Rostovtsev, V. V.; Green, L. G.; Fokin, V. V.; Sharpless, K. B., A stepwise Huisgen cycloaddition process: Copper(I)-catalyzed regioselective "ligation" of azides and terminal alkynes. *Angew. Chem. Int. Ed.* **2002,** *41* (14), 2596-2599.

96. Lee, J. W.; Kim, J. H.; Kim, B.-K.; Shin, W. S.; Jin, S.-H., Synthesis of Fréchet type dendritic benzyl propargyl ether and Fréchet type triazole dendrimer. *Tetrahedron* **2006,** *62* (5), 894-900.

97. Lee, J. W.; Kang, H.-S.; Han, S. C.; Sung, S. R.; Kim, J. H.; Oh, J.; Jin, S.-H., Synthesis of Poly(benzyl ether) Dendrimer Containing Tetra(ethyleneoxide) at Core Using Click Chemistry. *Molecular Crystals and Liquid Crystals* **2008,** *492* (1), 139/[503]-146/[510].

98. Dieter A. Schlüter, C. J. H., and Junji Sakamoto, *Synthesis of polymers New Structures and Methods*. 2012; Vol. 1.

99. ATSDR Toxicological Profile for Chlorobenzene. http://www.atsdr.cdc.gov/toxprofiles/tp.asp?id=489&tid=87.

100. ATSDR Toxicological Profile for Chlorophenols. http://www.atsdr.cdc.gov/toxprofiles/tp.asp?id=941&tid=195.

101. Andoh, K.; Kosaka, H.; Kumagai, S.; Matsunaga, I., Inhalation toxicokinetics of p -dichlorobenzene and daily absorption and internal accumulation in chronic low-level exposure to humans. *Archives of toxicology* **2002,** *76* (5-6), 306-315.

102. Nagyeri, G.; Valkusz, Z.; Radacs, M.; Ocsko, T.; Hausinger, P.; Laszlo, M.; Laszlo, F. A.; Juhasz, A.; Julesz, J.; Galfi, M., Behavioral and endocrine effects of chronic exposure to low doses of chlorobenzenes in Wistar rats. *Neurotoxicology and Teratology* **2012,** *34* (1), 9-19.

103. Schofield, W. C. E.; Bain, C. D.; Badyal*, J. P. S., HIERARCHICAL POROUS ARCHITECTURES FOR HIGH THROUGHPUT MOLECULAR CAPTURE AND RELEASE. Durham University: 2011; pp 1-29.

104. Cappadona, A. T.; Daniels, M. L.; Siddiquee, A. T., Host–Guest Complex of β-Cyclodextrin and Disulfide Form of 4-Aminothiophenol. *Applied Sciences* **2012,** *2* (4).

105. Sabapathy, R. C.; Bhattacharyya, S.; Cleland, W. E.; Hussey, C. L., Host−Guest Complexation in Self-Assembled Monolayers: Inclusion of a Monolayer-Anchored Cationic Ferrocene-Based Guest by Cyclodextrin Hosts. *Langmuir* **1998,** *14* (14), 3797-3807.

106. Del Valle, E. M. M., Cyclodextrins and their uses: a review. *Process Biochemistry* **2004,** *39* (9), 1033-1046.

107. Ringer, A. L.; Sinnokrot, M. O.; Lively, R. P.; Sherrill, C. D., The Effect of Multiple Substituents on Sandwich and T-Shaped π–π Interactions. *Chemistry – A European Journal* **2006,** *12* (14), 3821-3828.

108. Pirkle, W. H.; Schreiner, J. L., Chiral HPLC (high-performance liquid chromatographic) stationary phases. 4. Separation of the enantiomers of bi-.beta. naphthols and analogs. *The Journal of Organic Chemistry* **1981,** *46* (24), 4988-4991.

109. Mallat, T.; Orglmeister, E.; Baiker, A., Asymmetric Catalysis at Chiral Metal Surfaces. *Chemical Reviews* **2007,** *107* (11), 4863-4890.

110. Weissbuch, I.; Addadi, L.; Leiserowitz, L., Molecular Recognition at Crystal Interfaces. *Science* **1991,** *253* (5020), 637.

111. Hazen, R. M.; Sholl, D. S., Chiral selection on inorganic crystalline surfaces. *Nat Mater* **2003,** *2* (6), 367-374.

112. Gellman, A. J., Chiral Surfaces: Accomplishments and Challenges. *ACS Nano* **2010,** *4* (1), 5-10.

113. Rampulla, D.; Gellman, A., Enantioselectivity on Surfaces with Chiral Nanostructures. In *Dekker Encyclopedia of Nanoscience and Nanotechnology - Six Volume Set (Print Version)*, CRC Press: 2004.

114. Mahapatra, M.; Burkholder, L.; Garvey, M.; Bai, Y.; Saldin, D. K.; Tysoe, W. T., Enhanced hydrogenation activity and diastereomeric interactions of methyl pyruvate co-adsorbed with R-1-(1-naphthyl)ethylamine on Pd(111). *Nature Communications* **2016,** *7*, 12380.

115. Corey, E. J.; Huang, A. X., A Short Enantioselective Total Synthesis of the Third-Generation Oral Contraceptive Desogestrel. *Journal of the American Chemical Society* **1999,** *121* (4), 710-714.

116. List, B.; Lerner, R. A.; Barbas, C. F., Proline-Catalyzed Direct Asymmetric Aldol Reactions. *Journal of the American Chemical Society* **2000,** *122* (10), 2395-2396.

117. Elmekawy, A. A.; Sweeney, J. B.; Brown, D. R., Efficient synthesis of supported proline catalysts for asymmetric aldol reactions. *Catalysis Science & Technology* **2015,** *5* (2), 690-696.

118. Choi, S.-k., *Synthetic Multivalent Molecules : Concepts and Biomedical Applications*. Wiley-Interscience: Hoboken, New Jersey, 2004.

119. Newkome, G. R.; Moorefield, C. N.; Vögtle, F., Front Matter. In *Dendrimers and Dendrons*, Wiley-VCH Verlag GmbH & Co. KGaA: 2001; pp i-xii.

120. Appeldoorn, C. C. M.; Joosten, J. A. F.; Ait el Maate, F.; Dobrindt, U.; Hacker, J.; Liskamp, R. M. J.; Khan, A. S.; Pieters, R. J., Novel multivalent mannose compounds and their inhibition of the adhesion of type 1 fimbriated uropathogenic E. coli. *Tetrahedron: Asymmetry* **2005,** *16* (2), 361-372.

121. Pieters, R. J., Intervention with bacterial adhesion by multivalent carbohydrates. *Medicinal Research Reviews* **2007,** *27* (6), 796-816.

122. Blixt, O.; Brown, J.; Schur, M. J.; Wakarchuk, W.; Paulson, J. C., Efficient preparation of natural and synthetic galactosides with a recombinant beta-1,4-galactosyltransferase-/UDP-4 '-gal epimerase fusion protein. *Journal of Organic Chemistry* **2001,** *66* (7), 2442-2448.

123. Nieminen, J.; Kuno, A.; Hirabayashi, J.; Sato, S., Visualization of galectin-3 oligomerization on the surface of neutrophils and endothelial cells using fluorescence resonance energy transfer. *J Biol Chem* **2007,** *282* (2), 1374-83.

124. Fortuna-Costa, A.; Gomes, A. M.; Kozlowski, E. O.; Stelling, M. P.; Pavao, M. S., Extracellular galectin-3 in tumor progression and metastasis. *Front Oncol* **2014,** *4*, 138.

125. United States Environmental Protection Agency - Standards and Risk Management. http://water.epa.gov/drink/standardsriskmanagement.cfm.

126. Jain, A. K.; Gupta, V. K.; Jain, S.; Suhas, Removal of chlorophenols using industrial wastes. *Environ. Sci. Technol.* **2004,** *38* (4), 1195-1200.

127. Johnson, A. C.; Sumpter, J. P., Removal of endocrine-disrupting chemicals in activated sludge treatment works. *Environ. Sci. Technol.* **2001,** *35* (24), 4697-4703.

128. Mifflin, A. L.; Konek, C. T.; Geiger, F. M., Tracking oxytetracyline mobility across environmental interfaces by second harmonic generation. *J. Phys. Chem. B* **2006,** *110* (45), 22577-22585.

129. Azam, M. S.; Fenwick, S. L.; Gibbs-Davis, J. M., Orthogonally Reactive SAMs as a General Platform for Bifunctional Silica Surfaces. *Langmuir* **2011,** *27* (2), 741-750.

130. Chen, E. H.; Walter, S. R.; Nguyen, S. T.; Geiger, F. M., Arylsilanated SiOx Surfaces for Mild and Simple Two-Step Click Functionalization with Small Molecules and Oligonucleotides. *Journal of Physical Chemistry C* **2012,** *116* (37), 19886-19892.

131. Diaz, J. A.; Grewer, D. M.; Gibbs-Davis, J. M., Tuning Ratios, Densities, and Supramolecular Spacing in Bifunctional DNA-Modified Gold Nanoparticles. *Small* **2012,** *8* (6), 873-883.

132. Rekharsky, M. V.; Y., I., Complexation thermodynamic of cyclodextrins. *Chem. Rev.* **1998,** *98* (5), 1875-1917.

133. Schofield, W. C. E.; Bain, C. D.; Badyal, J. P. S., Cyclodextrin-Functionalized Hierarchical Porous Architectures for High-Throughput Capture and Release of Organic Pollutants from Wastewater. *Chem. Mat.* **2013,** *24* (9), 1645-1653.

134. Schofield, W. C. E.; Badyal, J. P. S., Controlled Fragrant Molecule Release from Surface-Tethered Cyclodextrin Host-Guest Inclusion Complexes. *ACS Appl. Mater. Interfaces* **2011,** *3* (6), 2051-2056.

135. Kellersberger, K. A.; Dejsupa, C.; Liang, Y. J.; Pope, R. M.; Dearden, D. V., Gas phase studies of ammonium-cyclodextrin compounds using Fourier transform ion cyclotron resonance. *Int. J. Mass Spectrom.* **1999,** *193* (2-3), 181-195.

136. Szejtli, J., Introduction and general overview of cyclodextrin chemistry. *Chem. Rev.* **1998,** *98* (5), 1743-1753.

137. Nad, S.; Kumbhakar, M.; Pal, H., Photophysical Properties of Coumarin-152 and Coumarin-481 Dyes: Unusual Behavior in Nonpolar and in Higher Polarity Solvents. *J. Phys. Chem. A* **2003,** *107* (24), 4808-4816.

138. Nad, S.; Pal, H., Unusual photophysical properties of coumarin-151. *J. Phys. Chem. A* **2001,** *105* (7), 1097-1106.

139. Roy, D.; Piontek, S.; Walker, R. A., Surface Induced Changes in Coumarin Solvation and Photochemistry at Polar Solid/Liquid Interfaces. *PCCP* **2011,** *13* (32), 14758-14766.

140. Ooshika, Y., Absorption Spectra of Dyes in Solution. *J. Phys. Soc. Jpn.* **1954,** *9* (4), 594-602.

141. McRae, E. G., Theory of Solvent Effects on Moplecular Electronic Spectra - Frequency Shifts. *J. Phys. Chem.* **1957,** *61* (5), 562-572.

142. Reynolds, L.; Gardecki, J. A.; Frankland, S. J. V.; Horng, M. L.; Maroncelli, M., Dipole Solvation in Nondipolar Solvents: Experimental Studies of Reorganization Energies and Solvation Dynamics. *J. Phys. Chem.* **1996,** *100* (24), 10337-10354.

143. Jones, G.; Jackson, W. R.; Kanoktanaporn, S., Solvent effects on photophysical parameters for coumarin laser-dyes. *Opt. Commun.* **1980,** *33* (3), 315-320.

144. Horng, M. L.; Gardecki, J. A.; Papazyan, A., Subpicosecond measurements of polar solvation dynamics. *J. Phys. Chem.* **1995,** *99* (48), 17311-17337.

145. Gardecki, J. A.; Maroncelli, M., Comparison of the single-wavelength and spectral-reconstruction methods for determining the solvation-response function. *J. Phys. Chem. A* **1999,** *103* (9), 1187-1197.

146. Jones, R. L.; Pearsall, N. C.; Batteas, J. D., Disorder in Alkylsilane Monolayers Assembled on Surfaces with Nanoscopic Curvature. *J. Phys. Chem. C* **2009,** *113* (11), 4507-4514.

147. Byun, H.-S.; Zhong, N.; Bittman, R., 6^{A}-O-P-Toluenesulfonyl-B-Cyclodextrin. *Org. Synth.* **2004,** *10*, 690.

148. Petter, R. C.; Salek, J. S.; Sikorski, C. T.; Kumaravel, G.; Lin, F. T., Cooperative Binding by Aggregated Mono-6-(Alkylamino)-Beta-Cyclodextrins. *J. Amer. Chem. Soc.* **1990,** *112* (10), 3860-3868.

149. Ortega-Munoz, M.; Lopez-Jaramillo, J.; Hernandez-Mateo, F.; Santoyo-Gonzalez, F., Synthesis of glyco-silicas by Cu(I)-catalyzed "click-chemistry" and their applications in affinity chromatography. *Adv. Syn. Catal.* **2006,** *348* (16-17), 2410-2420.

150. Wang, Y.; Xiao, Y.; Tan, T. T. Y.; Ng, S.-C., Click chemistry for facile immobilization of cyclodextrin derivatives onto silica as chiral stationary phases. *Tetrahedron Lett.* **2008,** *49* (35), 5190-5191.

151. Antoni, P.; Nystrom, D.; Hawker, C. J.; Hult, A.; Malkoch, M., A chemoselective approach for the accelerated synthesis of well-defined dendritic architectures. *Chem. Commun.* **2007,** (22), 2249-2251.

152. Choma, J.; Dziura, A.; Jamiola, D.; Nyga, P.; Jaroniec, M., Preparation and properties of silica-gold core-shell particles. *Colloids Surf., A* **2011,** *373* (1-3), 167-171.

153. Iliashevsky, O.; Amir, L.; Glaser, R.; Marks, R. S.; Lemcoff, N. G., Synthesis, characterization and protein binding properties of supported dendrons. *J. Mat. Chem.* **2009,** *19* (36), 6616-6622.

154. D'Acunzi, M.; Mammen, L.; Singh, M.; Deng, X.; Roth, M.; Auernhammer, G. K.; Butt, H.-J.; Vollmer, D., Superhydrophobic surfaces by hybrid raspberry-like particles. *Faraday Discussions* **2010,** *146*, 35-48.

155. Li, Z. B.; Rutan, S. C., Solvatochromic Studies of the Surface Polarity of Silica Under Normal-Phase Conditions. *Anal. Chim. Acta* **1995,** *312* (2), 127-139.

156. Richmond, G. L., Molecular bonding and interactions at aqueous surfaces as probed by vibrational sum frequency spectroscopy. *Chem. Rev.* **2002,** *102* (8), 2693-2724.

157. Bain, C. D., Sum-Frequency Vibrational Spectroscopy of the Solid/Liquid Interface. *Journal of the Chemical Society Faraday Transactions* **1995,** *91* (9), 1281-1296.

158. Lambert, A. G.; Davies, P. B.; Neivandt, D. J., Implementing the theory of sum frequency generation vibrational spectroscopy: A tutorial review. *Appl. Spec. Rev.* **2005,** *40* (2), 103-145.

159. Gobrogge, E. A.; Woods, B. L.; Walker, R. A., Liquid organization and solvation properties at polar solid/liquid interfaces. *Faraday Discussions* **2013,** *167*, 309-327.

160. Ding, F.; Zhong, Q.; Brindza, M. R.; Fourkas, J. T.; Walker, R. A., Ti:sapphire, broadband vibrational sum-frequency generation spectrometer with a counter-propagating geometry. *Opt. Express* **2009,** *17* (17), 14665-14675.

161. Li, X. Q.; Messmer, M. C., Comparison of model monomeric and polymeric alkyl stationary phases on silica using sum-frequency spectroscopy. *J. Chromatogr. A* **2003,** *984* (1), 19-28.

162. Huisgen, R.; Bayer, H. O.; Schaefer, F. C.; Gotthardt, H., New Type of Mesoionic Aromatic Compound and its 1,3-Dipolar Cycloaddition Reactions with Acetylene Derivatives. *Angew. Chem. Int. Ed.* **1964,** *3* (2), 136-137.

163. G. Beamson, D. B., *High resolution XPS of organic polymers: The Scienta ESCA 300 database.* John Wiley & Sons: Chichester, 1992; p 295.

164. Ciampi, S.; Boecking, T.; Kilian, K. A.; James, M.; Harper, J. B.; Gooding, J. J., Functionalization of acetylene-terminated monolayers on Si(100) surfaces: A click chemistry approach. *Langmuir* **2007,** *23* (18), 9320-9329.

165. Liu, X.; Zheng, H.-N.; Ma, Y.-Z.; Yan, Q.; Xiao, S.-J., Microwave irradiated click reactions on silicon surfaces via derivertization of covalently grafted poly(PEGMA) brushes. *Journal of colloid and interface science* **2011,** *358* (1), 116-122.

166. Neubauer, R.; Whelan, C. M.; Denecke, R.; Steinruck, H. P., The thermal chemistry of saturated layers of acetylene and ethylene on Ni(100) studied by in situ synchrotron x-ray photoelectron spectroscopy. *J. Chem. Phys.* **2003,** *119* (3), 1710-1718.

167. Liu, X.; Zheng, H.-N.; Ma, Y.-Z.; Yan, Q.; Xiao, S.-J., Microwave irradiated click reactions on silicon surfaces via derivertization of covalently grafted poly(PEGMA) brushes. *J. Colloid Interface Sci.* **2011,** *358* (1), 116-122.

168. Daugaard, A. E.; Hvilsted, S.; Hansen, T. S.; Larsen, N. B., Conductive polymer functionalization by click chemistry. *Macromolecules* **2008,** *41* (12), 4321-4327.

169. Freire, C. S. R.; Silvestre, A. J. D.; Neto, C. P.; Gandini, A.; Fardim, P.; Holmbom, B., Surface characterization by XPS, contact angle measurements and ToF-SIMS of cellulose fibers partially esterified with fatty acids. *J. Colloid Interface Sci.* **2006,** *301* (1), 205-209.

170. Belgacem, M. N.; Czeremuszkin, G.; Sapieha, S.; Gandini, A., Surface characterization of cellulose fibres by XPS and inverse gas chromatography. *Cellulose* **1995,** *2* (3), 145-157.

171. Moses, P. R.; Wier, L. M.; Lennox, J. C.; Finklea, H. O.; Lenhard, J. R.; Murray, R. W., Chemically Modified Electrodes .9. X-Ray Photoelectron-Spectroscopy of Alkylamine-Silanes Bound to Metal-Oxide Electrodes. *Anal. Chem.* **1978,** *50* (4), 576-585.

172. Hooper, A. E.; Werho, D.; Hopson, T.; Palmer, O., Evaluation of amine- and amide-terminated self-assembled monolayers as 'Molecular glues' for Au and SiO2 substrates. *Surf. Interface Anal.* **2001,** *31* (9), 809-814.

173. Li, W.; Lu, B.; Sheng, A.; Yang, F.; Wang, Z., Spectroscopic and theoretical study on inclusion complexation of beta-cyclodextrin with permethrin. *J. Mol. Struct.* **2010,** *981* (1-3), 194-203.

174. L'Abbé, G.; Beenaerts, L., Influence of electron-withdrawing N-1 substituents on the thermal behaviour of 5-azido-1,2,3-triazoles. *Tetrahedron* **1989,** *45* (3), 749-756.

175. Ennist, J. H.; Gobrogge, E. A.; Schlick, K. H.; Walker, R. A.; Cloninger, M. J., Cyclodextrin-Functionalized Chromatographic Materials Tailored for Reversible Adsorption. *ACS Applied Materials & Interfaces* **2014,** *6* (20), 18087-18097.

176. Grimes, K. D.; Gupte, A.; Aldrich, C. C., Copper(II)-Catalyzed Conversion of Aryl/Heteroaryl Boronic Acids, Boronates, and Trifluoroborates into the Corresponding Azides: Substrate Scope and Limitations. *Synthesis* **2010,** *2010* (09), 1441-1448.

177. Lee, M.-S.; Park, M.; Kim, H. Y.; Park, S.-J., Effects of Microporosity and Surface Chemistry on Separation Performances of N-Containing Pitch-Based Activated Carbons for CO2/N2 Binary Mixture. *Scientific Reports* **2016,** *6*, 23224.

178. Colombano, G.; Travelli, C.; Galli, U.; Caldarelli, A.; Chini, M. G.; Canonico, P. L.; Sorba, G.; Bifulco, G.; Tron, G. C.; Genazzani, A. A., A Novel Potent Nicotinamide Phosphoribosyltransferase Inhibitor Synthesized via Click Chemistry. *Journal of Medicinal Chemistry* **2009,** *53* (2), 616-623.

179. Schirwitz, C., *Purification of peptides in high-complexity arrays:a new method for the specific surface exchange and purification of entire peptide libraries* Springer: Cham, New York, 2013; p 132.

180. Barazzouk, S.; Daneault, C., Amino Acid and Peptide Immobilization on Oxidized Nanocellulose: Spectroscopic Characterization. *Nanomaterials* **2012,** *2* (2), 187-205.

181. Ramanathan, T.; Fisher, F. T.; Ruoff, R. S.; Brinson, L. C., Amino-Functionalized Carbon Nanotubes for Binding to Polymers and Biological Systems. *Chemistry of Materials* **2005,** *17* (6), 1290-1295.

182. Ahire, J. H.; Wang, Q.; Coxon, P. R.; Malhotra, G.; Brydson, R.; Chen, R.; Chao, Y., Highly Luminescent and Nontoxic Amine-Capped Nanoparticles from Porous Silicon: Synthesis and Their Use in Biomedical Imaging. *ACS Applied Materials & Interfaces* **2012,** *4* (6), 3285-3292.

183. Graf, N.; Yegen, E.; Gross, T.; Lippitz, A.; Weigel, W.; Krakert, S.; Terfort, A.; Unger, W. E. S., XPS and NEXAFS studies of aliphatic and aromatic amine species on functionalized surfaces. *Surface Science* **2009,** *603* (18), 2849-2860.

184. Choma, J.; Dziura, A.; Jamiola, D.; Nyga, P.; Jaroniec, M., Preparation and properties of silica-gold core-shell particles. *Colloids and Surfaces a-Physicochemical and Engineering Aspects* **2011,** *373* (1-3), 167-171.

185. Iliashevsky, O.; Amir, L.; Glaser, R.; Marks, R. S.; Lemcoff, N. G., Synthesis, characterization and protein binding properties of supported dendrons. *Journal of Materials Chemistry* **2009,** *19* (36), 6616-6622.

186. Lundquist; Pelletier, J. C., Improved Solid-Phase Peptide Synthesis Method Utilizing α-Azide-Protected Amino Acids. *Organic Letters* **2001,** *3* (5), 781-783.

187. Fields, G. B., Methods for Removing the Fmoc Group. In *Peptide Synthesis Protocols*, Pennington, M. W.; Dunn, B. M., Eds. Humana Press: Totowa, NJ, 1995; pp 17-27.

188. Carpino, L. A.; Han, G. Y., 9-Fluorenylmethoxycarbonyl amino-protecting group. *The Journal of Organic Chemistry* **1972,** *37* (22), 3404-3409.

189. Link, A. J.; Vink, M. K. S.; Tirrell, D. A., Presentation and Detection of Azide Functionality in Bacterial Cell Surface Proteins. *Journal of the American Chemical Society* **2004,** *126* (34), 10598-10602.

190. Battistini, L.; Burreddu, P.; Carta, P.; Rassu, G.; Auzzas, L.; Curti, C.; Zanardi, F.; Manzoni, L.; Araldi, E. M. V.; Scolastico, C.; Casiraghi, G., 4-Aminoproline-based arginine-glycine-aspartate integrin binders with exposed ligation points: practical in-solution synthesis, conjugation and binding affinity evaluation. *Organic & Biomolecular Chemistry* **2009,** *7* (23), 4924-4935.

191. Tarbell, D. S.; Yamamoto, Y.; Pope, B. M., New Method to Prepare N-t-Butoxycarbonyl Derivatives and the Corresponding Sulfur Analogs from di-t-Butyl Dicarbonate or di-t-Butyl Dithiol Dicarbonates and Amino Acids. *Proceedings of the National Academy of Sciences of the United States of America* **1972,** *69* (3), 730-732.

192. Walton, J.; Wincott, P.; Fairley, N.; Carrick, A., Peak Fitting with CasaXPS. Accolyte Science: Knutsford, UK, 2010.

APPENDICES

APPENDIX A

RELEVANT SPECTRAL DATA FROM CHAPTER TWO

Spectral Data

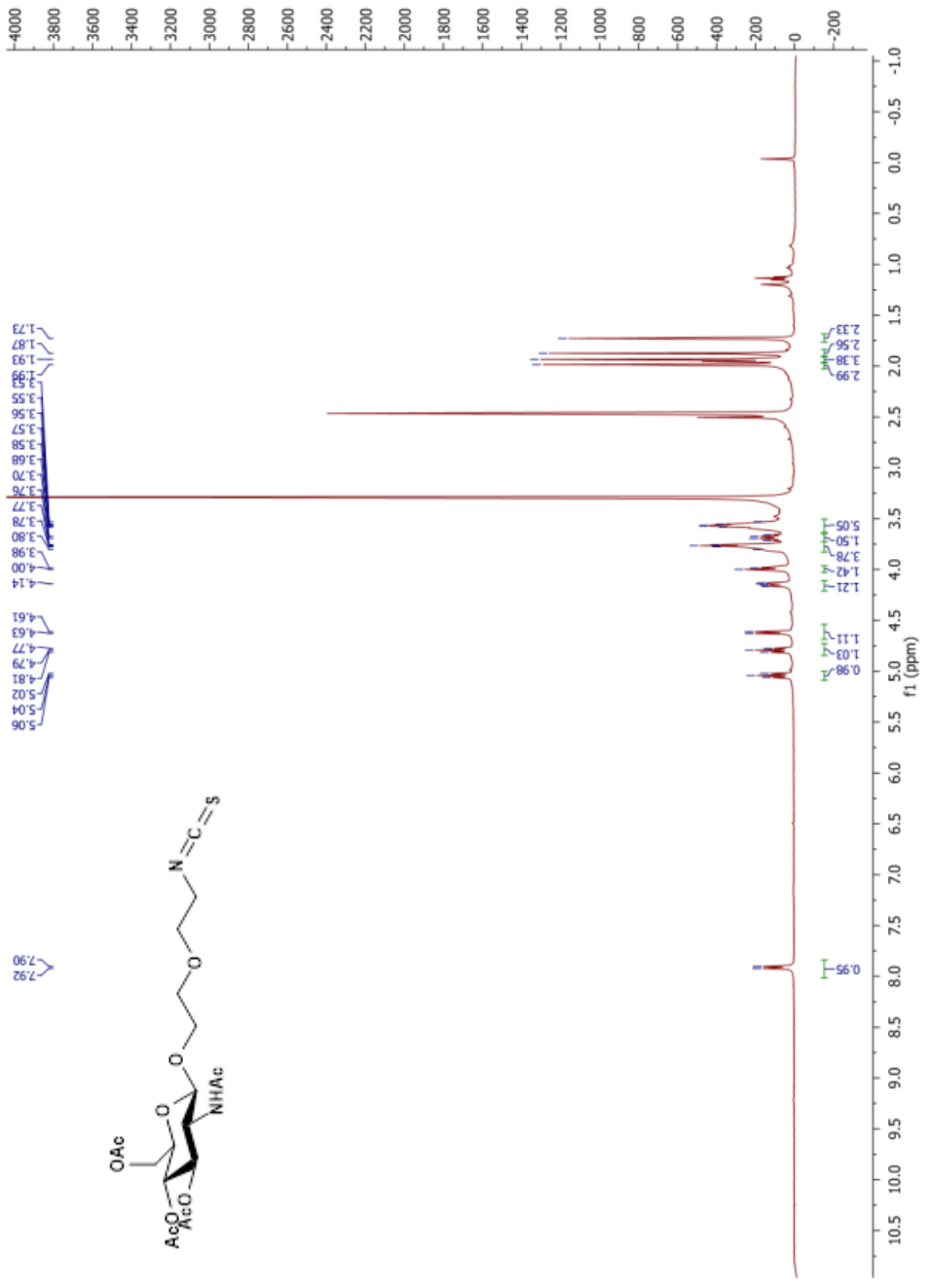

Figure 28: ^{1}H NMR spectrum (500 MHz, d_6-DMSO) of **3**.

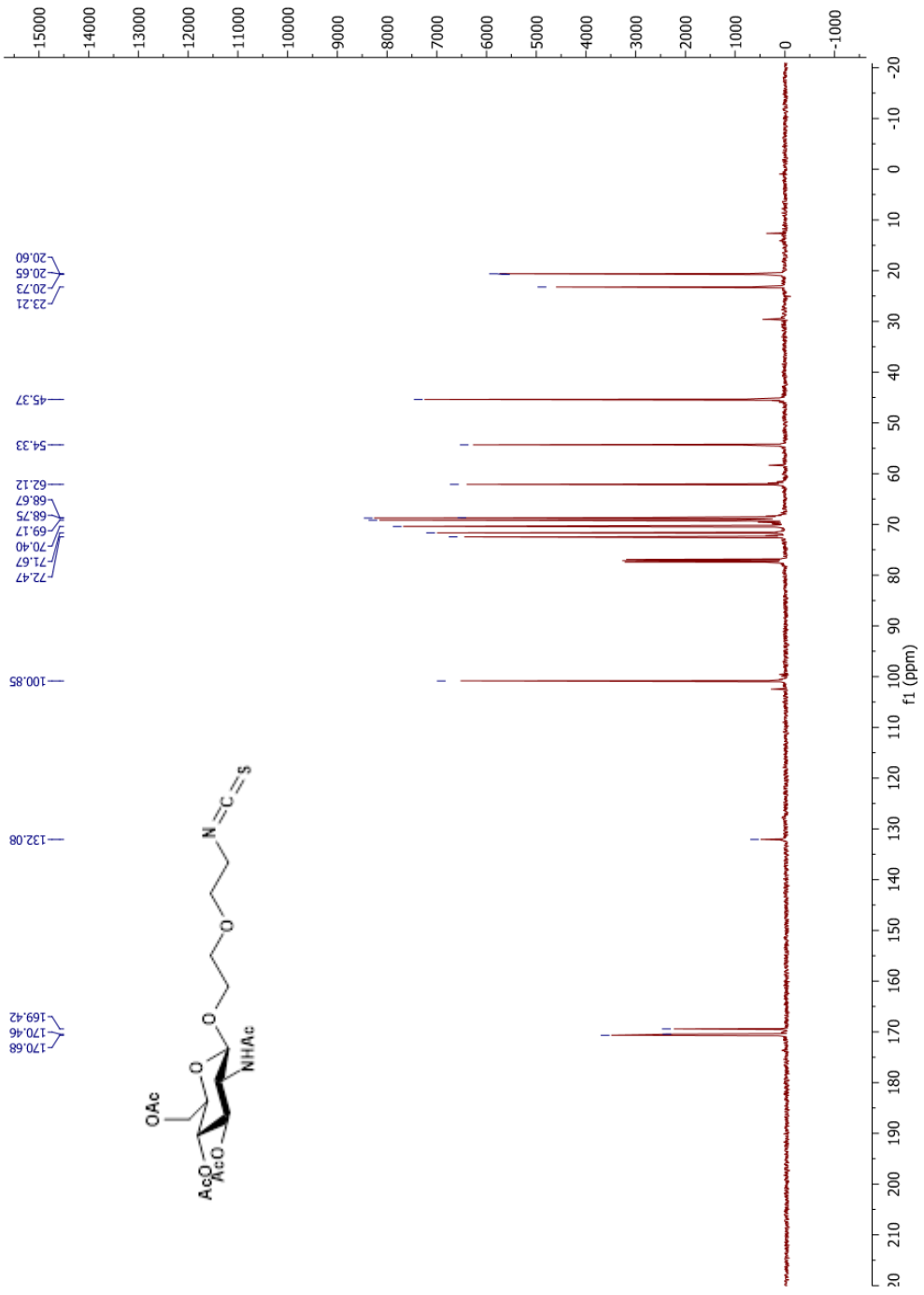

Figure 29: ^{13}C NMR spectrum (126 MHz, $CDCl_3$) of **3**.

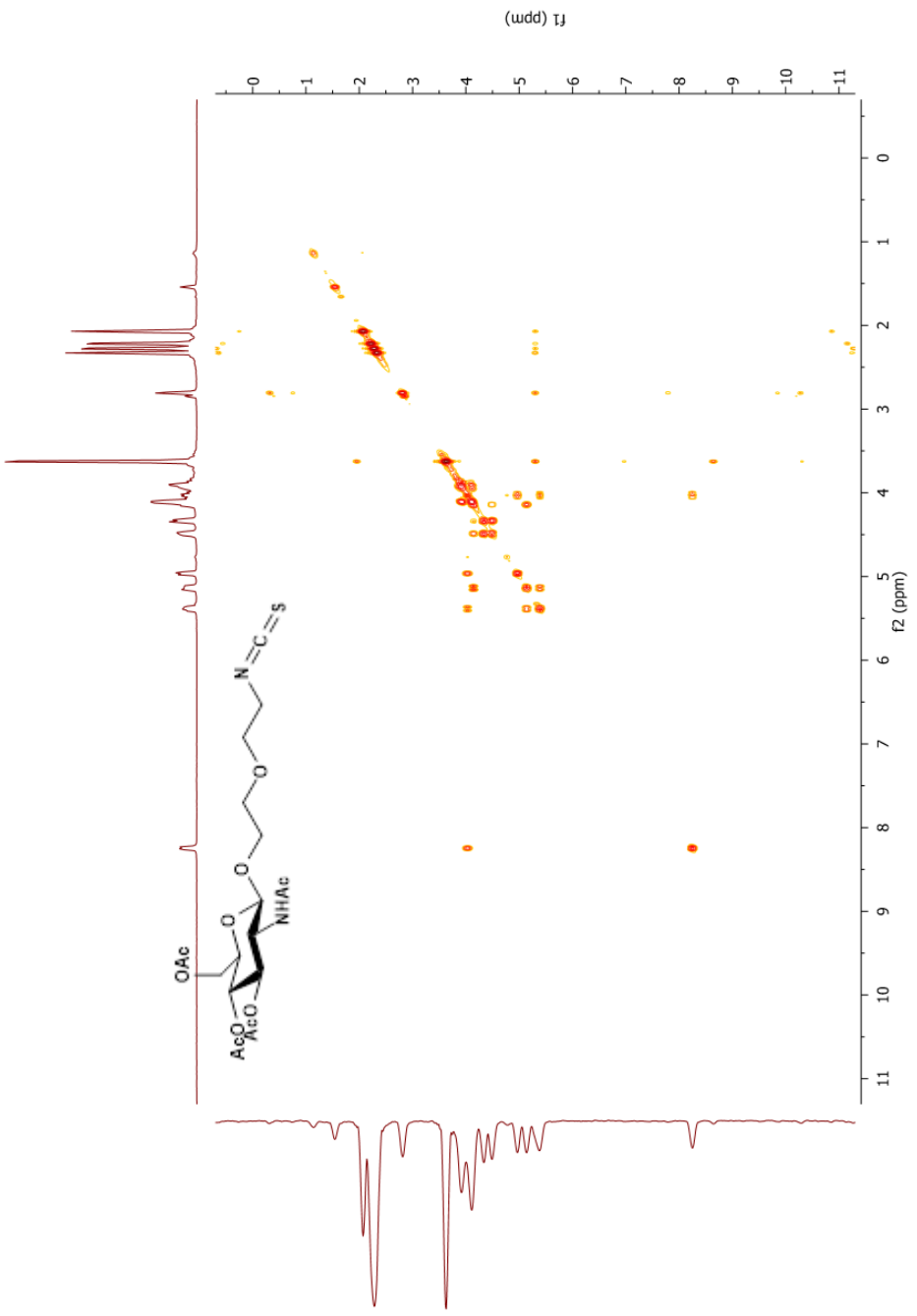

Figure 30: H-^{1}H COSY spectrum (500 MHz, d_6-DMSO) of **3.**

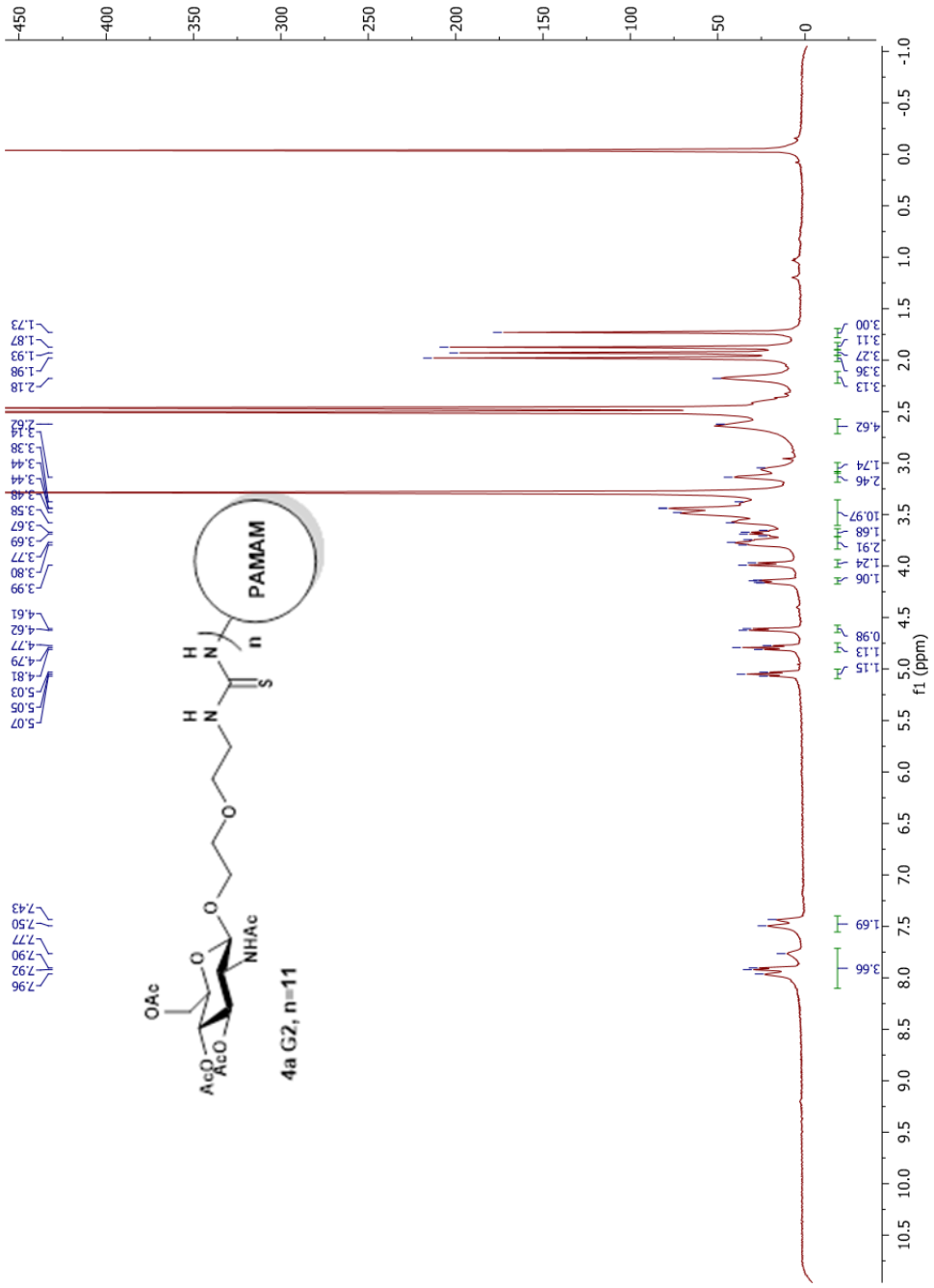

Figure 31: ^{1}H NMR spectrum (500 MHz, d_6-DMSO) of **4a**.

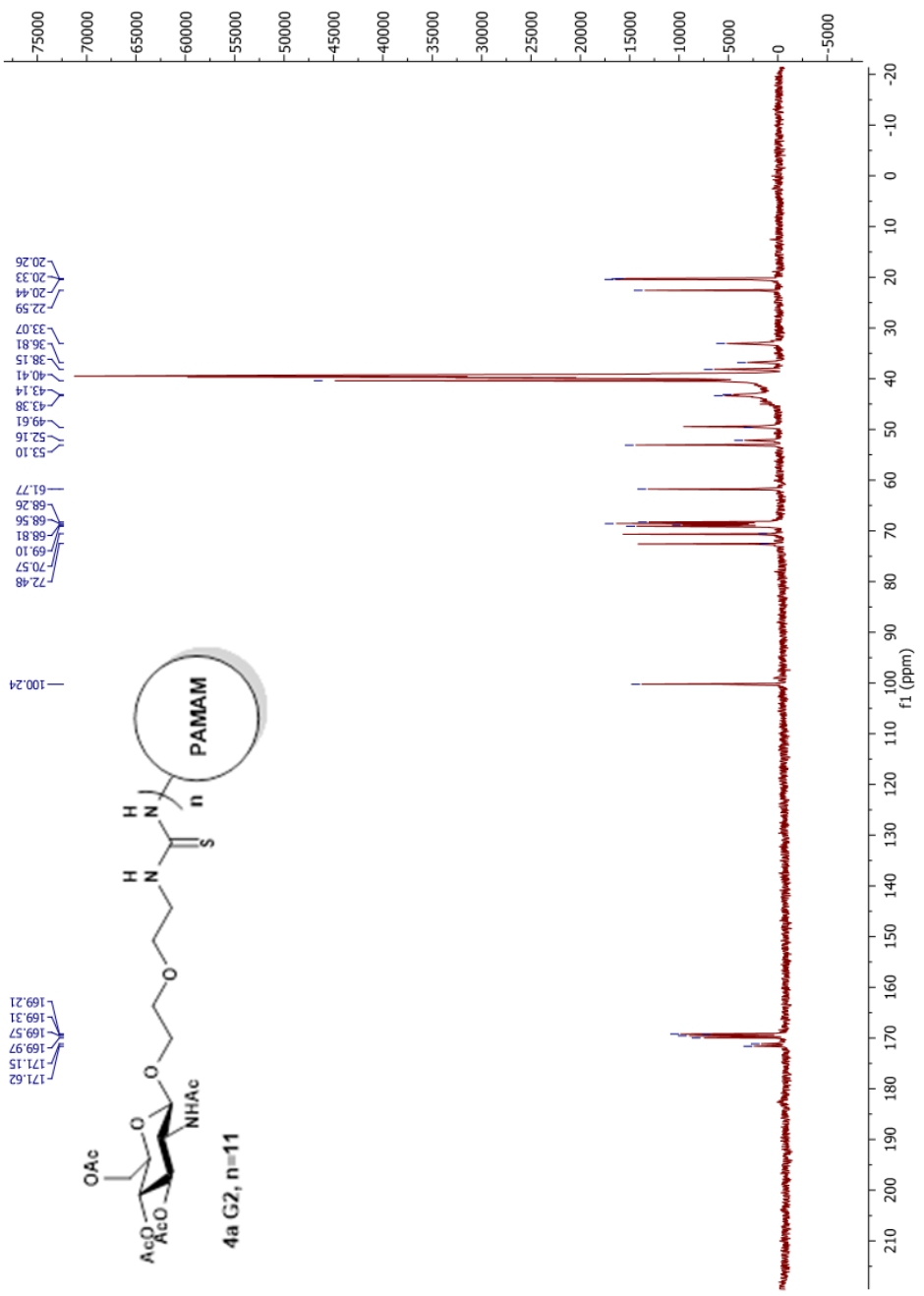

Figure 32: ^{13}C NMR spectrum (126 MHz, d_6-DMSO) of **4a**.

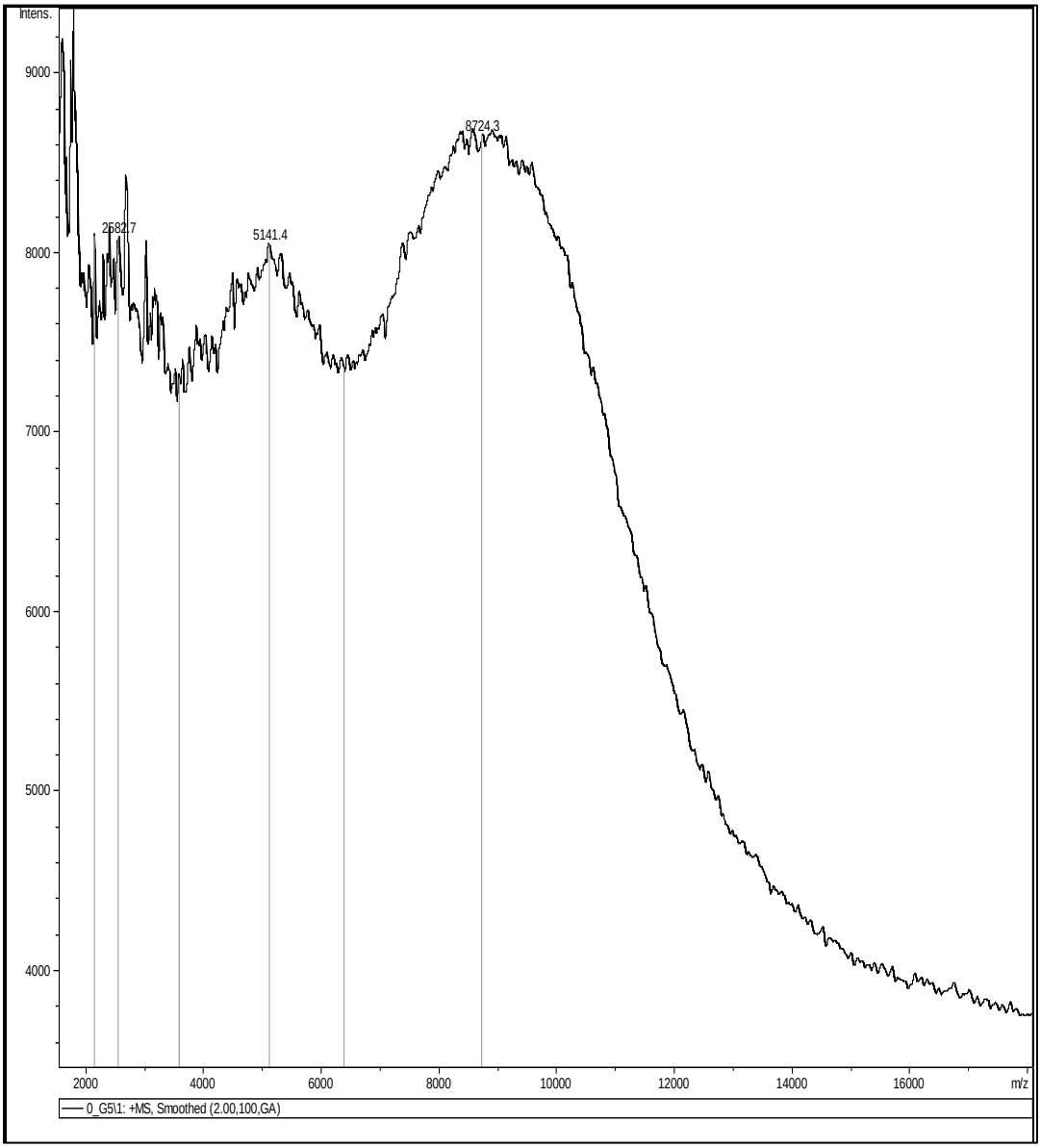

Figure 33: Smoothed MALDI TOF spectrum for compound **4a**. M_w = 8,300

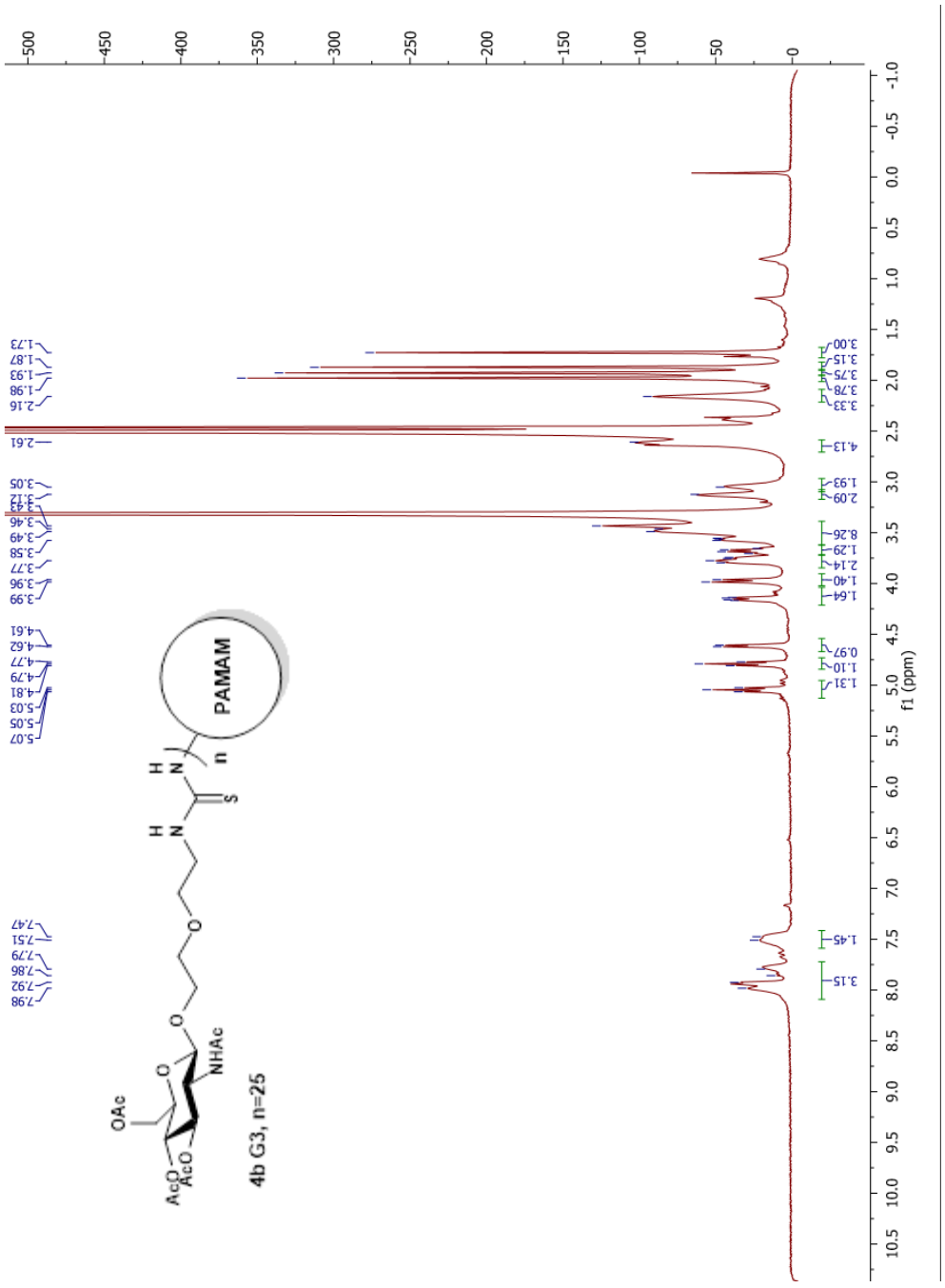

Figure 34: ^{1}H NMR spectrum (500 MHz, d_6-DMSO) of **4b**.

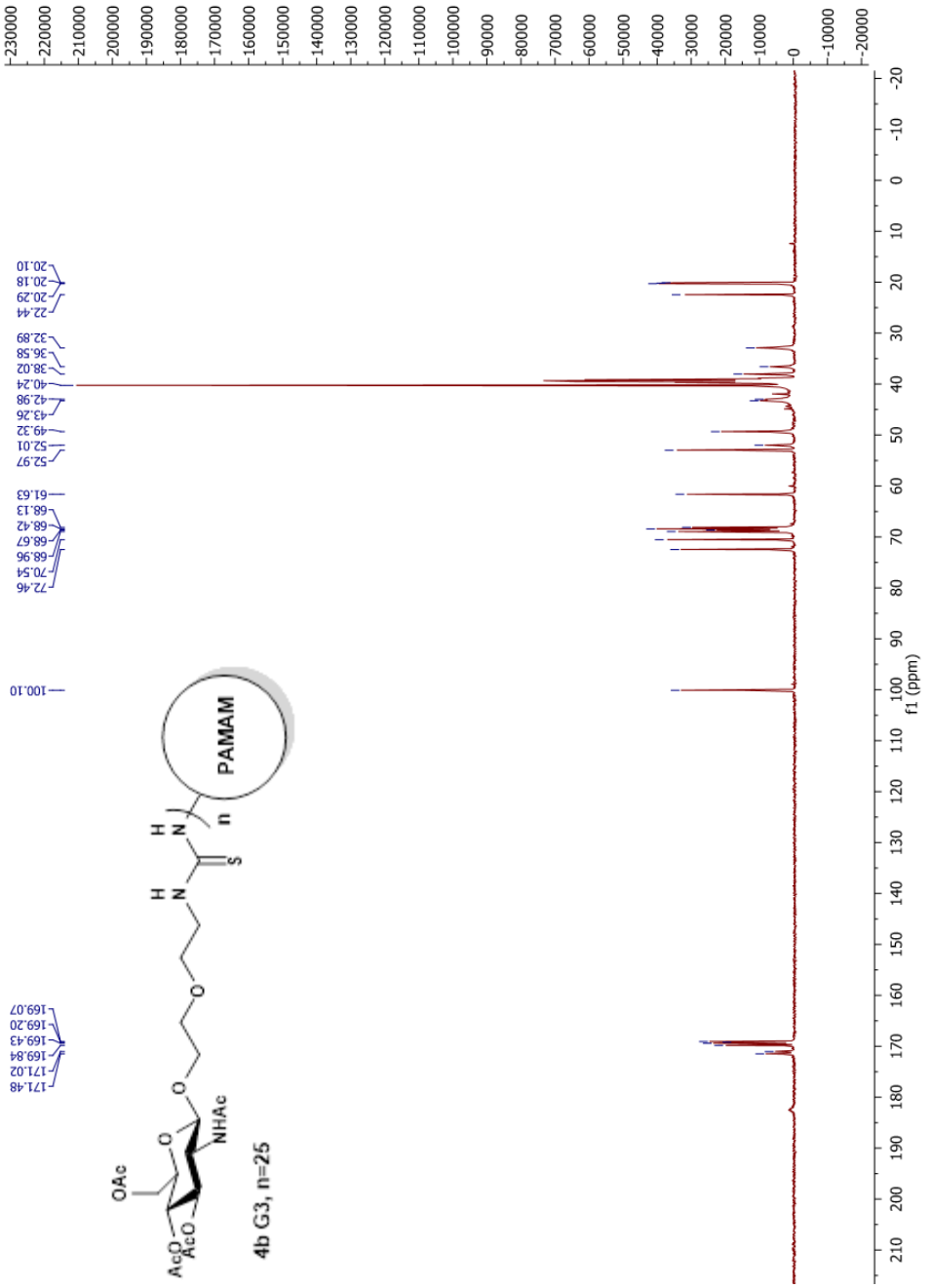

Figure 35: ^{13}C NMR spectrum (126 MHz, d_6-DMSO) of **4b**.

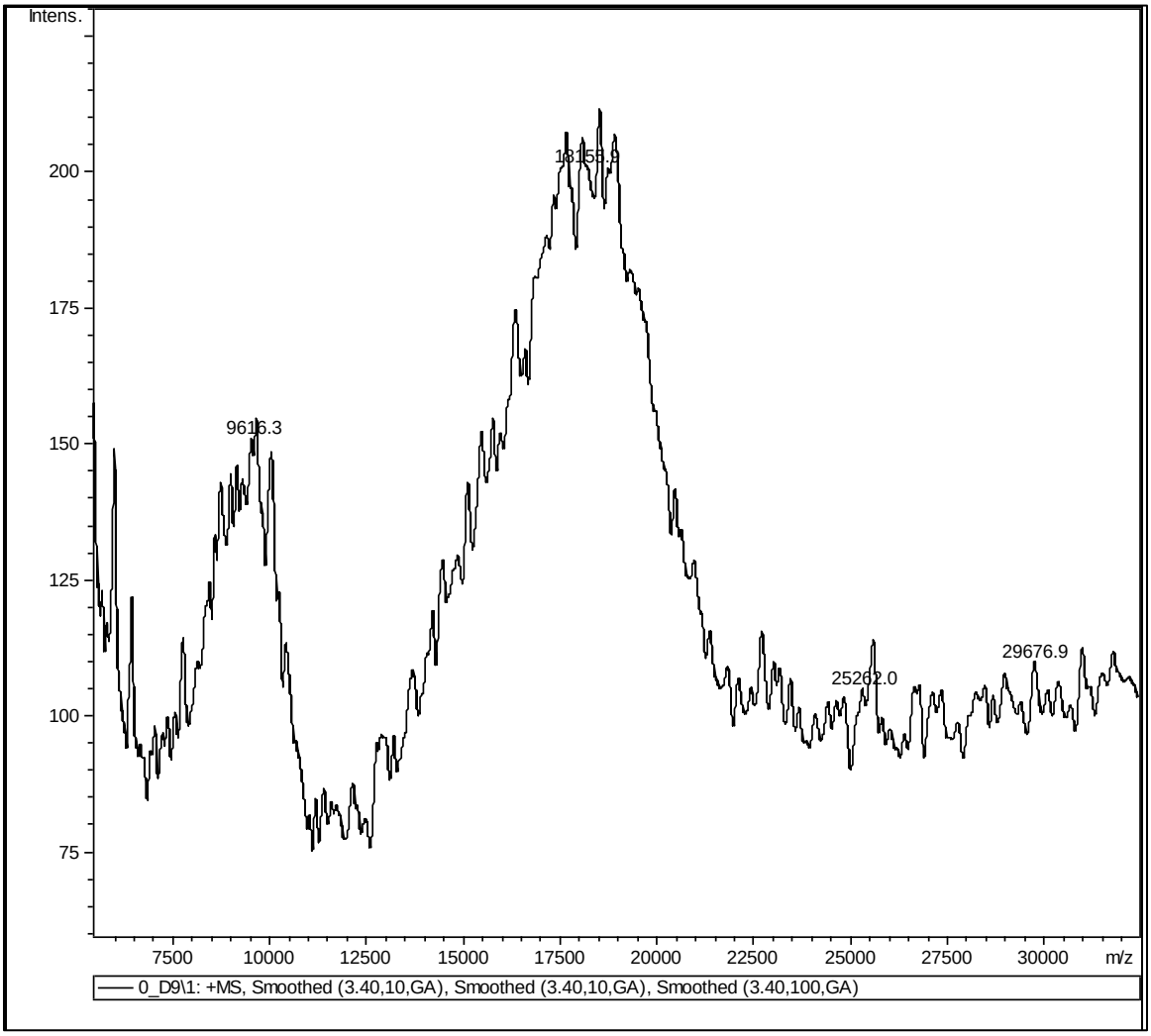

Figure 36: Smoothed MALDI TOF spectrum for compound **4b**. M_w = 17,800

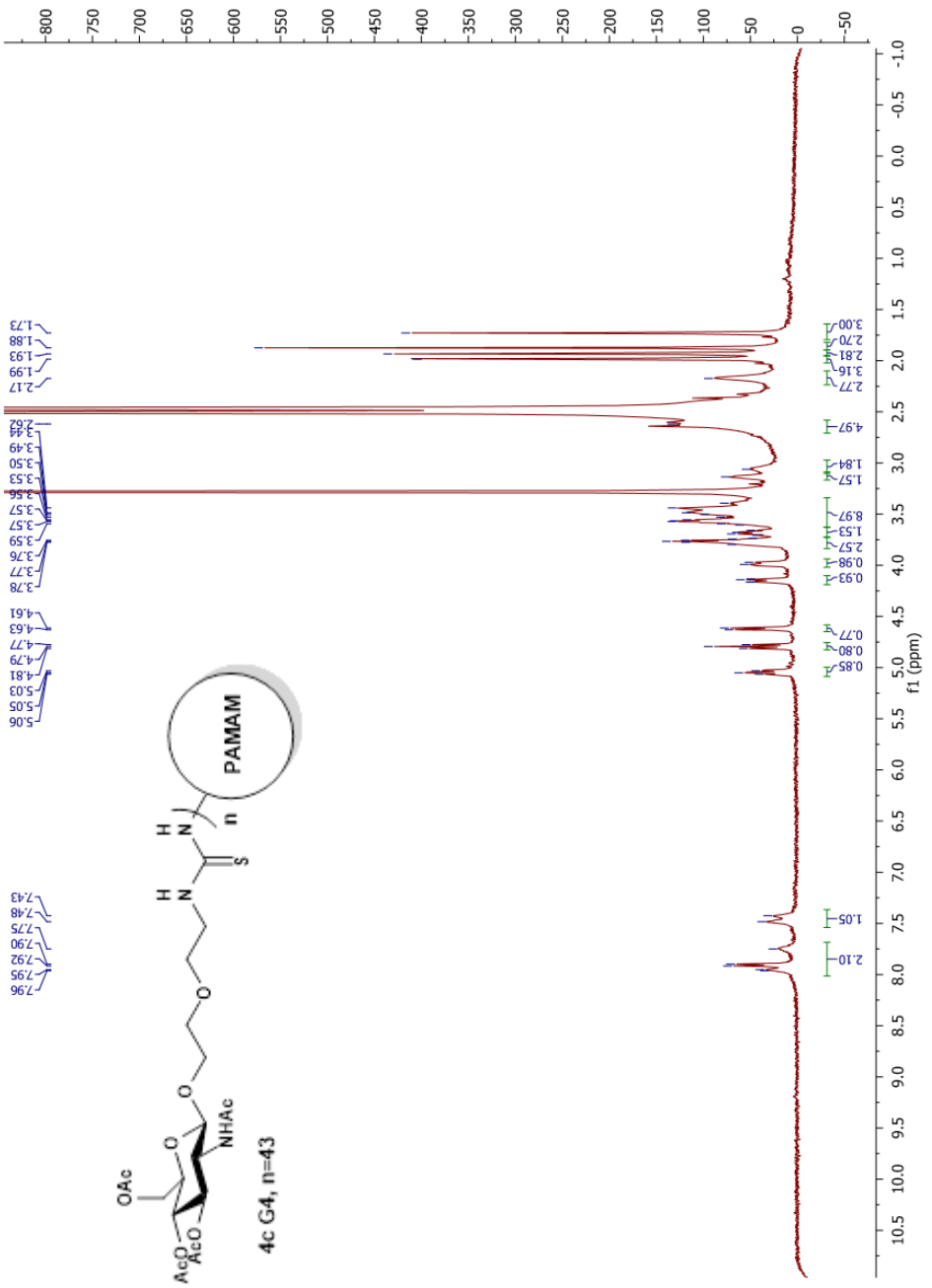

Figure 37: ^{1}H NMR spectrum (500 MHz, d_6-DMSO) of **4c**.

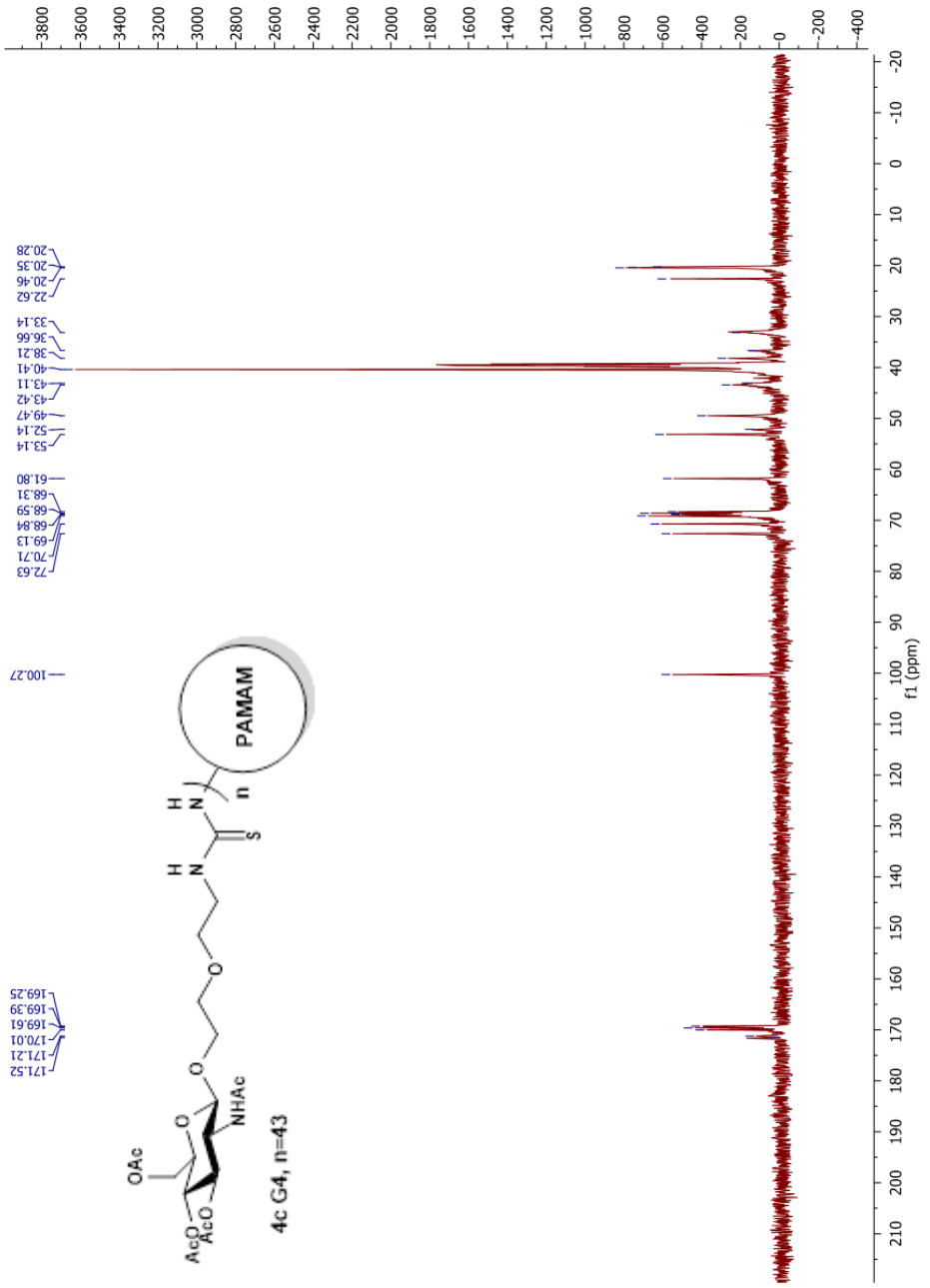

Figure 38: ^{13}C NMR spectrum (126 MHz, d_6-DMSO) of **4c**.

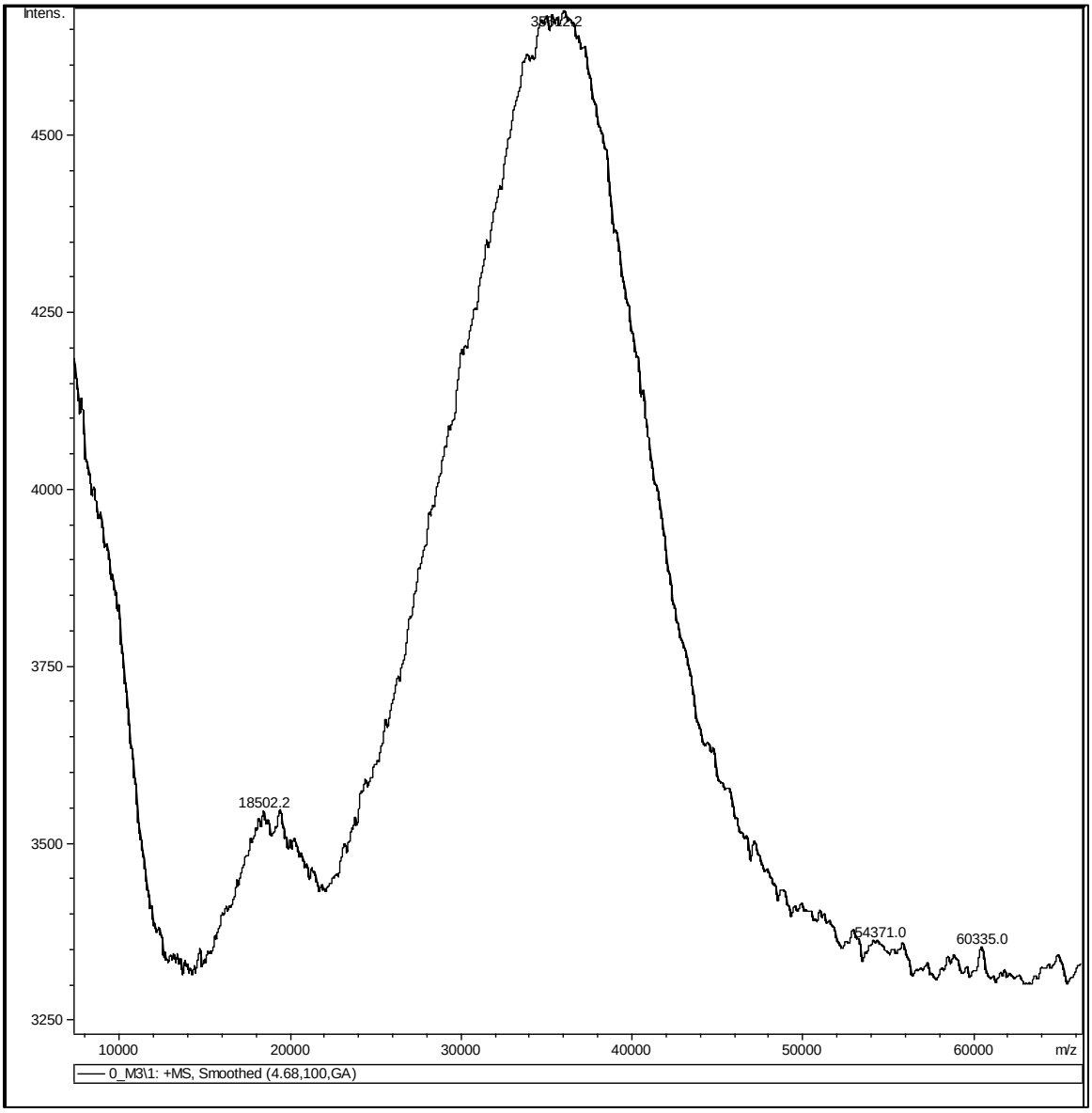

Figure 39: Smoothed MALDI TOF spectrum for compound **4c**. M_w = 35,000

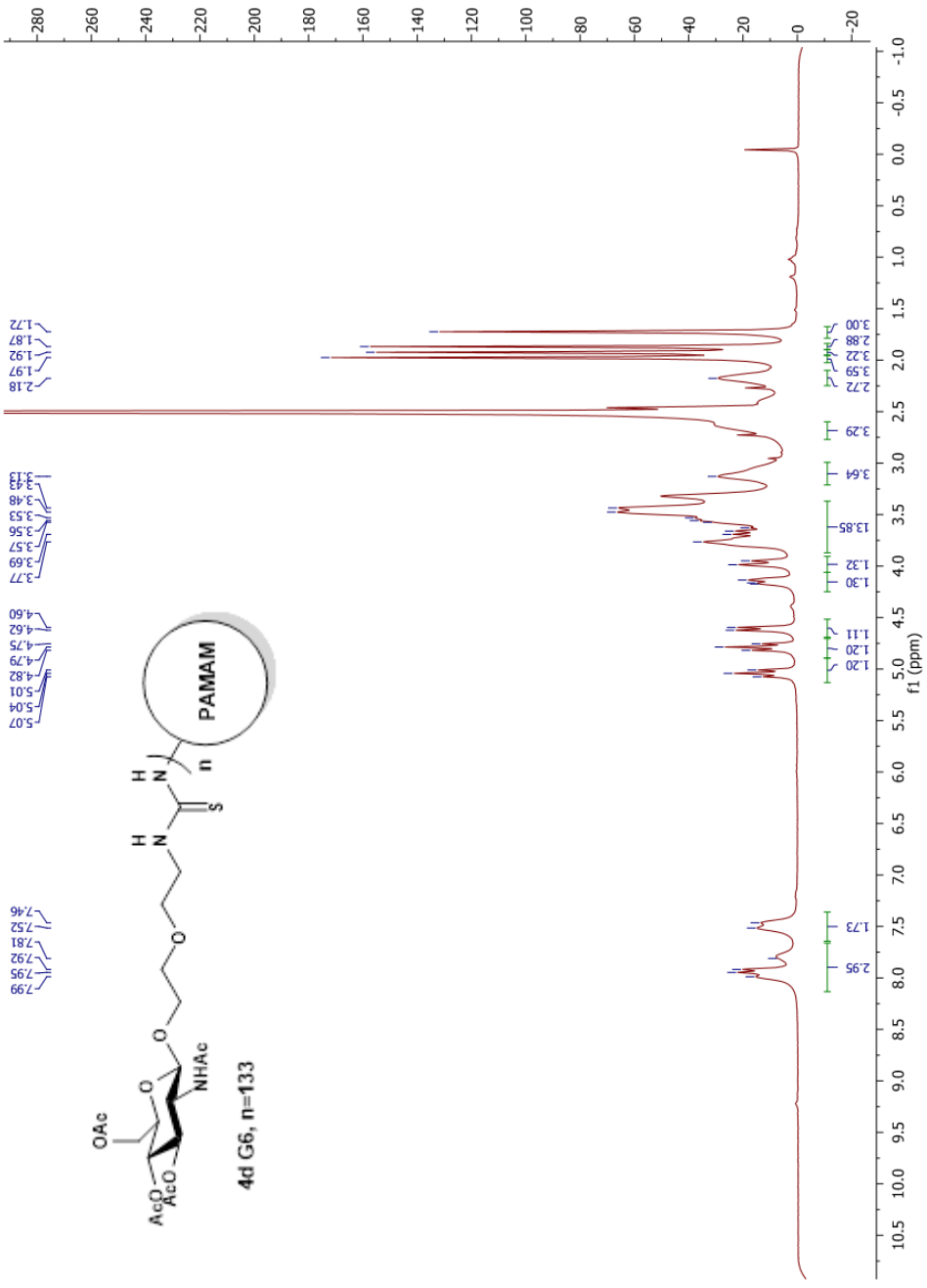

Figure 40: ^{1}H NMR spectrum (500 MHz, d_6-DMSO) of **4d**.

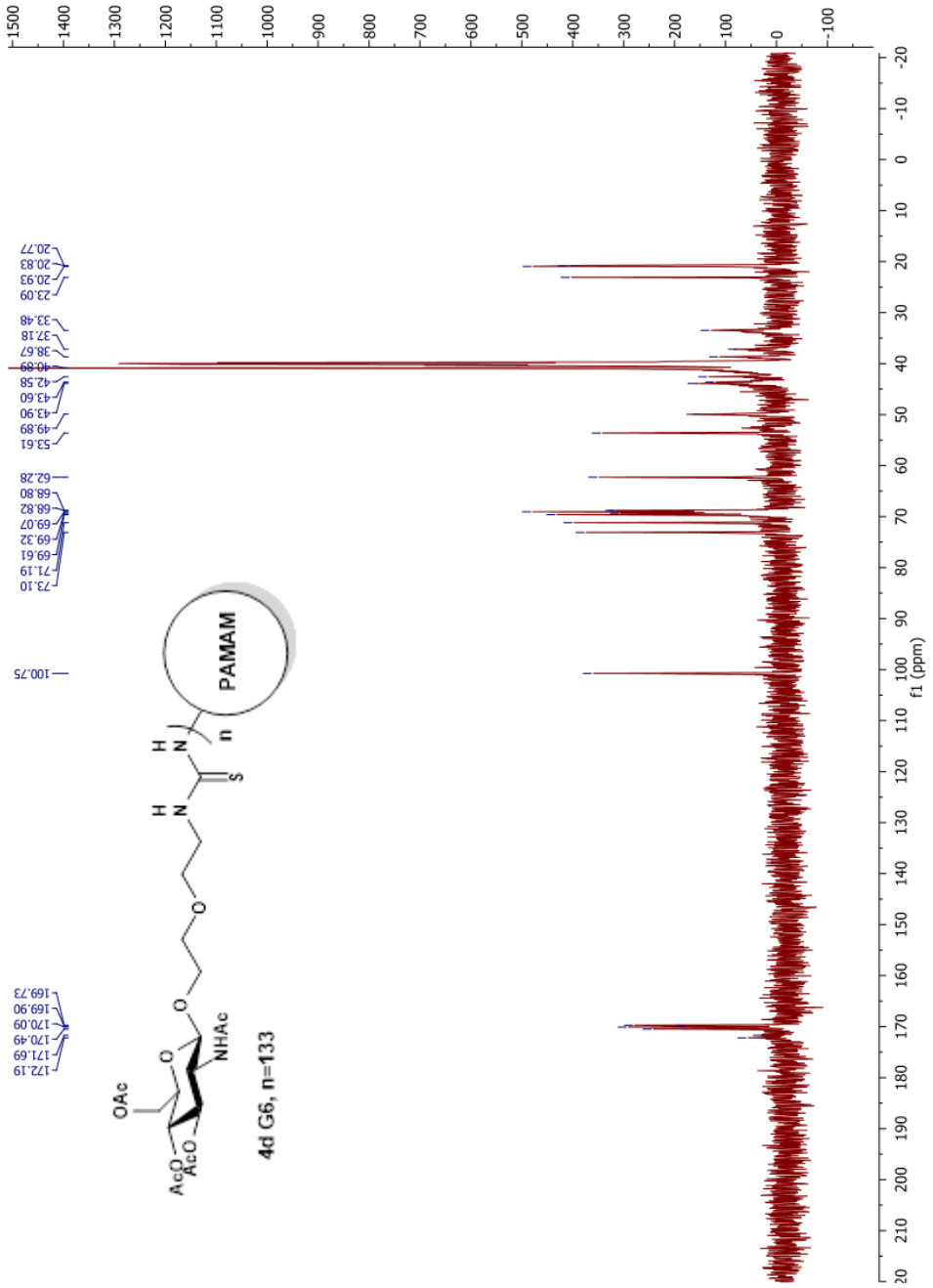

Figure 41: ^{13}C NMR spectrum (126 MHz, d_6-DMSO) of **4d**.

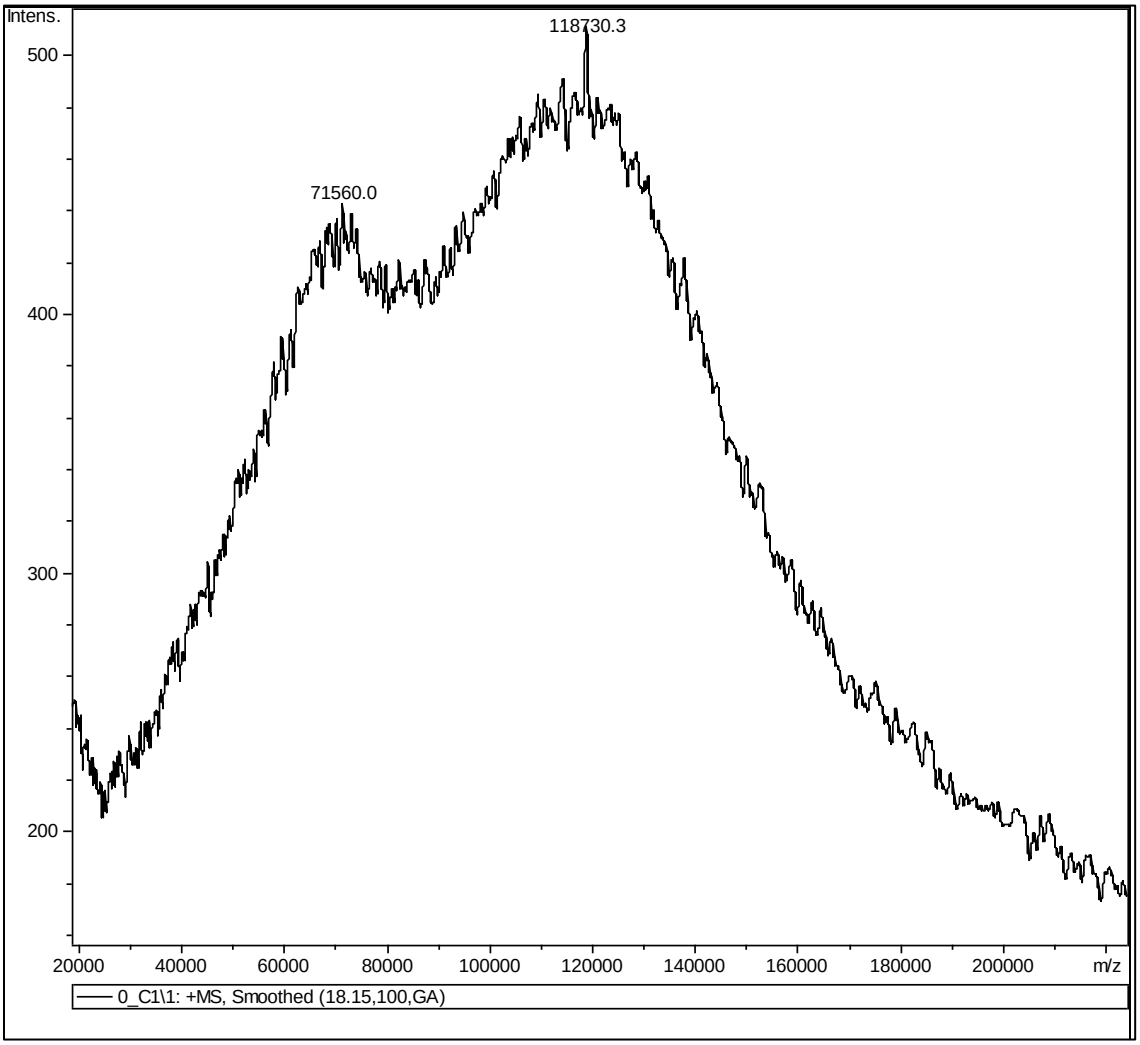

Figure 42: Smoothed MALDI TOF spectrum for compound **4d**. M_w = 119,600

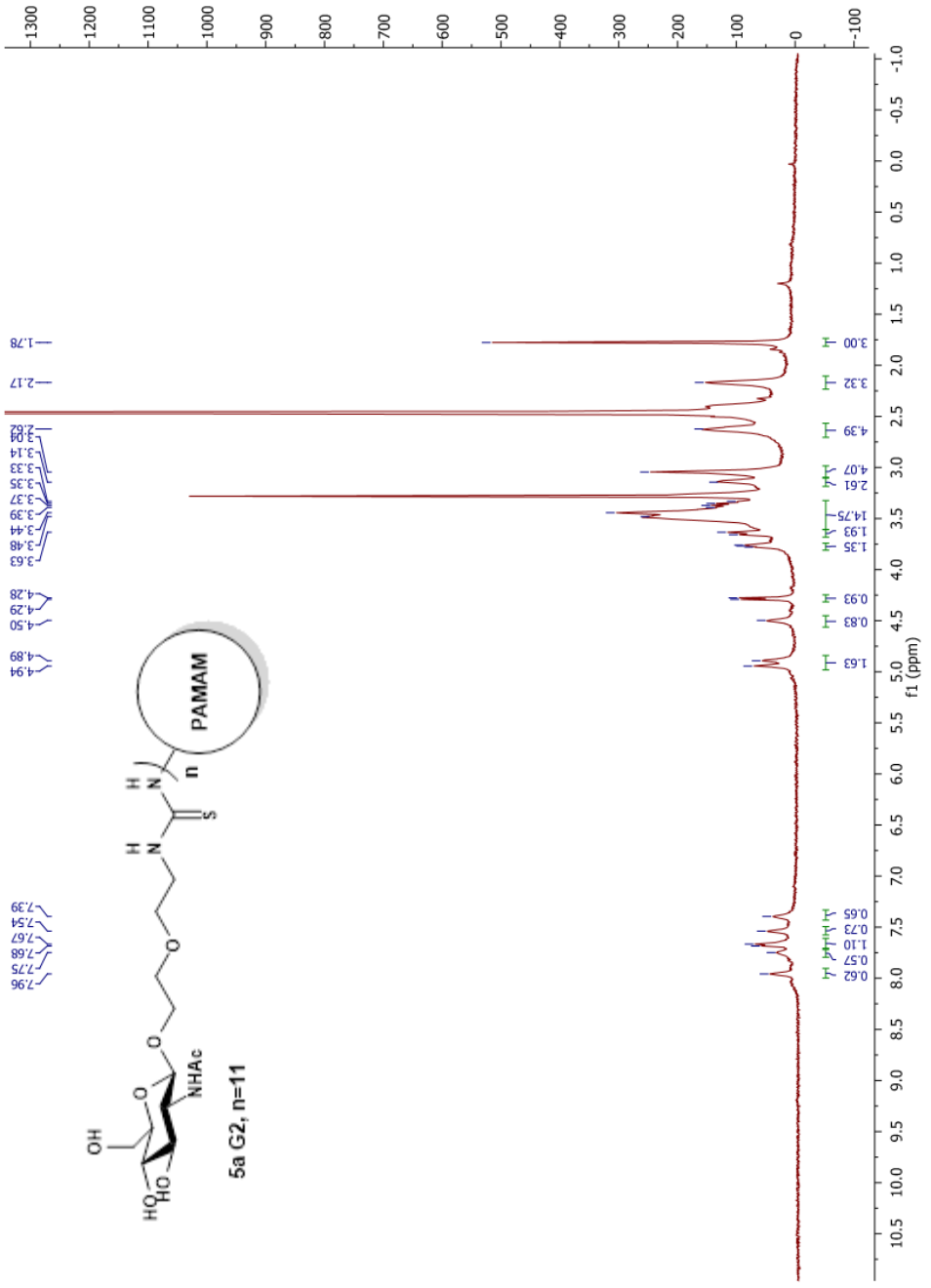

Figure 43: ^{1}H NMR spectrum (500 MHz, d_6-DMSO) of **5a**.

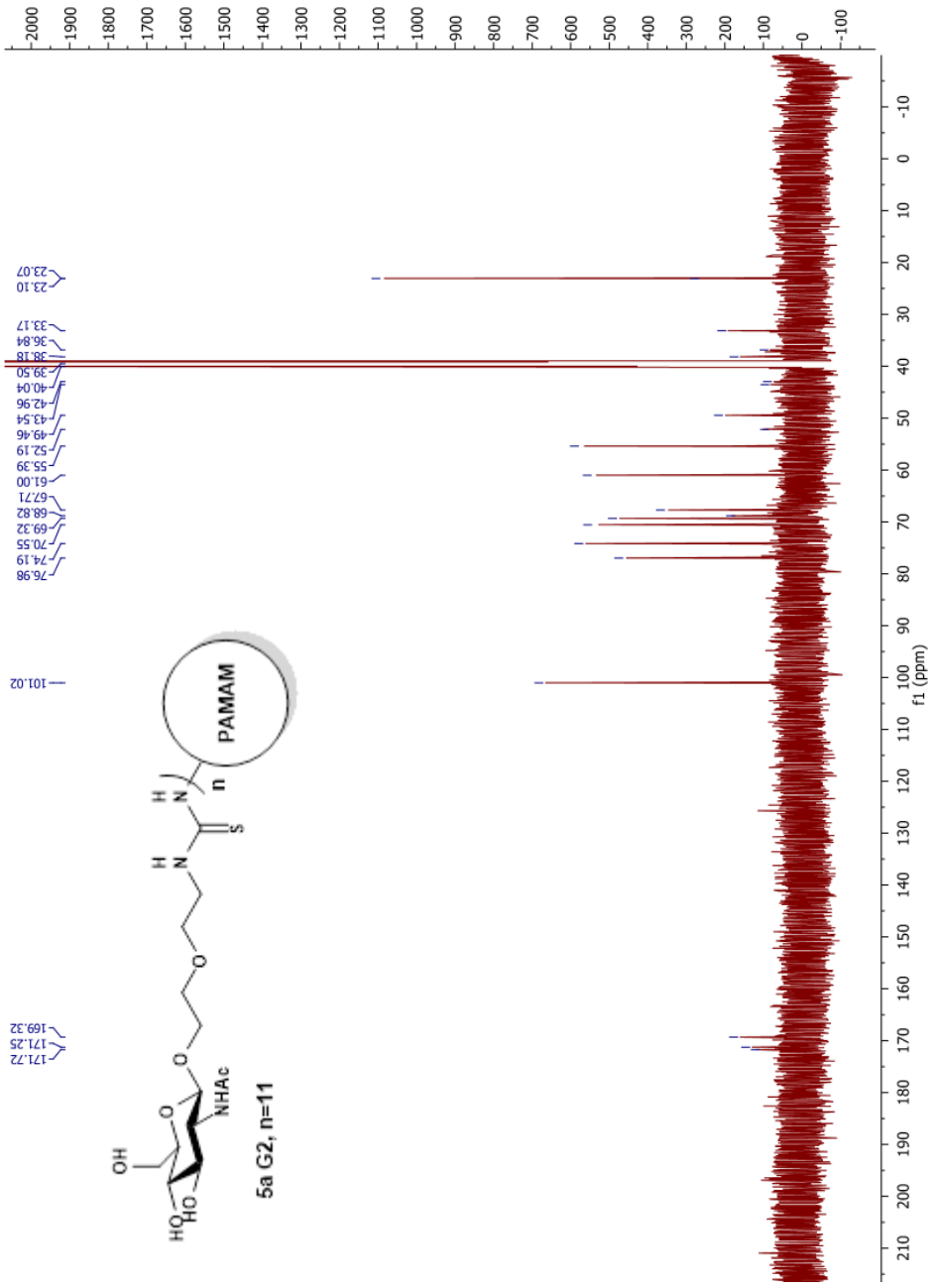

Figure 44: ^{13}C NMR spectrum (126 MHz, d_6-DMSO) of **5a**.

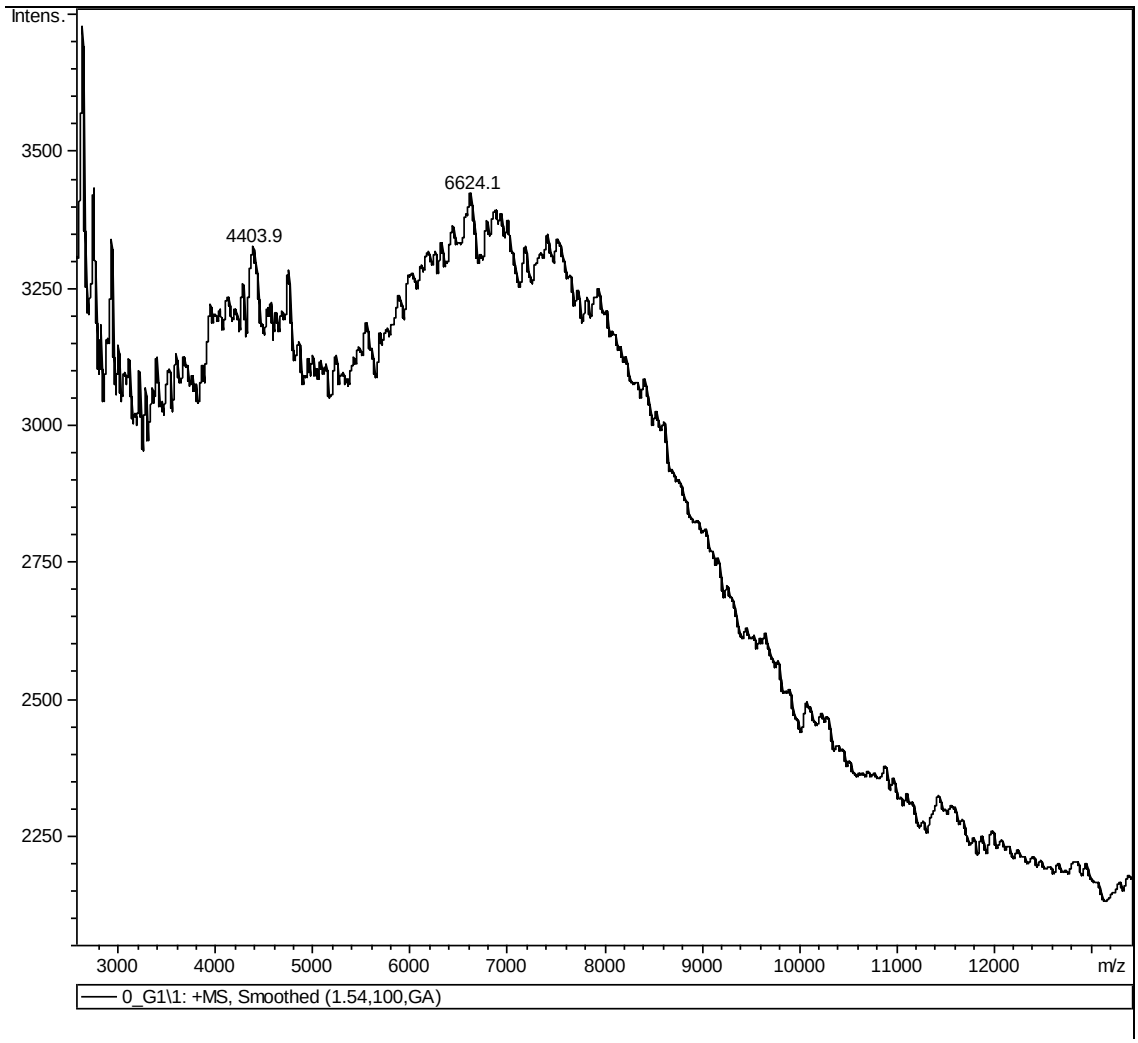

Figure 45: Smoothed MALDI TOF spectrum for compound **5a**. M_w = 7,000

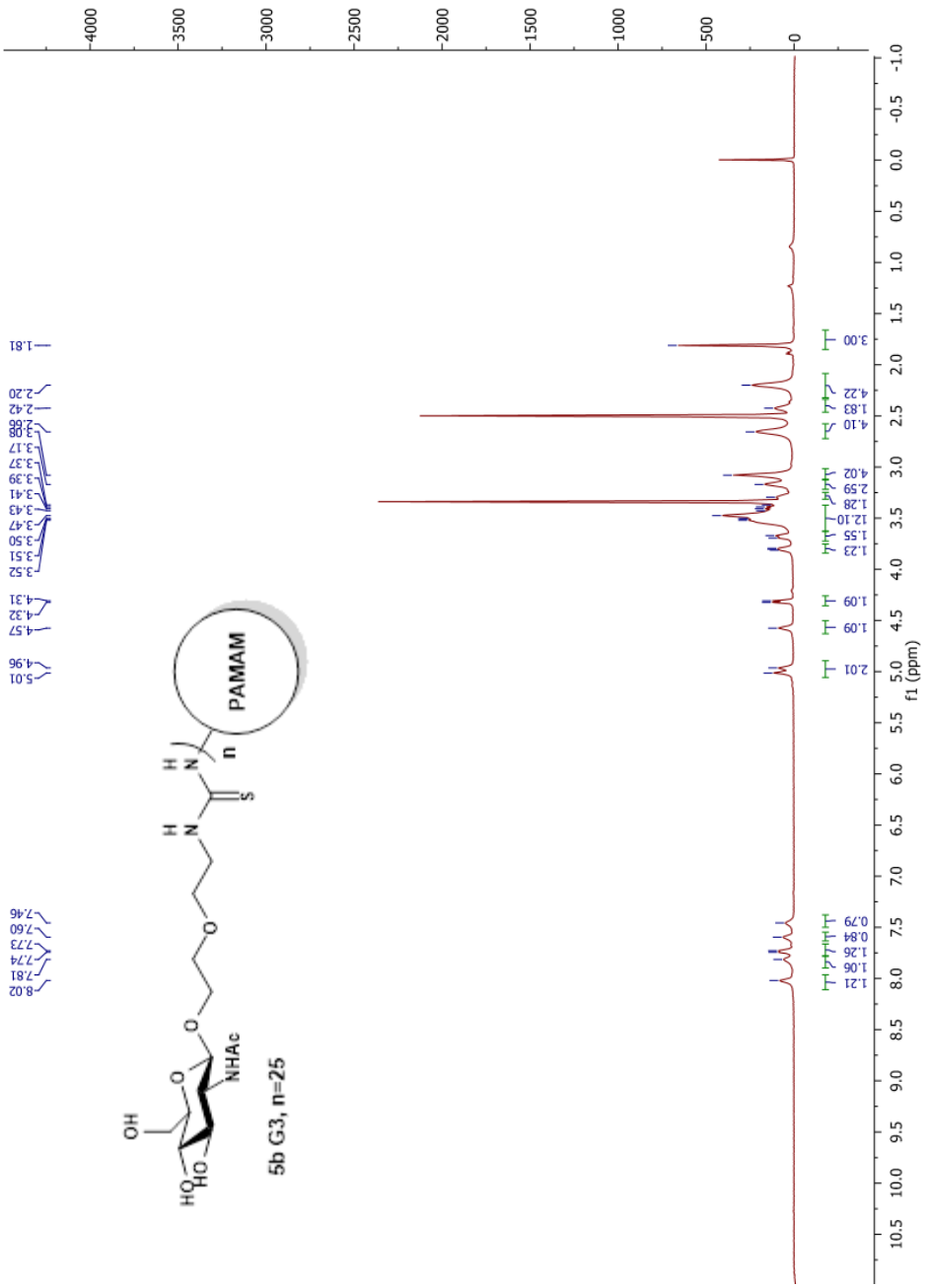

Figure 46: ^{1}H NMR spectrum (500 MHz, d_6-DMSO) of **5b**.

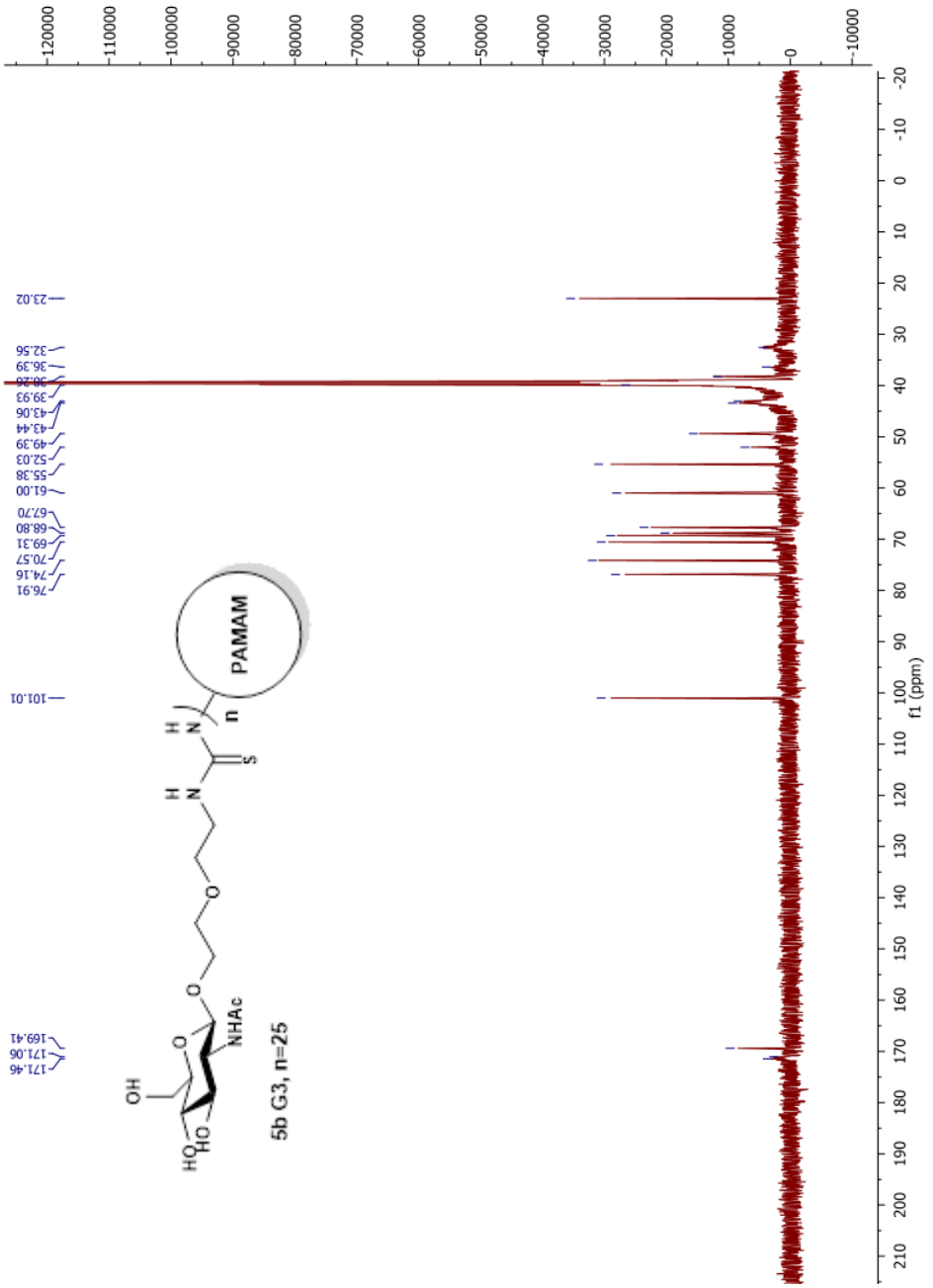

Figure 47: ^{13}C NMR spectrum (126 MHz, d_6-DMSO) of **5b**.

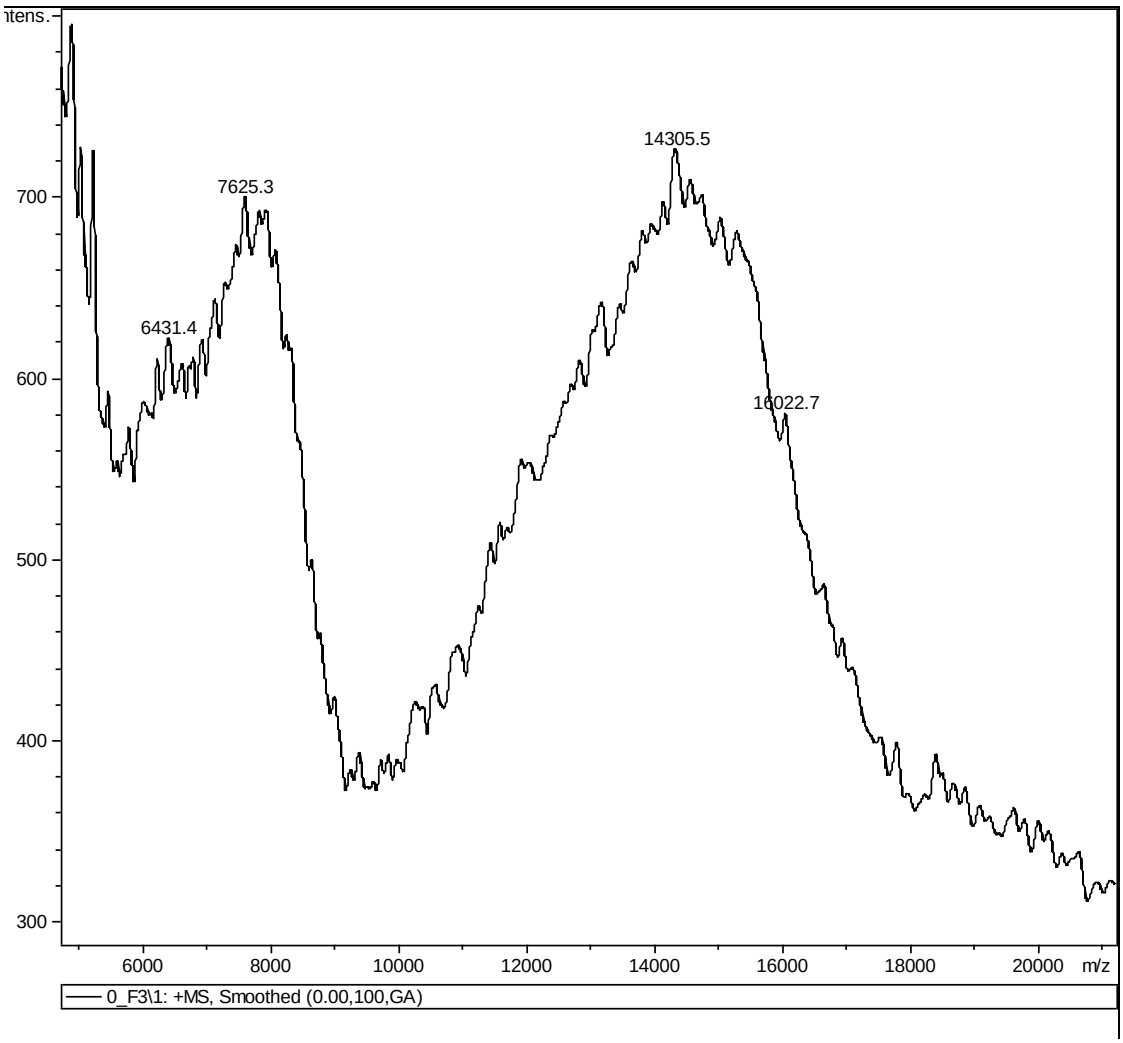

Figure 48: Smoothed MALDI TOF spectrum for compound **5b**. M_w = 14,100

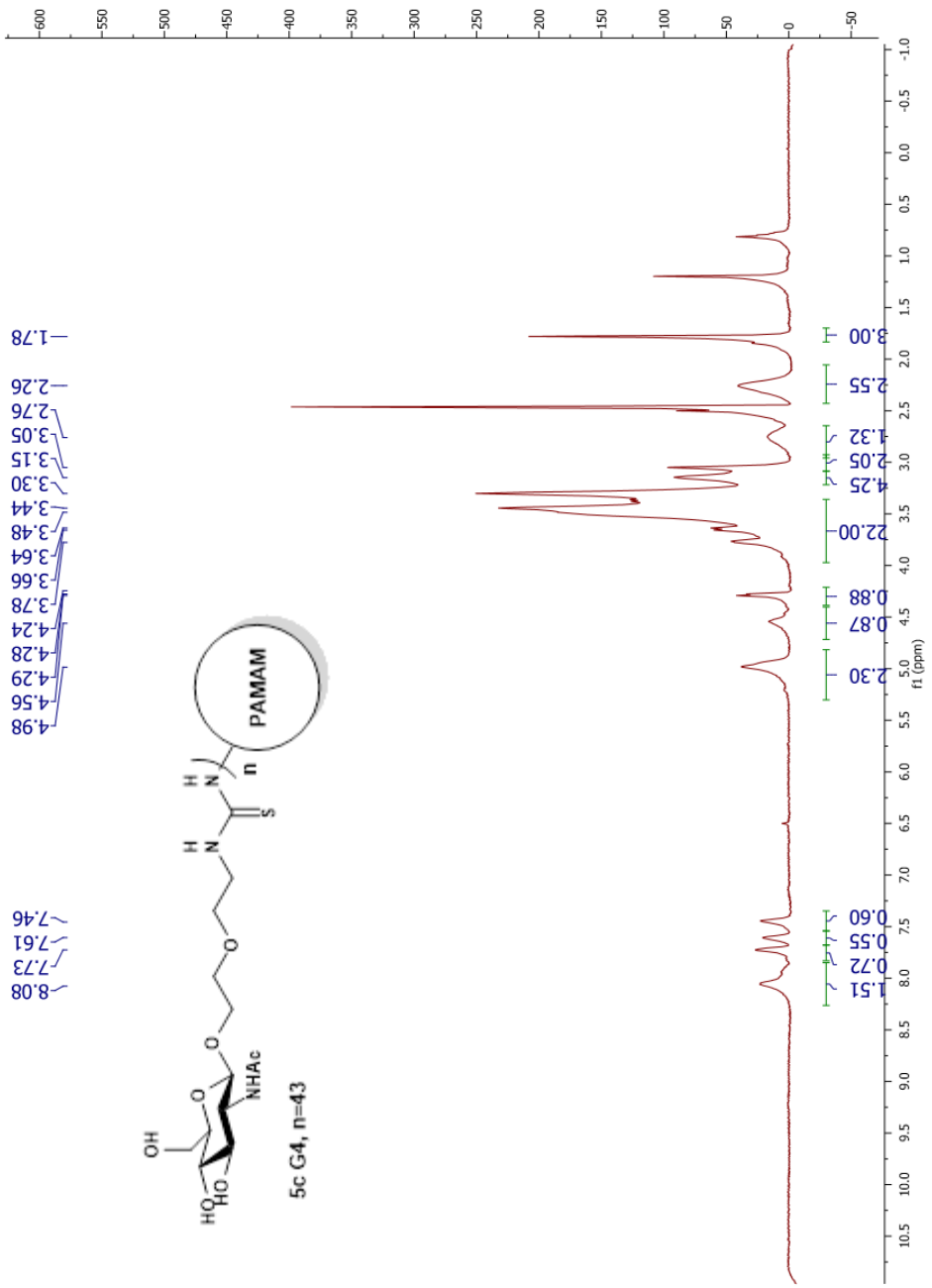

Figure 49: ^{1}H NMR spectrum (500 MHz, d_6-DMSO) of **5c**.

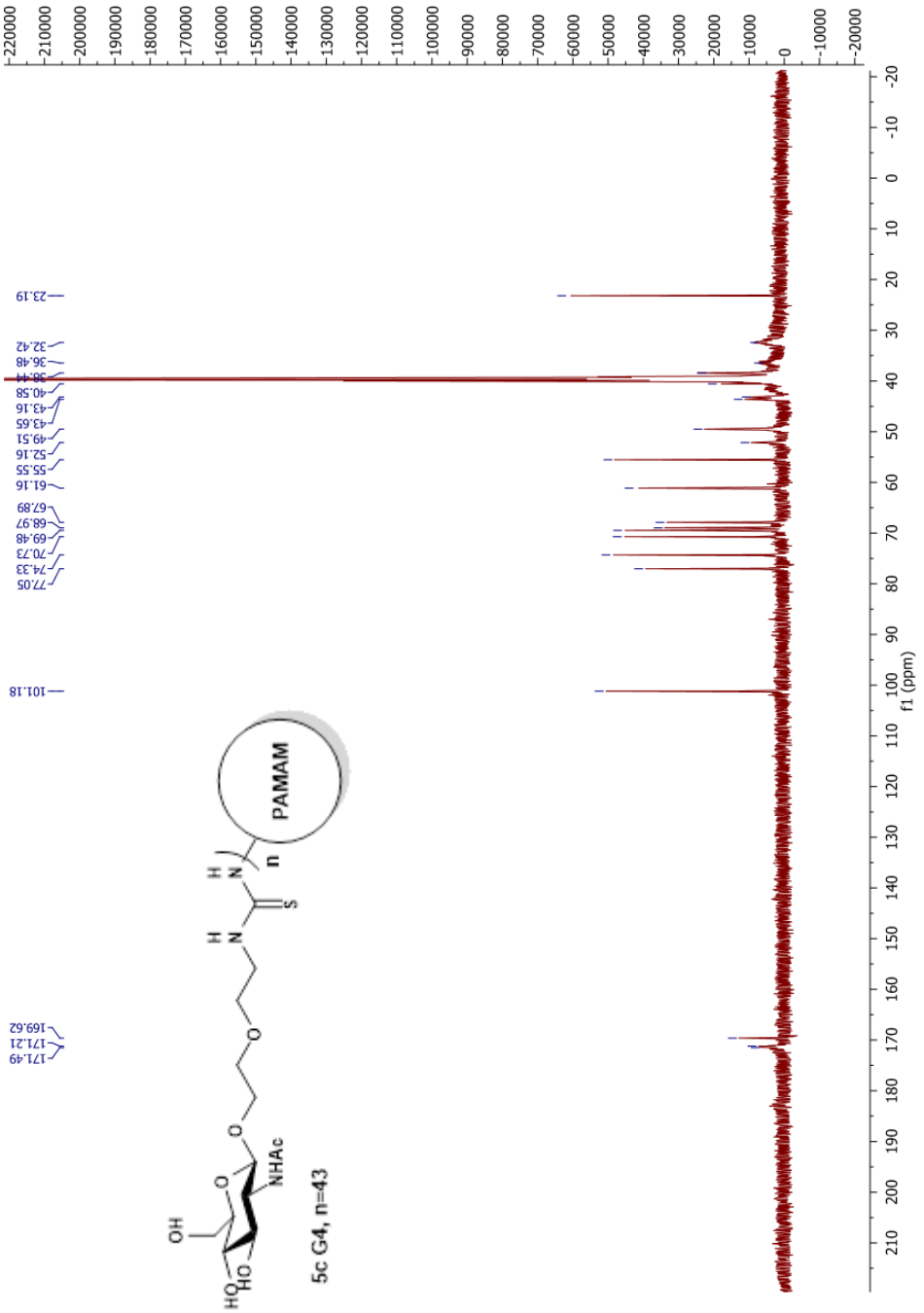

Figure 50: ^{13}C NMR spectrum (126 MHz, d_6-DMSO) of **5c**.

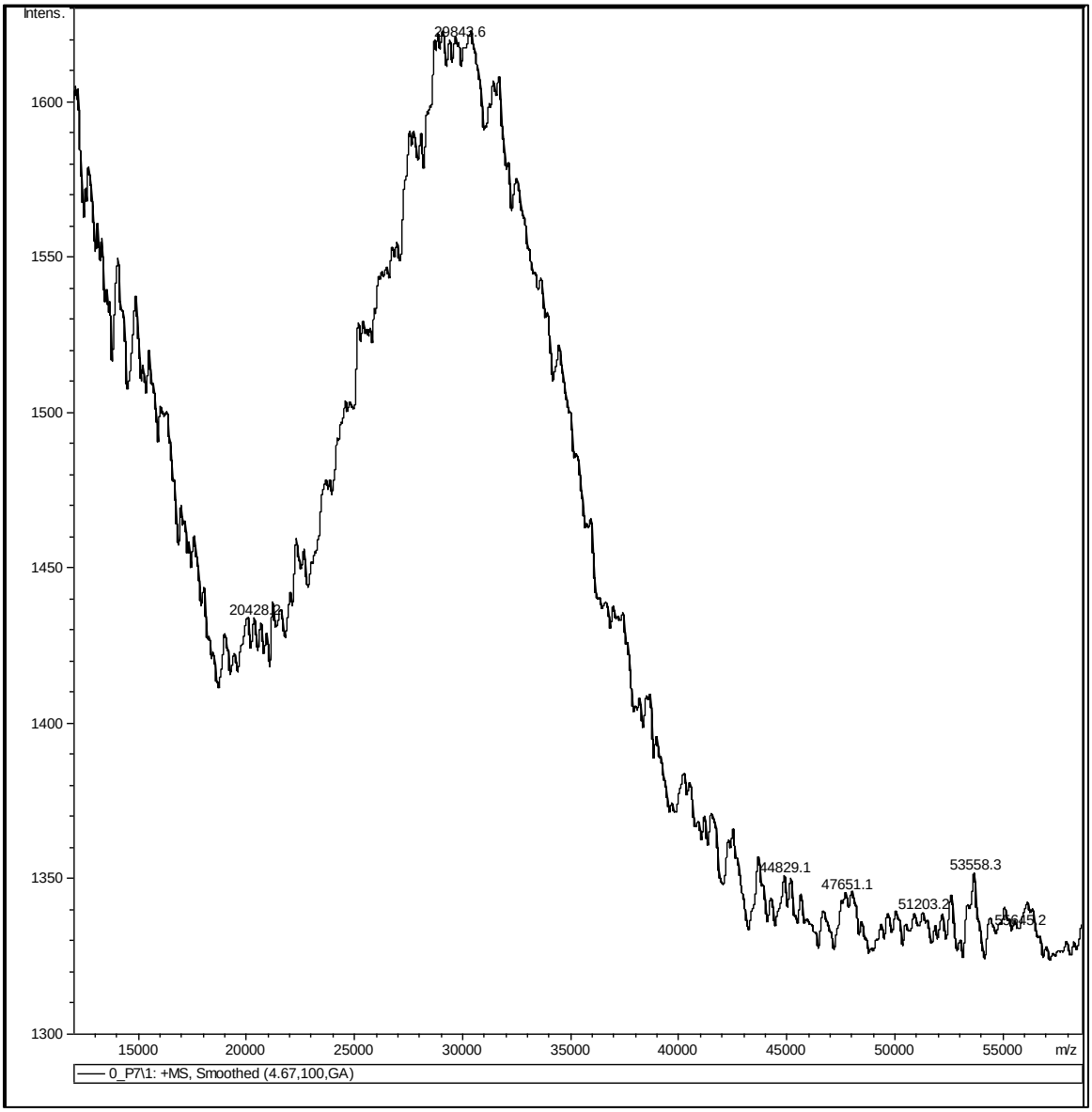

Figure 51: Smoothed MALDI TOF spectrum for compound **5c**. M_w = 35,000

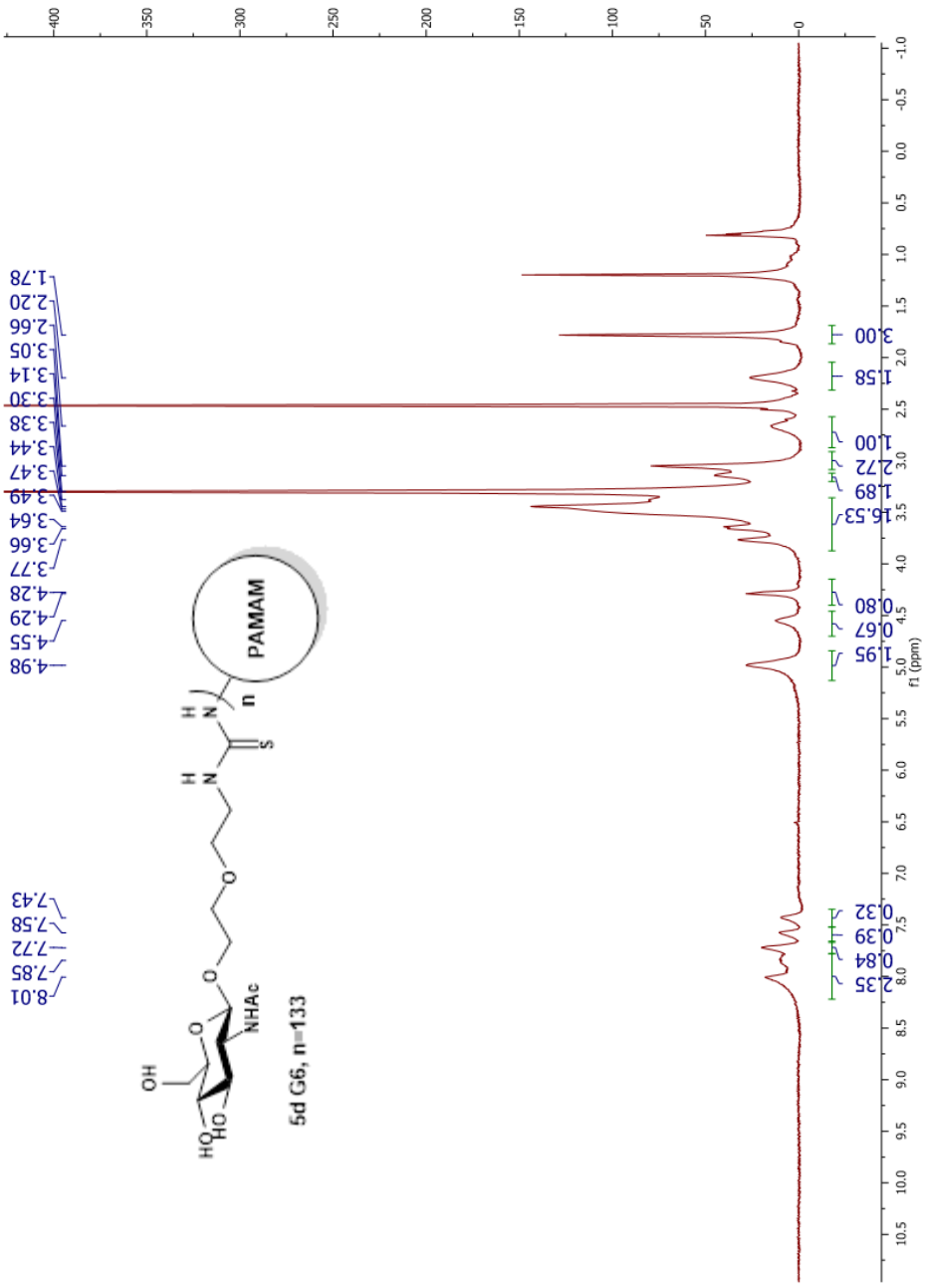

Figure 52: ^{1}H NMR spectrum (500 MHz, d_6-DMSO) of **5d**.

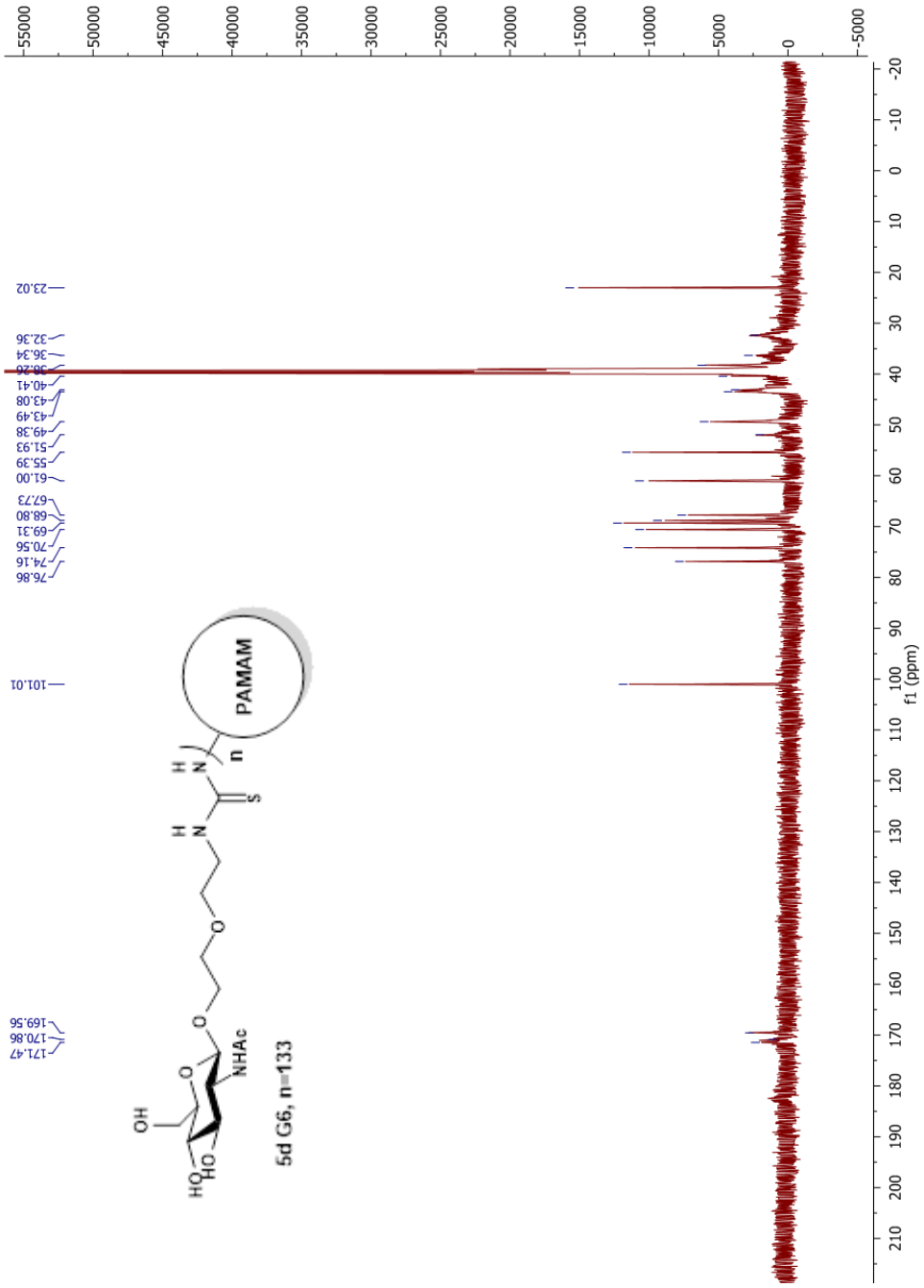

Figure 53: ^{13}C NMR spectrum (126 MHz, d_6-DMSO) of **5d**.

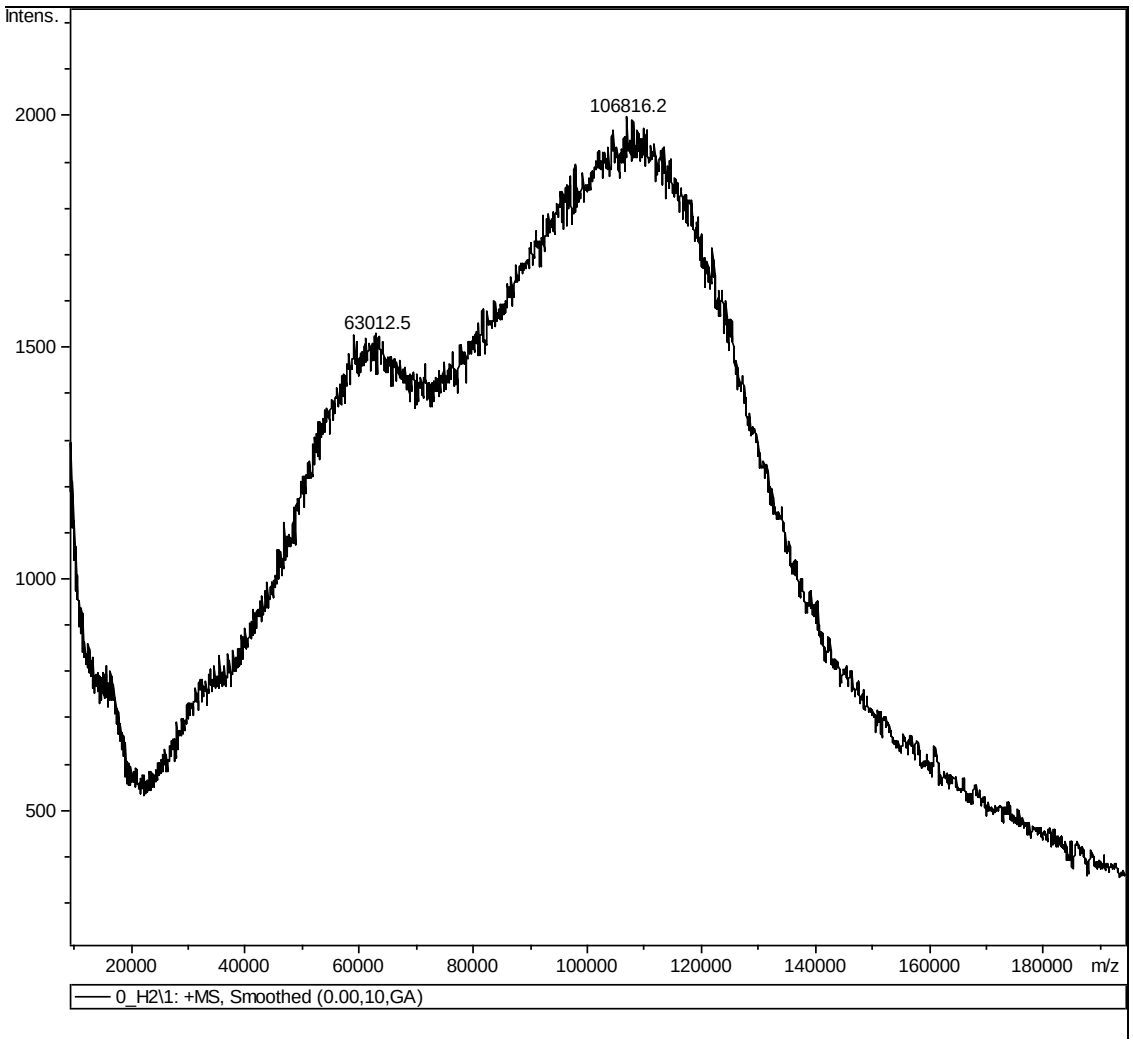

Figure 54: Smoothed MALDI TOF spectrum for compound **5d**. M_w = 104,600

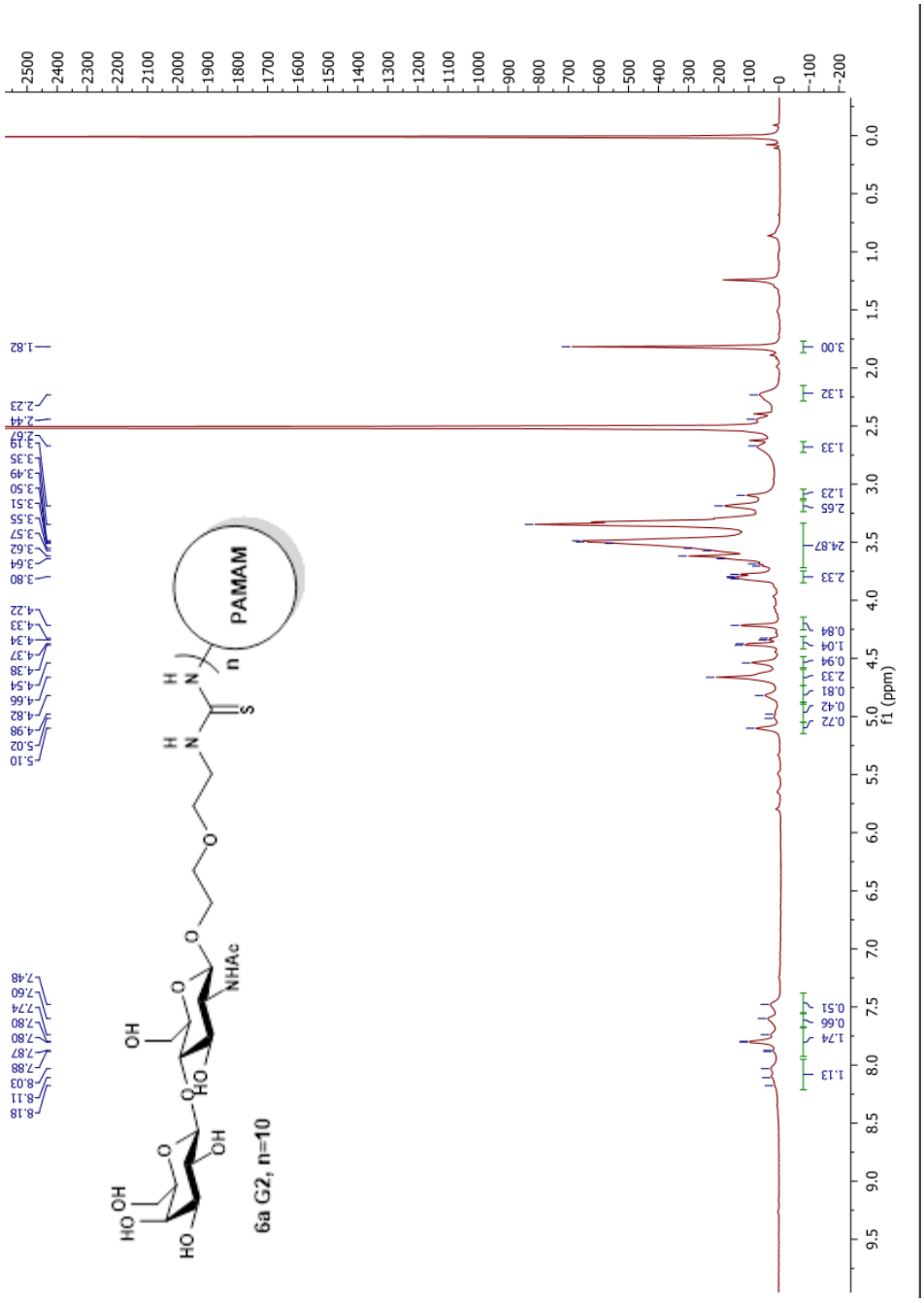

Figure 55: ^{1}H NMR spectrum (600 MHz, d_6-DMSO) of **6a**.

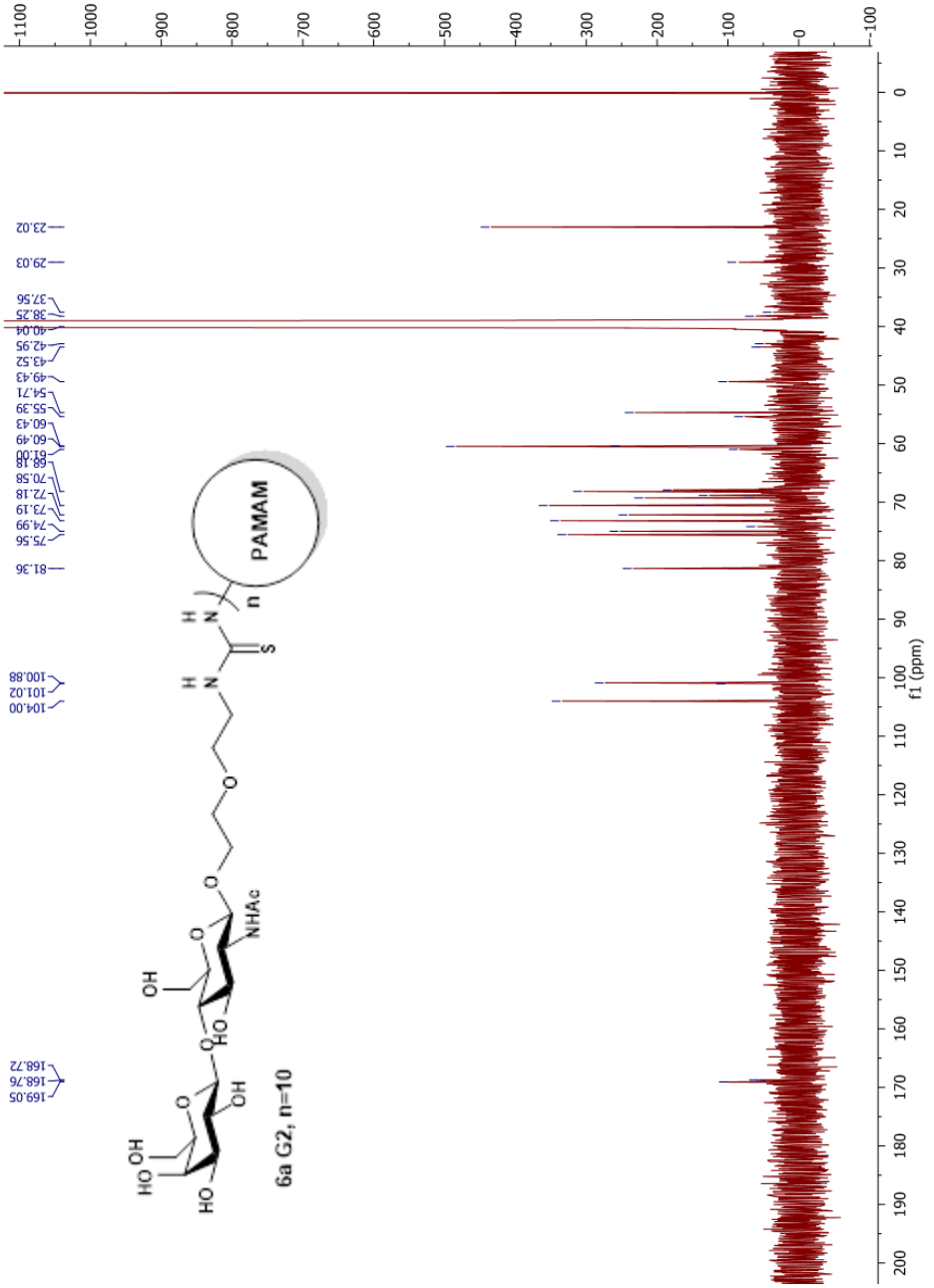

Figure 56: ^{13}C NMR spectrum (151 MHz, d_6-DMSO) of **6a**.

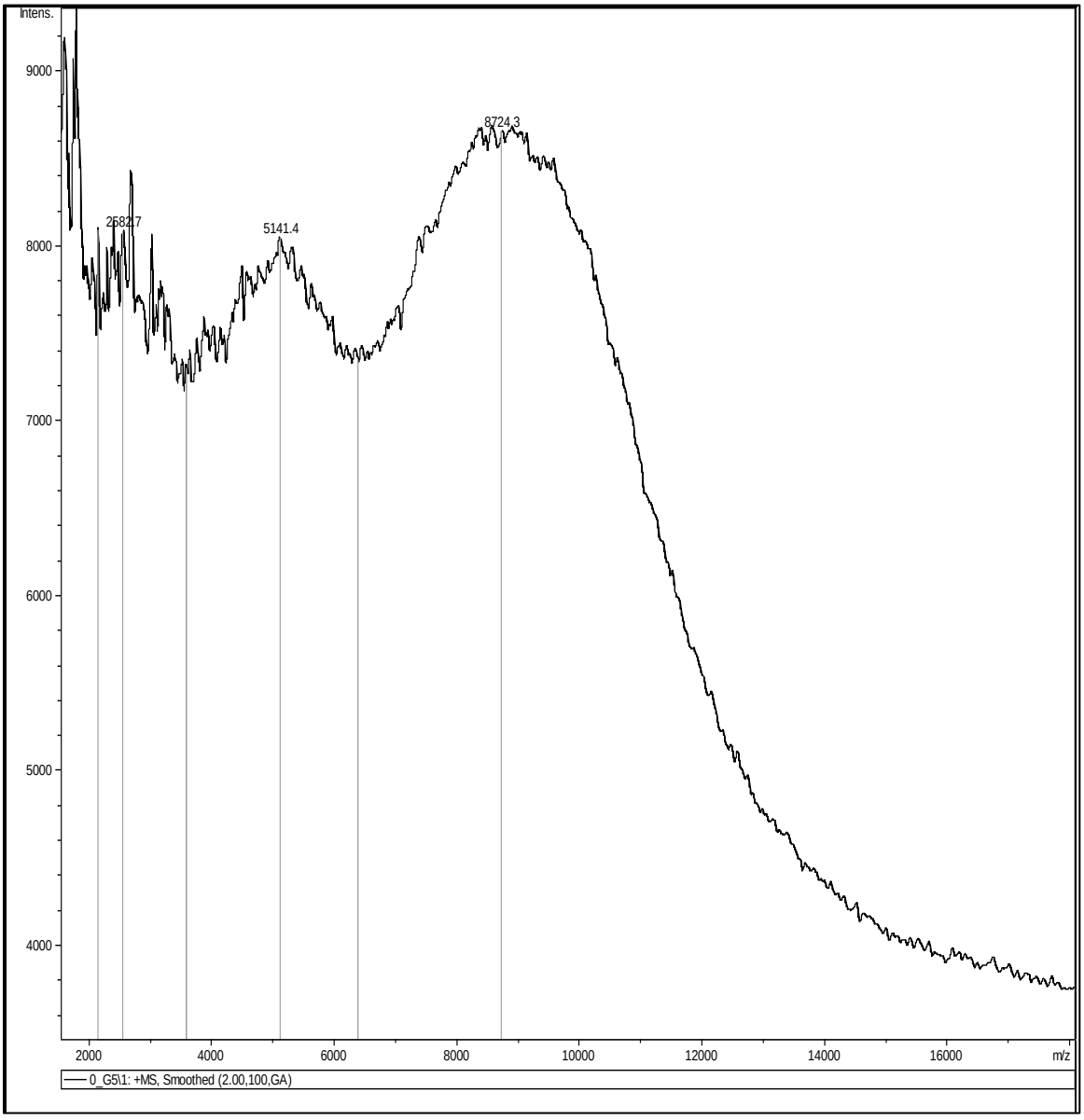

Figure 57: Smoothed MALDI TOF spectrum for compound **6a**. M_w = 8,700

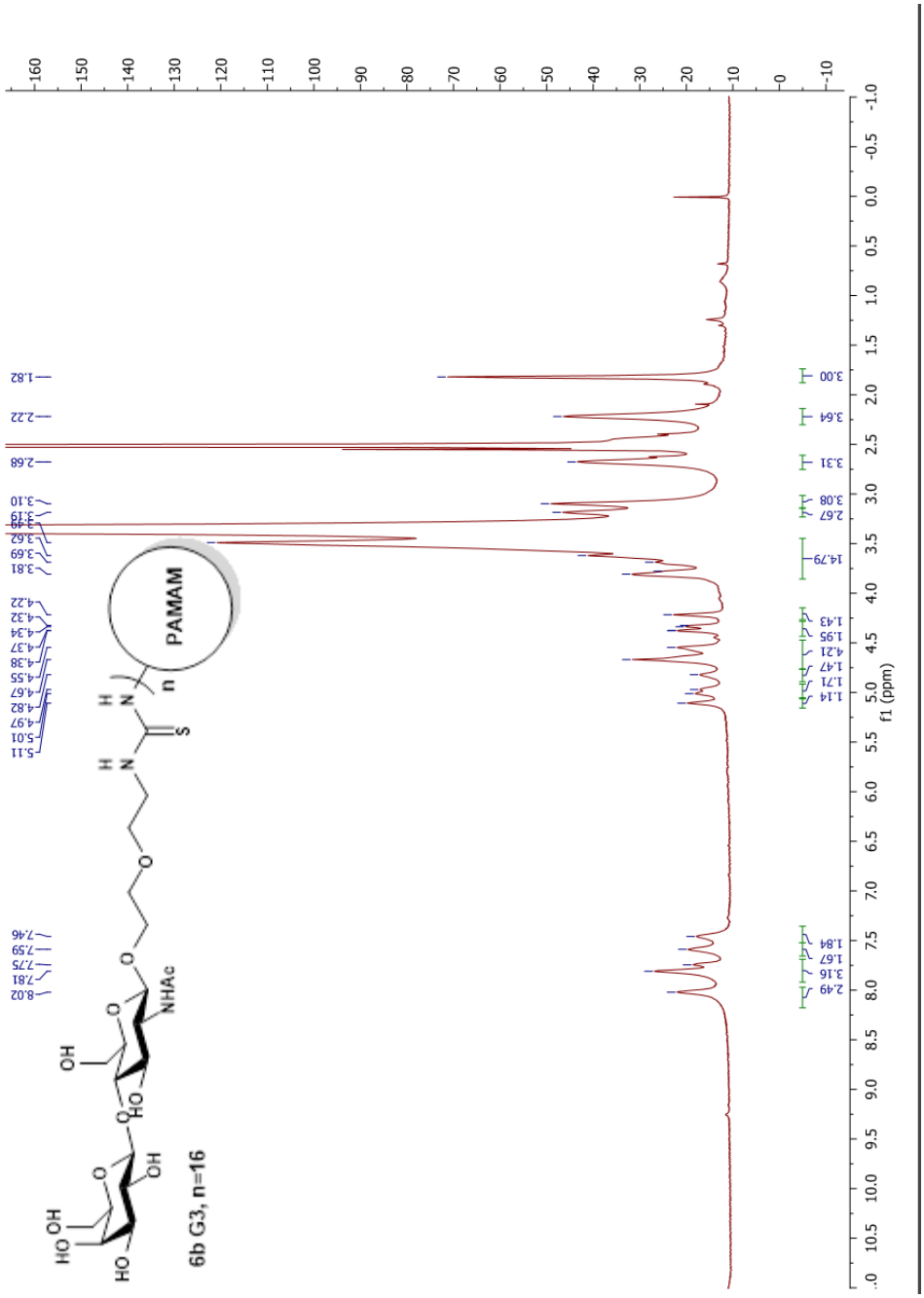

Figure 58: ^{1}H NMR spectrum (600 MHz, d_6-DMSO) of **6b**.

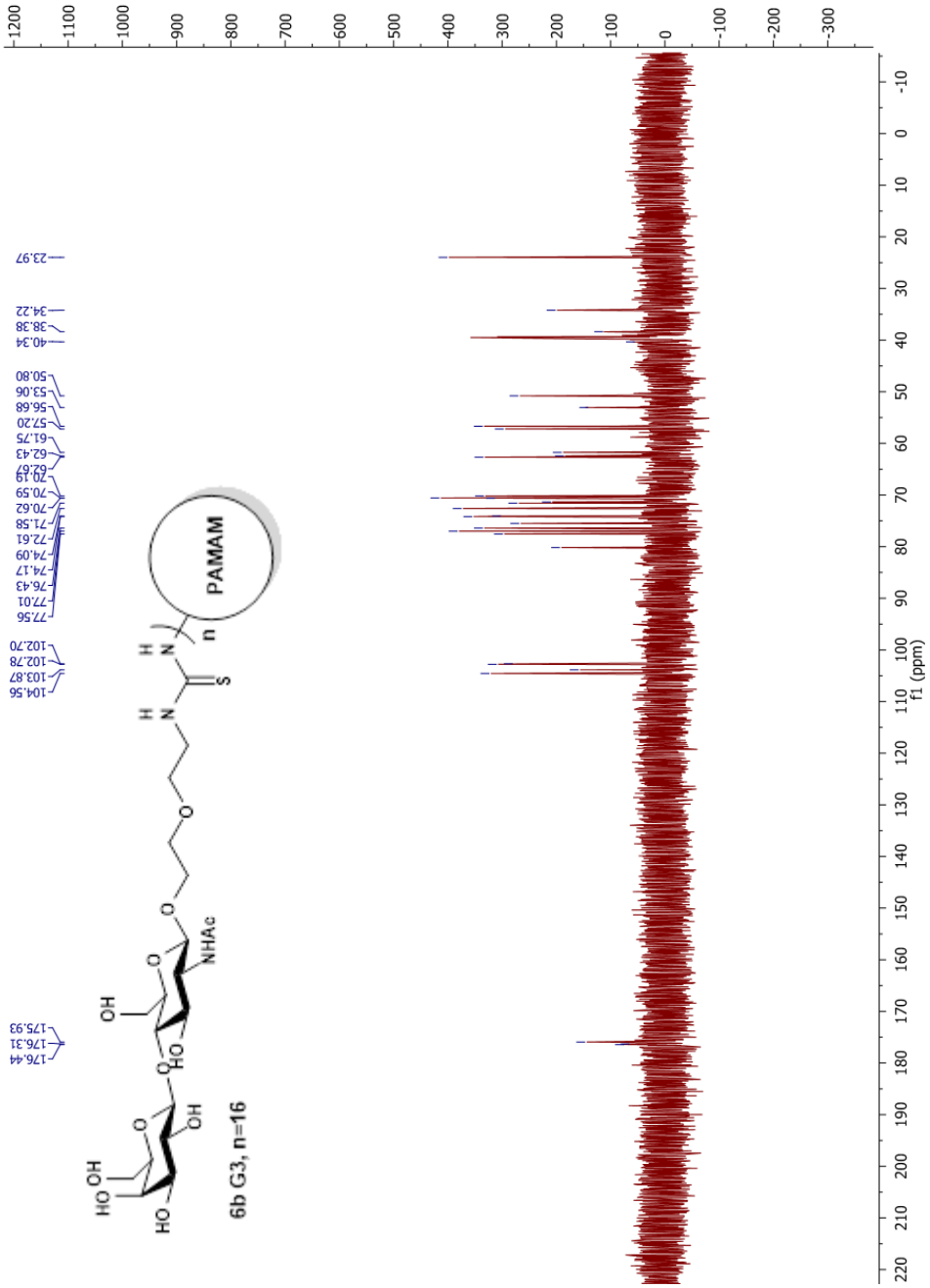

Figure 59: ^{13}C NMR spectrum (151 MHz, d_6-DMSO) of **6b**.

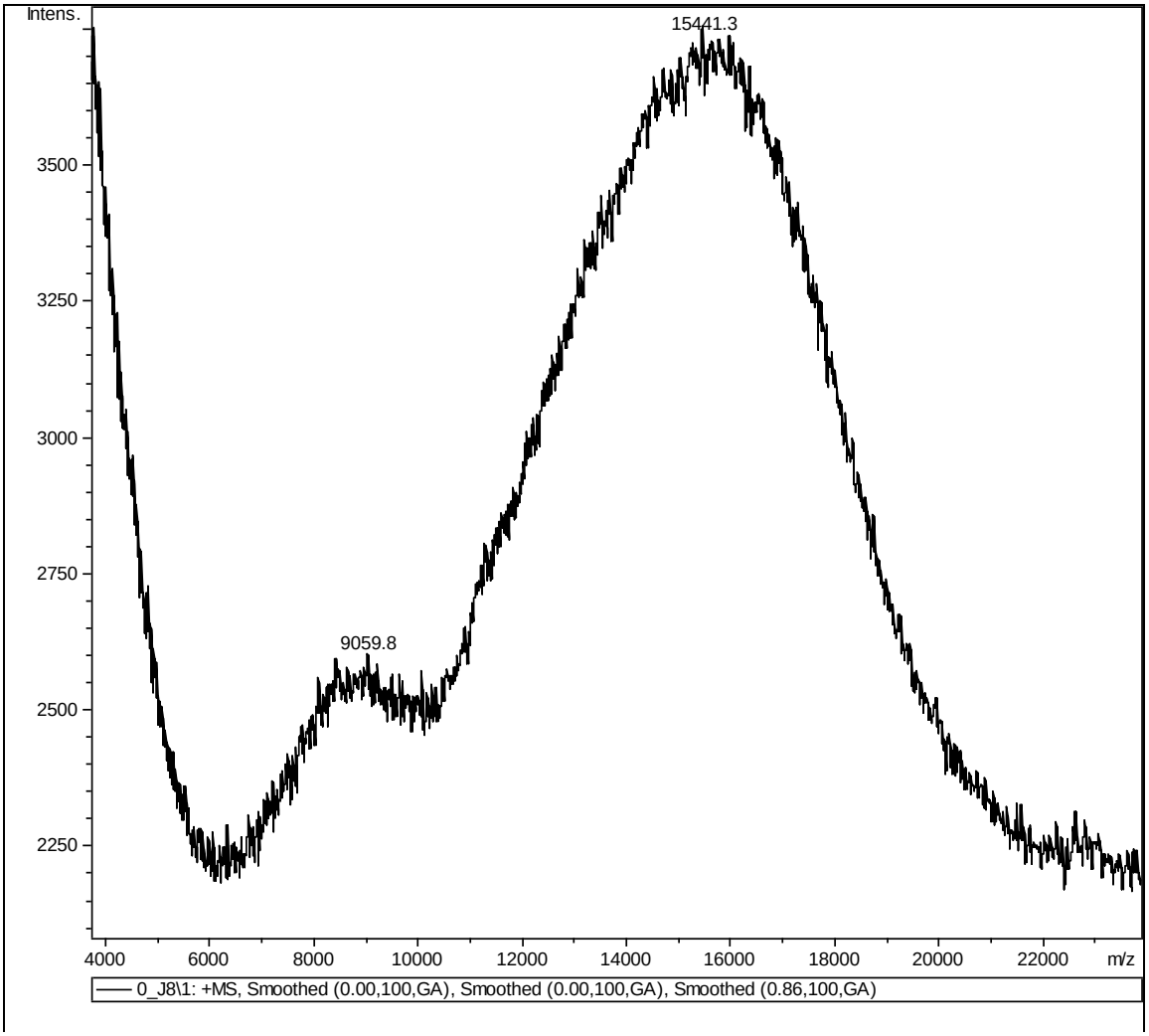

Figure 60: Smoothed MALDI TOF spectrum for compound **6b**. M_w = 16,400

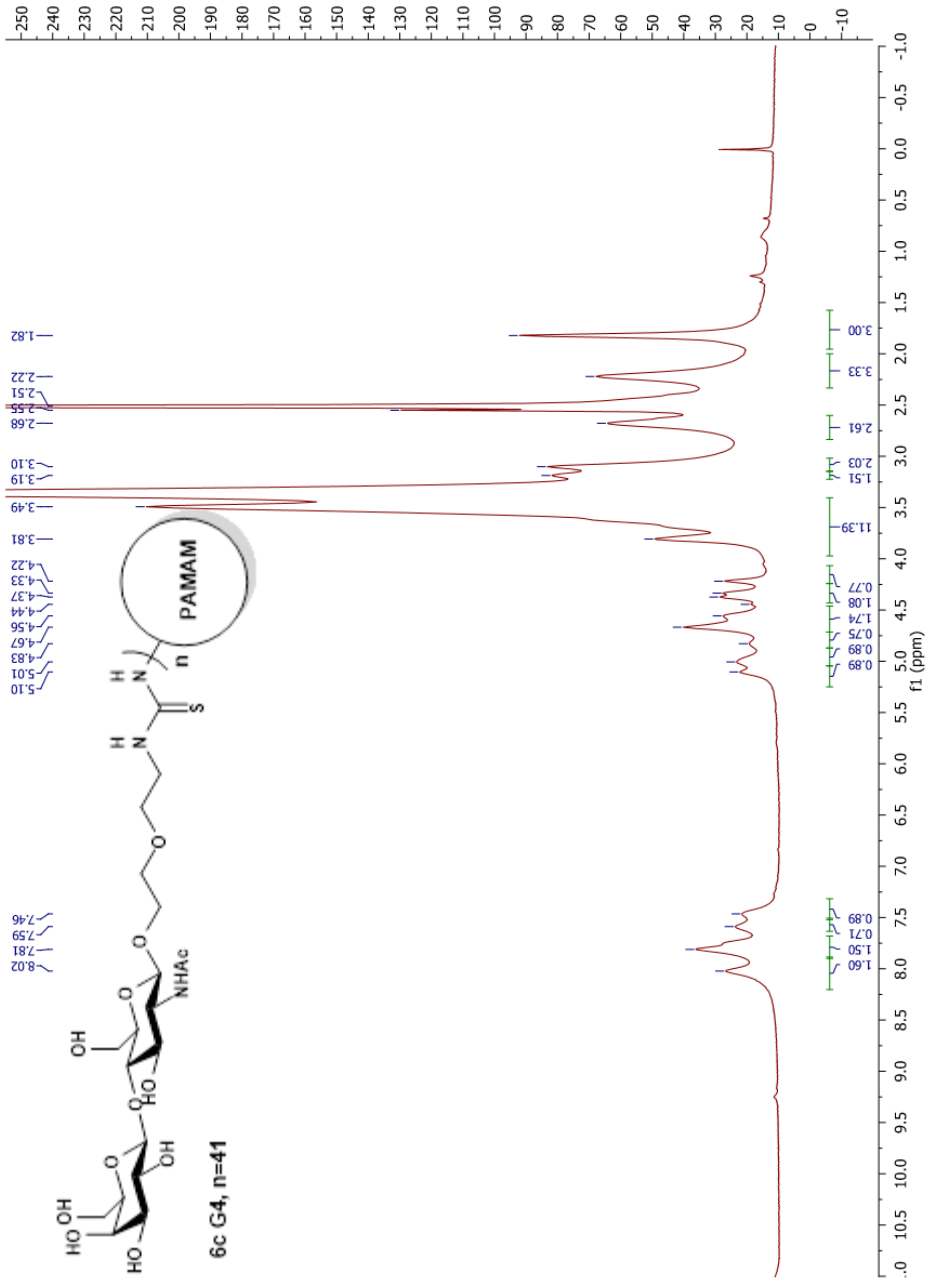

Figure 61: ^{1}H NMR spectrum (600 MHz, d_6-DMSO) of **6c**.

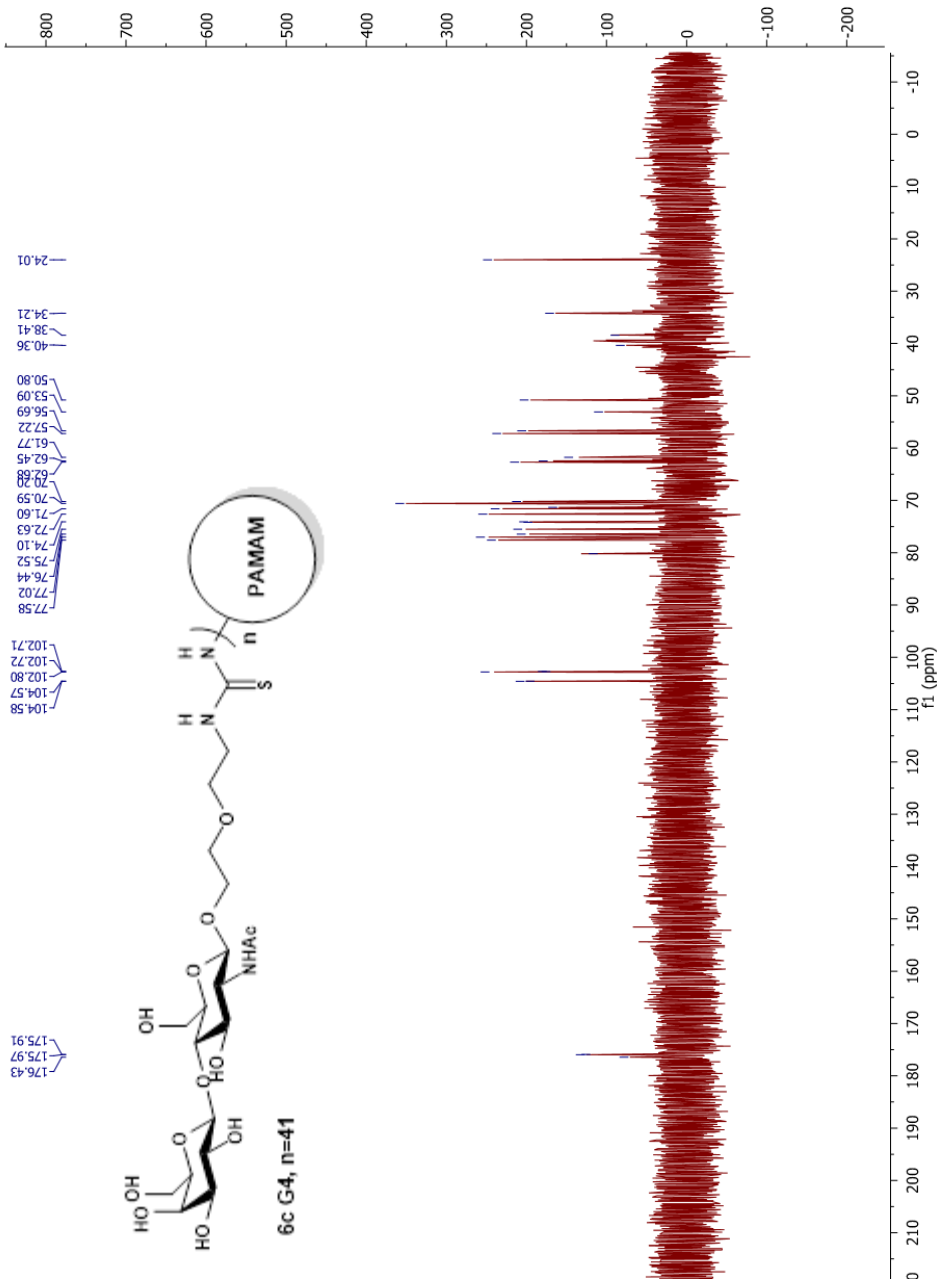

Figure 62: ^{13}C NMR spectrum (151 MHz, d_6-DMSO) of **6c**.

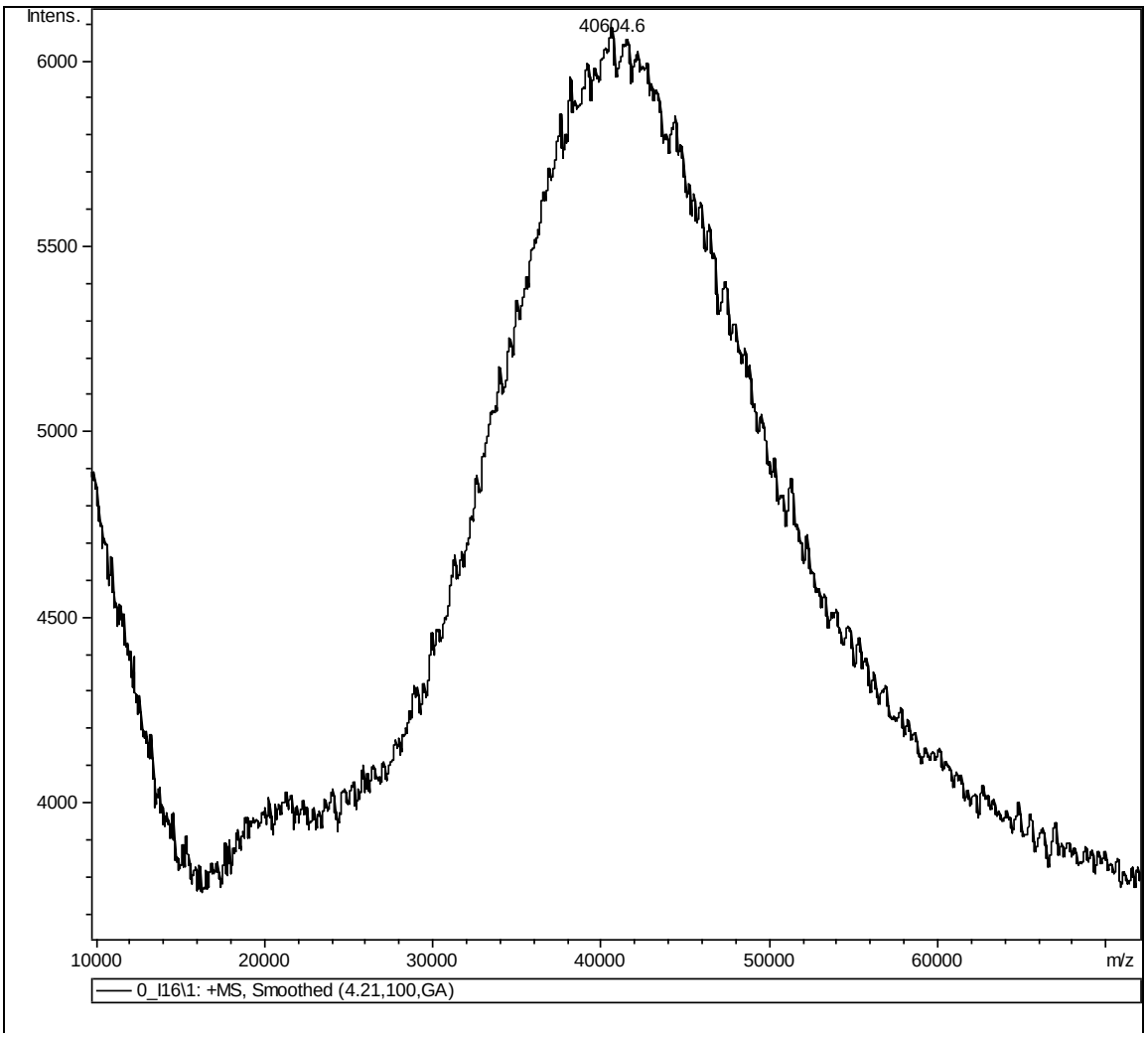

Figure 63: Smoothed MALDI TOF spectrum for compound **6c**. M_w = 37,000

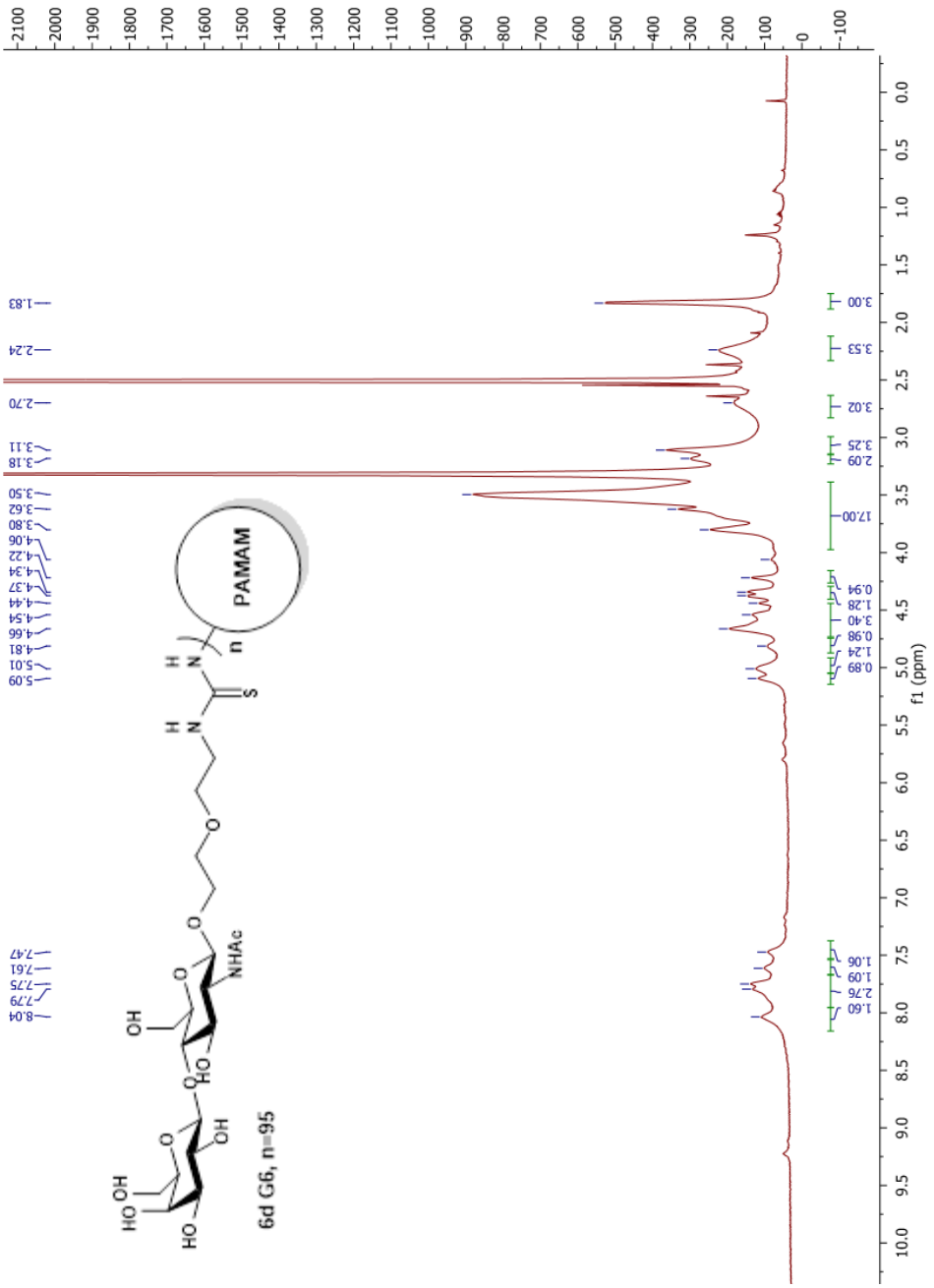

Figure 64: ^{1}H NMR spectrum (600 MHz, d_6-DMSO) of **6d**.

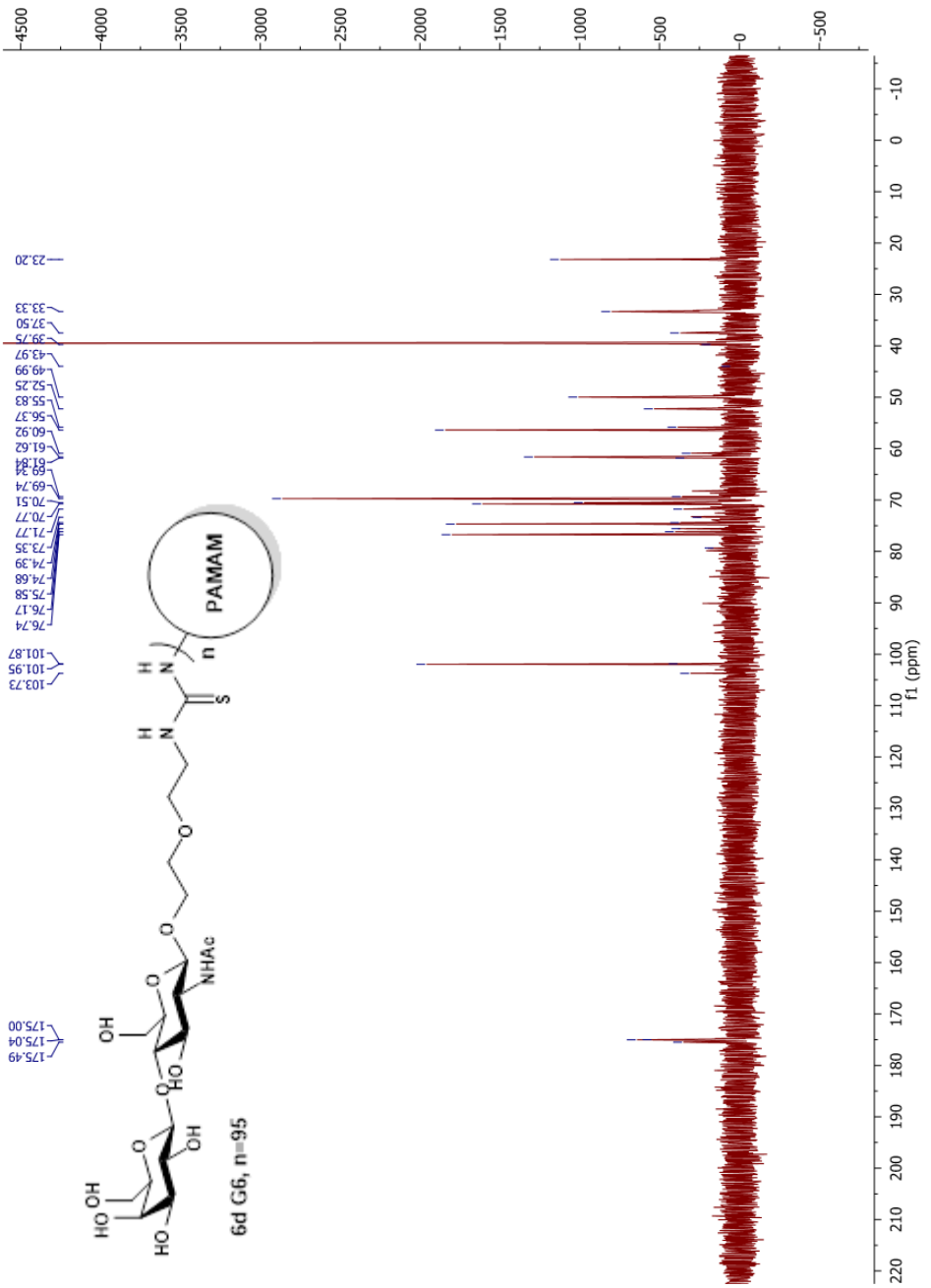

Figure 65: ^{13}C NMR spectrum (151 MHz, d_6-DMSO) of **6d**.

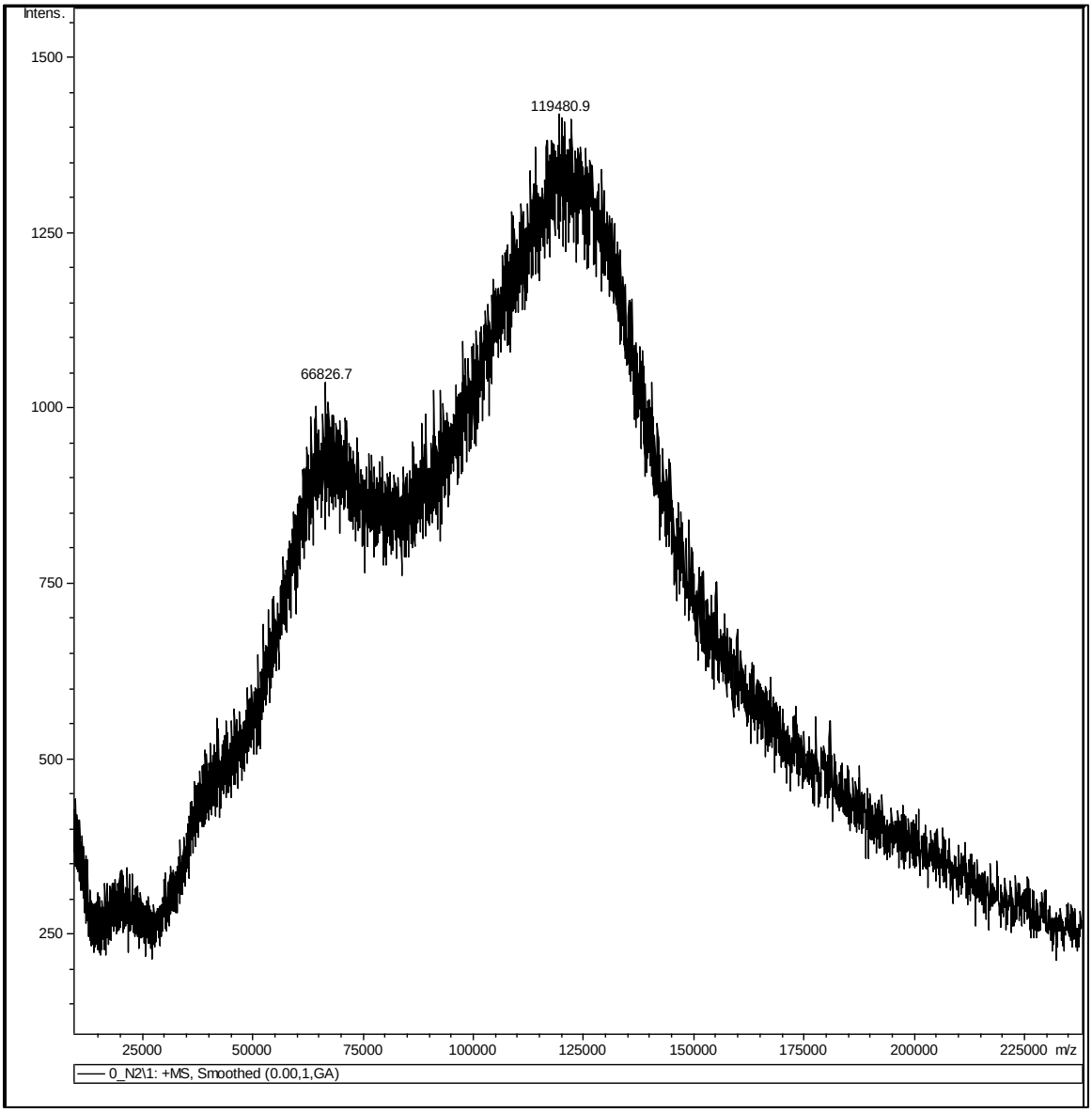

Figure 66: Smoothed MALDI TOF spectrum for compound **6d**. M_w = 119,400

Cellular Assay Data

The following figures are primary data from cellular aggregation assays. Images shown are composed of 12 compressed stills taken at 10x magnification then manipulated to black and white (Figure 67 to Figure 196).

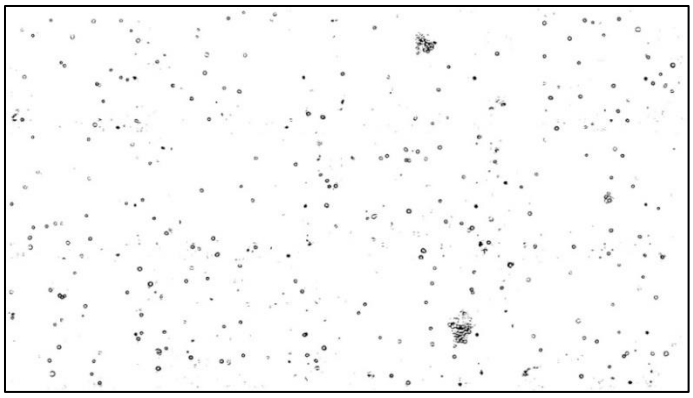

Figure 67: A-549 0 µM G2-*N*-acetyllactosamine functionalized dendrimer.

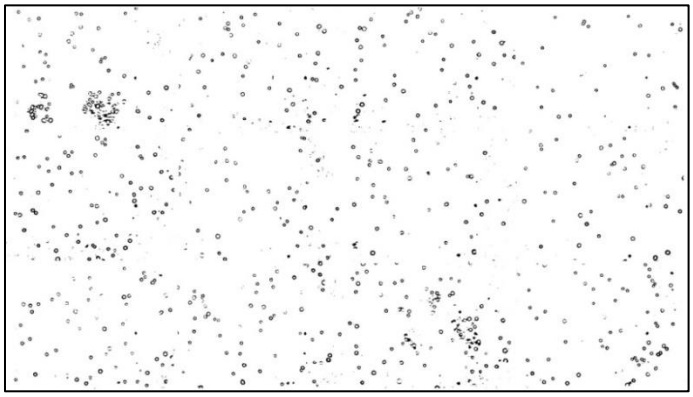

Figure 68: A-549 34 µM G2-*N*-acetyllactosamine functionalized dendrimer.

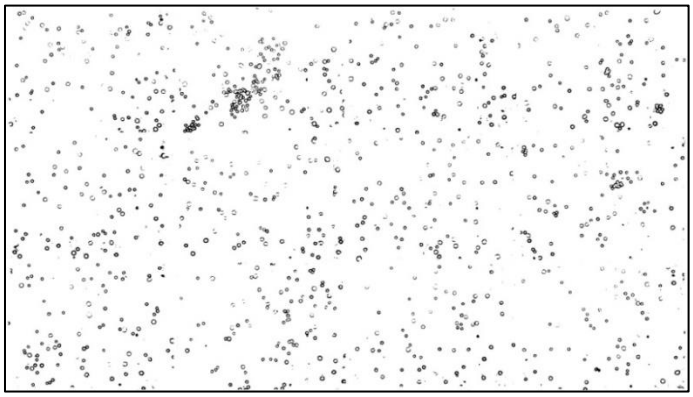

Figure 69: A-549 68 µM G2-*N*-acetyllactosamine functionalized dendrimer.

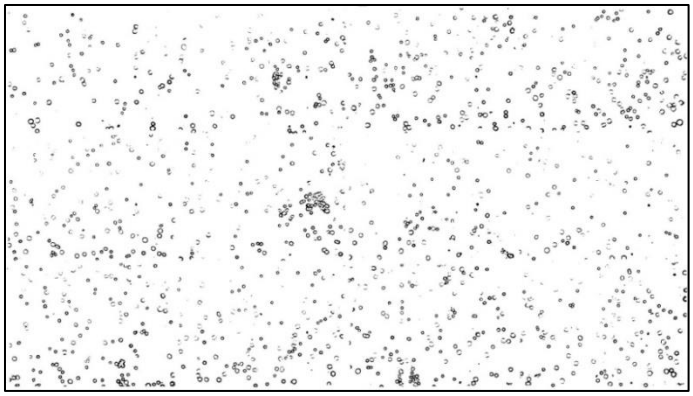

Figure 70: A-549 101 µM G2-*N*-acetyllactosamine functionalized dendrimer.

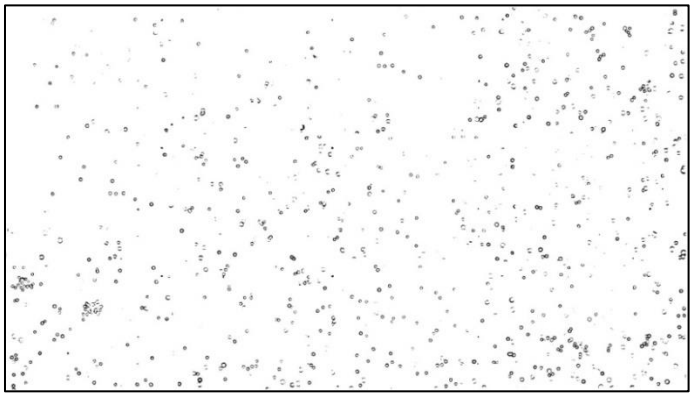

Figure 71: A-549 135 µM G2-*N*-acetyllactosamine functionalized dendrimer.

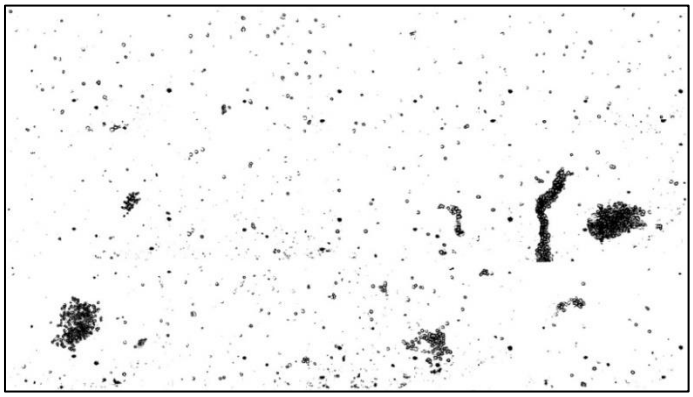

Figure 72: A-549, galectin-3, 0 µM G2-*N*-acetyllactosamine functionalized dendrimer.

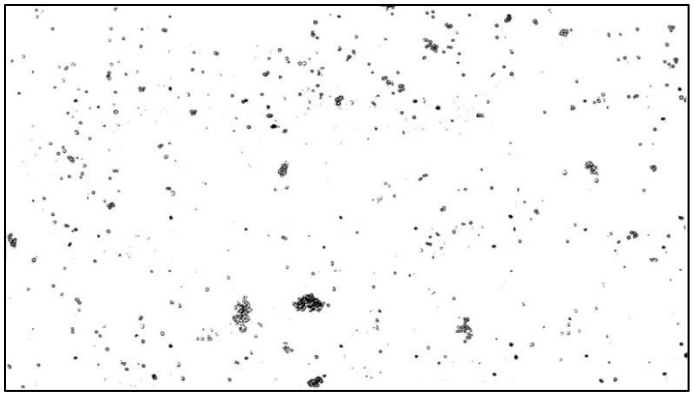

Figure 73: A-549, galectin-3, and 34 µM G2-*N*-acetyllactosamine functionalized dendrimer.

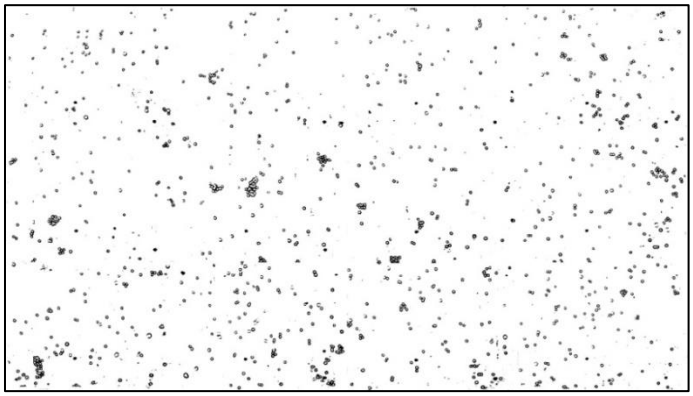

Figure 74: A-549, galectin-3, and 68 µM G2-*N*-acetyllactosamine functionalized dendrimer.

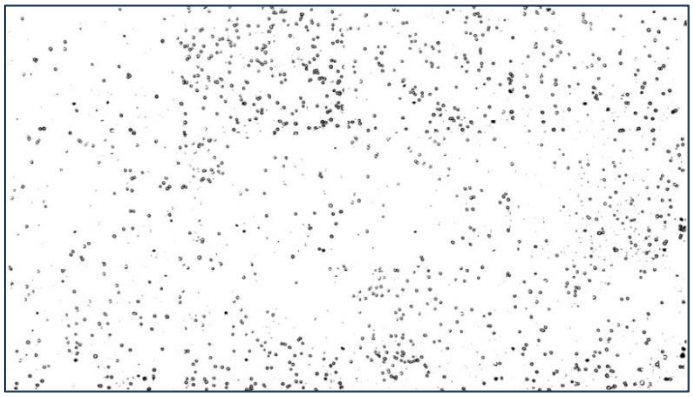

Figure 75: A-549, galectin-3, and 101 µM G2-*N*-acetyllactosamine functionalized dendrimer.

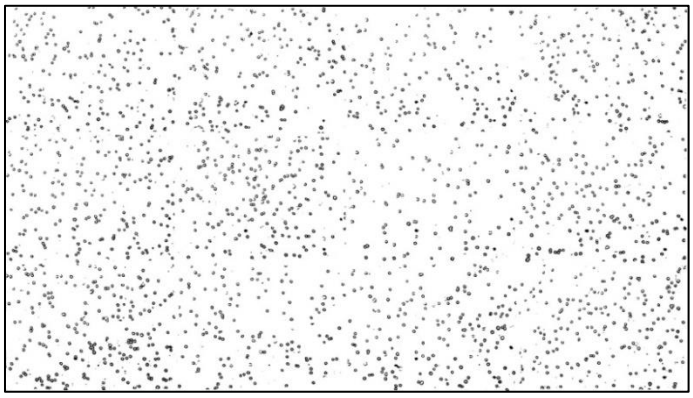

Figure 76: A-549, galectin-3, and 135 µM G2-*N*-acetyllactosamine functionalized dendrimer.

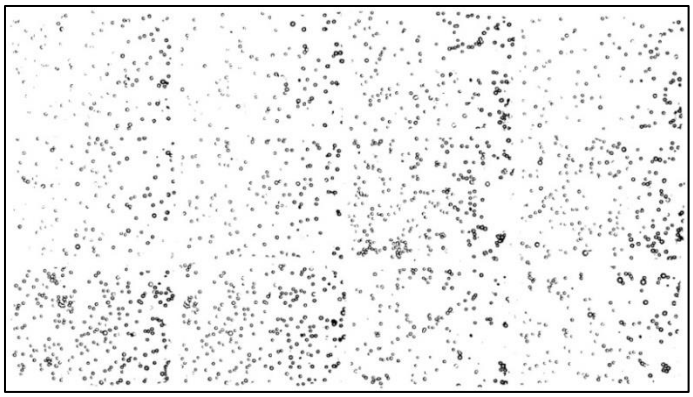

Figure 77:A-549 0 µM G3-*N*-acetyllactosamine functionalized dendrimer.

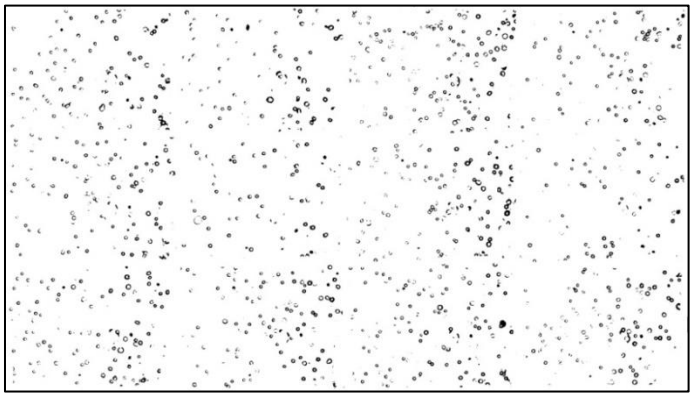

Figure 78: A-549 18 µM G3-*N*-acetyllactosamine functionalized dendrimer.

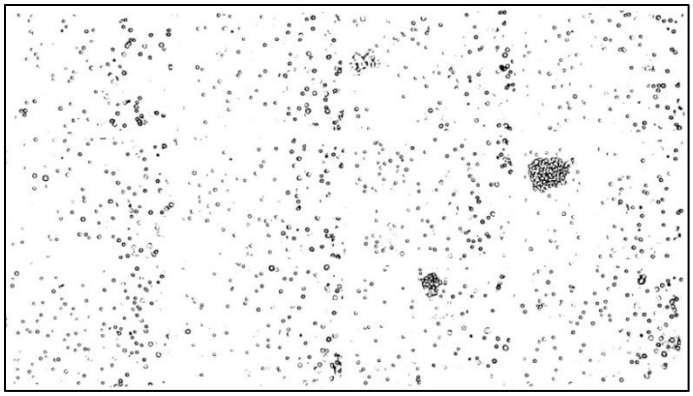

Figure 79: A-549 36 µM G3-*N*-acetyllactosamine functionalized dendrimer.

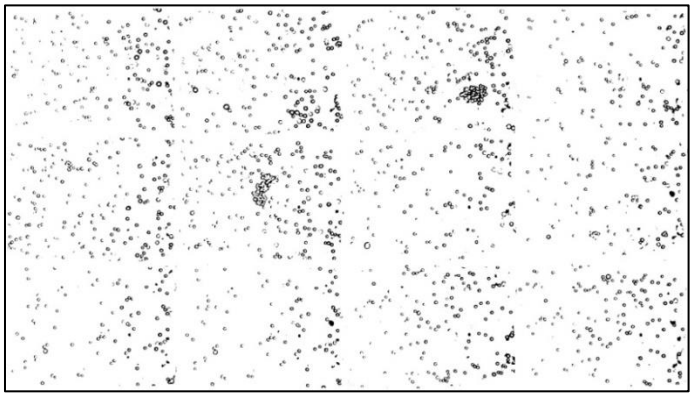

Figure 80: A-549 54 µM G3-*N*-acetyllactosamine functionalized dendrimer.

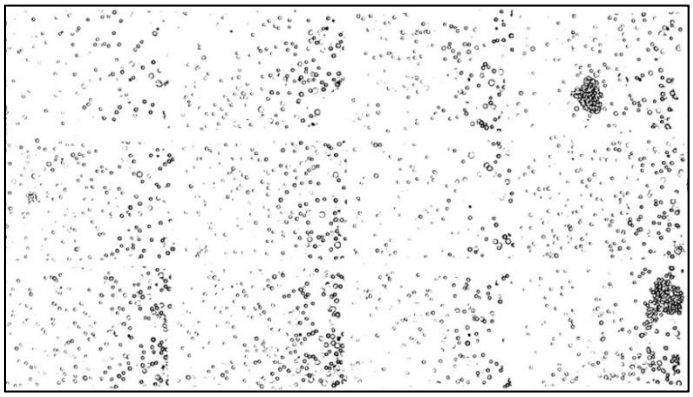

Figure 81: A-549 72 µM G3-*N*-acetyllactosamine functionalized dendrimer.

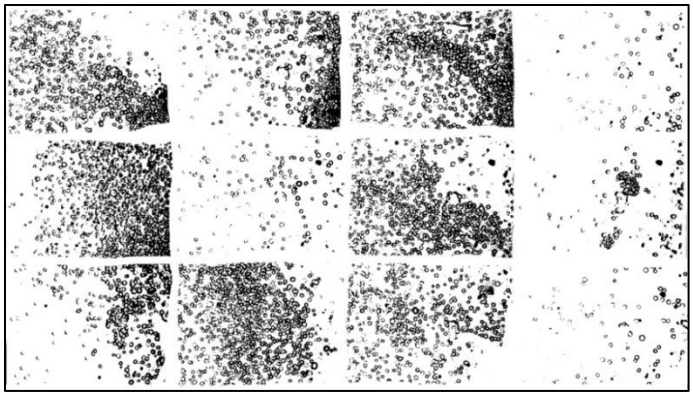

Figure 82: A-549, galectin-3, 0 µM G3-*N*-acetyllactosamine functionalized dendrimer.

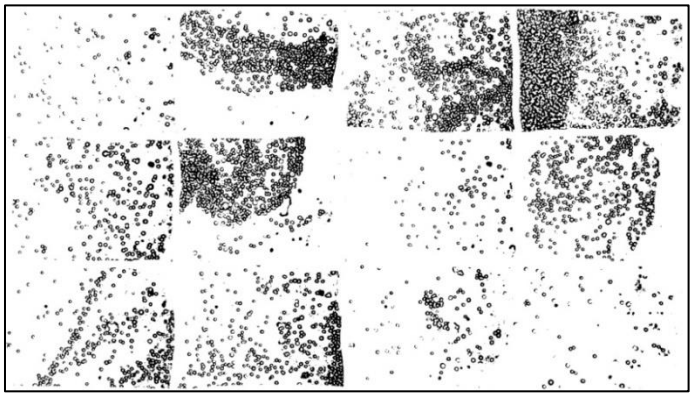

Figure 83: A-549, galectin-3, and 18 µM G3-*N*-acetyllactosamine functionalized dendrimer.

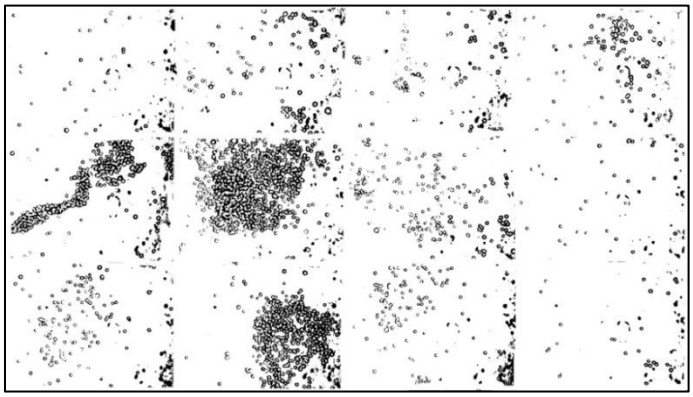

Figure 84: A-549, galectin-3, and 36 µM G3-*N*-acetyllactosamine functionalized dendrimer.

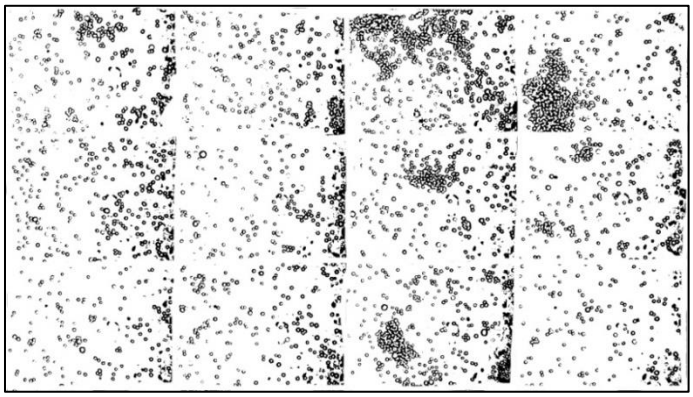

Figure 85: A-549, galectin-3, and 54 µM G3-*N*-acetyllactosamine functionalized dendrimer.

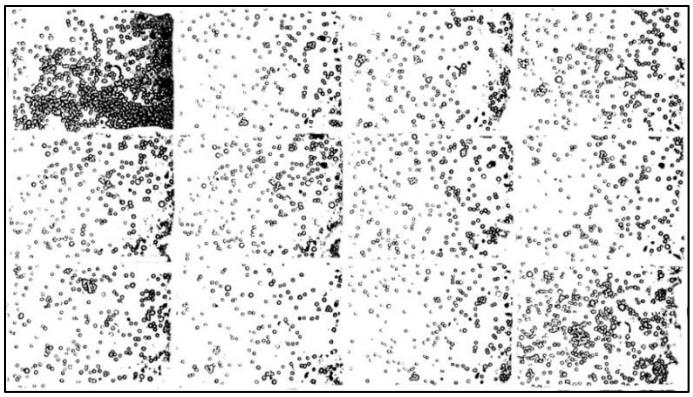

Figure 86: A-549, galectin-3, and 72 µM G3-*N*-acetyllactosamine functionalized dendrimer.

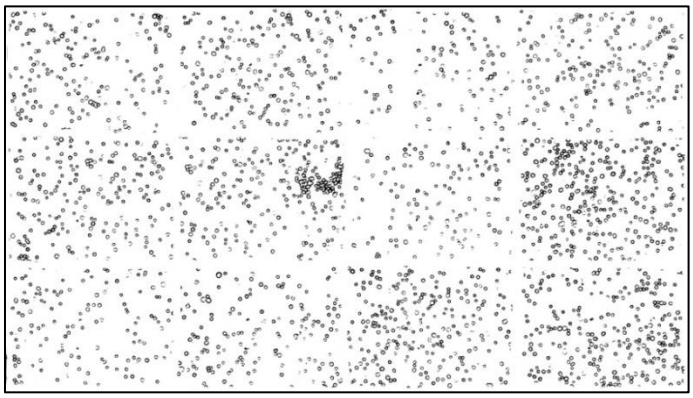

Figure 87: A-549 0 µM G4-*N*-acetyllactosamine functionalized dendrimer.

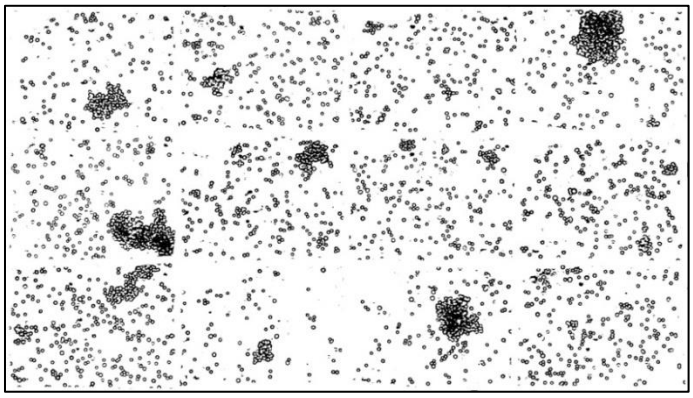

Figure 88: A-549 8 µM G4-*N*-acetyllactosamine functionalized dendrimer.

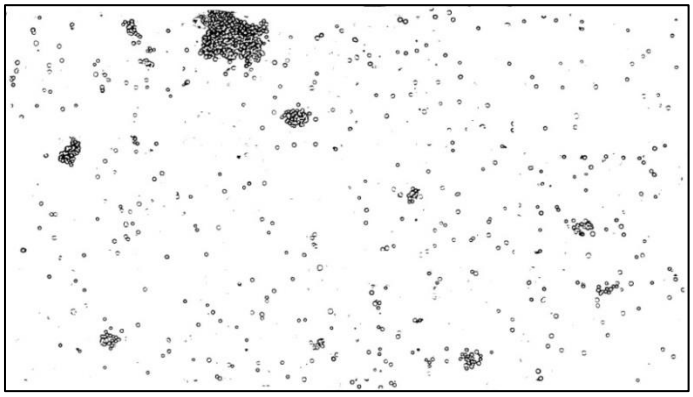

Figure 89: A-549 16 µM G4-*N*-acetyllactosamine functionalized dendrimer.

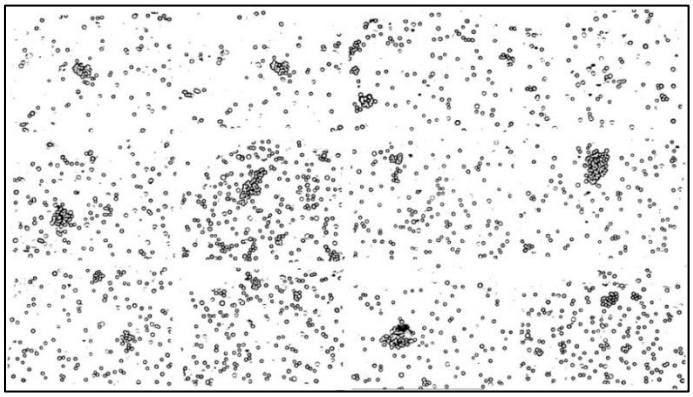

Figure 90: A-549 24 µM G4-*N*-acetyllactosamine functionalized dendrimer.

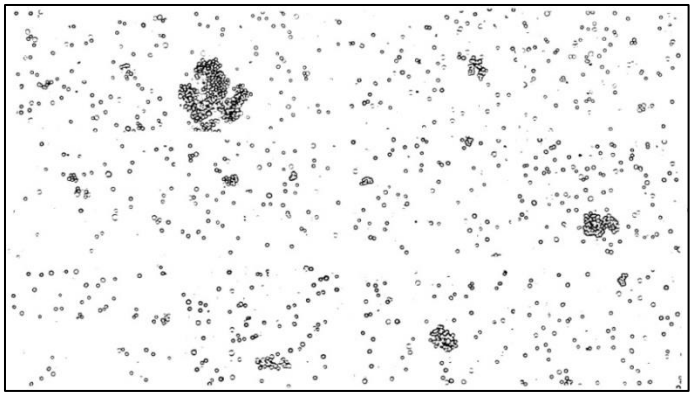

Figure 91: A-549 32 µM G4-*N*-acetyllactosamine functionalized dendrimer.

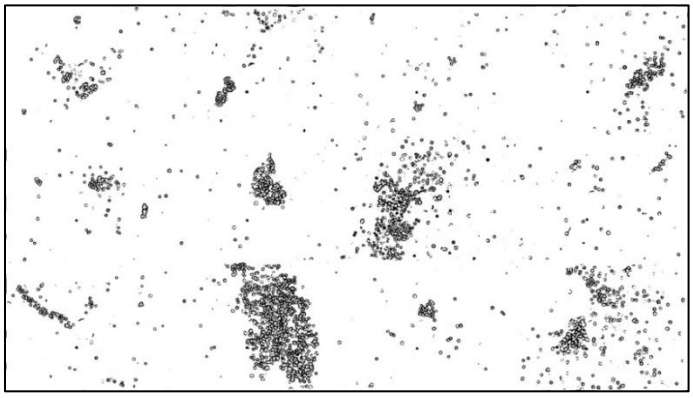

Figure 92: A-549, galectin-3, 0 µM G4-*N*-acetyllactosamine functionalized dendrimer.

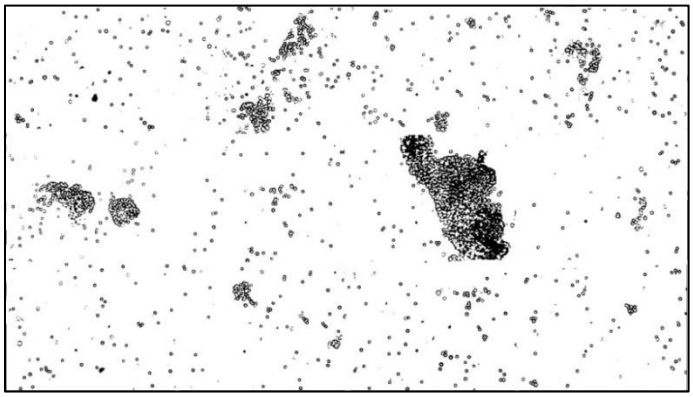

Figure 93: A-549, galectin-3, 8 µM G4-*N*-acetyllactosamine functionalized dendrimer.

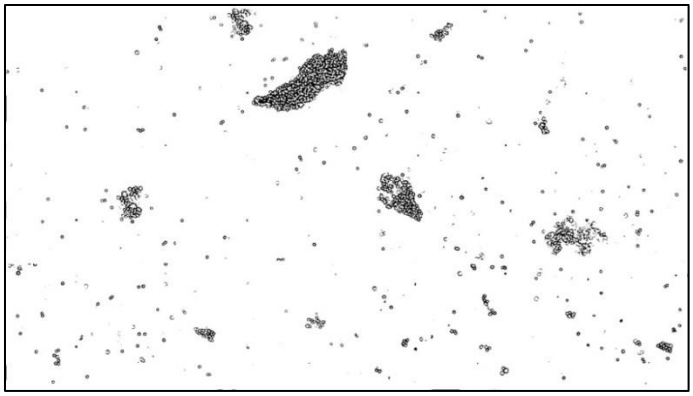

Figure 94: A-549, galectin-3, 16 µM G4-*N*-acetyllactosamine functionalized dendrimer.

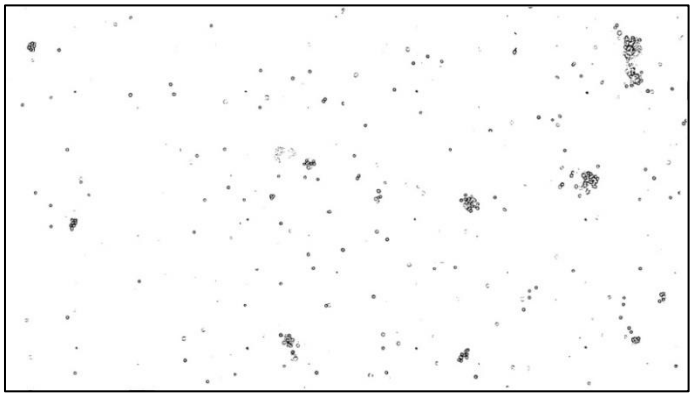

Figure 95: A-549, galectin-3, 24 µM G4-*N*-acetyllactosamine functionalized dendrimer.

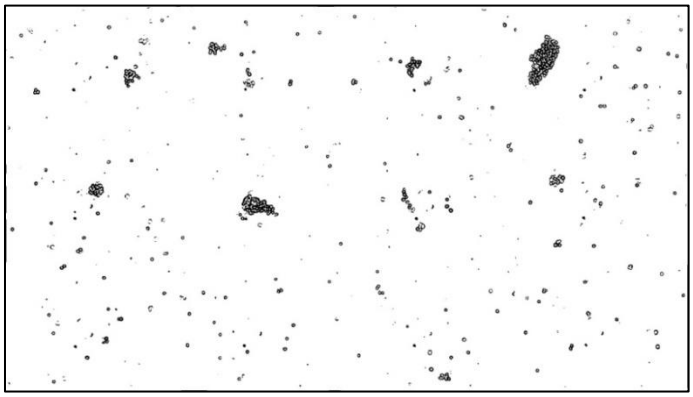

Figure 96: A-549, galectin-3, 32 µM G4-*N*-acetyllactosamine functionalized dendrimer.

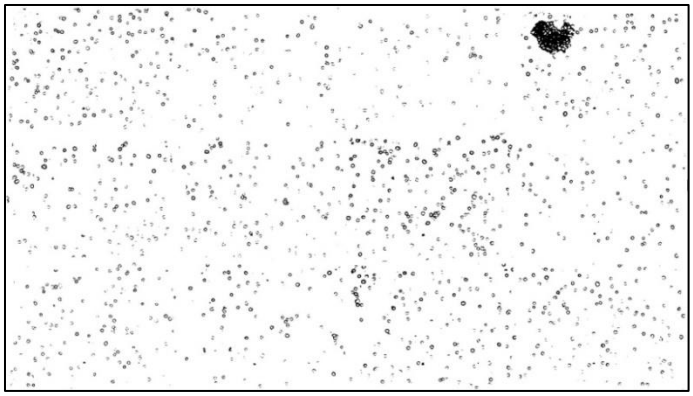

Figure 97: A-549 0 µM G6-*N*-acetyllactosamine functionalized dendrimer.

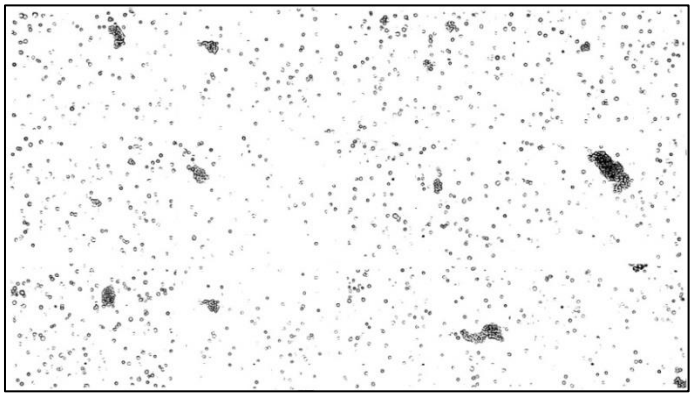

Figure 98: A-549 3 µM G6-*N*-acetyllactosamine functionalized dendrimer.

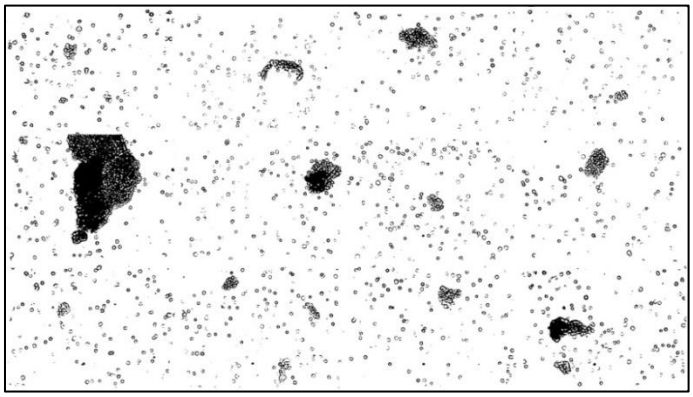

Figure 99: A-549 6 µM G6-*N*-acetyllactosamine functionalized dendrimer.

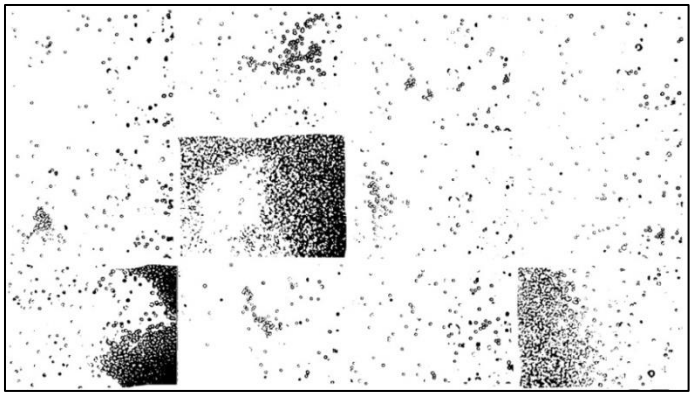

Figure 100: A-549 9 µM G6-*N*-acetyllactosamine functionalized dendrimer.

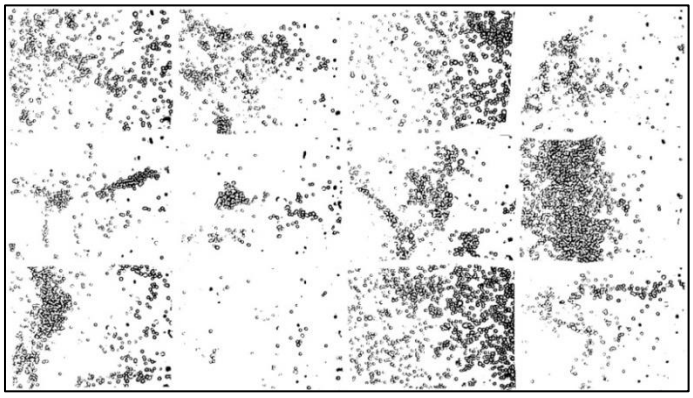

Figure 101: A-549 12 µM G6-*N*-acetyllactosamine functionalized dendrimer.

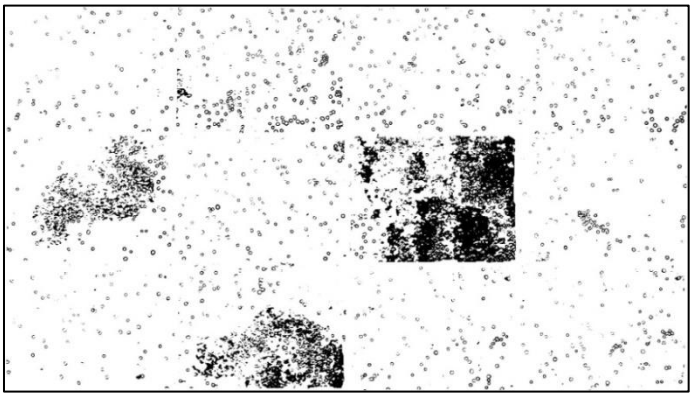

Figure 102: A-549, galectin-3, 0 µM G6-*N*-acetyllactosamine functionalized dendrimer.

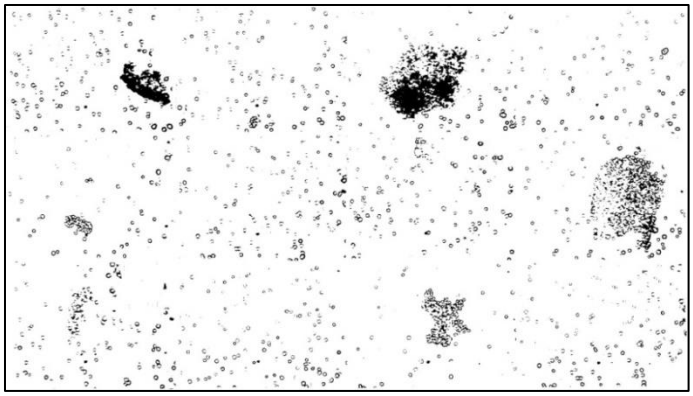

Figure 103: A-549, galectin-3, 3 µM G6-*N*-acetyllactosamine functionalized dendrimer.

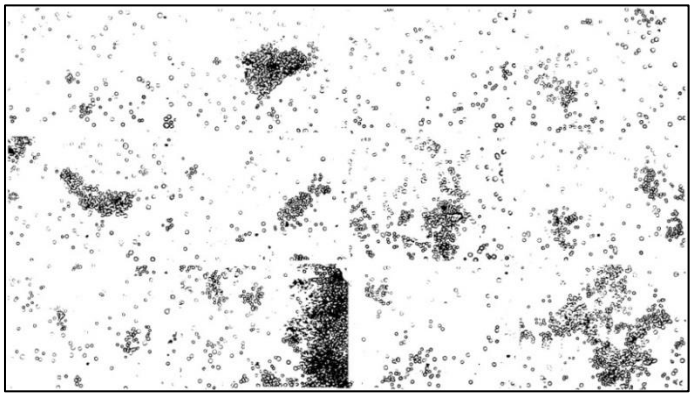

Figure 104: A-549, galectin-3, 6 µM G6-*N*-acetyllactosamine functionalized dendrimer.

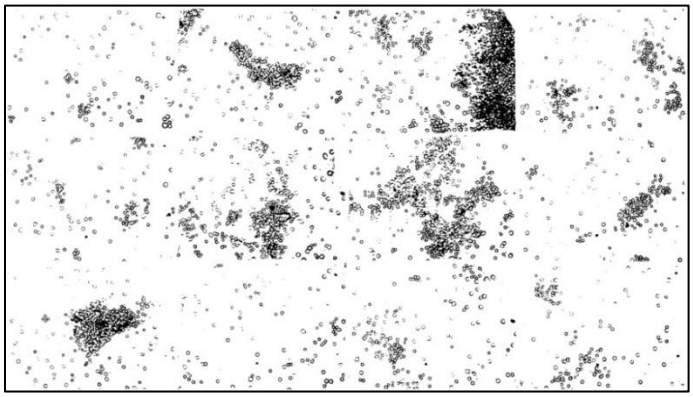

Figure 105: A-549, galectin-3, 9 µM G6-*N*-acetyllactosamine functionalized dendrimer.

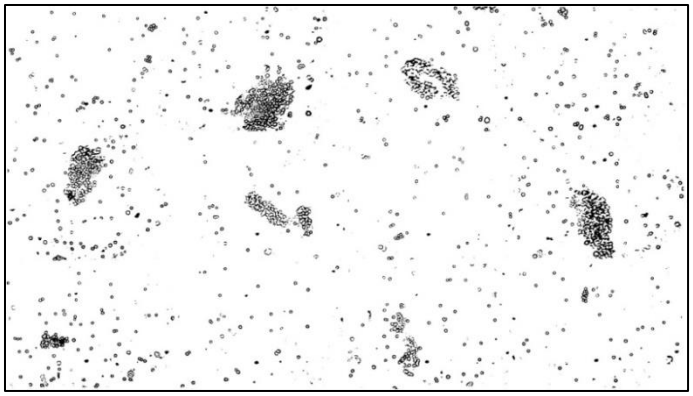

Figure 106: A-549, galectin-3, 12 µM G6-*N*-acetyllactosamine functionalized dendrimer.

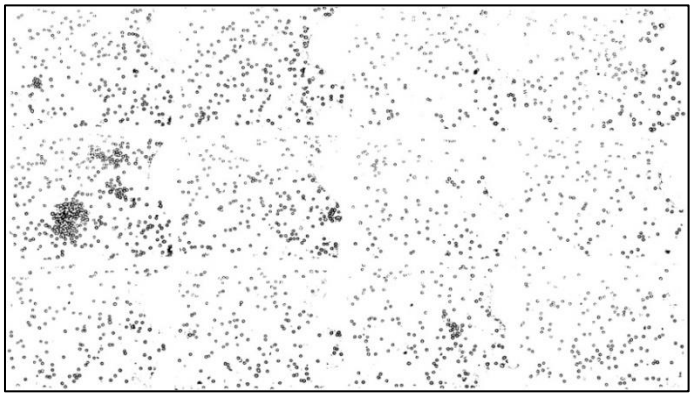

Figure 107: HT-1080 0 µM G2-*N*-acetyllactosamine functionalized dendrimer.

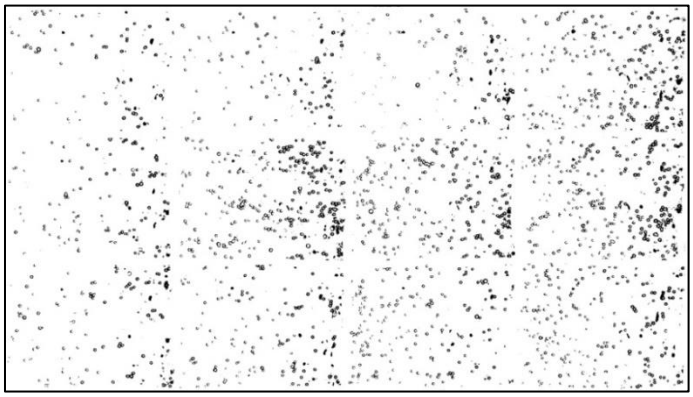

Figure 108: HT-1080 10 µM G2-*N*-acetyllactosamine functionalized dendrimer.

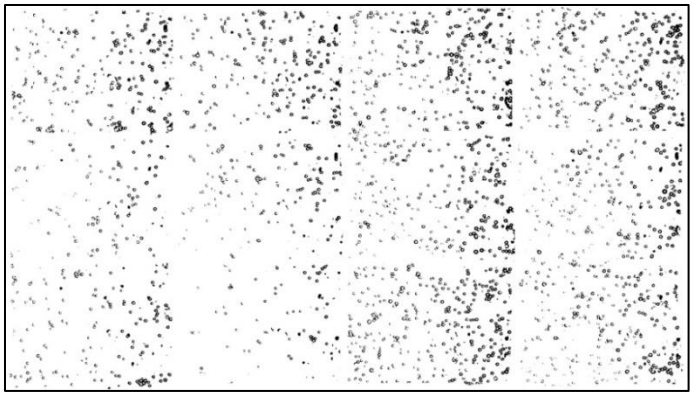

Figure 109: HT-1080 20 µM G2-*N*-acetyllactosamine functionalized dendrimer.

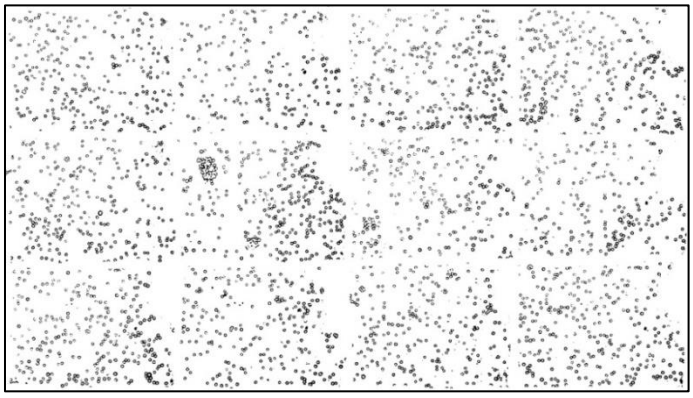

Figure 110: HT-1080 34 µM G2-*N*-acetyllactosamine functionalized dendrimer.

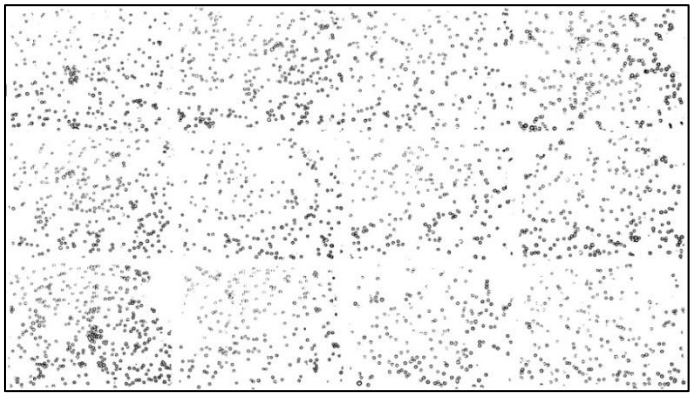

Figure 111: HT-1080 68 µM G2-*N*-acetyllactosamine functionalized dendrimer.

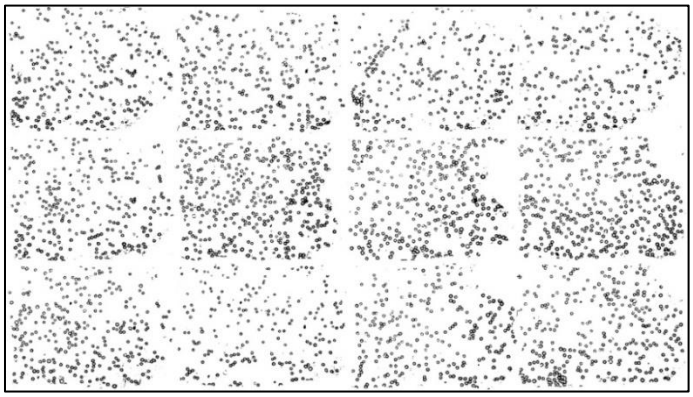

Figure 112: HT-1080 101 µM G2-*N*-acetyllactosamine functionalized dendrimer.

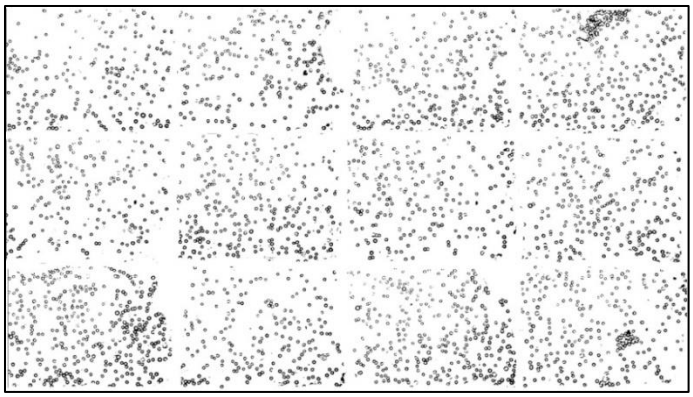

Figure 113: HT-1080 135 µM G2-*N*-acetyllactosamine functionalized dendrimer.

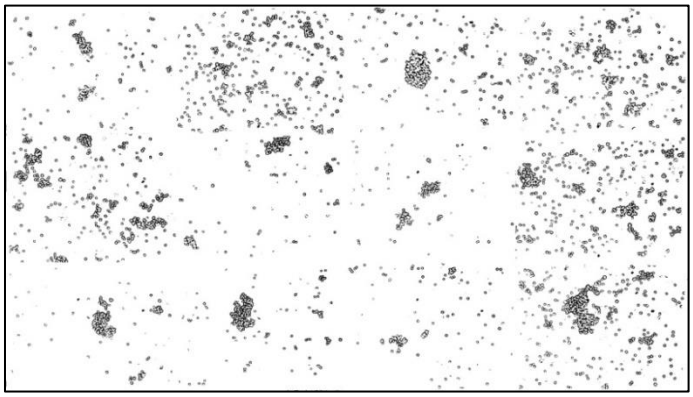

Figure 114: HT-1080, galectin-3, 0 µM G2-*N*-acetyllactosamine functionalized dendrimer.

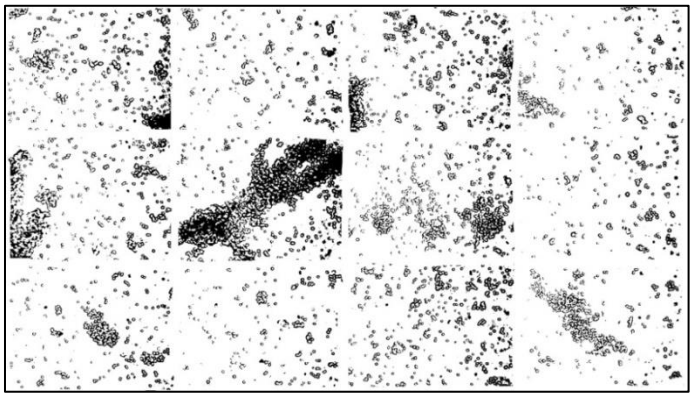

Figure 115: HT-1080, galectin-3, 10 µM G2-*N*-acetyllactosamine functionalized dendrimer.

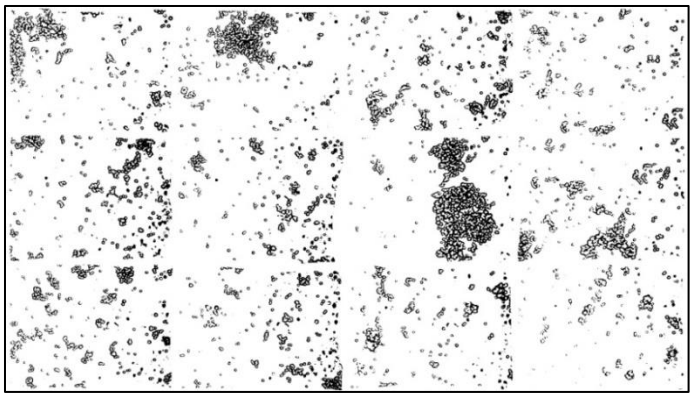

Figure 116: HT-1080, galectin-3, 20 µM G2-*N*-acetyllactosamine functionalized dendrimer.

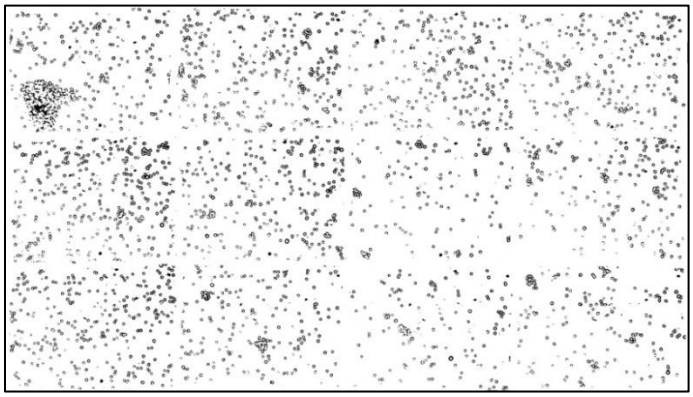

Figure 117: HT-1080, galectin-3, 34 µM G2-*N*-acetyllactosamine functionalized dendrimer.

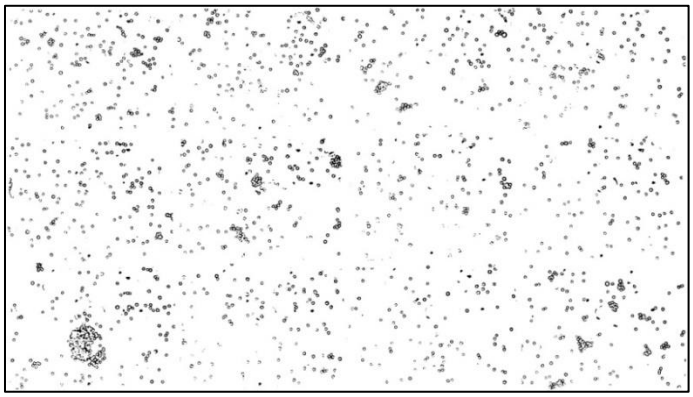

Figure 118: HT-1080, galectin-3, 68 µM G2-*N*-acetyllactosamine functionalized dendrimer.

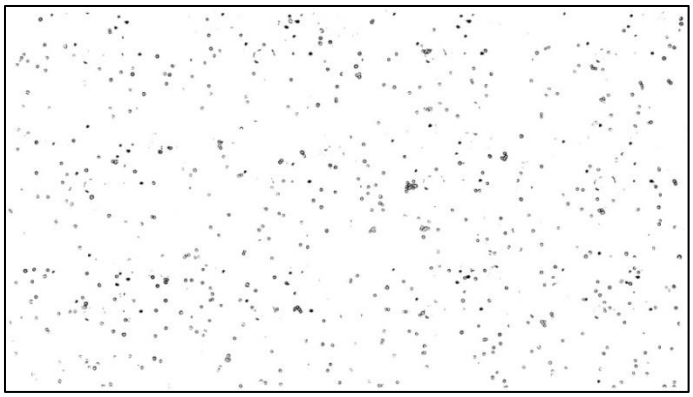

Figure 119: HT-1080, galectin-3, 101 µM G2-*N*-acetyllactosamine functionalized dendrimer.

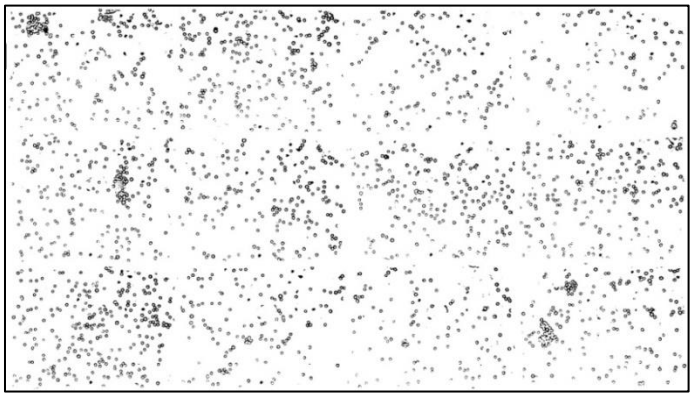

Figure 120: HT-1080, galectin-3, 135 µM G2-*N*-acetyllactosamine functionalized dendrimer.

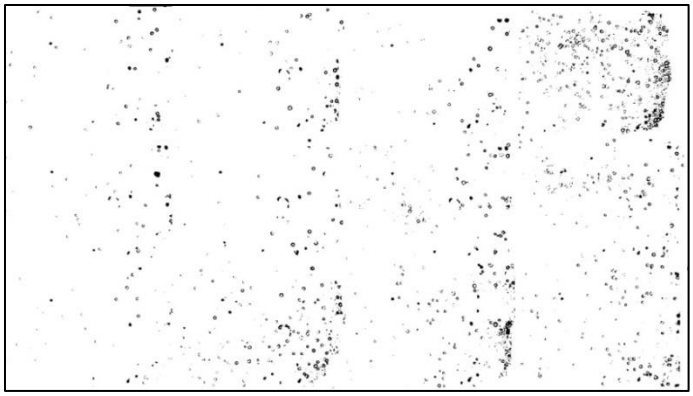

Figure 121: HT-1080 0 µM G3-*N*-acetyllactosamine functionalized dendrimer.

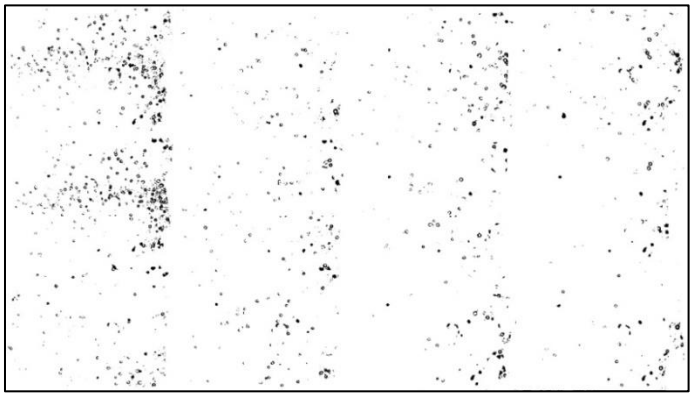

Figure 122: HT-1080 10 µM G3-*N*-acetyllactosamine functionalized dendrimer.

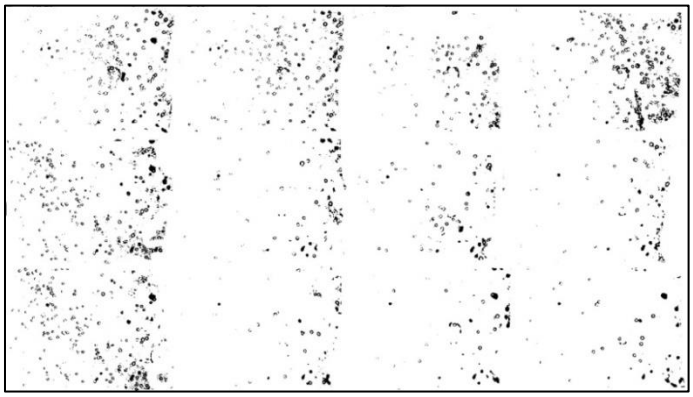

Figure 123: HT-1080 20 µM G3-*N*-acetyllactosamine functionalized dendrimer.

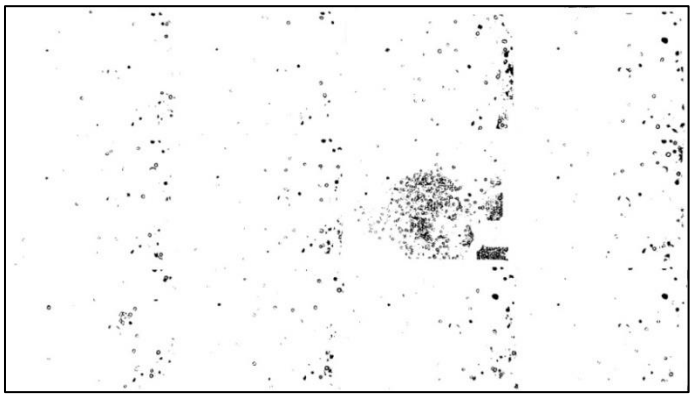

Figure 124: HT-1080 34 µM G3-*N*-acetyllactosamine functionalized dendrimer.

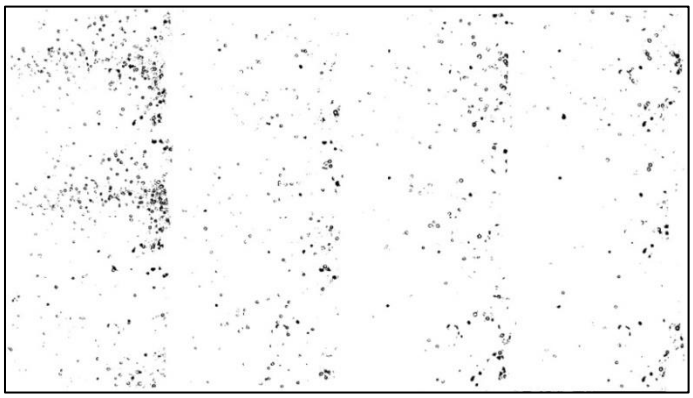

Figure 125: HT-1080 68 µM G3-*N*-acetyllactosamine functionalized dendrimer.

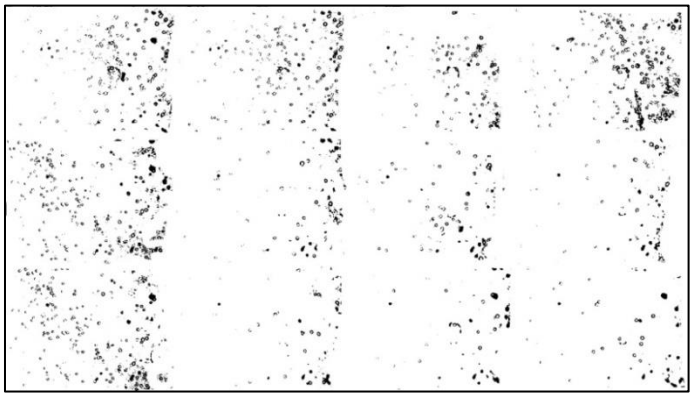

Figure 126: HT-1080 101 µM G3-*N*-acetyllactosamine functionalized dendrimer.

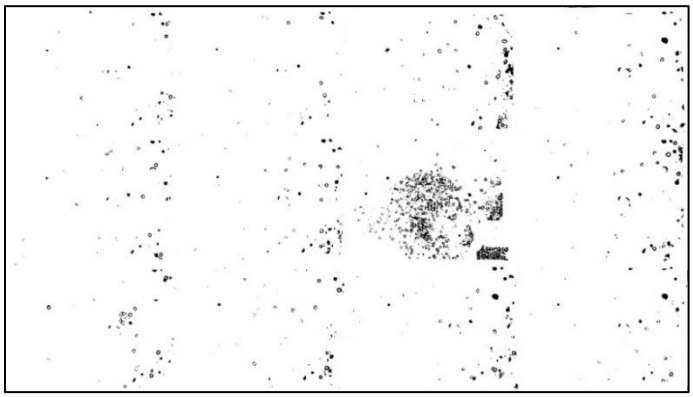

Figure 127: HT-1080 135 µM G3-*N*-acetyllactosamine functionalized dendrimer.

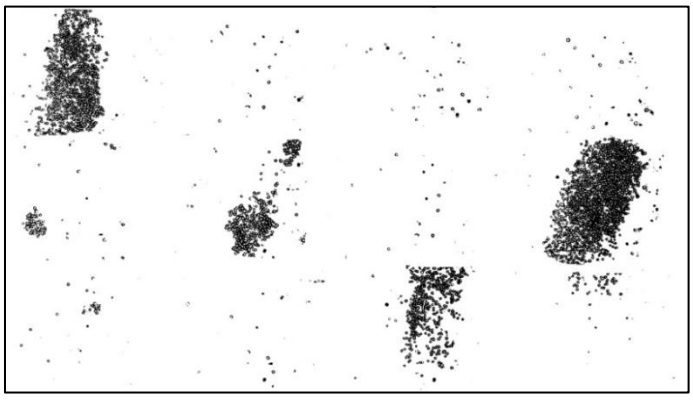

Figure 128: HT-1080, galectin-3, 0 µM G3-*N*-acetyllactosamine functionalized dendrimer.

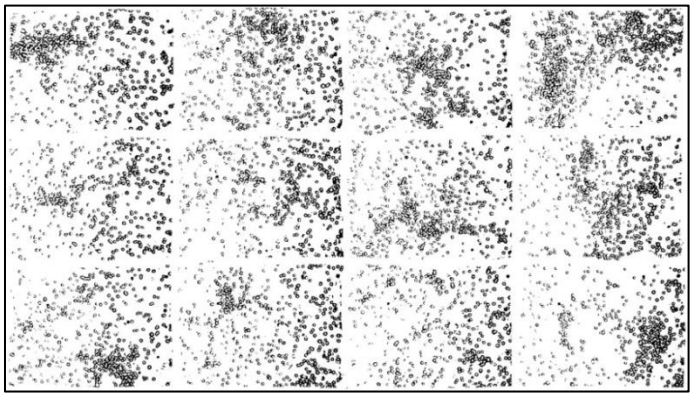

Figure 129: HT-1080, galectin-3, 18 µM G3-*N*-acetyllactosamine functionalized dendrimer.

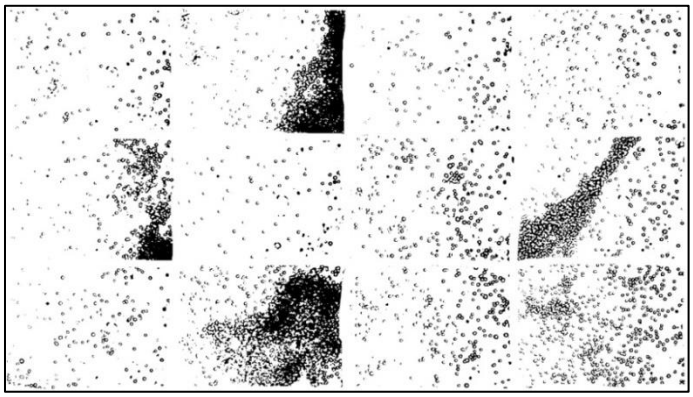

Figure 130: HT-1080, galectin-3, 36 µM G3-*N*-acetyllactosamine functionalized dendrimer.

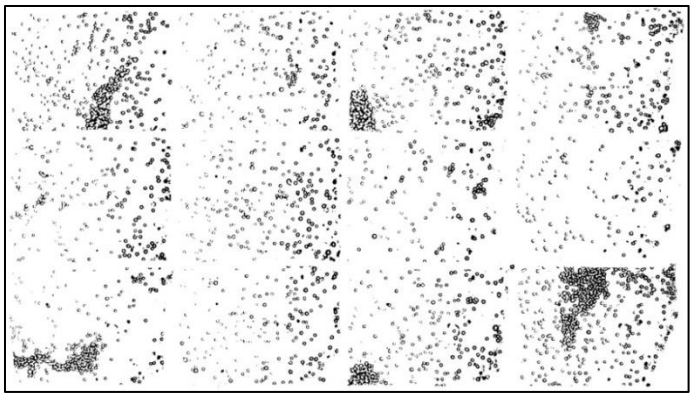

Figure 131: HT-1080, galectin-3, 54 µM G3-*N*-acetyllactosamine functionalized dendrimer.

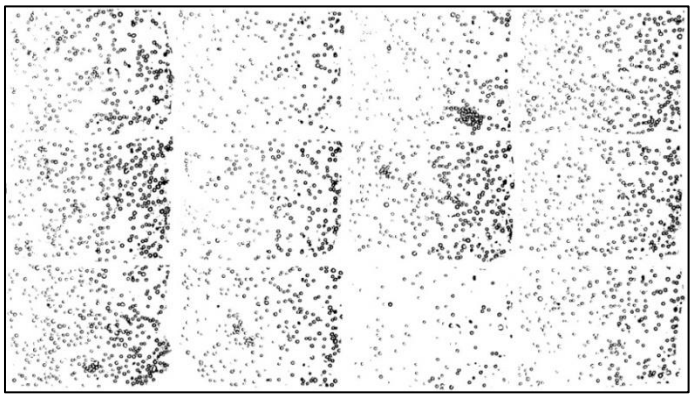

Figure 132: HT-1080, galectin-3, 72 µM G3-*N*-acetyllactosamine functionalized dendrimer.

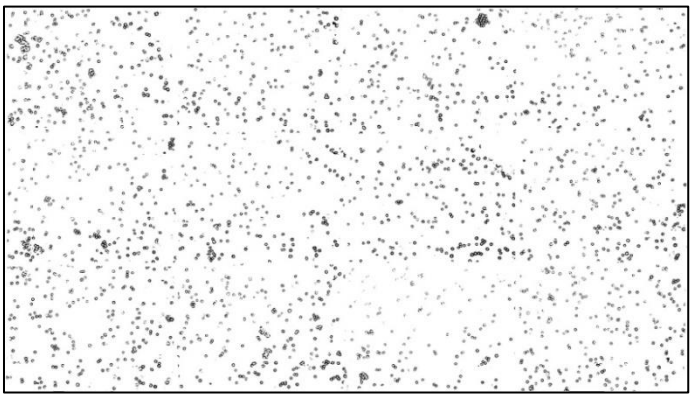

Figure 133: HT-1080 0 µM G4-*N*-acetyllactosamine functionalized dendrimer.

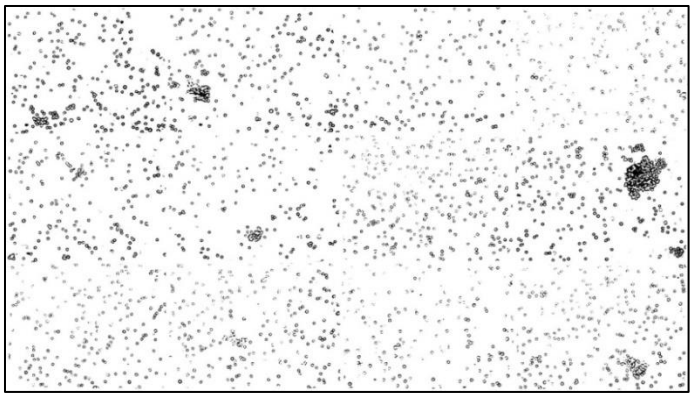

Figure 134: HT-1080 8 µM G4-*N*-acetyllactosamine functionalized dendrimer.

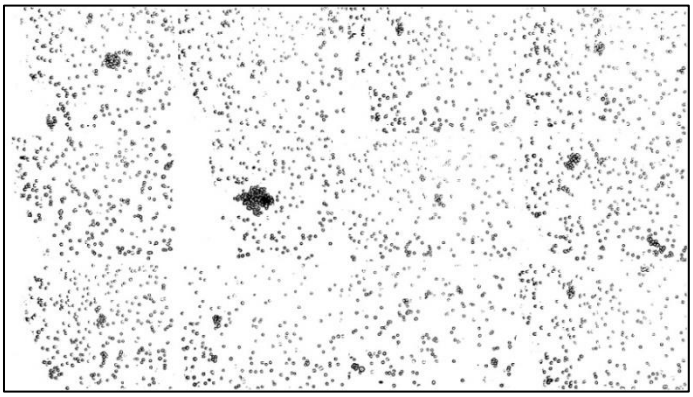

Figure 135: HT-1080 16 µM G4-*N*-acetyllactosamine functionalized dendrimer.

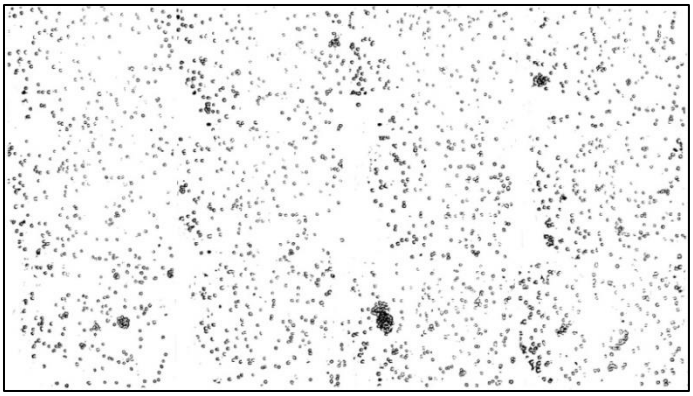

Figure 136: HT-1080 24 µM G4-*N*-acetyllactosamine functionalized dendrimer.

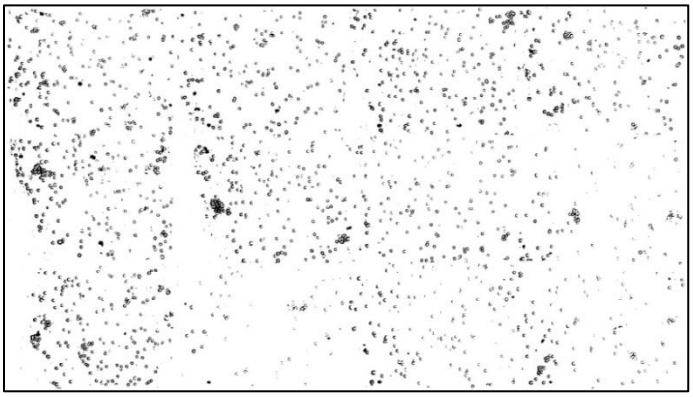

Figure 137: HT-1080 32 µM G4-*N*-acetyllactosamine functionalized dendrimer.

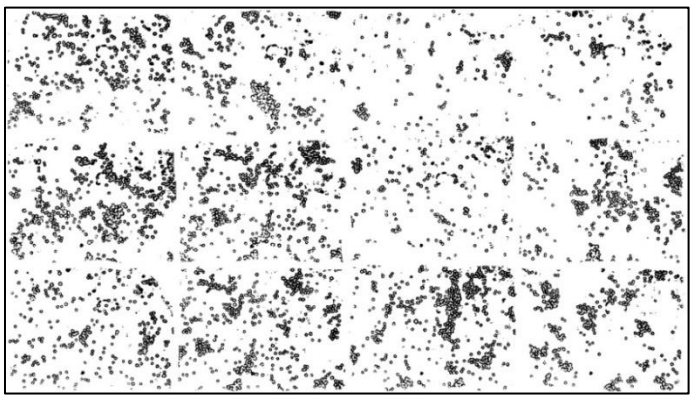

Figure 138: HT-1080, galectin-3, 0 µM G4-*N*-acetyllactosamine functionalized dendrimer.

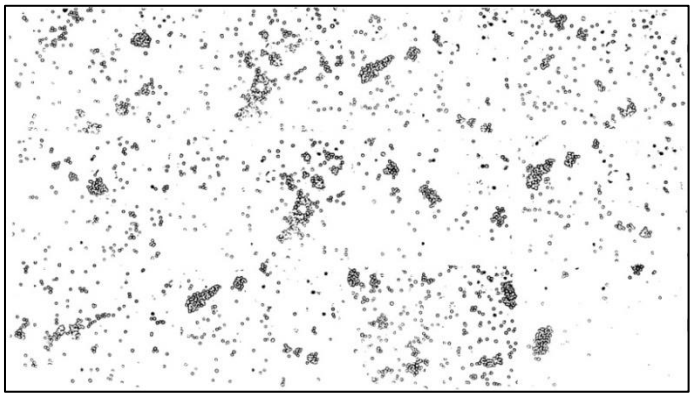

Figure 139: HT-1080, galectin-3, 8 µM G4-*N*-acetyllactosamine functionalized dendrimer.

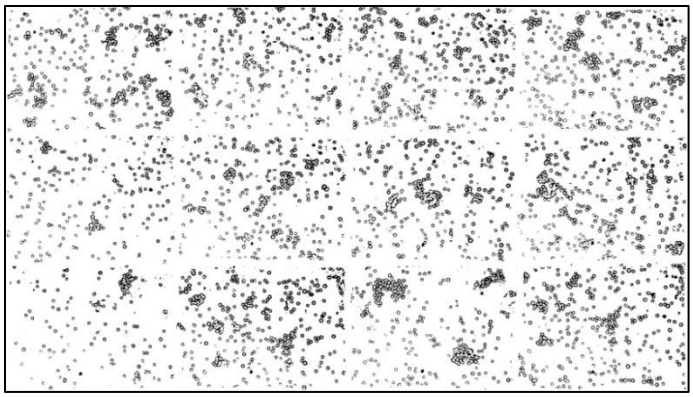

Figure 140: HT-1080, galectin-3, 16 µM G4-*N*-acetyllactosamine functionalized dendrimer.

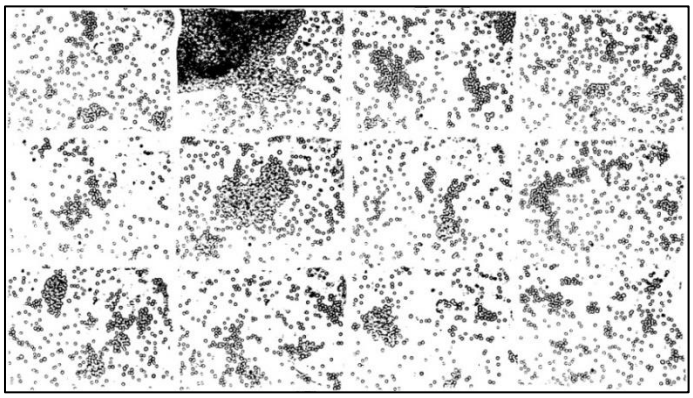

Figure 141: HT-1080, galectin-3, 24 µM G4-*N*-acetyllactosamine functionalized dendrimer.

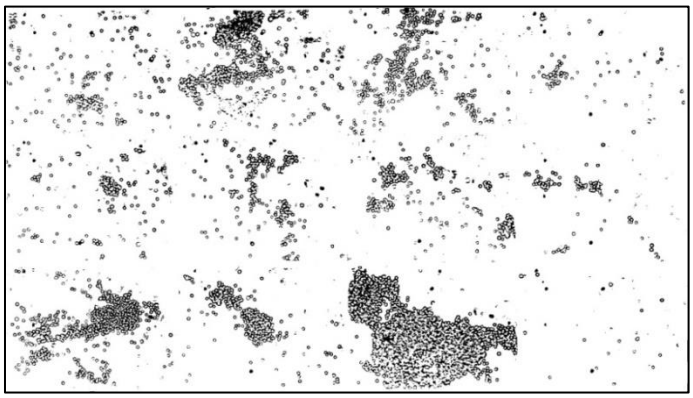

Figure 142: HT-1080, galectin-3, 32 µM G4-*N*-acetyllactosamine functionalized dendrimer.

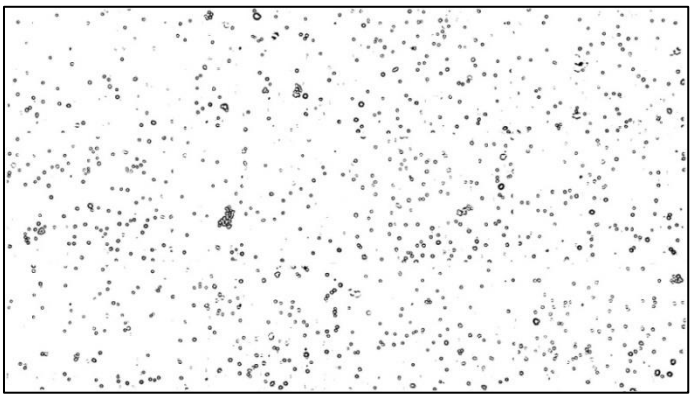

Figure 143: HT-1080 0 µM G6-*N*-acetyllactosamine functionalized dendrimer.

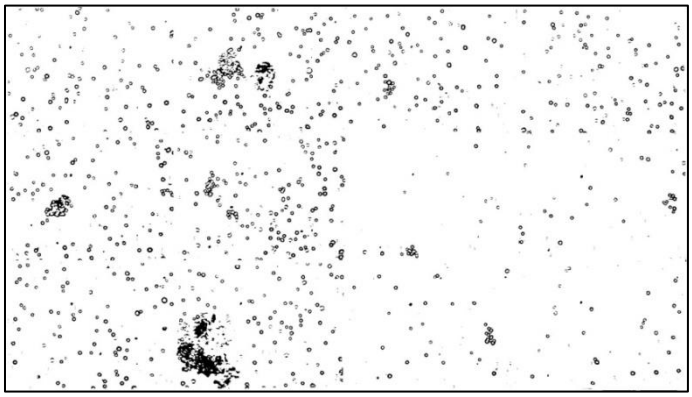

Figure 144: HT-1080 3 µM G6-*N*-acetyllactosamine functionalized dendrimer.

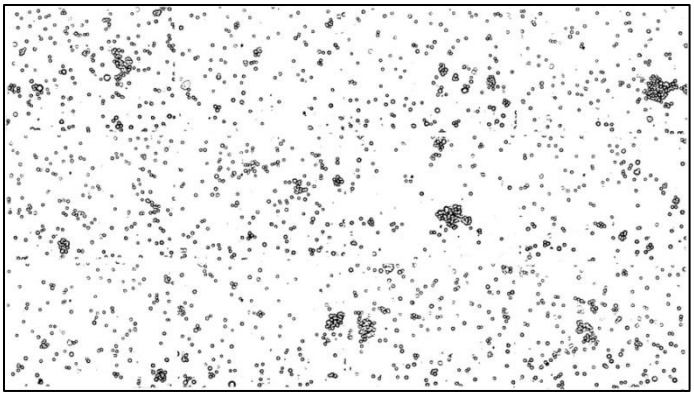

Figure 145: HT-1080 6 µM G6-*N*-acetyllactosamine functionalized dendrimer.

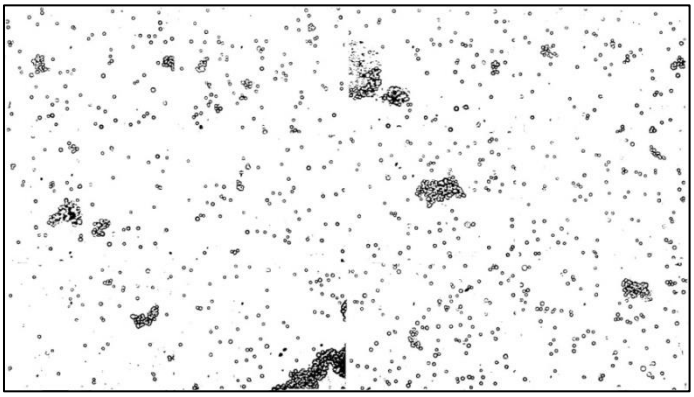

Figure 146: HT-1080 9 µM G6-*N*-acetyllactosamine functionalized dendrimer.

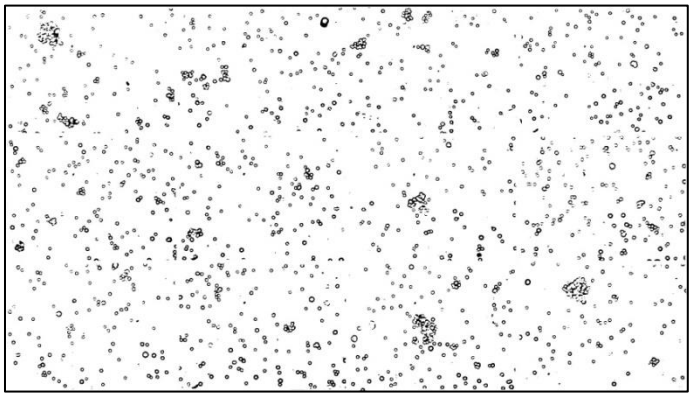

Figure 147: HT-1080 12 µM G6-*N*-acetyllactosamine functionalized dendrimer.

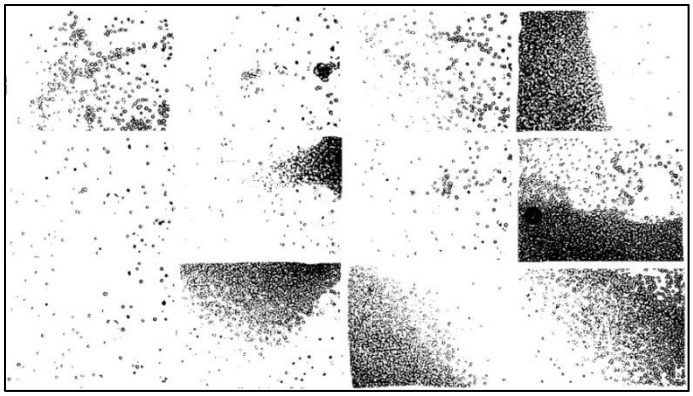

Figure 148: HT-1080, galectin-3, 0 µM G6-*N*-acetyllactosamine functionalized dendrimer.

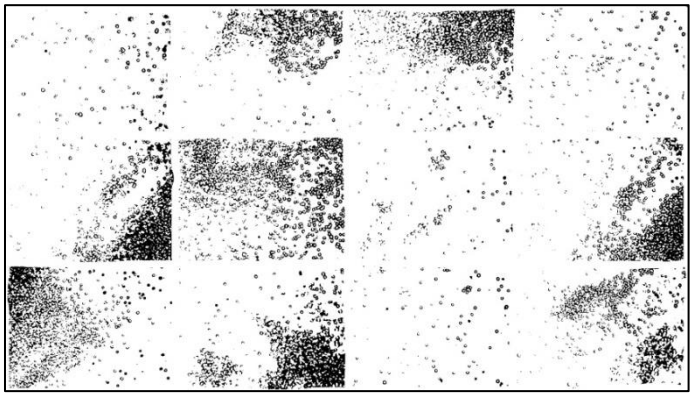

Figure 149: HT-1080, galectin-3, 3 µM G6-*N*-acetyllactosamine functionalized dendrimer.

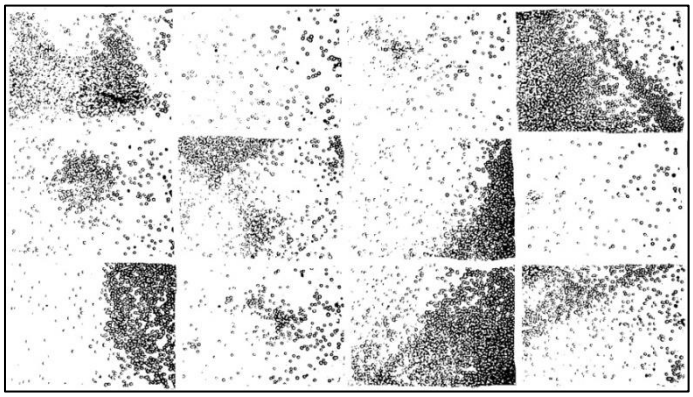

Figure 150: HT-1080, galectin-3, 6µM G6-*N*-acetyllactosamine functionalized dendrimer.

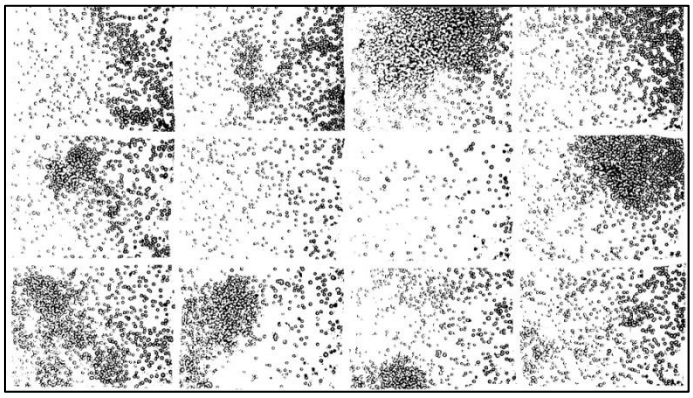

Figure 151: HT-1080, galectin-3, 9 µM G6-*N*-acetyllactosamine functionalized dendrimer.

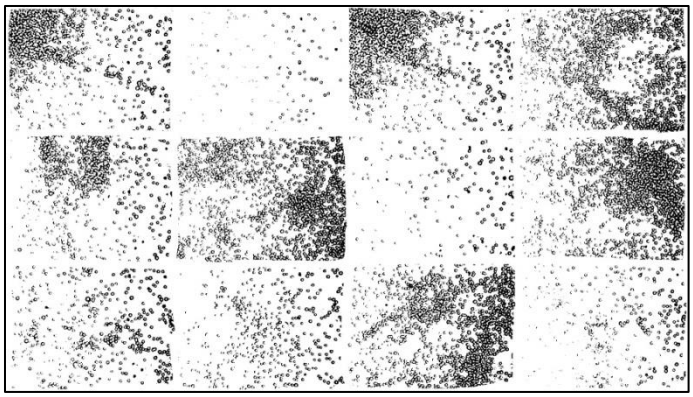

Figure 152: HT-1080, galectin-3, 12 µM G6-*N*-acetyllactosamine functionalized dendrimer.

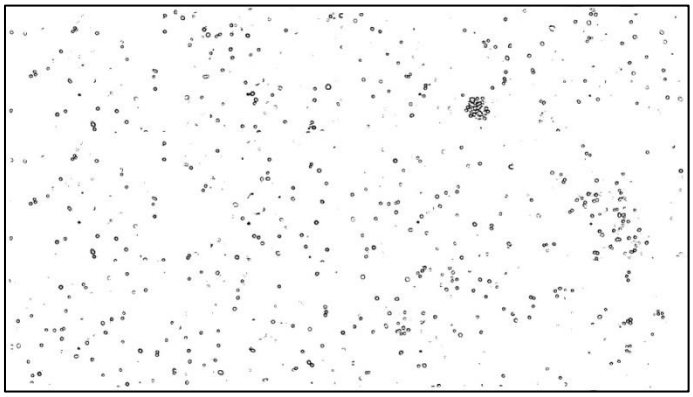

Figure 153: DU-145 0 µM G2-*N*-acetyllactosamine functionalized dendrimer.

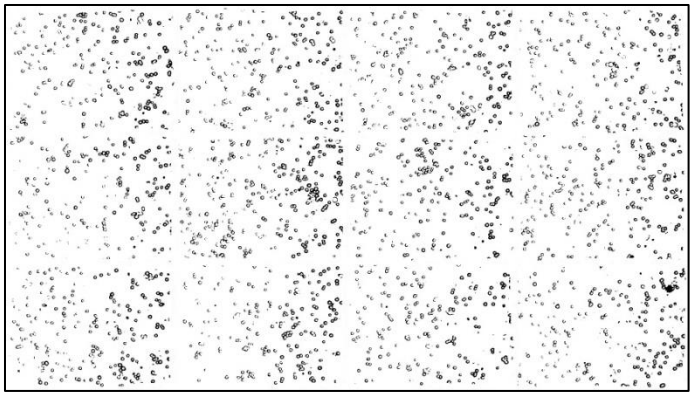

Figure 154: DU-145 10 µM G2-*N*-acetyllactosamine functionalized dendrimer.

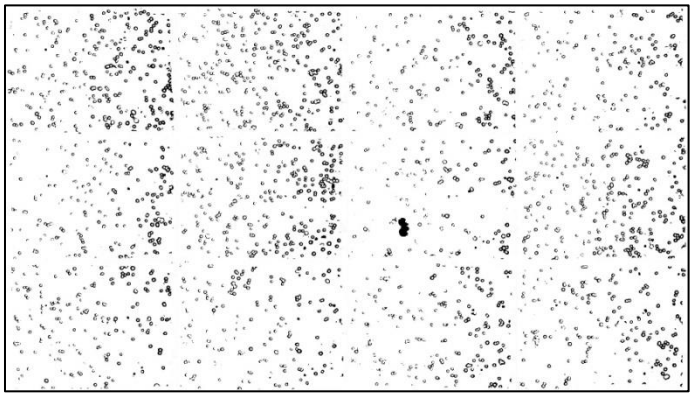

Figure 155: DU-145 20 µM G2-*N*-acetyllactosamine functionalized dendrimer.

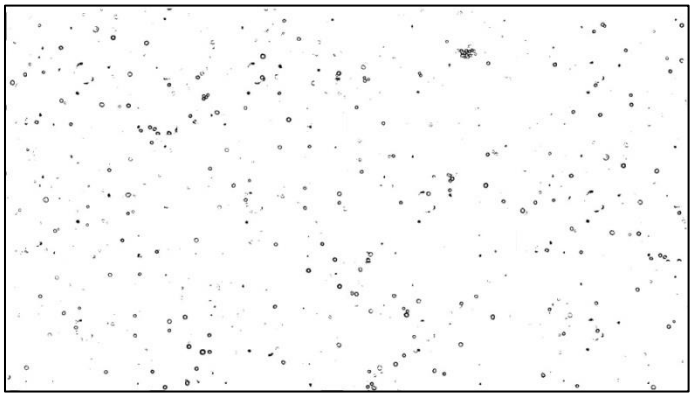

Figure 156: DU-145 34 µM G2-*N*-acetyllactosamine functionalized dendrimer.

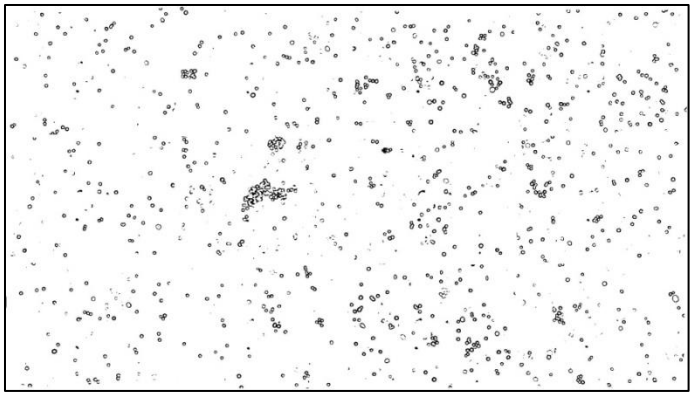

Figure 157: DU-145 68 µM G2-*N*-acetyllactosamine functionalized dendrimer.

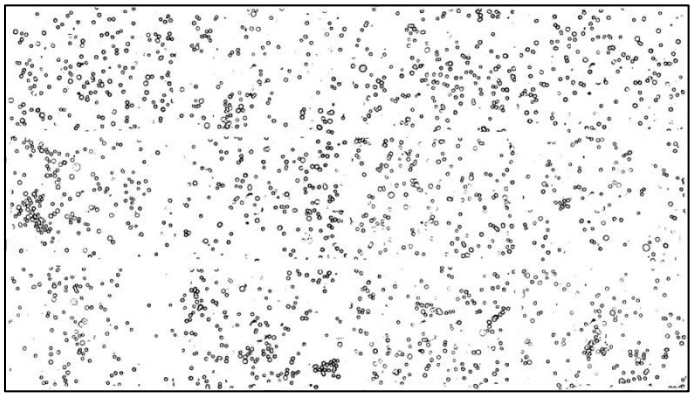

Figure 158: DU-145 101 µM G2-*N*-acetyllactosamine functionalized dendrimer.

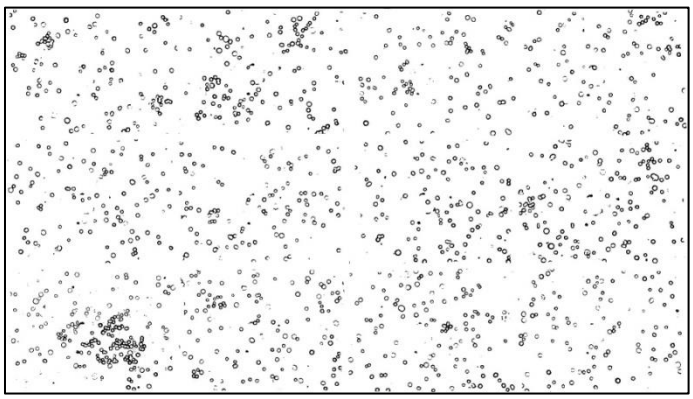

Figure 159: DU-145 135 µM G2-*N*-acetyllactosamine functionalized dendrimer.

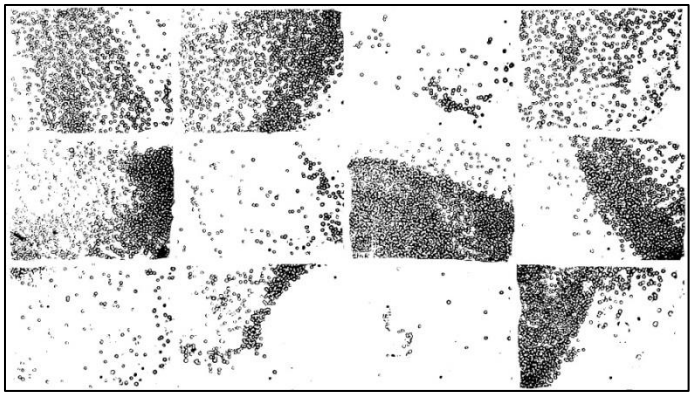

Figure 160: DU-145, galectin-3, 0 µM G2-*N*-acetyllactosamine functionalized dendrimer.

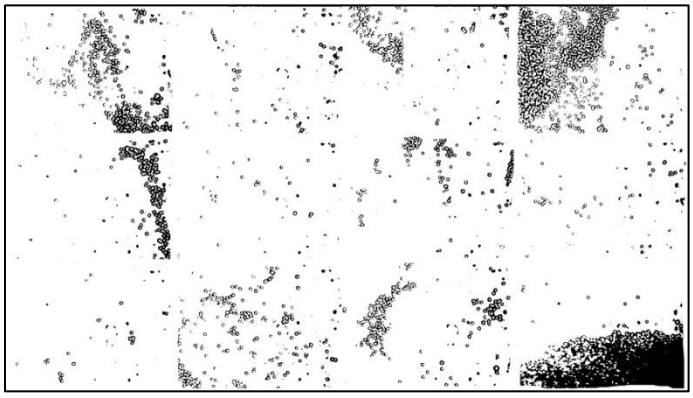

Figure 161: DU-145, galectin-3, 10 µM G2-*N*-acetyllactosamine functionalized dendrimer.

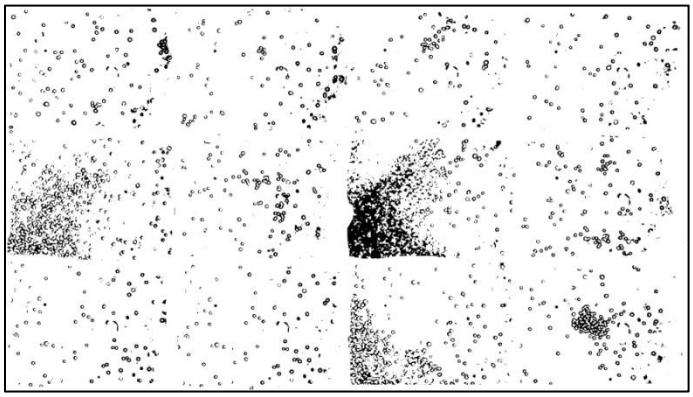

Figure 162: DU-145, galectin-3, 20 µM G2-*N*-acetyllactosamine functionalized dendrimer.

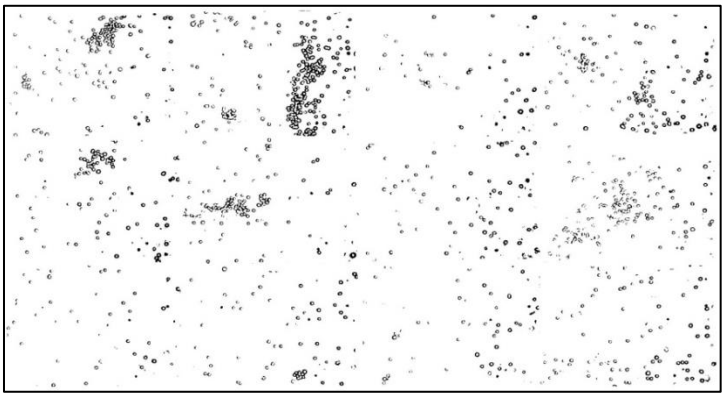

Figure 163: DU-145, galectin-3, 34 µM G2-*N*-acetyllactosamine functionalized dendrimer.

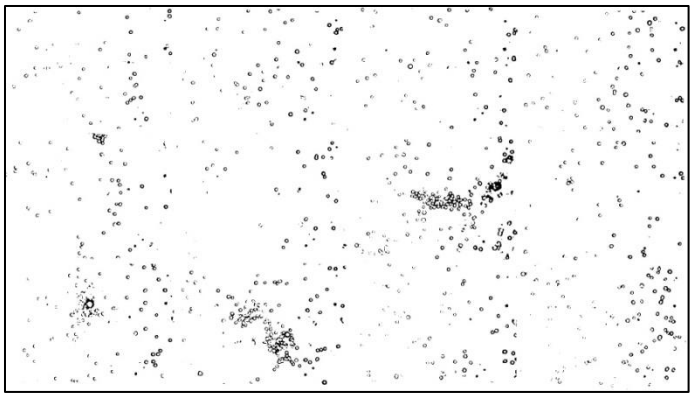

Figure 164: DU-145, galectin-3, 68 µM G2-*N*-acetyllactosamine functionalized dendrimer.

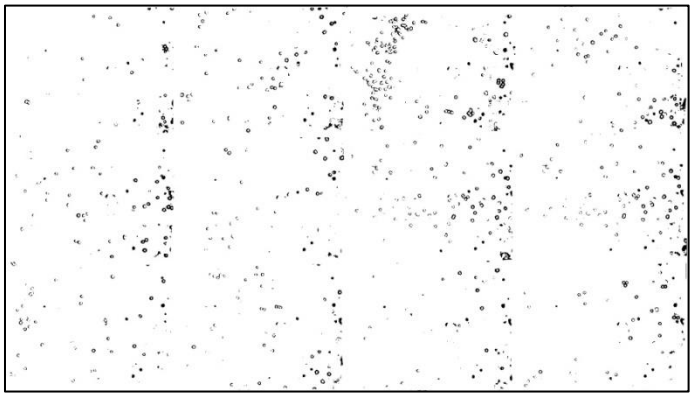

Figure 165: DU-145, galectin-3, 101 µM G2-*N*-acetyllactosamine functionalized dendrimer.

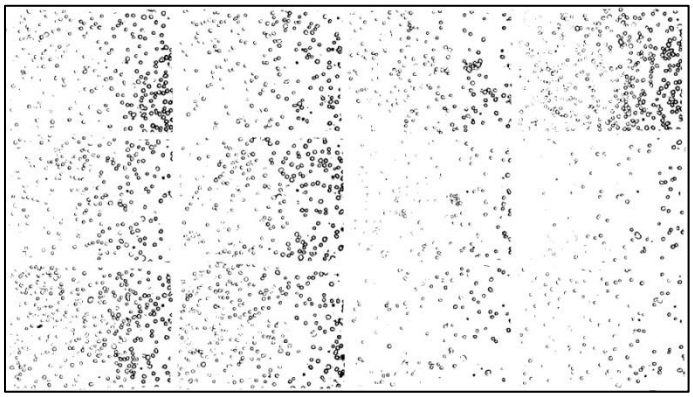

Figure 166: DU-145, galectin-3, 135 µM G2-*N*-acetyllactosamine functionalized dendrimer.

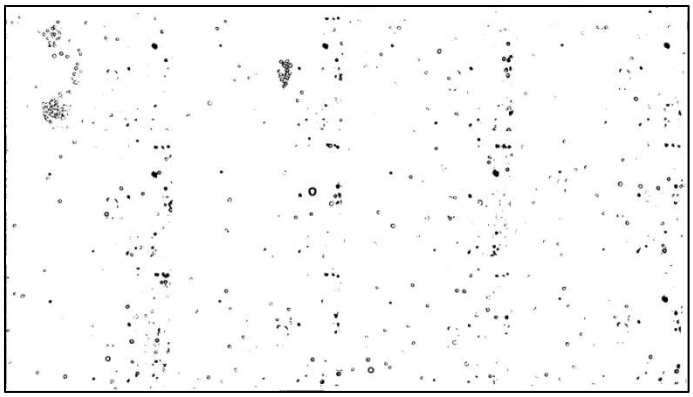

Figure 167: DU-145 0 µM G3-*N*-acetyllactosamine functionalized dendrimer.

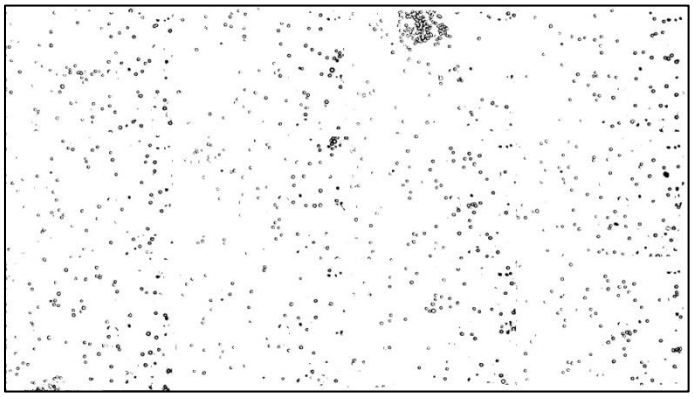

Figure 168: DU-145 18 µM G3-*N*-acetyllactosamine functionalized dendrimer.

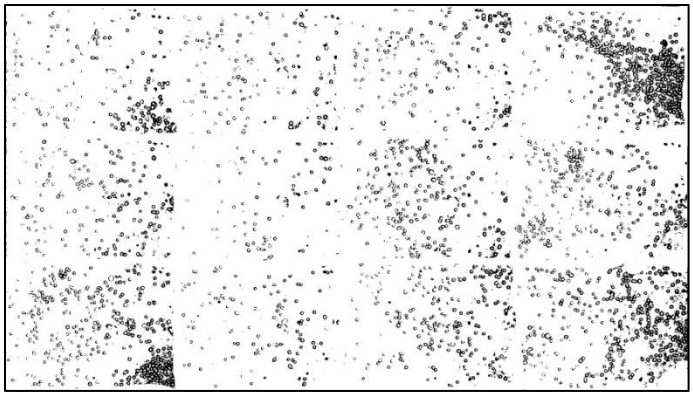

Figure 169: DU-145 36 µM G3-*N*-acetyllactosamine functionalized dendrimer.

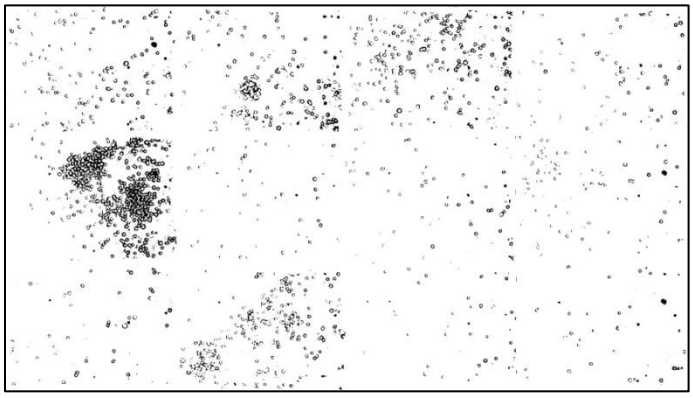

Figure 170: DU-145 54 µM G3-*N*-acetyllactosamine functionalized dendrimer.

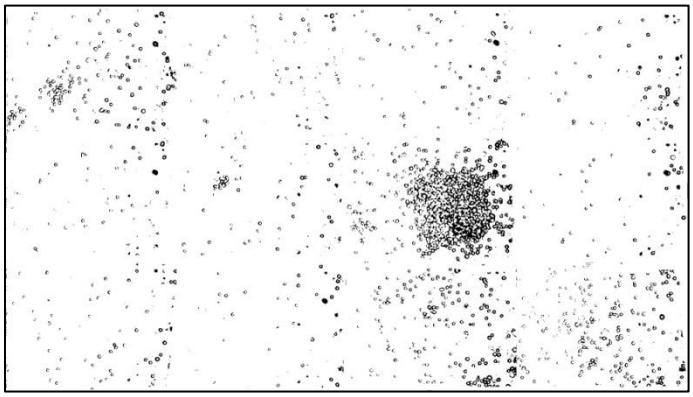

Figure 171: DU-145 72 µM G3-*N*-acetyllactosamine functionalized dendrimer.

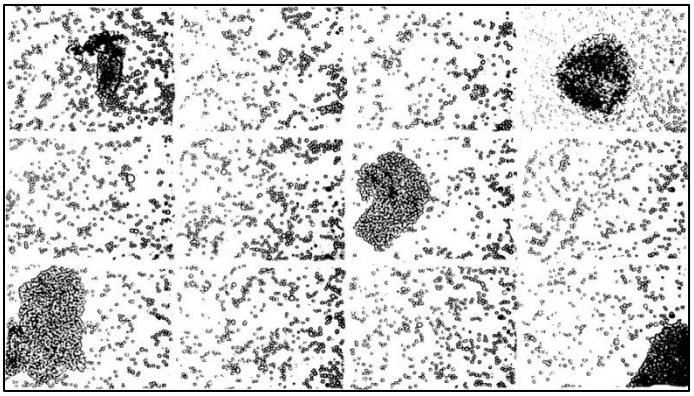

Figure 172: DU-145, galectin-3, 0 µM G3-*N*-acetyllactosamine functionalized dendrimer.

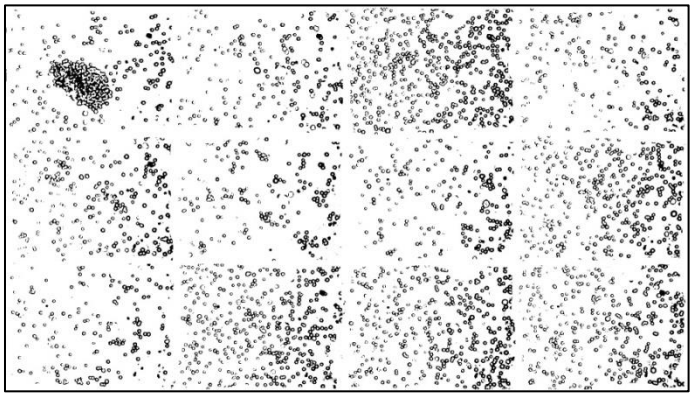

Figure 173: DU-145, galectin-3, 18 µM G3-N-acetyllactosamine functionalized dendrimer.

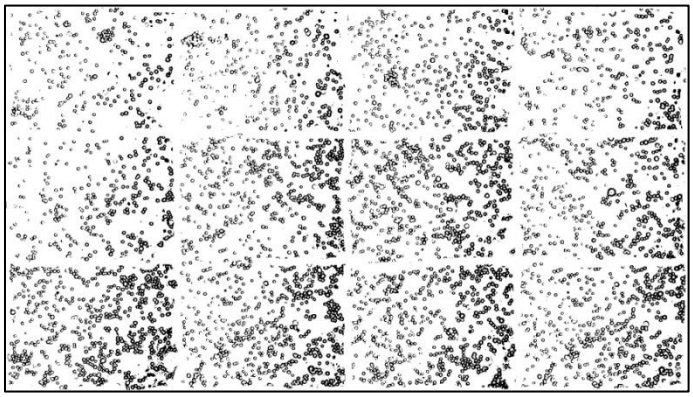

Figure 174: DU-145, galectin-3, 36 µM G3-N-acetyllactosamine functionalized dendrimer.

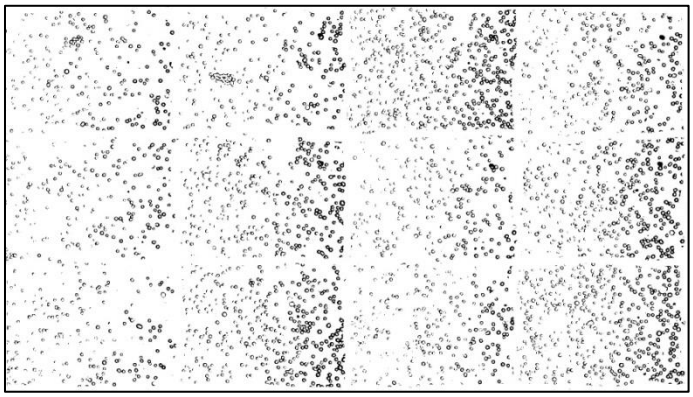

Figure 175: DU-145, galectin-3, 54 µM G3-N-acetyllactosamine functionalized dendrimer.

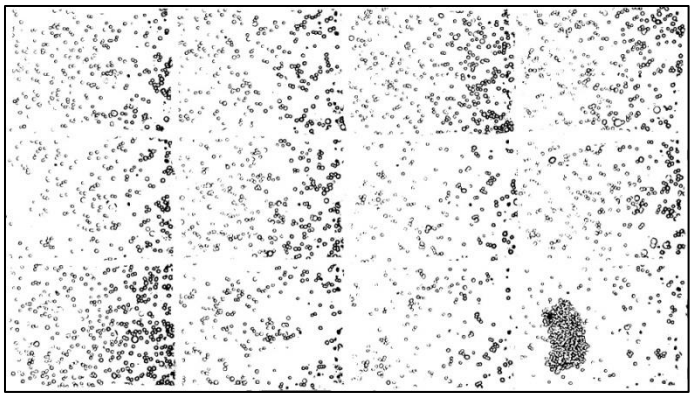

Figure 176: DU-145, galectin-3, 72 µM G3-*N*-acetyllactosamine functionalized dendrimer.

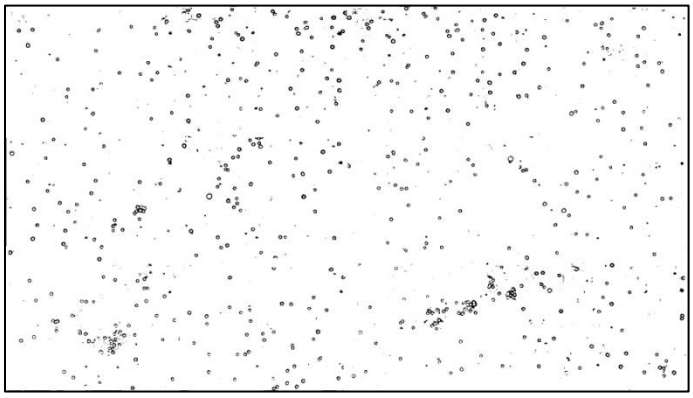

Figure 177: DU-145 0 µM G4-*N*-acetyllactosamine functionalized dendrimer.

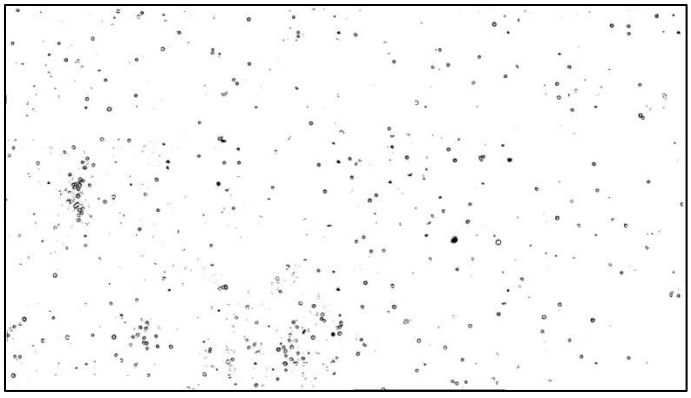

Figure 178: DU-145 8 µM G4-N-acetyllactosamine functionalized dendrimer.

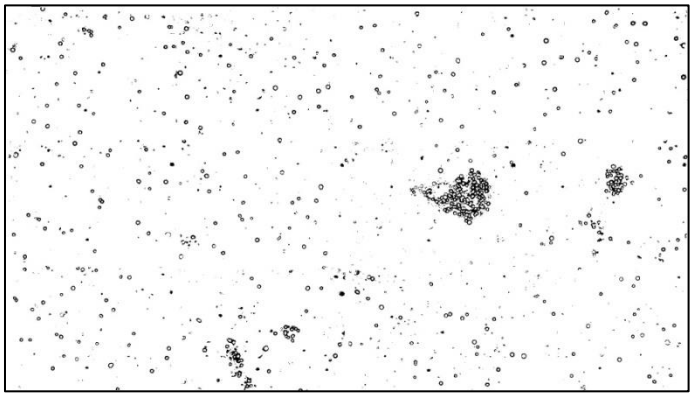

Figure 179: DU-145 16 µM G4-*N*-acetyllactosamine functionalized dendrimer.

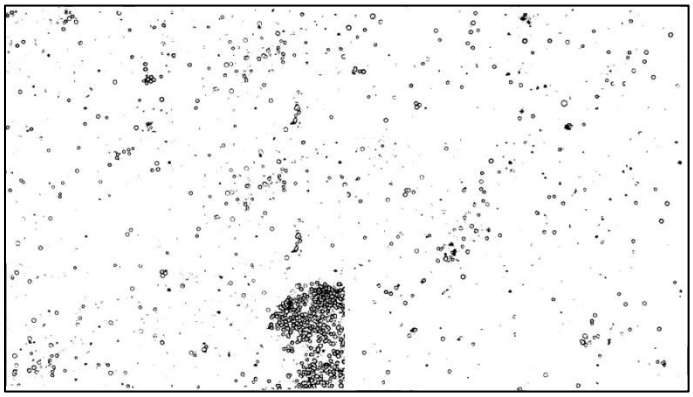

Figure 180: DU-145 24 µM G4-*N*-acetyllactosamine functionalized dendrimer.

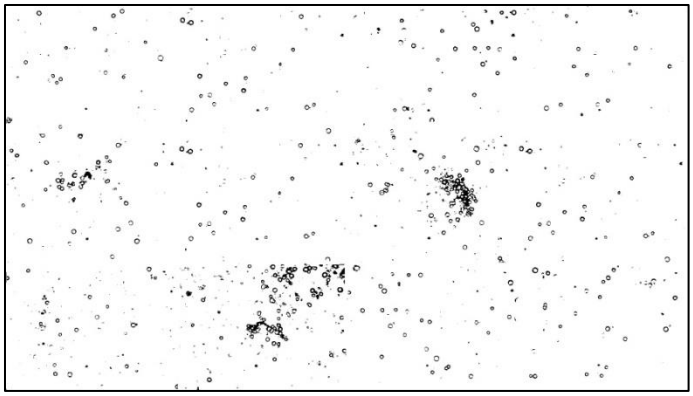

Figure 181: HT-1080 135 µM G2-N-acetyllactosamine functionalized dendrimer.

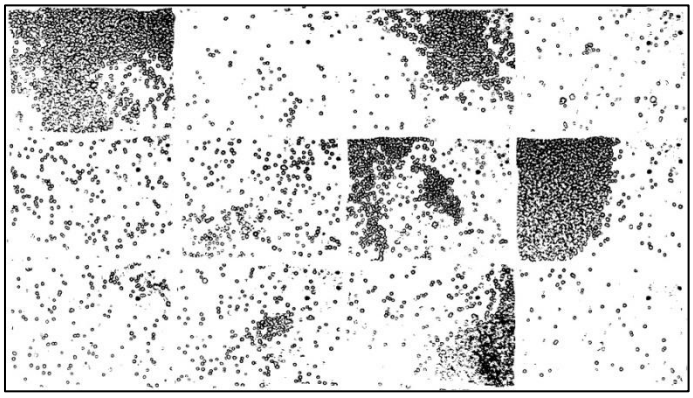

Figure 182: DU-145, galectin-3, 0 µM G4-*N*-acetyllactosamine functionalized dendrimer.

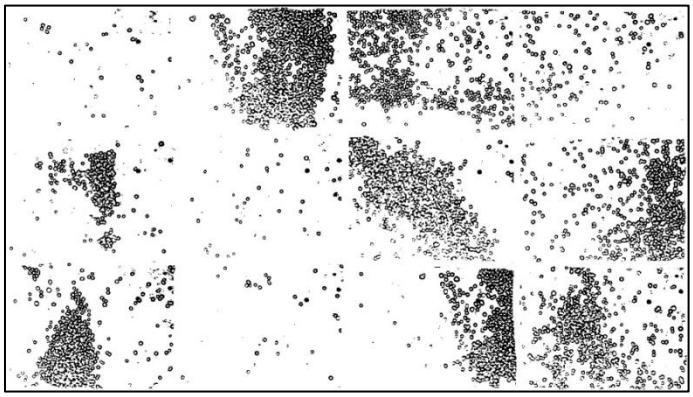

Figure 183: DU-145, galectin-3, 8 µM G4-*N*-acetyllactosamine functionalized dendrimer.

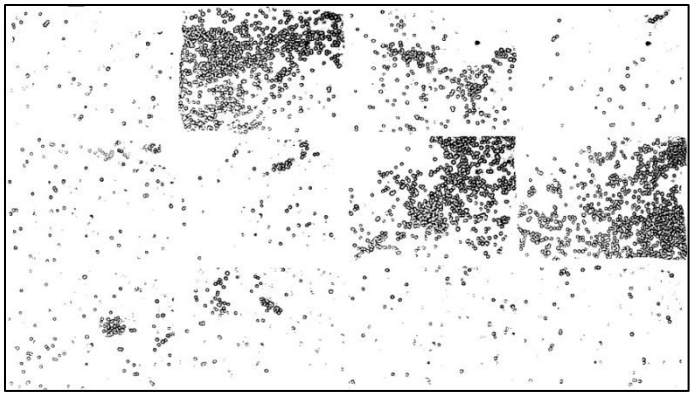

Figure 184: DU-145, galectin-3, 16 µM G4-*N*-acetyllactosamine functionalized dendrimer.

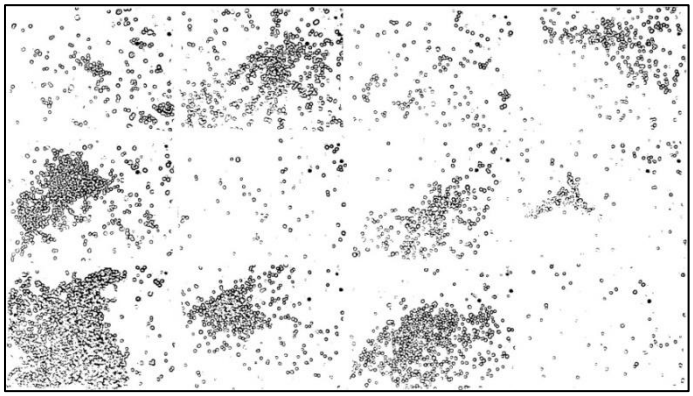

Figure 185: DU-145, galectin-3, 24 µM G4-*N*-acetyllactosamine functionalized dendrimer.

Figure 186: DU-145, galectin-3, 32 µM G4-*N*-acetyllactosamine functionalized dendrimer.

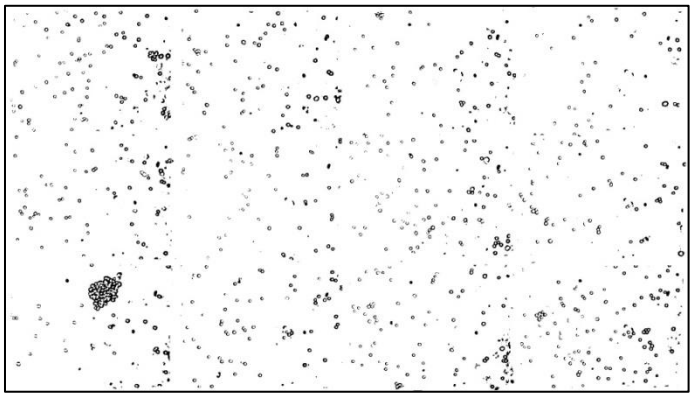

Figure 187: DU-145 0 µM G6-*N*-acetyllactosamine functionalized dendrimer.

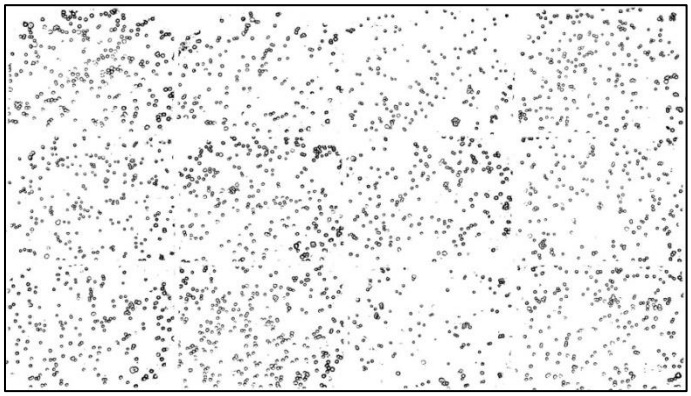

Figure 188: DU-145 3 µM G6-*N*-acetyllactosamine functionalized dendrimer.

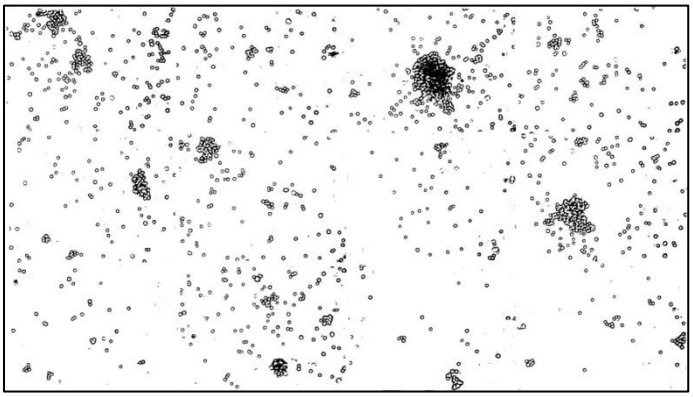

Figure 189: DU-145 6 µM G6-*N*-acetyllactosamine functionalized dendrimer.

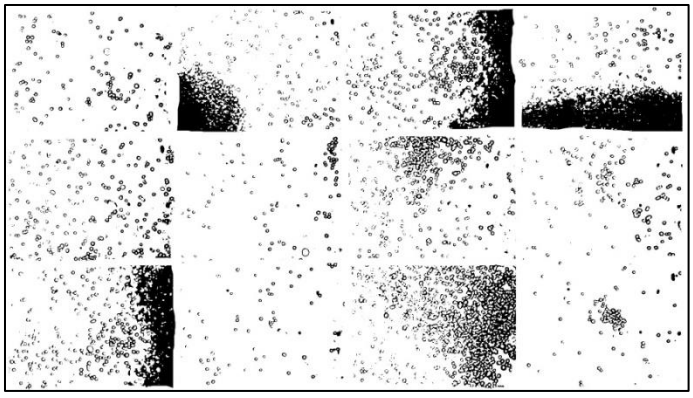

Figure 190: DU-145 9 µM G6-*N*-acetyllactosamine functionalized dendrimer.

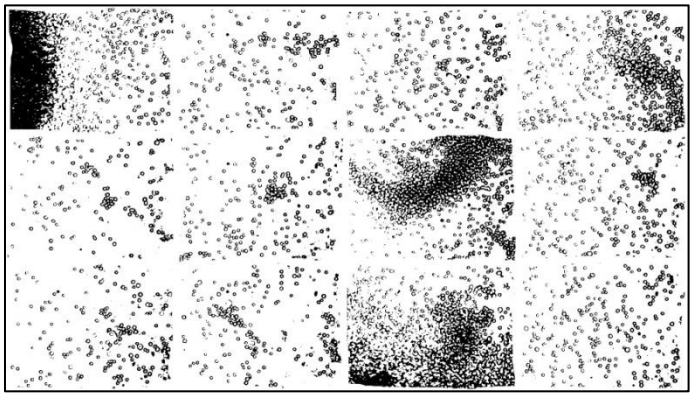

Figure 191: DU-145 12 µM G6-*N*-acetyllactosamine functionalized dendrimer.

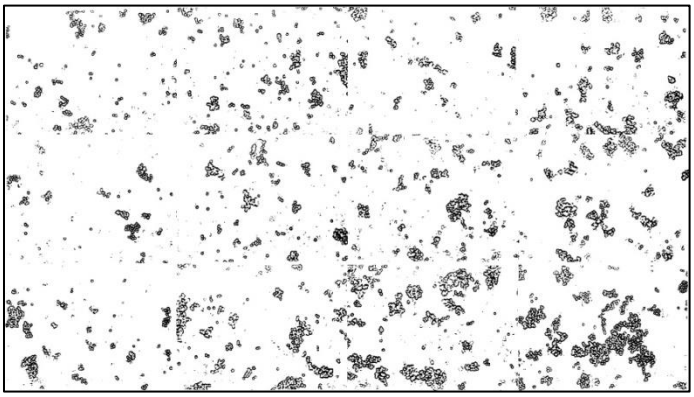

Figure 192: DU-145, galectin-3, 0 µM G6-*N*-acetyllactosamine functionalized dendrimer.

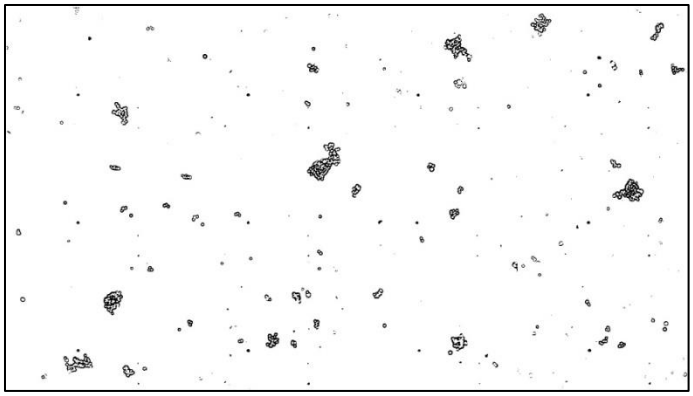

Figure 193: DU-145, galectin-3, 3 µM G6-*N*-acetyllactosamine functionalized dendrimer.

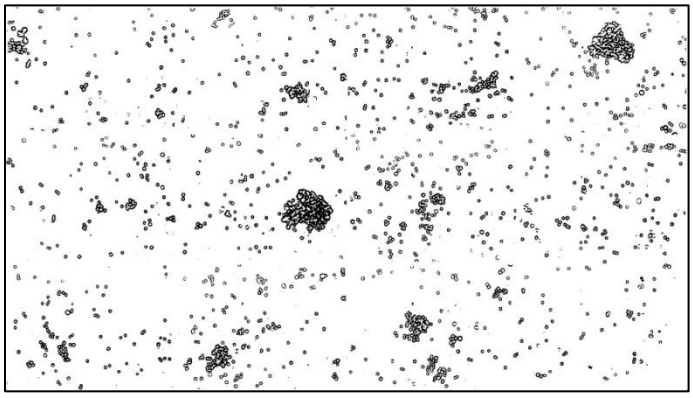

Figure 194: DU-145, galectin-3, 6 µM G6-N-acetyllactosamine functionalized dendrimer.

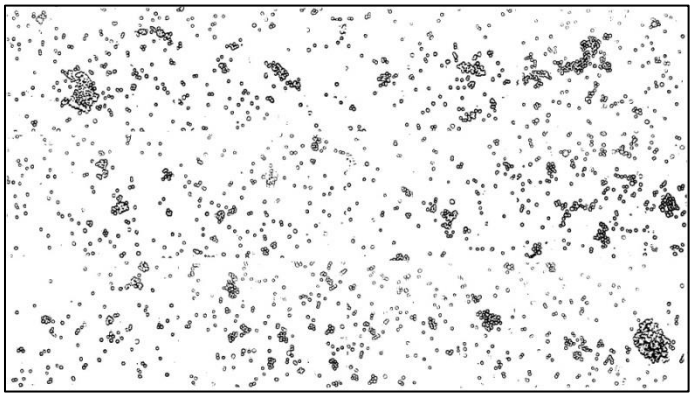

Figure 195: DU-145, galectin-3, 9 µM G6-N-acetyllactosamine functionalized dendrimer.

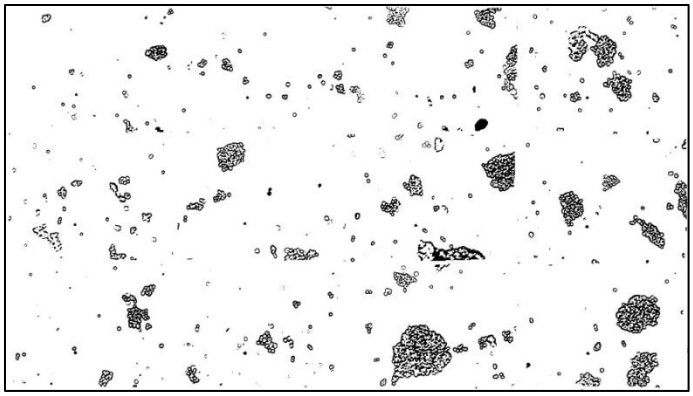

Figure 196: DU-145, galectin-3, 0 µM G6-N-acetyllactosamine functionalized dendrimer.

APPENDIX B

RELEVANT DATA FROM CHAPTER THREE

Chapter 3 Supporting Information

Supporting Information

Cyclodextrin-functionalized Chromatographic Materials Tailored for Reversible Adsorption.

Jessica H. Ennist‡, Eric A. Gobrogge‡, Kristian H. Schlick, Robert A. Walker, Mary J. Cloninger**

Department of Chemistry and Biochemistry, Montana State University, Bozeman, MT 59717

Corresponding Authors

*M. J. Cloninger. E-mail: mcloninger@chemistry.montana.edu

*R. A. Walker. Email: rawalker@chemistry.montana.edu

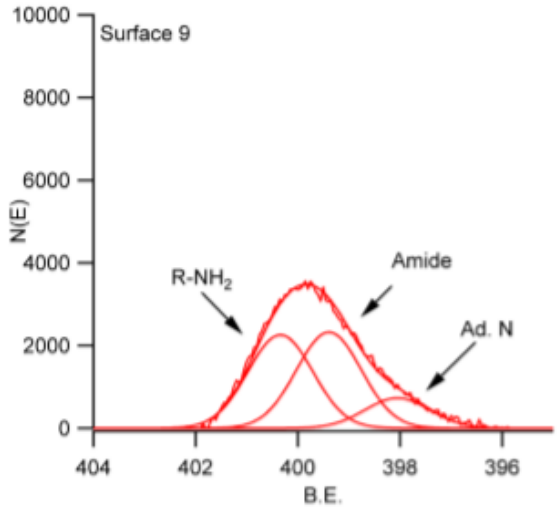

Figure S1. High resolution XPS scan of the nitrogen 1s region of surface **9**.

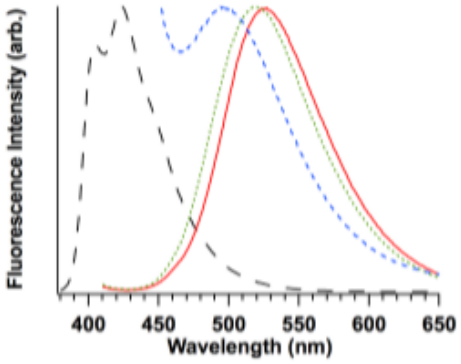

Figure S2. Fluorescence spectra of coumarin 152 in water (solid red), in water with excess β-cyclodextrin (dotted green), adsorbed to a β-cyclodextrin functionalized surface (small dashed blue), and in hexane (large dashed black).

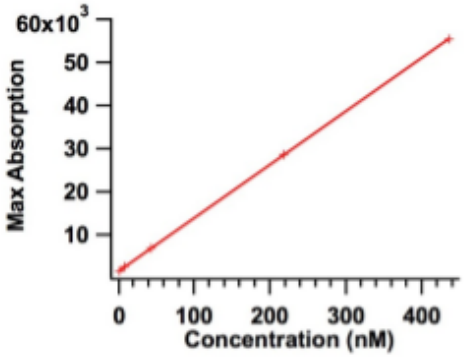

Figure S3. Calibration plot for quantifying wash from functionalized slides. The best-fit line has a slope of 124.07 ± 0.3008 and a y-intercept of 1530.6 ± 67.3.

Quantitative XPS Analysis of Surface Functionalization

Quantitative analysis of the XPS was performed using the methodology published by Geiger and co-workers.[1]

Dendronization: The data from the XPS N 1s spectra was used to calculate the dendronization as expressed in the equation 1.

$$\%\ Dendonization = \frac{A_{399}}{A_{399}+A_{400}+A_{401}}(100\%) \qquad \text{(eq. S1)}$$

The integrated areas from the peaks centered at 399.0 eV, 400.1 eV and 401.2 eV that are attributed to the secondary amine formed from successful dendronization, the primary amine, and protonated amine signal are expressed as A_{399}, A_{400}, and A_{401}. The percent dendronization is calculated by dividing the A_{399} term, which is assigned to one equivalent of the assigned functional group. This term is divided by the denominator, which is composed of one total equivalent of amine in its unprotonated and protonated form and the secondary amine.

Triazole Formation: To determine the percent conversion of the alkynyl endgroups to triazoles, 1 equivalent of the signal that is assigned to each triazole formed is determined using equation 2. One equivalent of signal from triazole species A_{Tri} is equal to the change in the integrated area centered at 401.5 eV, $A_{401.5}$, minus the signal from the protonated amine species, as shown in equation 3. Equation 4 was derived to calculate this percent conversion, with an asterisk used to designate the integrated areas after 1,3 cycloaddition has occurred.

$$\frac{A_{399}}{A_{401.5}} = \frac{A*_{399}}{A*_{401.5}-A_{Tri}} \qquad \text{(eq.S2)}$$

$$A_{Tri} = A*_{401.5} - \left(\frac{A_{401.5}\cdot A*_{399}}{A_{399}}\right) \qquad \text{(eq. S3)}$$

$$\%\ Triazole\ Formation = \frac{A_{Tri}}{A^*_{399}}(100\%) \qquad \text{(eq. S4)}$$

The site composition of the triazole species was calculated by dividing one equivalent of the signal from the triazoles by one equivalent of signal from all of the species present (dendron, amine, and secondary amine). This was repeated for each species, as shown in equations 5, 6, and 7.

$$Total\ triazole\ \% = \frac{A_{Tri}}{A^*_{399}+A^*_{400}+A^*_{401.5}-2A_{Tri}} \qquad \text{(eq. S5)}$$

$$Total\ dendron\ \% = \frac{A^*_{399}}{A^*_{399}+A^*_{400}+A^*_{401.5}-2A_{Tri}} \qquad \text{(eq. S6)}$$

$$Total\ amine\ \% = \frac{A^*_{400}+A^*_{401.5}-3A_{Tri}}{A^*_{399}+A^*_{400}+A^*_{401.5}-2A_{Tri}} \qquad \text{(eq. S7)}$$

For surface **3**, equations were derived to determine the % triazole formation and the site composition. The N 1s spectrum for formation of surface **9** had no integrated area for a peak centered at 401.2 eV. Accordingly, $A_{401.5}$ was attributed to 1 equivalent of triazole.

Table S1. Yields for surface functionalization reactions and site composition calculations.

Slide	Reaction Yields		Site Compositions (for 3, 6, and 7)[a]		
	Dendronization (surface)	Triazole Formation (surface)	Amine	Amide or Dendron	Triazole
Single Layer		31% (**3**)	23%	49%	15%
Generation 1	36% (**4**)	31% (**6**)	53%	36%	11%
Generation 2	27% (**5**)	48% (**7**)	48%	30%	15%

[a]Adventitious N is not reported but was sometimes detected, which is why the site composition numbers do not always equal 100%.

References

(1) Chen, E. H.; Walter, S. R.; Nguyen, S. T.; Geiger, F. M. Arylsilanated Siox Surfaces for Mild and Simple Two-Step Click Functionalization with Small Molecules and Oligonucleotides. *J. Phys. Chem. C* **2012,** *116*, 19886-19892.

Chapter 3 XPS Spectra

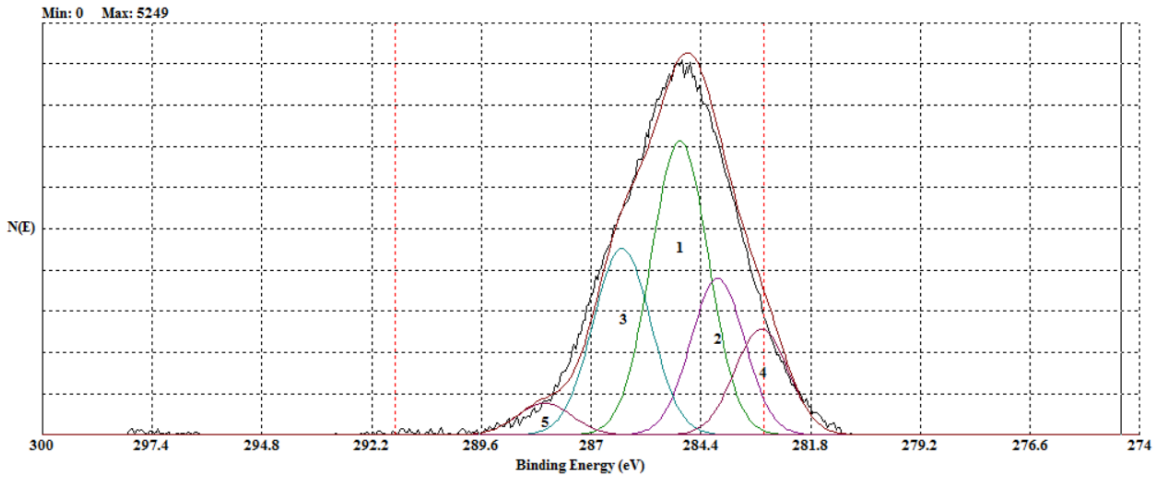

Figure 197: High resolution narrow scan of C 1s region of G3 dendronized surface. This surface was not described in the manuscript but was characterized as described for the dendronized surfaces. This surface was synthesized but not used in the studies described in Chapter 3.

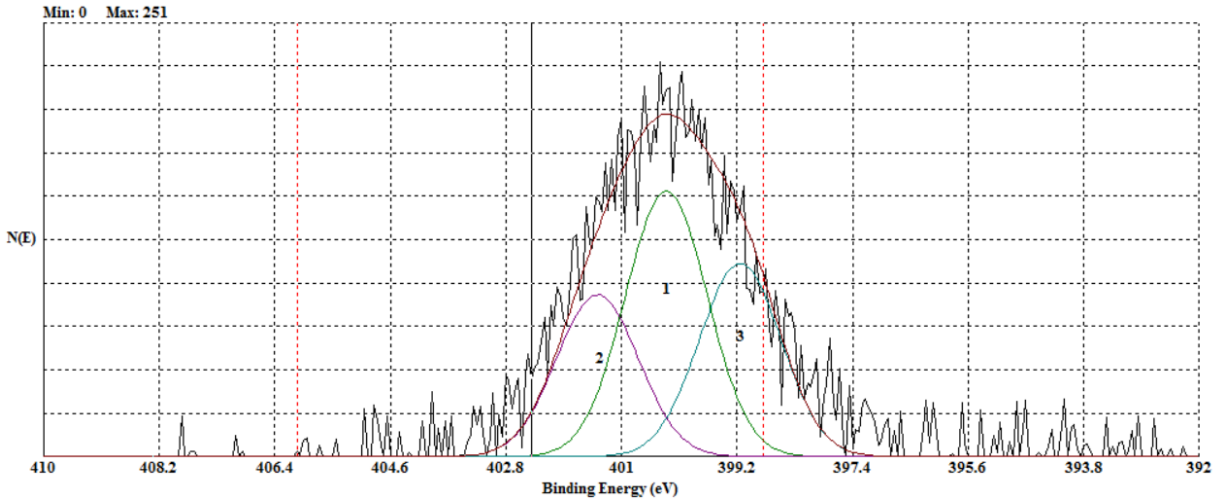

Figure 198: High resolution narrow scan of N 1s region of G3 dendronized surface. This surface was not described in the manuscript but was characterized as described for the dendronized surfaces. This surface was synthesized but not used in the studies described in Chapter 3.

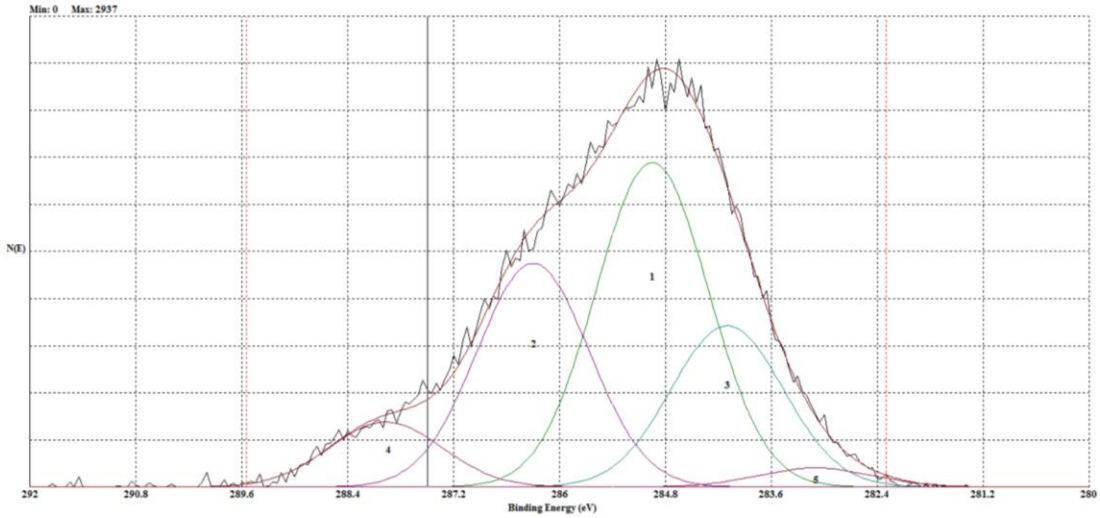

Figure 199: High resolution narrow scan of C 1s region of *β*-cyclodextrin functionalized G3 dendronized surface. This surface was not described in the manuscript but was characterized as described for the dendronized surfaces. This surface was synthesized but not used in the studies described in Chapter 3.

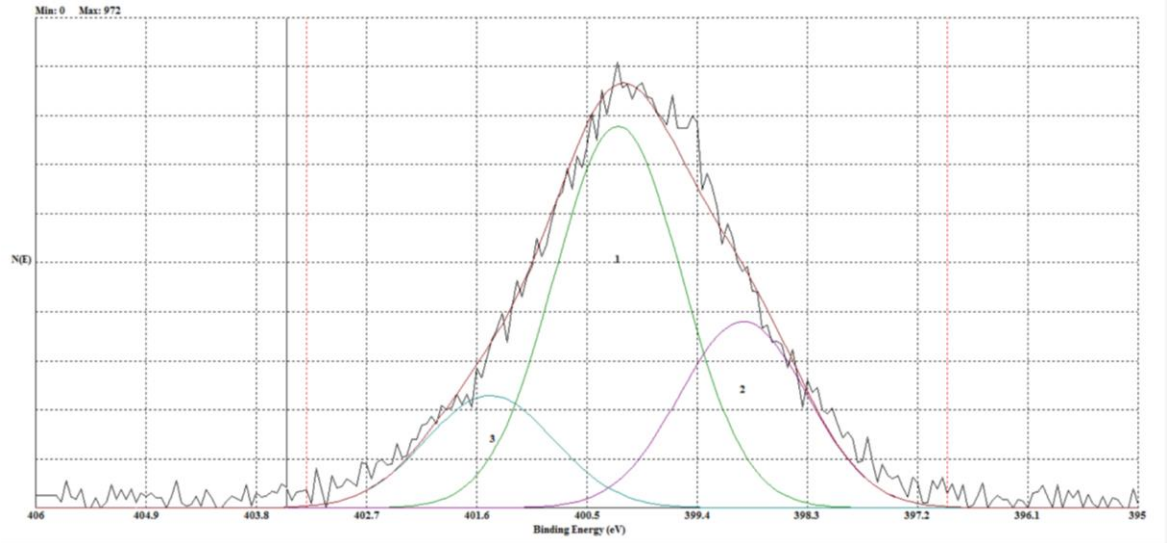

Figure 200: High resolution narrow scan of N 1s region of *β*-cyclodextrin functionalized G3 dendronized surface. This surface was not described in the manuscript but was characterized as described for the dendronized surfaces. This surface was synthesized but not used in the studies described in Chapter 3.

APPENDIX C

RELEVANT SPECTRAL DATA FROM CHAPTER FOUR

Chapter 4 XPS Spectra

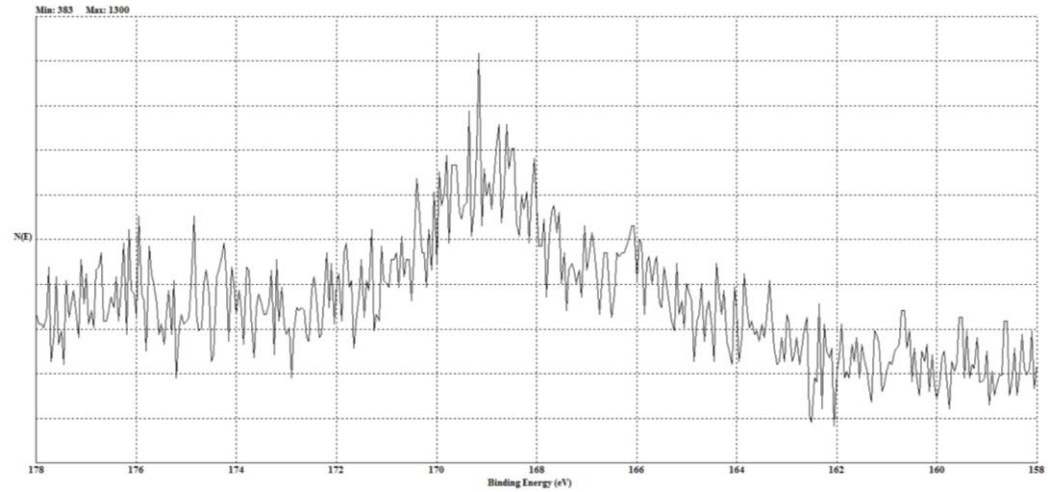

Figure 201: High resolution narrow scan of S 2p region of p-azidobenzenesulfonic acid **6**

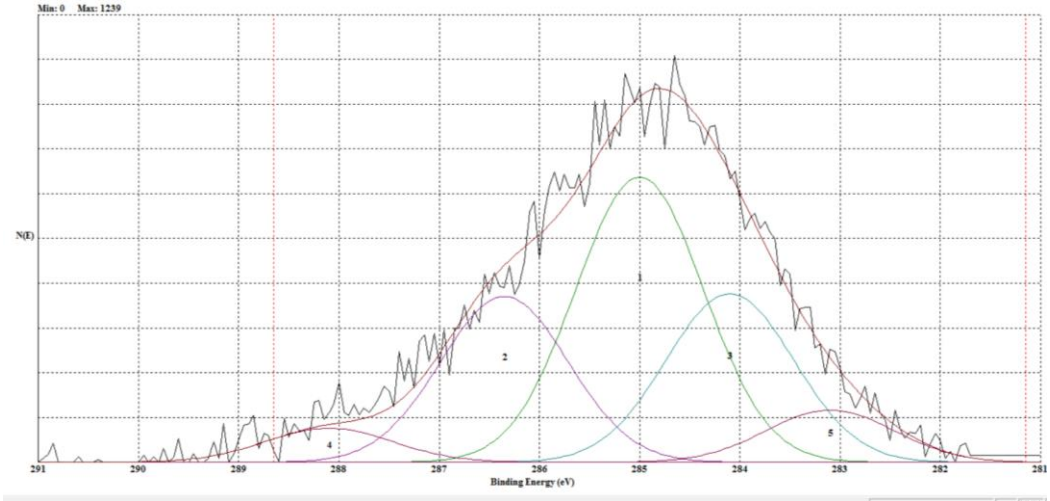

Figure 202: High resolution narrow scan of C 1s region of G1 dendronized surface **2**.

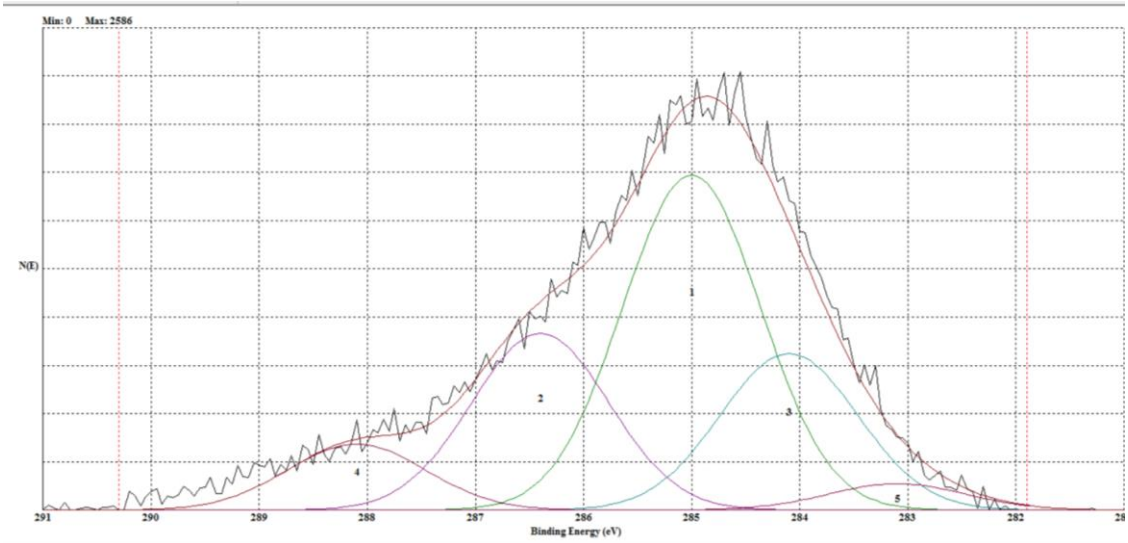

Figure 203: High resolution narrow scan of C 1s region of pyridine functionalized G1 dendronized surface **3**.

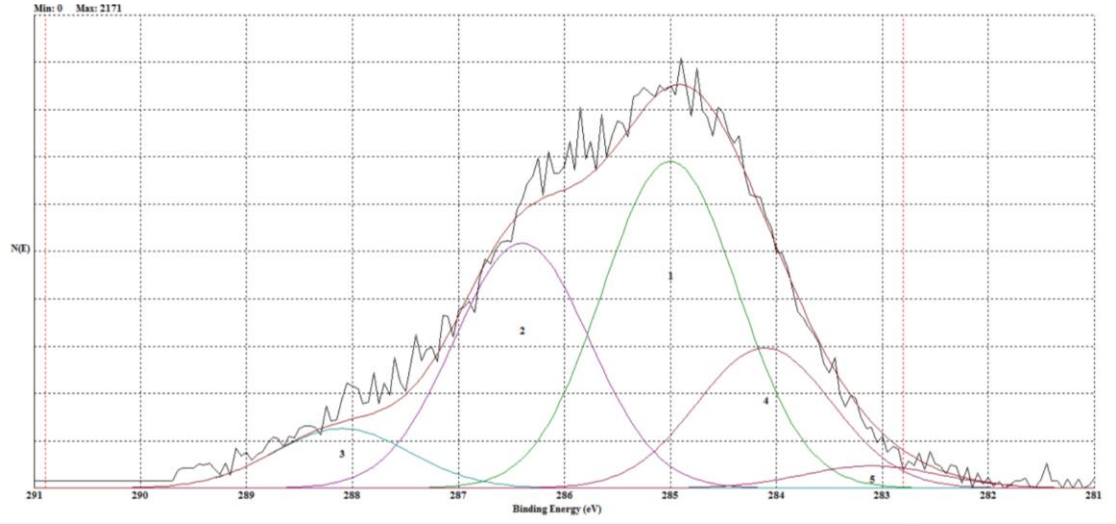

Figure 204: High resolution narrow scan of C 1s region of sulfonic acid functionalized G1 dendronized surface **7**.

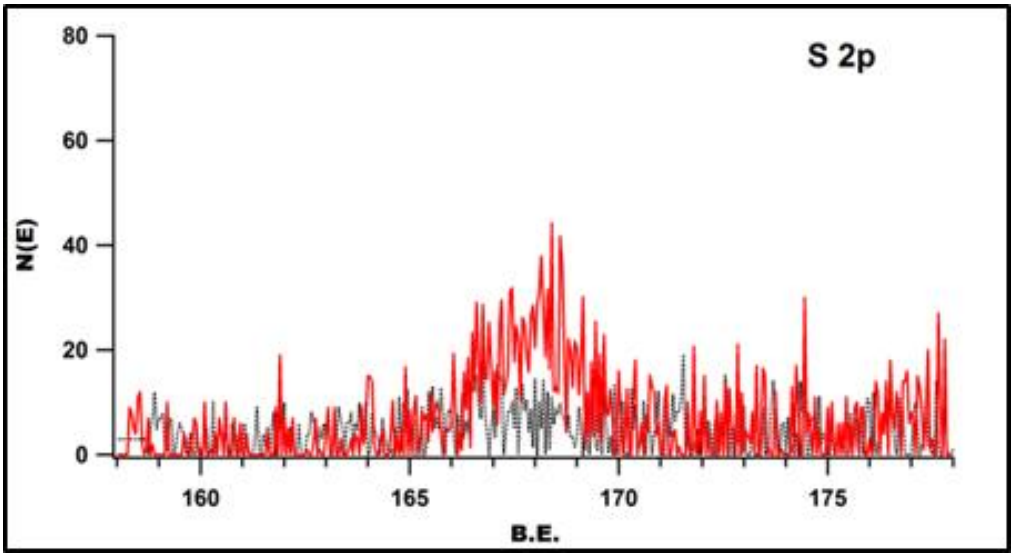

Figure 205: High resolution XPS narrow scan of the sulfur 2p region of surface **7.** The sulfur 2p signal of G1 dendronized surface **2** is absent as shown in the black trace of figure 18. The presence of the sulfur 2p signal of sulfonic acid functionalized surface **7** is shown as red trace.

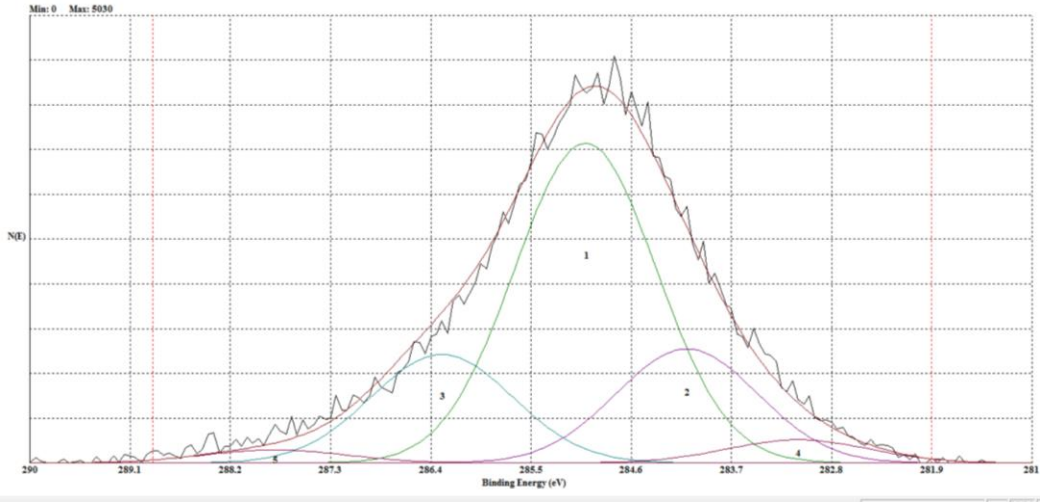

Figure 206: High resolution narrow scan of C 1s region of heterogeneously functionalized G1 dendronized surface **8**.

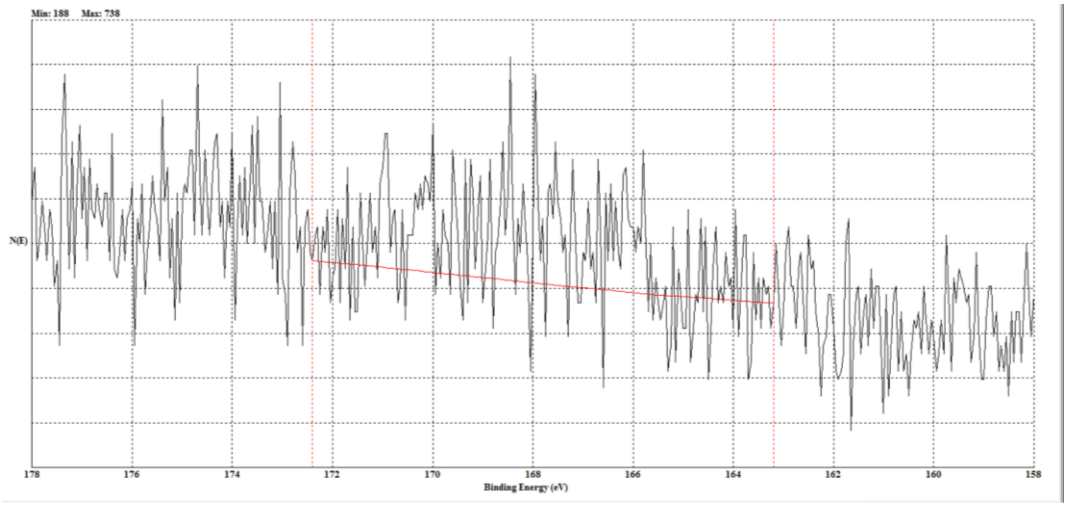

Figure 207: High resolution narrow scan of S 2p region of heterogeneously functionalized G1 dendronized surface **8**.

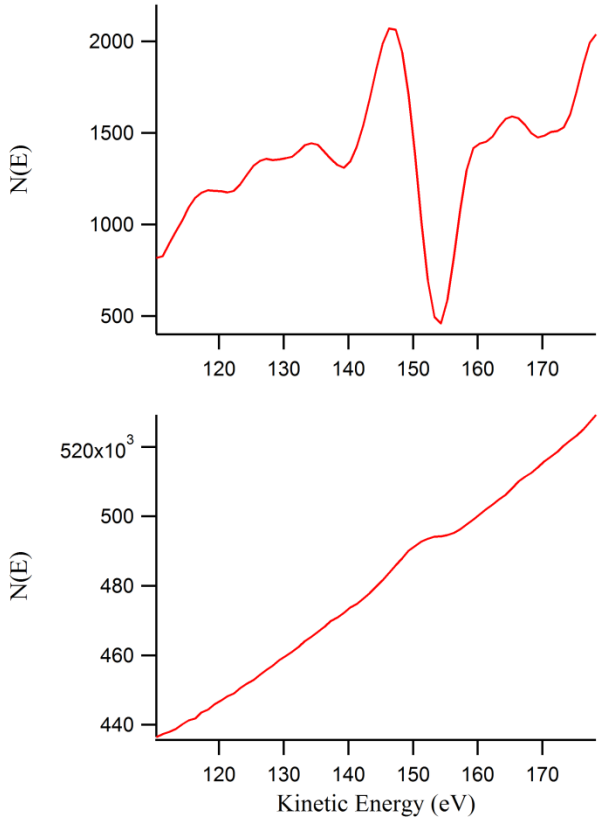

Figure 208: AES spectra from the high resolution scan of the sulfur LVV region for homogeneously functionalized G1 surface **7**. (a) The derivative of the sulfur signal (b) acquired from heterogeneously functionalized surface **7**.

Spectral Data

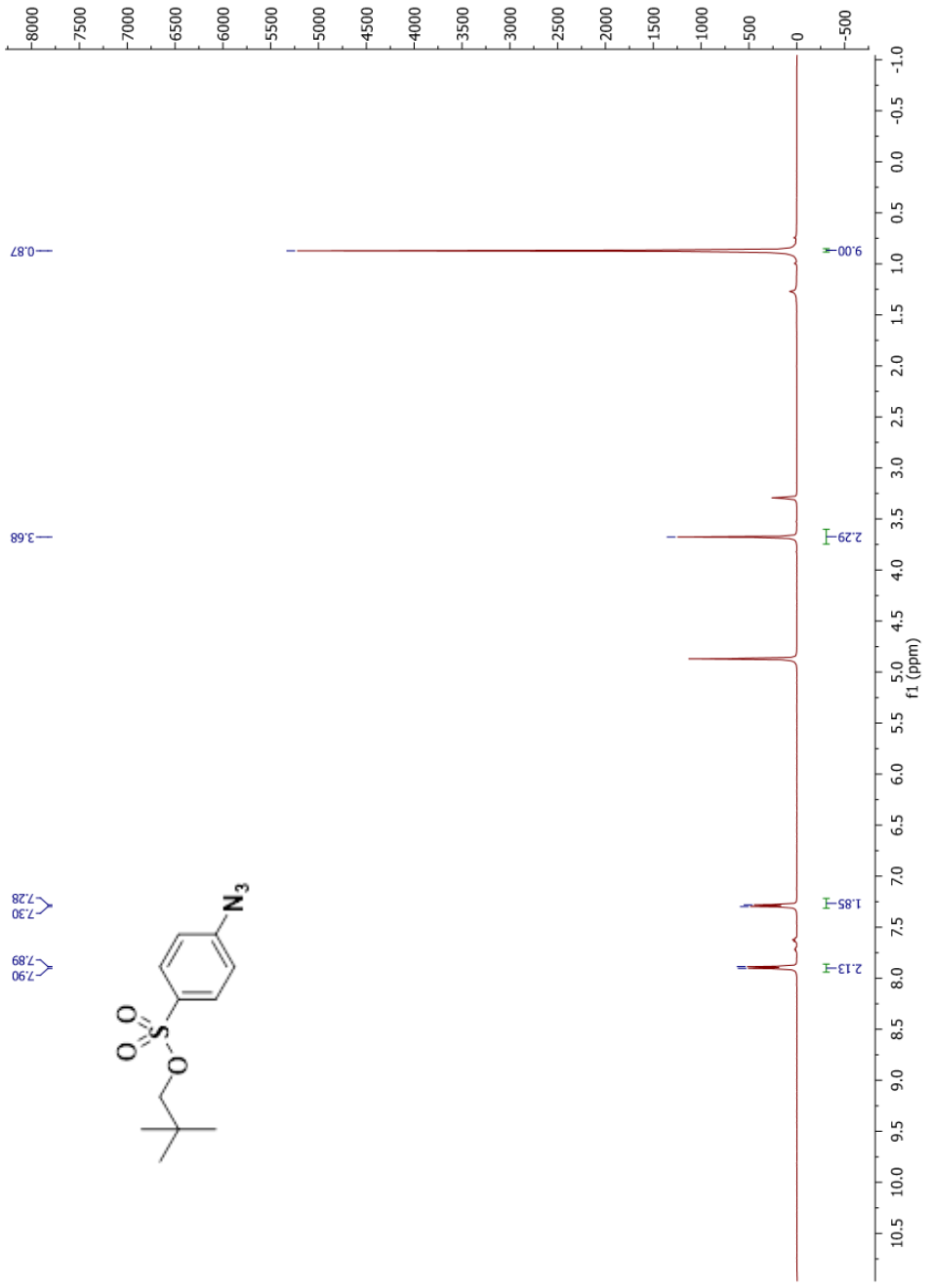

Figure 209: ^{1}H NMR spectrum (500 MHz, d_4-MeOD) of **5**.

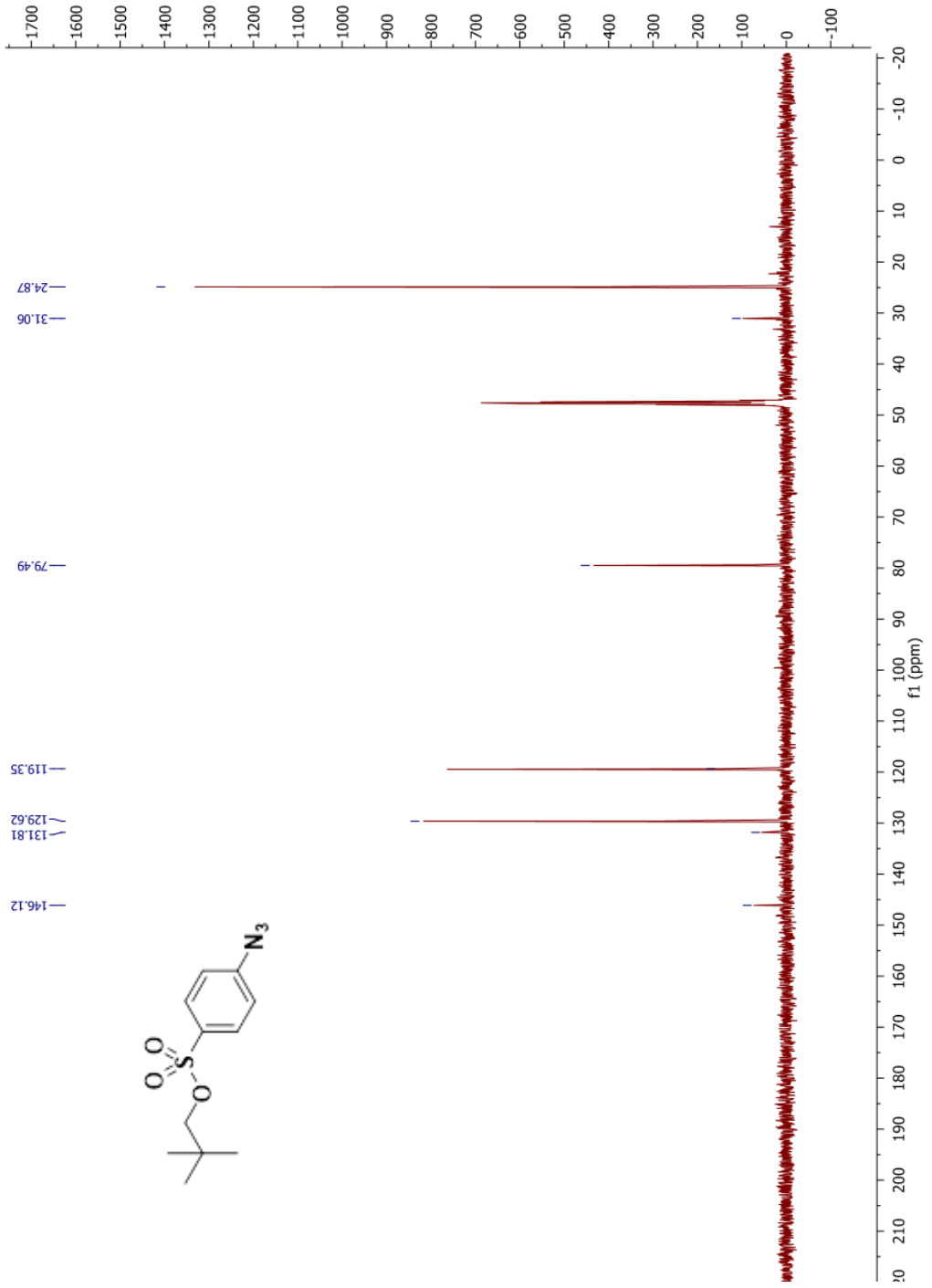

Figure 210: ^{13}C NMR spectrum (126 MHz, d_4-MeOD) of **5.**

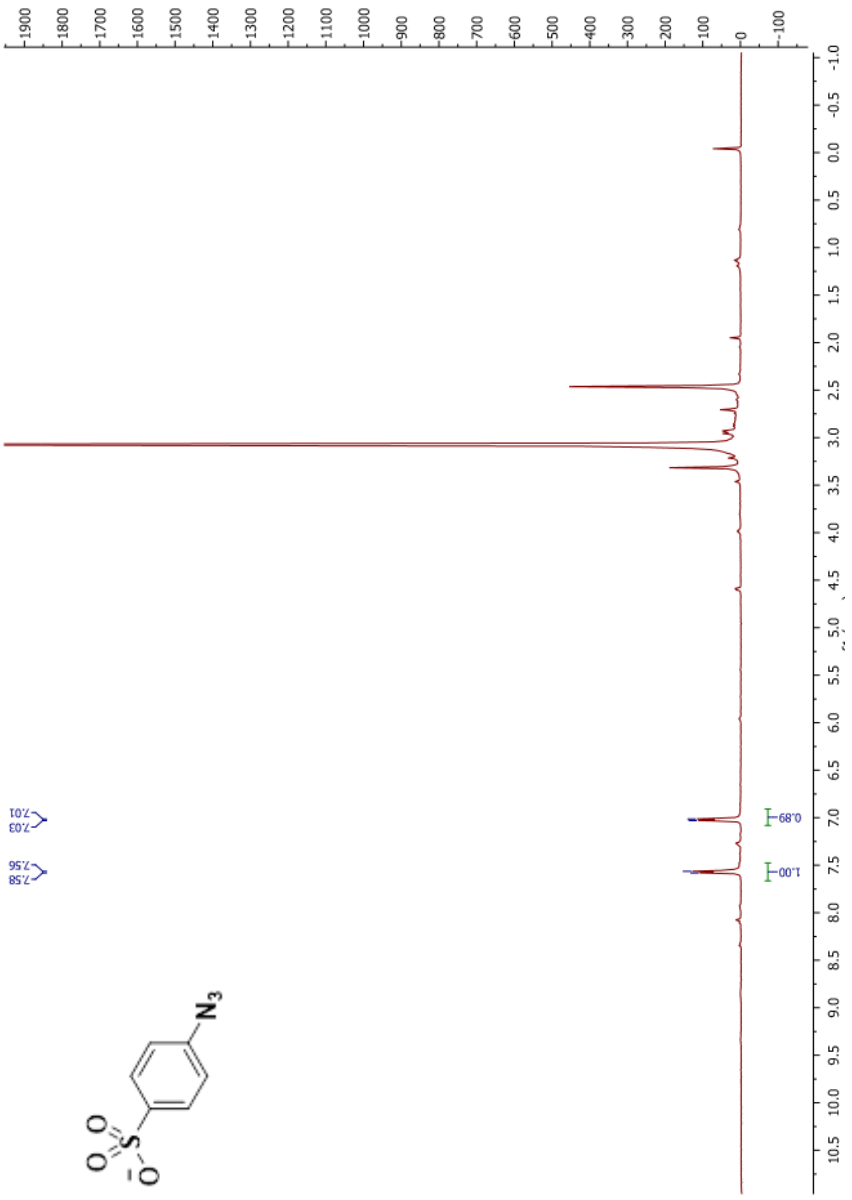

Figure 211: ^{1}H NMR spectrum (500 MHz, d_4-MeOD) of **6**.

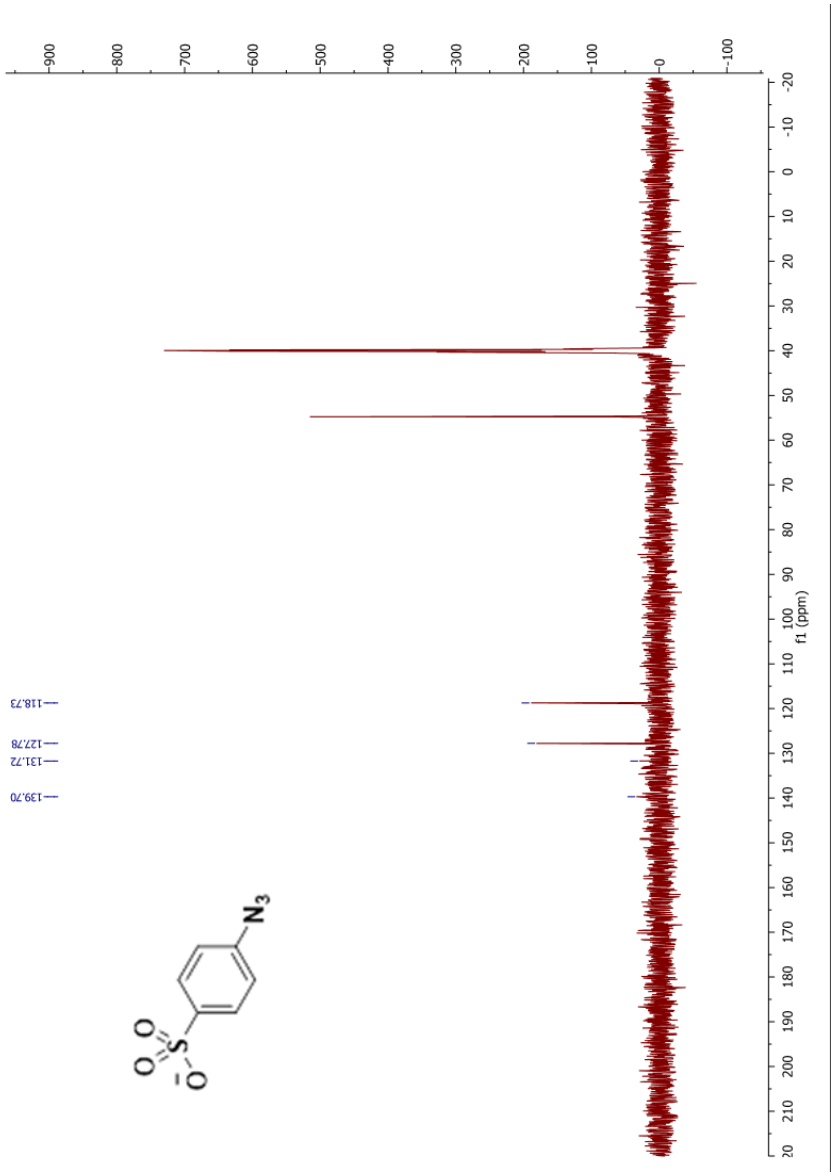

Figure 212: ^{13}C NMR spectrum (126 MHz, d_4-MeOD) of **6**

APPENDIX D

RELEVANT SPECTRAL DATA FROM CHAPTER FIVE

Chapter 5 XPS Spectra

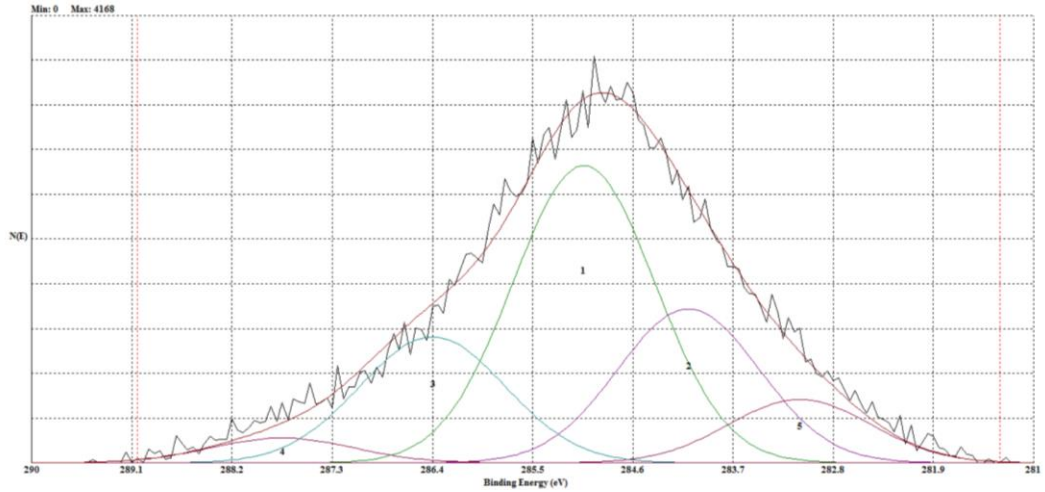

Figure 213: High resolution narrow scan of C 1s region of G1 dendronized surface **4.**

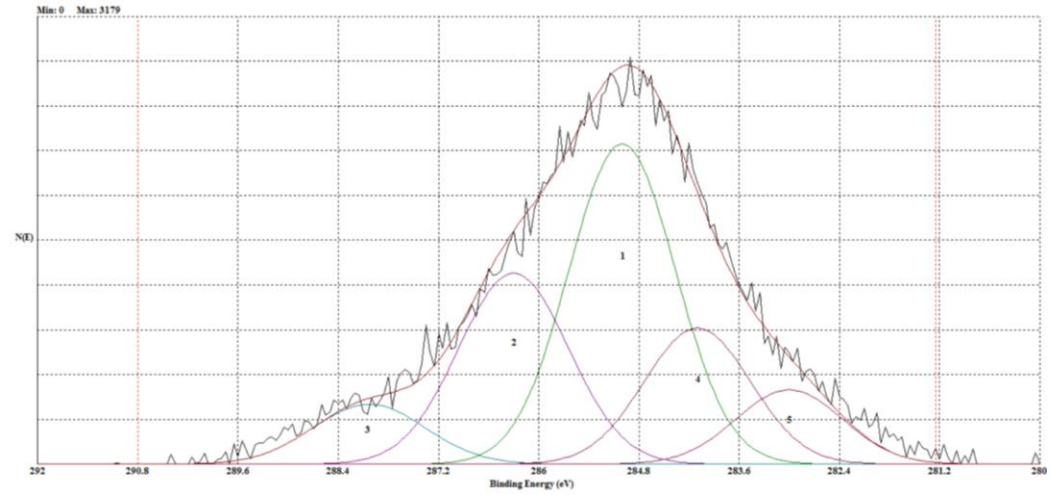

Figure 214: High resolution narrow scan of C 1s region of G1 dendronized surface **8.**

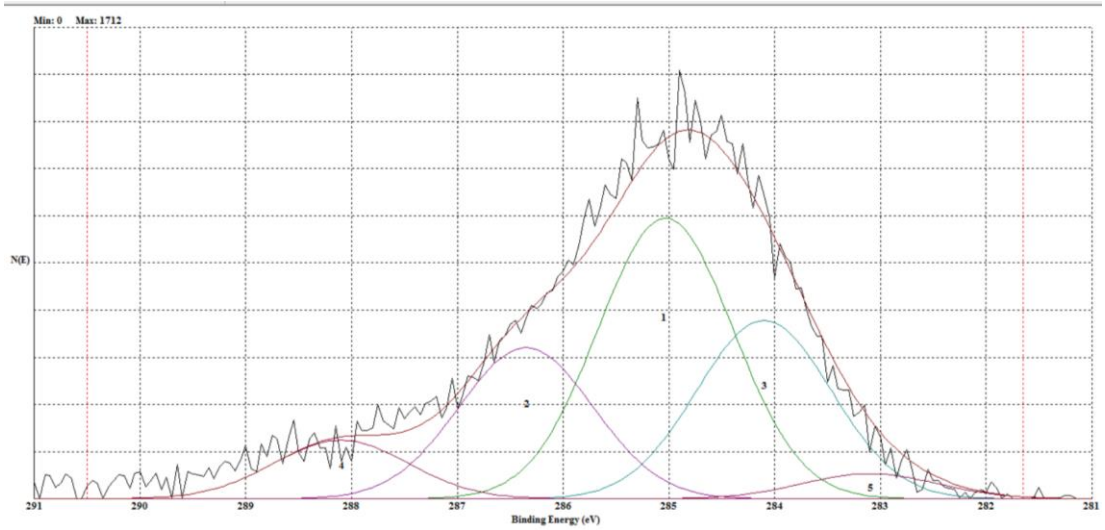

Figure 215: High resolution narrow scan of C 1s region of G1 dendronized surface **9.**

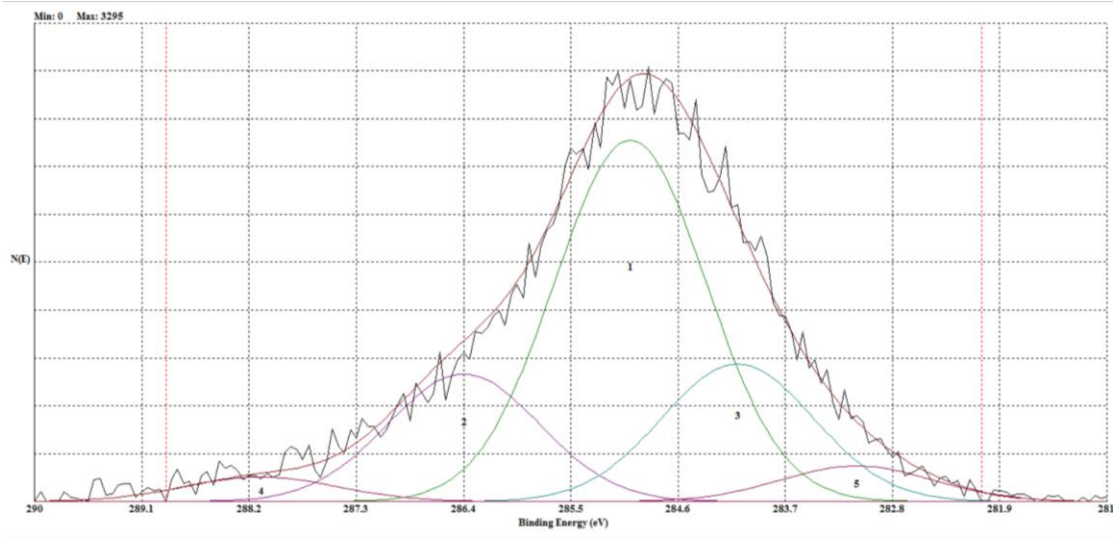

Figure 216: High resolution narrow scan of C 1s region of G1 dendronized surface **10.**

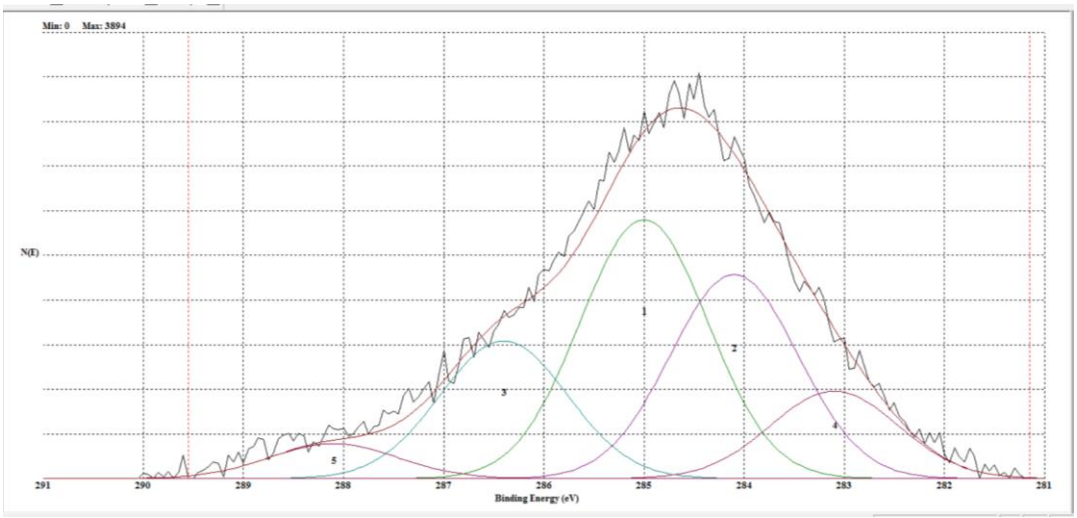

Figure 217: High resolution narrow scan of C 1s region of proline functionalized G2 dendronized surface **11.**

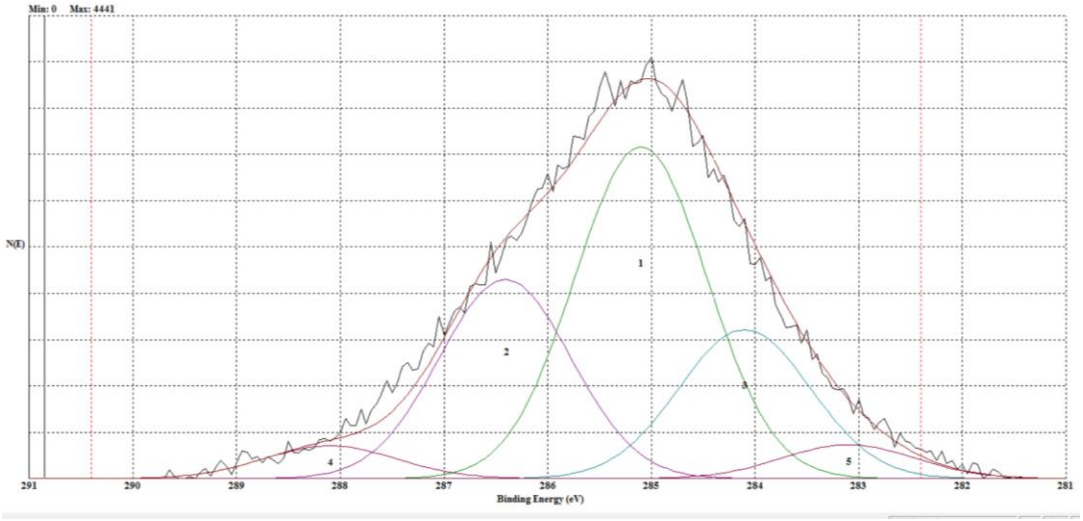

Figure 218: High resolution narrow scan of C 1s region of proline functionalized G2 dendronized surface **12.**

APPENDIX E

COPYRIGHT INFORMATION FOR REPRINTED MATERIALS

Figures 1.

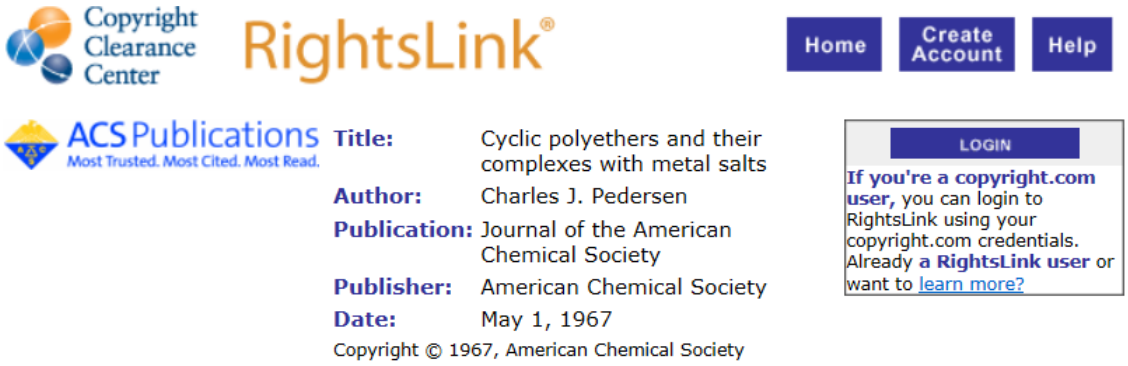

PERMISSION/LICENSE IS GRANTED FOR YOUR ORDER AT NO CHARGE

This type of permission/license, instead of the standard Terms & Conditions, is sent to you because no fee is being charged for your order. Please note the following:

- Permission is granted for your request in both print and electronic formats, and translations.
- If figures and/or tables were requested, they may be adapted or used in part.
- Please print this page for your records and send a copy of it to your publisher/graduate school.
- Appropriate credit for the requested material should be given as follows: "Reprinted (adapted) with permission from (COMPLETE REFERENCE CITATION). Copyright (YEAR) American Chemical Society." Insert appropriate information in place of the capitalized words.
- One-time permission is granted only for the use specified in your request. No additional uses are granted (such as derivative works or other editions). For any other uses, please submit a new request.

If credit is given to another source for the material you requested, permission must be obtained from that source.

BACK CLOSE WINDOW

Title: Host-guest complexation. 35. Spherands, the first completely preorganized ligand systems

Author: Donald J. Cram, Takahiro Kaneda, Roger C. Helgeson, et al

Publication: Journal of the American Chemical Society

Publisher: American Chemical Society

Date: Jun 1, 1985

PERMISSION/LICENSE IS GRANTED FOR YOUR ORDER AT NO CHARGE

This type of permission/license, instead of the standard Terms & Conditions, is sent to you because no fee is being charged for your order. Please note the following:

- Permission is granted for your request in both print and electronic formats, and translations.
- If figures and/or tables were requested, they may be adapted or used in part.
- Please print this page for your records and send a copy of it to your publisher/graduate school.
- Appropriate credit for the requested material should be given as follows: "Reprinted (adapted) with permission from (COMPLETE REFERENCE CITATION). Copyright (YEAR) American Chemical Society." Insert appropriate information in place of the capitalized words.
- One-time permission is granted only for the use specified in your request. No additional uses are granted (such as derivative works or other editions). For any other uses, please submit a new request.

If credit is given to another source for the material you requested, permission must be obtained from that source.

Copyright Clearance Center RightsLink®

Home | Account Info | Help

Title: Diaza-polyoxa-macrocycles et macrobicycles
Author: B. Dietrich,J.M. Lehn,J.P. Sauvage
Publication: Tetrahedron Letters
Publisher: Elsevier
Date: 1969

Logged in as:
Jessica ennist
LOGOUT

Order Completed

Thank you for your order.

This Agreement between Jessica ennist ("You") and Elsevier ("Elsevier") consists of your license details and the terms and conditions provided by Elsevier and Copyright Clearance Center.

Your confirmation email will contain your order number for future reference.

Printable details.

License Number	4102661158594
License date	May 05, 2017
Licensed Content Publisher	Elsevier
Licensed Content Publication	Tetrahedron Letters
Licensed Content Title	Diaza-polyoxa-macrocycles et macrobicycles
Licensed Content Author	B. Dietrich,J.M. Lehn,J.P. Sauvage
Licensed Content Date	1969
Licensed Content Volume	10
Licensed Content Issue	34
Licensed Content Pages	4
Type of Use	reuse in a thesis/dissertation
Portion	figures/tables/illustrations
Number of figures/tables/illustrations	1
Format	both print and electronic
Are you the author of this Elsevier article?	No
Will you be translating?	No
Order reference number	
Original figure numbers	Figure 1
Title of your thesis/dissertation	THE SYNTHESIS OF N-ACETYLLACTOSAMINE FUNCTIONALIZED DENDRIMERS, AND THE FUNCTIONALIZATION OF SILICA SURFACES USING TUNABLE DENDRONS AND β-CYCLODEXTRINS
Expected completion date	Jun 2017
Estimated size (number of pages)	350
Elsevier VAT number	GB 494 6272 12
Requestor Location	Jessica ennist 103 Chemistry and Biochemistry Montana State university bozeman mt 59718 BOZEMAN, MT 59718 United States Attn: Jessica ennist
Publisher Tax ID	98-0397604
Total	0.00 USD

ORDER MORE | CLOSE WINDOW

Figure 6.

Copyright Clearance Center RightsLink®

Home | Account Info | Help

Title: Lactose-Functionalized Dendrimers Arbitrate the Interaction of Galectin-3/MUC1 Mediated Cancer Cellular Aggregation
Author: Anna K. Michel,Pratima Nangia-Makker,Avraham Raz,Mary J. Cloninger
Publication: ChemBioChem
Publisher: John Wiley and Sons
Date: Aug 19, 2014

Logged in as:
Jessica ennist
Account #: 3001148252
LOGOUT

Order Completed

Thank you for your order.

This Agreement between Jessica ennist ("You") and John Wiley and Sons ("John Wiley and Sons") consists of your license details and the terms and conditions provided by John Wiley and Sons and Copyright Clearance Center.

Your confirmation email will contain your order number for future reference.

Printable details.

License Number	4104390293788
License date	May 08, 2017
Licensed Content Publisher	John Wiley and Sons
Licensed Content Publication	ChemBioChem
Licensed Content Title	Lactose-Functionalized Dendrimers Arbitrate the Interaction of Galectin-3/MUC1 Mediated Cancer Cellular Aggregation
Licensed Content Author	Anna K. Michel,Pratima Nangia-Makker,Avraham Raz,Mary J. Cloninger
Licensed Content Date	Aug 19, 2014
Licensed Content Pages	7
Type of use	Dissertation/Thesis
Requestor type	University/Academic
Format	Print and electronic
Portion	Figure/table
Number of figures/tables	1
Original Wiley figure/table number(s)	Figure 1
Will you be translating?	No
Title of your thesis / dissertation	THE SYNTHESIS OF N-ACETYLLACTOSAMINE FUNCTIONALIZED DENDRIMERS, AND THE FUNCTIONALIZATION OF SILICA SURFACES USING TUNABLE DENDRONS AND β-CYCLODEXTRINS
Expected completion date	Jun 2017
Expected size (number of pages)	350
Requestor Location	Jessica ennist 103 Chemistry and Biochemistry Montana State university bozeman mt 59718 BOZEMAN, MT 59718 United States Attn: Jessica ennist
Publisher Tax ID	EU826007151
Billing Type	Invoice
Billing address	Jessica ennist 103 Chemistry and Biochemistry Montana State university bozeman mt 59718 BOZEMAN, MT 59718 United States Attn: Jessica ennist
Total	0.00 USD

Would you like to purchase the full text of this article? If so, please continue on to the content ordering system located here: Purchase PDF

If you click on the buttons below or close this window, you will not be able to return to the content ordering system.

ORDER MORE | CLOSE WINDOW

Figure 8.

Copyright Clearance Center RightsLink®

Home | Account Info | Help

Title: Introduction to galectins
Author: Hakon Leffler
Publication: Glycoconjugate Journal
Publisher: Springer
Date: Jan 1, 2002
Copyright © 2002, Kluwer Academic Publishers

Logged in as:
Jessica ennist
Account #: 3001148252
LOGOUT

Order Completed

Thank you for your order.

This Agreement between Jessica ennist ("You") and Springer ("Springer") consists of your license details and the terms and conditions provided by Springer and Copyright Clearance Center.

Your confirmation email will contain your order number for future reference.

Printable details.

License Number	4106650408454
License date	May 12, 2017
Licensed Content Publisher	Springer
Licensed Content Publication	Glycoconjugate Journal
Licensed Content Title	Introduction to galectins
Licensed Content Author	Hakon Leffler
Licensed Content Date	Jan 1, 2002
Licensed Content Volume	19
Licensed Content Issue	7
Type of Use	Thesis/Dissertation
Portion	Figures/tables/illustrations
Number of figures/tables/illustrations	3
Author of this Springer article	No
Order reference number	
Original figure numbers	Figure 3
Title of your thesis / dissertation	THE SYNTHESIS OF N-ACETYLLACTOSAMINE FUNCTIONALIZED DENDRIMERS, AND THE FUNCTIONALIZATION OF SILICA SURFACES USING TUNABLE DENDRONS AND β-CYCLODEXTRINS
Expected completion date	Jun 2017
Estimated size(pages)	350
Requestor Location	Jessica ennist 103 Chemistry and Biochemistry Montana State university bozeman mt 59718 BOZEMAN, MT 59718 United States Attn: Jessica ennist
Billing Type	Invoice
Billing address	Jessica ennist 103 Chemistry and Biochemistry Montana State university bozeman mt 59718 BOZEMAN, MT 59718 United States Attn: Jessica ennist
Total	0.00 USD

ORDER MORE | CLOSE WINDOW

Figure 11.

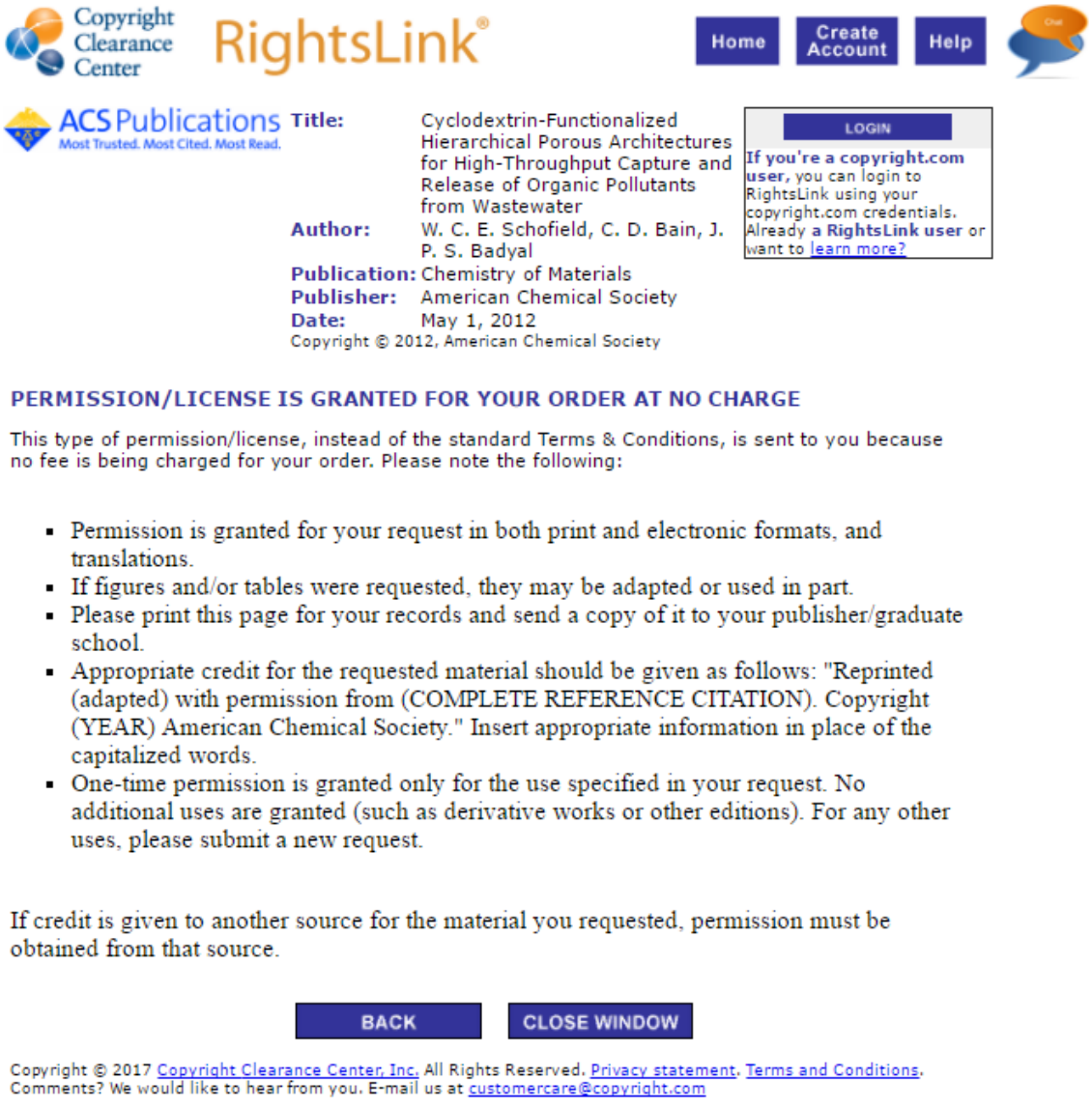

Copyright Clearance Center RightsLink®

Home | Create Account | Help

ACS Publications
Most Trusted. Most Cited. Most Read.

Title: Cyclodextrin-Functionalized Hierarchical Porous Architectures for High-Throughput Capture and Release of Organic Pollutants from Wastewater
Author: W. C. E. Schofield, C. D. Bain, J. P. S. Badyal
Publication: Chemistry of Materials
Publisher: American Chemical Society
Date: May 1, 2012
Copyright © 2012, American Chemical Society

LOGIN

If you're a copyright.com user, you can login to RightsLink using your copyright.com credentials. Already a RightsLink user or want to learn more?

PERMISSION/LICENSE IS GRANTED FOR YOUR ORDER AT NO CHARGE

This type of permission/license, instead of the standard Terms & Conditions, is sent to you because no fee is being charged for your order. Please note the following:

- Permission is granted for your request in both print and electronic formats, and translations.
- If figures and/or tables were requested, they may be adapted or used in part.
- Please print this page for your records and send a copy of it to your publisher/graduate school.
- Appropriate credit for the requested material should be given as follows: "Reprinted (adapted) with permission from (COMPLETE REFERENCE CITATION). Copyright (YEAR) American Chemical Society." Insert appropriate information in place of the capitalized words.
- One-time permission is granted only for the use specified in your request. No additional uses are granted (such as derivative works or other editions). For any other uses, please submit a new request.

If credit is given to another source for the material you requested, permission must be obtained from that source.

BACK | CLOSE WINDOW

Copyright © 2017 Copyright Clearance Center, Inc. All Rights Reserved. Privacy statement. Terms and Conditions.
Comments? We would like to hear from you. E-mail us at customercare@copyright.com

Figure 13

Copyright Clearance Center RightsLink®

Home | Create Account | Help

ACS Publications
Most Trusted. Most Cited. Most Read.

Title: Proline-Catalyzed Direct Asymmetric Aldol Reactions
Author: Benjamin List, Richard A. Lerner, Carlos F. Barbas
Publication: Journal of the American Chemical Society
Publisher: American Chemical Society
Date: Mar 1, 2000
Copyright © 2000, American Chemical Society

LOGIN

If you're a copyright.com user, you can login to RightsLink using your copyright.com credentials. Already a RightsLink user or want to learn more?

PERMISSION/LICENSE IS GRANTED FOR YOUR ORDER AT NO CHARGE

This type of permission/license, instead of the standard Terms & Conditions, is sent to you because no fee is being charged for your order. Please note the following:

- Permission is granted for your request in both print and electronic formats, and translations.
- If figures and/or tables were requested, they may be adapted or used in part.
- Please print this page for your records and send a copy of it to your publisher/graduate school.
- Appropriate credit for the requested material should be given as follows: "Reprinted (adapted) with permission from (COMPLETE REFERENCE CITATION). Copyright (YEAR) American Chemical Society." Insert appropriate information in place of the capitalized words.
- One-time permission is granted only for the use specified in your request. No additional uses are granted (such as derivative works or other editions). For any other uses, please submit a new request.

If credit is given to another source for the material you requested, permission must be obtained from that source.

BACK | CLOSE WINDOW

Copyright © 2017 Copyright Clearance Center, Inc. All Rights Reserved. Privacy statement. Terms and Conditions.
Comments? We would like to hear from you. E-mail us at customercare@copyright.com